

Integrated Microsystems for Wireless Sensing
Applications

Thesis by
Muhammad Mujeeb-U-Rahman

In Partial Fulfillment of the Requirements for the degree
of
Doctor of Philosophy



CALIFORNIA INSTITUTE OF TECHNOLOGY

Pasadena, California

2014

(Defended 05 March, 2014)

Dedicated to

To my parents Muhammad Latif Babar and Musfra Begum,

my siblings,

my Wife Zain Javeria and our kids

Muhammad Arshman and Muhammad Ayaan.

ACKNOWLEDGEMENTS

When I look back towards my journey as a graduate student, I feel very lucky to be around such good people without whom I would not be able to achieve anything. I feel that I was very lucky to be able to become part of this prestigious institute and be able to work with such intelligent and wonderful people. I am really thankful to the entire Caltech community for providing such an awesome research experience and in making the difficult jobs easy for everyone.

I would like to specially thank Professor Scherer for taking me into his group and guiding me continuously in every aspect of research. He always encouraged me and appreciated every small thing that I did in my work. He kept smiling and made me laugh whenever things were not working. He went to the lab with me and helped me in every way a mentor can. His understanding of the most important and fundamental challenges in doing complex tasks is amazing and every discussion with him encouraged me to try something new and to work harder. I will always be indebted to him for his teaching and training.

I also want to thank the Electrical Engineering department in arranging and teaching such diverse and in depth curriculum. I especially like to thank Professor Ali Hajimiri for teaching analog circuit design which helped me a lot in my research work. I also like to thank Professor Sandy Weinreb for letting us use his equipment for testing our devices. I would also like to thank Professor Hyuck Choo for his continuous encouragement and understanding during our brief meetings. I am also thankful to Professor David Rutledge and Professor Scott Fraser for their encouraging comments during my candidacy. I got many interesting ideas from the discussions and also got to expand my thinking about the project. Finally, I will like to thank Dr. Joyce Wong for her kind suggestions.

I would also like to thank the entire Scherer group, both current and previous members. I would specially like to mention Mehmet Sencan who has worked with me since the beginning of this project and has been a part of all the ups and downs during this process. I believe he has a very good research career ahead of him and his experience from this project would help him a lot in the future. My special thanks are for Meisam Honarvar Nazari. Meisam is an expert in circuit design and he taught me a lot about circuit designs during my initial years at Caltech. Also, since he has been a member of Scherer group beginning last year, he helped us achieve our goals for this project in a short period and has worked very hard to make this happen. I also want to thank Sith

Domrongkitchaiporn for his help with tedious parts of packaging and testing. I would also like to thank Akram Sadek for his help during the middle phase of this project. He taught me a lot about medical sciences and technology and I am very grateful to him for that. My special thanks are also for Jeff Chang and Dvin Adalian for their help with different aspects of the project. I also like to thank Sameer Walavalkar, Andrew Homyk and Jingqing Huang for teaching me intricacies of nanofabrication. I am also thankful to Dr. William Fegadolli for sharing the troubles of refining recipes and processing as we both started nanofabrication at almost the same time. Finally, I am thankful to everyone else who has been supportive and encouraging to me and helped me with different aspects of the project; Imran Malik, Mark Goldberg, Xiomara Madero, Erika Garcia, Max Jones, Samuel Njoroge you are all awesome people.

I should also thank Professor Scherer's administrative assistant Kate Finigan who helped me during the entire research project in getting materials and supplies on time to be able to meet all the deadlines. She has also facilitated my work with undergraduate students that has helped me achieving good mentoring experience.

My special thanks are for Sanofi for providing resources for this project. I like to thank Dr. Oliver Plettenburg and Dr. Matthias Lohen for their help with different aspects of the project. I am also grateful to MOSIS and CMP for providing access to circuit fabrication for this research. I am thankful to Kavli Nanoscience Institute (KNI) at Caltech and the staff there who makes doing fabrication so much easier for all of us.

I would like to thank my family, my father Muhammad Latif Babar and my mother Musfra Begum who always loved me and encouraged me to follow my dreams despite of all the problems they had to face for that. They always took care of all my needs so that I could focus on my studies. I would have never made it without their help. It was their training that helped me become what I am now. My siblings have always respected me and loved me even though I could not do much for them due to my busy schedule. Finally, my special thanks are for my wife Zain Javeria, who stood with me when I was alone and whose support gave me strength to pursue the research goals that I had set. I also want to thank her for taking care of our kids, Muhammad Arshman and Muhammad Ayaan, while I was busy doing my research.

Thank you all for being part of my life!

ABSTRACT

Personal health monitoring is being considered the future of a sustainable health care system. Biosensing platforms are a very important component of this system. Real-time and accurate sensing is essential for the success of personal health care model. Currently, there are many efforts going on to make these sensors practical and more useful for such measurements. Implantable sensors are considered the most widely applicable and most reliable sensors for such accurate health monitoring applications. However, macroscopic (cm scale) size has proved to be a limiting factor for successful use of these systems for long time and in large numbers. This work is focused to resolve the issues related with miniaturizing these devices to a microscopic (mm scale) size scale which can minimize many practical difficulties associated with their larger counterparts currently.

To accomplish this goal of miniaturization while retaining or even improving on the necessary capabilities for such sensing platforms, an integrated approach is presented which focuses on system-level miniaturization using standard fabrication procedures. First, it is shown that a completely integrated and wireless system is the best solution to achieve desired miniaturization without sacrificing the functionality of the system. Hence, design and implementation of the different components comprising the complete system needs to be done according to the requirements of the overall integrated system. This leads to the need of on-chip functional sensors, integrated wireless power supply, integrated wireless communication and integrated control system for realization of such system. In this work, different options for implementation of each of these subsystems are compared and an optimal solution is presented for each subsystem. For such complex systems, it is imperative to use a standard fabrication process which can provide the required functionality for all subsystems at smallest possible size scale. Complementary Metal Oxide Semiconductor (CMOS) process is the most appropriate of the technologies in this regard

and has enabled incredible miniaturization of the computing industry. It also provides options for designing different subsystems on the same platform in a monolithic process with very high yield. This choice then leads to actual designs of subsystems in the CMOS technology using different possible methods. Careful comparison of these subsystems provides insights into different design adjustments that are made until the desired functions are achieved at the desired size scale. Integration of all these compatible subsystems in the same platform is shown to provide the smallest possible sensing platform to date.

The completely wireless system can measure a host of different important analyte and can transmit the data to an external device which can use it for appropriate purpose. Results on measurements in phosphate buffer solution, blood serum and whole blood along with wireless communication in real biological tissues are provided. Specific examples of glucose and DNA sensors are presented and the use for many other relevant applications is also proposed. Finally, insights into animal model studies and future directions of the research are discussed.

Contents

Chapter 1 Problem Introduction	26
1.1 Biomedical Measurements: State-of-the-Art.....	28
1.2 Miniaturized Implants	35
1.3 Need for new Technology.....	36
1.4 Thesis Focus	37
1.5 Thesis Outline.....	37
Chapter 2 System Design	39
2.1 Design Perspectives.....	40
2.1.1 Biocompatibility	44
2.2 Proposed Design.....	46
2.3 Summary.....	48
Chapter 3 Integrated Sensor	49
3.1 Basic Electrochemistry.....	51
3.2 Sensor Design and Operation.....	53
3.3 Material Aspects.....	62
3.4 Patterned Electrochemical Sensors	71

3.5 Electrochemical Measurements	75
3.6 Surface Functionalization.....	82
3.7 Enzyme Kinetics.....	84
3.8 Glucose Sensing	87
3.8.1 Testing in Body Fluids	94
3.8.2 Interference Issues	97
3.8.3 Lifetime and Repeatability	103
3.8.4 Optimization of Sensor Response	107
3.9 Nucleic Acid Sensing	110
3.9.1 Sensor Design	110
3.9.2 Functionalization	110
3.9.3 Results.....	112
3.10 Protein Sensing.....	115
3.10.1 Sensor Design and Testing.....	115
3.11 pH Sensing.....	117
3.12 Simultaneous Sensing of Multiple Analyte	119
3.13 Comparison of Electrochemical Measurement Techniques.....	119
3.14 Summary.....	119

Chapter 4 Wireless Powering	121
4.1 Optical Properties of Tissue	122
4.2 Modeling Light Transport in Tissue	127
4.3 Design of CMOS Power Harvesting System.....	129
4.4 CMOS PV Design	134
4.5 Testing and Results.....	143
4.6 Effect of Tissue on Power Transfer:	148
4.6.1 Thermal Effects	149
4.6.2 Effects of Non-uniform Illumination	150
4.7 Compound Semiconductor Photodiodes.....	150
4.8 Silicon-on-Insulator (SOI) based Power Harvesting System.....	151
4.9 Safety Issues	153
4.10 Electrical Power Transfer.....	155
4.11 Optimizing Electrical Power Transfer	164
4.12 Implementation of Electrical Powering	165
4.12.1 Proof-of-Concept using Discrete Coils	165
4.12.2 PCB based Design	167
4.12.3 Silicon Based Custom Designs	168

4.12.4 Integrated Coil Design.....	173
4.12.5 External Device	177
4.13 RF Safety and Regulatory Issues	177
4.14 Comparison of Power Harvesting Methods.....	179
4.15 Summary.....	180
Chapter 5 Wireless Telemetry	181
5.1 Optical Telemetry	183
5.2 Optical Telemetry Link Design.....	184
5.2.1 Optical Transmitter.....	184
5.2.2 Optical Receiver Design.....	186
5.3 Optical Link Capacity	188
5.4 Alignment in Optical Telemetry Links	190
5.5 Optimum Modulation Scheme	191
5.6 Optical Telemetry Circuit.....	192
5.7 Communication through Skin and Tissue.....	198
5.8 Effect of Power Laser	200
5.9 Reverse Link Design	201
5.10 Optical Communication Results	201

5.11 Electrical Telemetry	203
5.11.1 Electrical Link Capacity	206
5.12 Electrical Telemetry Designs	207
5.12.1 Discrete Coil Design.....	207
5.12.2 PCB Design	208
5.12.3 CMOS Design.....	209
5.13 Reverse Telemetry.....	209
5.14 Comparison of Telemetry Schemes	210
5.15 Summary.....	210
Chapter 6 Control Circuit.....	211
6.1 Low Power Potentiostat Design.....	213
6.2 Potentiostat Readout Circuit.....	217
6.3 Reference Voltage Generation	220
6.4 Control Circuit Testing.....	220
6.5 Ultra-Low Power Control Circuit	223
6.6 Summary	224
Chapter 7 Conclusion and Future Directions	225
7.1 Fully Integrated Systems	225

7.1.1 Version 1	225
7.1.2 Version 2	226
7.1.3 Version 3	228
7.2 Conclusion	231
7.3 Original Contributions of this work	231
7.4 Work in Progress	232
7.4.1 Special Shapes	232
7.4.2 Compensating lag between ISF and blood values	232
7.4.3 Optimal Implantation Site	233
7.4.4 Implantation Procedure	234
7.4.5 Body Powered Implants	235
7.4.6 Enhancing Biocompatibility	235
7.4.7 Sterilization	237
7.4.8 In-vivo Testing	237
7.4.9 Future Applications	237
7.4.10 Sensor Calibration	238
7.5 Software Development	238
Chapter 8 Experimental Methods	239

8.1 Fabrication	239
8.1.1 Planar Sensors.....	239
8.1.2 Micro/Nanopatterned Sensors.....	241
8.1.3 Nano sensors on CMOS	247
8.2 Sensor Functionalization	248
8.3 Sensor Cleaning.....	249
8.4 Nucleic Acid Functionalization.....	250
8.5 Sensor Testing	251

Appendix I**Appendix II****Appendix III****Bibliography**

List of Figures

Figure 1 : Personal Health Care Network.....	27
Figure 2 : Effect of discrete diabetes management events on personal health [9].....	28
Figure 3 : Gluowatch Non-invasive Glucose Sensor [7].....	29
Figure 4 : Raman Spectroscopy based Glucose Sensor [16].....	29
Figure 5 : Smart Epidermal Temperature Sensor [22]	30
Figure 6 : Contact Lens glucose Sensor [21].....	31
Figure 7 : Transdermal Sonophoretic Glucose Sensor [23]	31
Figure 8 : : Implantable Glucose Sensor having 1 year lifetime [35]	33
Figure 9 : Fluorescent based Glucose Sensor [36]	33
Figure 10 :: Typical CGM system with a closed loop Insulin delivery system [39]	35
Figure 11 : A miniaturized Implantable Glucose Sensor [41]	36
Figure 12 : A Miniaturized CGM System [42]	36
Figure 13 : Implantable System Architecture.....	39
Figure 14 : Sequence of Foreign Body Response in subcutaneous Tissue [62].....	45
Figure 15 : Proposed Design of Integrated Sensing Platform.....	48
Figure 16 : Schematic of Integrated Electrochemical Sensor	54

Figure 17 : CMOS Integrated Electrochemical Sensors	58
Figure 18 : (a) Design A (Pt RE) (b) Design M (AgCl RE) (c) Design G (Ag RE) (d) Design N Ag (RE).....	59
Figure 19 : Design Comparison for Sensitivity (a) Ag/AgCl RE (b) Pt RE.....	60
Figure 20 : Electrochemical Impedance of different sensor geometries in PBS	60
Figure 21 : Electrochemical Impedance of sensor geometries in 20mM Peroxide.....	61
Figure 22 : Impedance comparison between Ag/AgCl and Pt RE sensors.....	61
Figure 23 : Electrochemical Stability of Electrode Materials in 50mM Peroxide solution	63
Figure 24 : Effect of Repetitive testing on electrode material (a) Au (b) Pt.....	64
Figure 25 : Silver based integrated Reference Electrodes.....	65
Figure 26 : Thin Film Reference Electrode Materials (a) Ag (b) AgCl.....	66
Figure 27 : Spectrum of Ti/Pt/Ag/AgCl electrode	66
Figure 28 : Thin Film Reference Electrode Materials (a) Pt (b) 'Pt/PtOx'	68
Figure 29 : Spectroscopic Measurement of Pt based RE materials (a) Pt (b) PtOx	68
Figure 30 : Open Circuit Test for electrode Stability and Interference Effects.....	70
Figure 31 : Comparison of Pt and Ag/AgCl RE.....	71
Figure 32 : Nanopatterned electrochemical sensor coated with a functionalizing matrix	73
Figure 33 : Integrated Nanopatterned Electrochemical Sensors.....	75

Figure 34 : Randles equivalent electrical model of an electrochemical cell.....	78
Figure 35 : Impedance Comparison between Planar and Nanopatterned Electrodes.....	80
Figure 36 : Comparison between Impedance of Planar and Patterned Sensor.....	81
Figure 37 : Fitting sensor response for Enzyme Kinetics	86
Figure 38 : In vitro sensing of Glucose using electrode immobilized w/ GOx	89
Figure 39 : Glucose sensing using integrated sensors with (a) GOx (b) GDH.....	90
Figure 40 : Nanopatterned Glucose Sensor performance.....	91
Figure 41 : Comparison of Nanopatterned and Planar Sensors	92
Figure 42 : Chronocoulometric Sensing of Glucose in PBS.....	93
Figure 43 : Amperometric Glucose Sensing using an integrated planar sensor.....	94
Figure 44 : Sensor w/GDH, test in mouse blood.....	96
Figure 45 : Improving Sensitivity using Signal Processing	97
Figure 46 : Interference on Pt electrodes (a) in PBS (b) with 0.1 mM AA	98
Figure 47 : Effect of PPh on Peroxide Detection on Pt electrode.....	99
Figure 48 : Effect of O ₂ bubbling on GOx Sensor	101
Figure 49 : Effect of O ₂ bubbling on GDH Sensor	102
Figure 50 : Response of a Glucose Sensor over 3 weeks.....	103
Figure 51 : Chronocoulometric Response of a Glucose Sensor over 3 weeks	104

Figure 52 : Sensor to Sensor Variation within a batch.....	106
Figure 53 : Effect of Nafion coating on Peroxide Detection.....	108
Figure 54 : Frequency Dependence of MB Redox Peak.....	111
Figure 55 : Comparison of Macro and Micro Planar Sensor as function of Hybridization time.....	113
Figure 56 : Hybridization Detection using Nanopatterned Sensor	113
Figure 57 : Electrochemical Insulin Detection using Aptamer	116
Figure 58 : pH Sensing using open circuit potential of Pt/PtOx vs. Ag/AgCl	118
Figure 59 : Anatomy of Human Skin [124].....	124
Figure 60 : Wavelength-dependent absorption of different components of human skin (-stratum corneum,2-living epidermis, 3-papillary dermis,4-upper blood net dermis,5-reticular dermis,6-deep blood net dermis and 7-subcutaneous fat)	125
Figure 61 : Scattering coefficients of different layers of the skin tissue, and fitting results from Mie and Rayleigh theories [122].....	126
Figure 62 : Reflectance as a function of wavelength in skin (a) White Caucasian (b) Japanese and (c) black African [129]	127
Figure 63 : CMOS Integrated Photovoltaic Power Harvesting System.....	129
Figure 64 : Penetration depth in Si and Ge as a function of wavelength [134].....	130
Figure 65 : Simple Equivalent Circuit of a Photodiode	135
Figure 66 : Types of Junctions in Standard CMOS.....	137

Figure 67 : Types of Junction Diodes in Standard CMOS.....	137
Figure 68 : Photoresponsivity of different p-n diodes in CMOS [139]	138
Figure 69 : Effect of Parasitic Devices on Diode Stacking.....	139
Figure 70 : Types of Junctions in Deep N-Well CMOS Process.....	140
Figure 71 : Connections and equivalent circuit of three photovoltaic cells powering integrated circuit.....	141
Figure 72 : CMOS photovoltaic on die utilizing deep n-well based devices	141
Figure 73 : Parasitic BJTs in deep N-Well CMOS.....	142
Figure 74 : I-V Characteristics of stacked Photodiode (d1).....	145
Figure 75 : Different Photodiode Geometries	147
Figure 76 : Different regions in Silicon-on-Insulator CMOS	151
Figure 77 : Backside view of SOI-CMOS after Etching.....	152
Figure 78 : MPE guidelines for Skin exposure in NIR	154
Figure 79 : COMSOL simulation of tissue heating due to laser exposure	155
Figure 80 : Electrical Power Transfer System.....	156
Figure 81 : A typical series RLC Resonator circuit.....	159
Figure 82 : Current in series RLC resonator as a function of input frequency.....	160
Figure 83 : Circuit Model for Resonant Power Transfer.....	162

Figure 84 : Testing Resonant Coupling using Discrete Coils	166
Figure 85 : PCB system for testing resonant coupling	167
Figure 86 : Effect of Geometric Shape on Inductance value	169
Figure 87 : Simple Electrical Model of On-Chip Inductor [166].....	170
Figure 88 : A Silicon Coil Design for Impedance Testing.....	171
Figure 89 : Wireless Power Transfer to CMOS chip using Resonant Coupling	176
Figure 90 : General Optical Telemetry Link for Implants	184
Figure 91 : SEM image of VCSEL chip from ULM [143].....	185
Figure 92 : Effect of substrate etching on VCSEL properties	186
Figure 93 : Pulse Width Modulation Circuit for Optical Telemetry.....	193
Figure 94 : PWM circuit utilizing seven stage voltage controlled oscillator.....	194
Figure 95 : VCSEL with bonding wires	195
Figure 96 : Current versus Frequency Response of the Telemetry Circuit	196
Figure 97 : Unmodulated Data from the Optical Telemetry Link	197
Figure 98 : Results of Optical Telemetry Using VCSEL.....	198
Figure 99 : Optical Telemetry through an ex-vivo tissue.....	198
Figure 100 : Optical Telemetry through Tissue (a) Raw Data (b) Results after 4x Integration.....	199
Figure 101 : Cross section of the VCSEL Structure showing Mirrors	201

Figure 102 : circuit Model for Load Modulation Telemetry.....	204
Figure 103 : CMOS circuit for Backscattering Communication	205
Figure 104 : Load Modulation Results for Discrete Coils	208
Figure 105 : PCB testing of Load Shift Keying based Communication.....	208
Figure 106 : Load Modulation using CMOS circuit	209
Figure 107 : Schematic representation of a Potentiostat	212
Figure 108 : Classical Potentiostat Circuit [76].....	212
Figure 109 : Current Conveyor based Potentiostat Design	214
Figure 110 : PMOS based Control Amplifier Design	217
Figure 111 : Common TIA topologies using resistive and capacitive feedback	218
Figure 112 : CMOS Potentiostat with isolation and readout circuit	219
Figure 113 : A picture of one of the Potentiostat on the CMOS die.....	219
Figure 114 : CMOS Potentiostat testing using Dummy Electrical Cell	221
Figure 115 : Peroxide Detection using integrated Potentiostat.....	222
Figure 116 : Control Circuit Design-Version-2.....	223
Figure 117 : Glucose Sensing using CMOS and a commercial Potentiostat.....	224
Figure 118 : Integrated Sensing Platform -Version I	226
Figure 119 : schematic of Integrated System -Version II	227

Figure 120 : CMOS integrated system-Version II	227
Figure 121 : Schematic of the Integrated System-Version III	229
Figure 122 : Wireless Operation of the Integrated System	230
Figure 123 : Subcutaneous Injection Procedures [218].....	234
Figure 124 : Subcutaneous Implantation System [219]	234
Figure 125 : Intramuscular and Intradermis implantation for 7 weeks in Wistar Rat.....	235
Figure 126 : Device with holes for improved Biocompatibility	236
Figure 127 : An example integrated sensor on CMOS (Pt RE).....	240
Figure 128 : SEM of AgCl/Ag RE interface	240
Figure 129 : Electrochemical Oxidation of Platinum in Sulphuric Acid Solution (0.1M) in PBS. .	241
Figure 130 : SEM image of ICP-RIE plasma-etched Si nanopillars	243
Figure 131 : Si Pillar bending due to capillary forces (aspect ratio of ~25).....	243
Figure 132 : Nanopillar Array after thermal oxidation	244
Figure 133 : Nanopillars after PECVD Passivation coating	244
Figure 134 : Nanopillars after electron beam evaporation metal coating.....	245
Figure 135 : Nanopillars after sputter coating of 50nm of Au	245
Figure 136 : Confirmation of coating on pillars' interface with the planar surface	246
Figure 137 : Nanopillars after ion beam induced metal coating	246

Figure 138 : SU8 Encapsulation around sensors	247
Figure 139 : Pad Stack in TSMC 250nm CMOS Process.....	247
Figure 140 : Nanopillar Arrays on top Aluminum Pads of CMOS	248
Figure 141 : Hydrogel Immobilization Procedure.....	249
Figure 142 : Sensor Functionalization using Hydrogel.....	249
Figure 143 : Electrochemical Cleaning of Au Electrodes.....	250
Figure 144 : Sensor Packaging for Wired Testing	252
Figure 145 : Sensor Testing Setup	253
Figure 146 : Implantation Study in Rats.....	253
Figure 147 : Simulation of Planar Sensors of Different Geometries	254
Figure 148 : Pillar array and corresponding CV, in COMSOL	255
Figure 149 : COMSOL Simulations of Planar Inductors.....	256
Figure 150 : Simulation of Coupling between two coils.....	257
Figure 151 : Spectrophotometric Testing of Immobilization Chemistry.....	258
Figure 152 : GDH Thermal Cycling Test.....	259
Figure 153 : Glucose sensing activity of GDH after 1 month.....	259

List of Tables

Table 1 Comparison of Different Reference Electrode's Performance	70
Table 2 Comparison of Functionalization Methods	84
Table 3 Comparison of Different Glucose Sensing Enzymes.....	110
Table 4 Comparison of Electrochemical Testing Techniques	119
Table 5 Illuminated characteristics of Stacked CMOS Photovoltaic Devices	144
Table 6 Effect of Laser focusing on performance of stacked PV system.....	146
Table 7 Photodiode Geometry Comparison	148
Table 8 Effect of Tissue on Performance of PV System.....	149
Table 9 comparison of Electrical Power Transfer Modes.....	158
Table 10 Comparison of different methods to power wireless implants	179
Table 11 Comparison between integrated power transfer methods.....	179
Table 12 Comparison of Telemetry schemes for implant applications	210
Table 13 Comparison with State-of-the-Art Implantable Glucose Sensors	230

Table 14 Comparison of Different Implantation Sites	233
Table 15 Some Common Enzymes and their Sensing Applications	238
Table 16 ICP-RIE Parameters for Si etching.....	242
Table 17 Doping Concentrations for Different CMOS regions	263
Table 18 Minority carrier lifetimes and Diffusion Lengths for CMOS.....	263
Table 19 Junction Widths in CMOS Process (calculated using doping densities).....	264

Chapter 1 Problem Introduction

The world expenses on health care are increasing with time, as is the population. The expenditure of resources on health care is enormous (e.g. 6.5 Trillion US\$ in year 2012) and the access of the growing population to the available infrastructure is increasing [1]. Hence, a smart and affordable personal health care system focusing on preventative approaches is essential for creating a sustainable future for at least the health care system.

Personal health is a complex problem to quantify. There are some standard measurements which can provide insights about this otherwise very involved problem. These measurements include, for example, metabolic information (e.g. glucose levels), cardiovascular information or neural measurements [2]. A reliable and continuous measurement of all or some of these indicators can quantify many aspects of a person's health. Many efforts have been pursued to provide such health related sensing capabilities. Glucose sensors comprise by far the largest part of such biomedical sensing devices (85%) [3] because of significance of glucose to the metabolism of healthy persons, as well as on diabetics. According to WHO, almost 10% of world population will soon be diabetic and the numbers are increasing. It is estimated that in 2030, Diabetes will be seventh leading cause of death [4] and a similar trend is true for most other non-infectious diseases (e.g. cardiovascular diseases).

Smart continuous sensing platforms can offer a solution to this alarming trend in health care [2]. These systems can be used for continuous, real-time monitoring of different aspects of an individual's health. This can help in both preventative and curative settings, as well as in monitoring the state of a larger group as in an epidemic. The use of smart materials and processing techniques, along with the progress made by the electronics industry have the potential

now to create such smart integrated platforms which can, in real-time, monitor chemical or neural changes in the body [5]. This data can be used by a health care system (e.g. doctor, emergency crew) to monitor a person's health or even suggest therapies. The advent of such smart implants can change biomedical research and diagnostics completely and can form the basis for a closed loop medical monitoring system as depicted in following schematic.

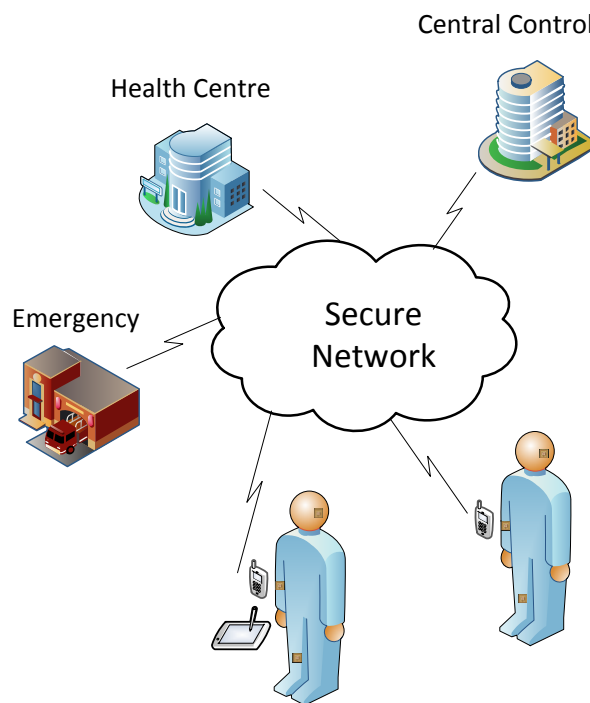


Figure 1 : Personal Health Care Network

Such 'health networks' have been of interest for some time and different sophisticated networks have been proposed in the literature [6]. However, many fundamental challenges still remain in implementing the personal monitoring system to make meaningful biomedical measurements that could enable the realization of this concept.

1.1 Biomedical Measurements: State-of-the-Art

Today, accurate continuous glucose monitoring is currently done by measuring glucose in the blood resulting from a fingerpick procedure. For diabetics, this reading is then used to either take medication (e.g. insulin) or to adjust their lifestyle accordingly. However, this method has many limitations and problems associated with it such as painful and discrete measurements. Regardless of how many readings one takes, the entire dynamics of glucose sensing cannot be captured by sporadic measurements [7]. Ideally, a reading is required 5 to 10 minutes [8]. This is demonstrated by comparing glucose levels in a diabetic and a healthy person's metabolism over time in Figure 2.

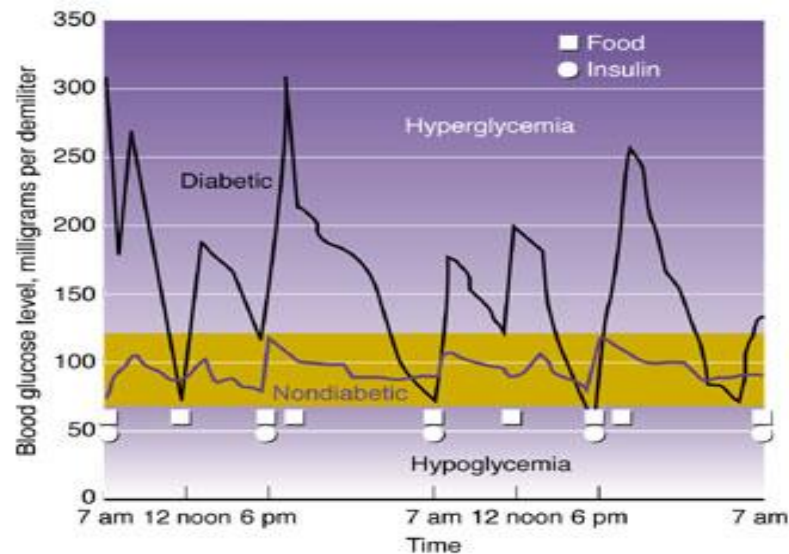


Figure 2 : Effect of discrete diabetes management events on personal health [9]

It has been shown that continuous, real-time glucose monitoring along with an accurate closed loop drug delivery system are essential for proper management of diabetes [10]. However, development of such continuous sensing platforms involves many challenges and, although efforts have been

going on for long time for their development, there are many challenges remaining before such devices can become a reality[11].

There are two main approaches which have been taken to make such biomedical measurements for different applications. The first approach is trying to make diagnostic measurements without putting any foreign object in the body, i.e., using the so called *non-invasive* measurements. Techniques which are applied for such measurement systems include dielectric spectroscopy[12], reverse electro-osmosis [13], Raman Spectroscopy [14], Near Infrared Spectroscopy [15]. Some examples of these systems are shown in next few Figures.

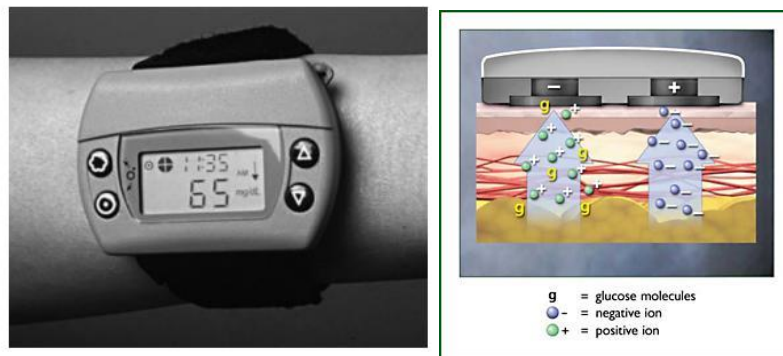


Figure 3 : Gluowatch Non-invasive Glucose Sensor [7]

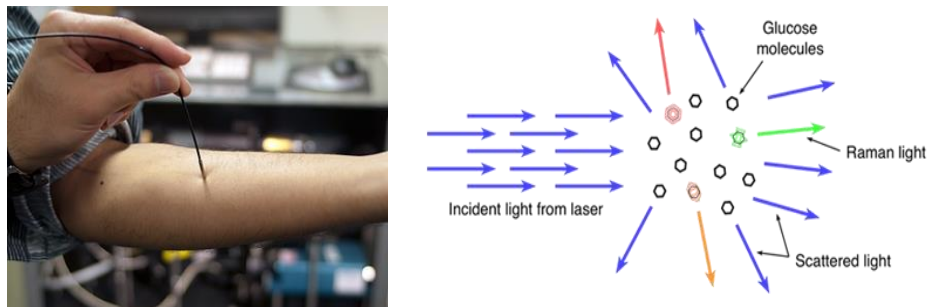


Figure 4 : Raman Spectroscopy based Glucose Sensor [16]

Although, such non-invasive devices have shown lots of promise, there are still many fundamental challenges in realizing these at the size scale and accuracy for personal use [17]. One big concern is that the quality of non-invasive testing suffers when direct non-invasive signature may not be accessible near the skin surface. Practically, it is very challenging to realize a continuous closed-loop system using these devices although with the advent of new technology, this may be possible [18] for some chronic diseases. However, these can be used in clinical environments for faster screening.

The other approach is to make use of Invasive systems, providing the advantage that these can be used for direct and accurate measurements close to the source chemistry. There are many different examples of such systems in the literature [19] ranging from minimally invasive sensors to completely invasive ‘implantable’ systems.

Minimally invasive (wearable) sensors do not need to be completely implanted and still can provide information about some important metabolic signals. Typical examples of these systems include skin sensing ‘tattoos’[20] and contact lens glucose measurement systems [21].

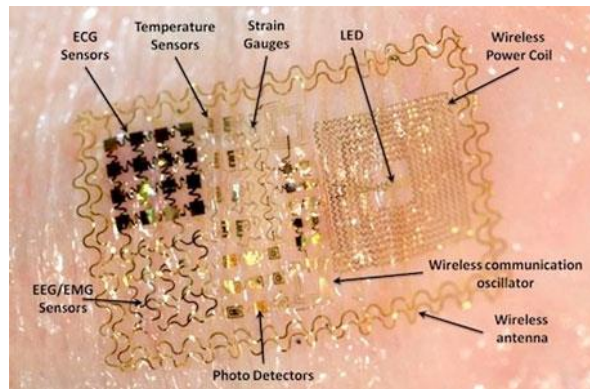


Figure 5 : Smart Epidermal Temperature Sensor [22]

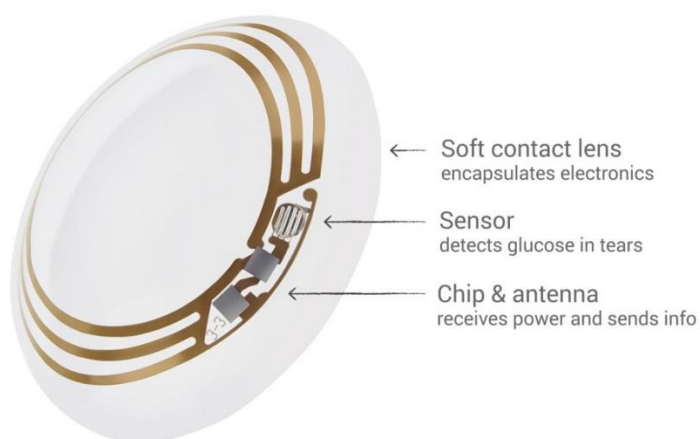


Figure 6 : Contact Lens glucose Sensor [21]

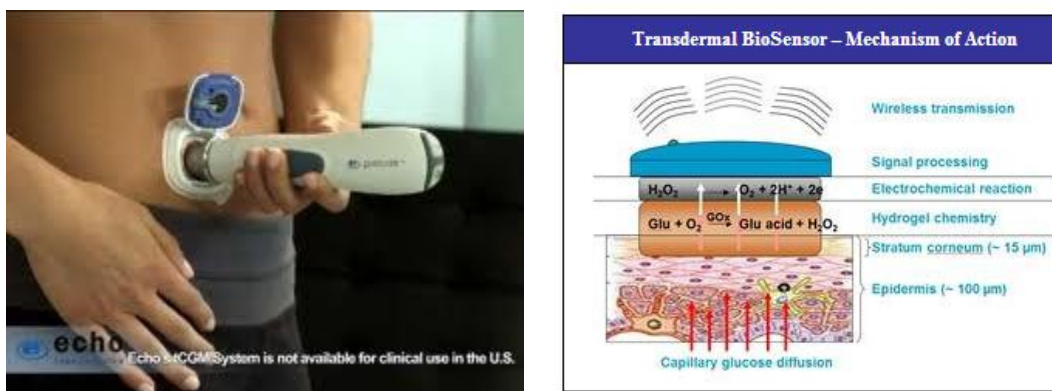


Figure 7 : Transdermal Sonophoretic Glucose Sensor [23]

However, these systems are limited by many factors including the type of signals which are available in their environment. For example, the wearable tattoos can only measure external signals such as temperature and electrical signals like ECG, EEG etc. Similarly, the contact lens sensor is limited by the glucose level in tear duct which is different from that in blood and

interstitial fluid and suffers from the large delay in the changes in this glucose level as compared to the changes in blood [21]. The acoustic sensor only works on fresh skin and can only measure in the solution that can diffuse to it [23]. Also, these devices are exposed and are susceptible to the external environment.

Fully implantable systems are designed to work while located completely inside the body. Such devices have been designed and built for a long time [24] and have been used for many applications including Pacemakers [25], Cochlear Implants[26], Defibrillators [27], Neural Implants [28], Neuromuscular Stimulators[29] , Retinal Implants [30], Spinal Implants [31], Metabolic Implants [32], and Pressure Sensors [33]. While design for each case has different requirements, there are some common needs for most of these applications as well, e.g. , biocompatibility, small size, low risk, etc. For example, neurological signal monitors need to have a bandwidth of interest from DC to 10KHz [34] whereas most other metabolic signals vary quite slowly. Hence, for proper operation of neural implants, even at low sampling rates (20KSamples/sec) and low bits/sample (8 bits/sample), data transmission rates of 160kbps are needed for one channel. For metabolic signals, this rate can be much slower. Hence, fundamentally different communication schemes (fast versus slow) are needed for these applications. On the other hand, both neural and metabolic implants need to be biocompatible and functional for long-time for proper use.

Of all the different modes of operations mentioned previously, implantation is the most direct method of measuring body chemistry. It also provides access to real-time changes in the body. Fully implantable systems have been able to provide stable signals under many conditions and have been actively researched for some time. For example, an implantable glucose sensor has

been shown to work for one year in animal tests and showed the potential of long term continuous glucose monitoring [35].

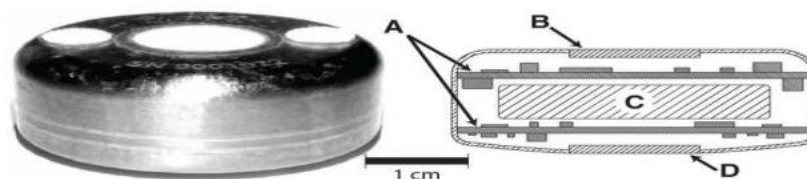


Fig. 1. Sensor array with integrated telemetry system before implantation. The implant is 3.4 cm in diameter and 1.5 cm thick. The top surface of the implant includes two polyester velour patches for tissue adhesion. Cross-sectional schematic view shows electronics modules (A), telemetry transmission portal (B), battery (C), and sensor array (D).

Figure 8 : : Implantable Glucose Sensor having 1 year lifetime [35]

Furthermore, invasive devices can use many different sensing mechanisms, enabled by the direct and close access to the measurement sites and local chemistry. For example, fluorescent measurements have been used in different applications including glucose sensing [36].

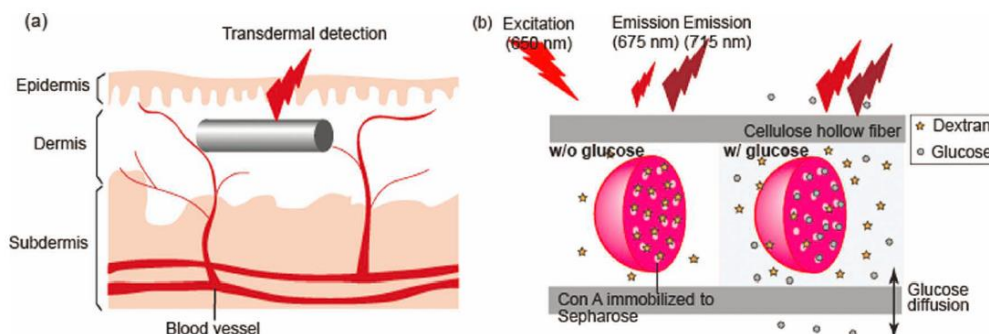


Figure 9 : Fluorescent based Glucose Sensor [36]

Historically, implanted devices have required a battery and other discrete elements, resulting in rather large systems. These macro scale devices pose some fundamental challenges. First, these

devices tend to need complex surgical implantation procedures which are expensive and also increase the implantation damage leading towards more severe body reaction and possible failure of the devices. Moreover, these devices exhibit sensor to sensor and subject to subject variations and need individual calibration procedures [35]. While this may not be a limitation, it will be more useful to have the smallest possible variation due to the macro scale device and variable body response to it. Furthermore, these macro devices mostly limit the implantation sites to large organs and tissues which limit the possible set of measurements that these devices can do. For example, measurements requiring direct access to blood or to specific cells (e.g. neurons) can only be made with smaller devices capable of more local measurement without causing traumatic damage to their local environment. Also, these macro devices cannot be used for local measurements (for example, a cancer tumor). These devices also create irritation to the surrounding tissue due to relative motion.

Another category of devices exists between the non-invasive and completely implantable extremes. These systems have an invasive probe that penetrates through the skin and connects to an external control unit. As continuous glucose measurement (CGM) has emerged as the best method to manage diabetes [37], these systems have been employed for glucose measurements and are being developed for other applications as well. Because of the sensor penetrating through the skin, these CGM systems pose a significant infection risk [38] and cannot replace the finger-prick methods to estimate accurate levels of glucose in the body. These systems measure glucose levels in interstitial fluid in the subcutaneous tissue and use predictive algorithms to estimate the value of blood glucose level for continuous monitoring (cBGM). Some typical cBGM (or CGM in short) systems are shown in Figure 10.

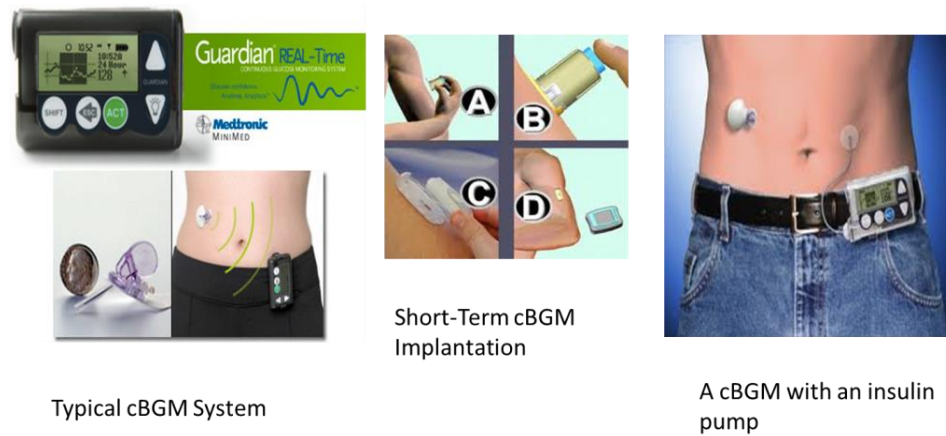


Figure 10 :: Typical CGM system with a closed loop Insulin delivery system [39]

The discussion above highlights that a completely implantable and accurate CGM system is still desired which, together with in-vivo drug delivery devices, i.e., insulin pumps, can create the complete closed loop systems also known as artificial pancreas[40].

1.2 Miniaturized Implants

As discussed in the previous section, existing biomedical implantable devices are quite large and some even use long wires. These limitations have to be removed before such devices can be used for many clinical applications. There are many reasons for these bigger sizes including the use of off-chip components (e.g. sensors, antennas etc.), use of non-standard manufacturing (e.g. using wires), and use of batteries to power the systems. The need for integrating several different components together makes the miniaturization difficult and non-repeatable. Examples of some state-of-the-art miniaturized systems in glucose sensing applications are shown in Figure 11.

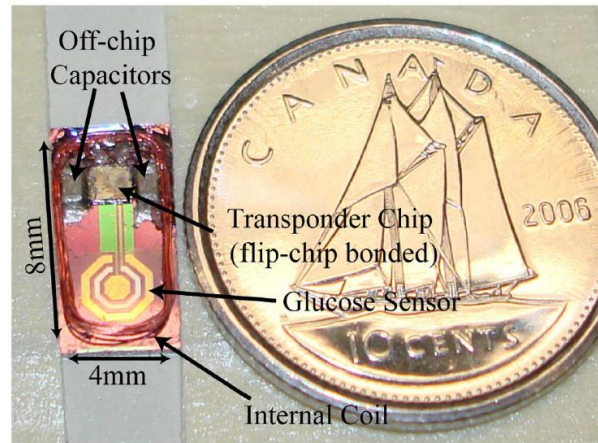


Figure 11 : A miniaturized Implantable Glucose Sensor [41]

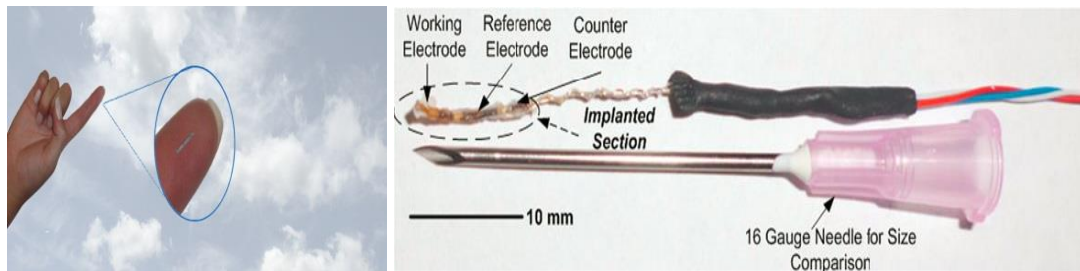


Figure 12 : A Miniaturized CGM System [42]

Although, these systems are quite small and very promising for actual uses, the use of off-chip and non-standard components prevents extreme miniaturization and easy manufacturing.

1.3 Need for new Technology

It is believed that extreme miniaturization of the implantable systems holds the key to make their long term use a reality [43]. In general, the neural implants need to be very small to minimize damage to surrounding tissue as well as to be able to measure as locally as possible. Metabolic

sensors do not need to be as small as neural implants, but can perform better if miniaturized. The small size scale can have many advantages over the traditional macro scale systems that exist already [44]. This size scale can make the implantation and subsequent explanation easier and cheaper (e.g. simple injection as compared to surgery). It can also minimize the implantation damage and hence decrease the subsequent body reaction. This can also make it possible to do many different types of measurements in many different types of local environments inside body in real-time. These small systems would induce minimal implantation and explanation damage and would allow easier and quicker healing, which is especially important for diabetics. The use of standard fabrication processes would also allow mass production and decrease costs substantially.

1.4 Thesis Focus

The design and realization of aforementioned miniaturized and integrated functional implants is the focus of this thesis. We will demonstrate that this extreme miniaturization calls for the use of complete integration of the different components of the system. It is fitting to note that this same method has been used by the microelectronics industry to realize a different set of challenges which called for miniaturization as well. We will also show that such integrated systems have a unique set of challenges and we will present our results in overcoming some of these challenges to achieve a fully functional integrated system capable of being used for clinical applications.

1.5 Thesis Outline

This thesis is divided into seven chapters and 4 appendices. The first chapter introduced the concept of miniaturized implants and their need to solve some important health care needs. Diabetes was presented as an example although the reasons for implant miniaturization are quite universal across many different applications. In Chapter 2, we discuss important design tradeoffs

and will introduce a preliminary design to realize a miniaturized integrated sensing platform. The next four chapters describe the four essential subsystem of the proposed design along with different methods which can be used to realize these subsystems (the sensor, the power supply, the communication system, and the control unit of the system). Then, chapter 7 shows different versions of completely integrated systems and the system level performance of these versions. It demonstrates an integrated and fully functional implant that has been completely characterized wirelessly in-vitro and is currently being tested for in-vivo performance in mice. We also provide details on some important ongoing work that would enable the animal testing of the proposed system which would lead to a rapid path towards human testing for regulatory approvals of these systems.

Chapter 2 System Design

As discussed in Chapter 1, the main design goal of this work is to realize a miniaturized system which can sense an analyte of interest *in-vivo* and can report this information to an external reader. This data can then be used for feedback to adjust the treatment. To satisfy these design objectives, the complete system needs to have many subsystems working together. First, there needs to be a sensor to sense the analyte of interest and transduce its concentration into some form of signal that can be read by the signal processing system. A power supply to power the system, control system to control the entire system operation, signal processing module to process sensor output and an output stage to transmit the signal to an outside reader all have to be integrated with this sensor. Such a system is shown schematically in Figure 13.

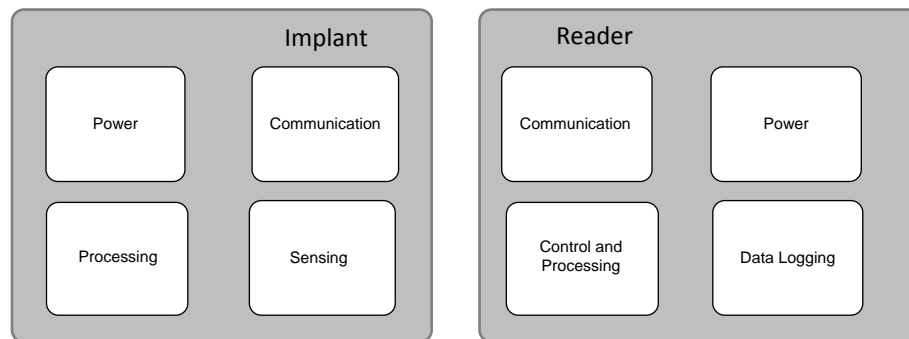


Figure 13 : Implantable System Architecture

2.1 Design Perspectives

Implementation of the architecture described in Figure 13 for a completely integrated and miniaturized system is quite involved and challenging. There are many unknown factors and these need to be carefully studied. Here, we provide some insight into the important design aspects.

The sensor is the most important component of our system and the choice of the sensor controls the design of the rest of the system components. There are different mechanisms which can be used for sensing and the sensing technique needs to be easily integratable with signal processing subsystem, provide excellent selectivity and sensitivity (both of which are very important in complex environments such as the human body), and should be easy to miniaturize using standard micro/nano techniques. The resulting devices should be able to work for long periods without the need of complex or toxic reagents. The measurement technique depends upon the application and some techniques are easily adapted to many applications while others are specific to a very particular application. Electrochemical and optical techniques are two of the most relevant methods for implants, as they can function in such complex environments and are easily integrated with electronics[5]. These sensing techniques do not need complex fabrication procedures or special materials which are not available in standard fabrication processes. This keeps post-processing to a minimum, increases system yield, and decreases cost.

Complementary Metal Oxide Semiconductor (CMOS) based systems are ideal candidates for performing control and signal processing operations in compact systems. These processes offer excellent signal processing capabilities while consuming minimal power at very small size scales. These systems are available for commercial fabrication from reliable sources with excellent yield and control over design parameters [45].

Powering the system is another very important aspect of implantable microsystems. Conventionally, powering implants transdermally with wires was the standard mode of operation and is still used in CGM systems today [46]. However, wires pose a permanent risk of infection, irritation, and mechanical damage. Hence, they are being replaced with better alternatives. Autonomous systems were made replacing wires with batteries which were large enough to remain operational for a long time [47]. However, batteries are bulky and risky since they can leak inside the body and eventually wear out. Hence, a completely autonomous system is ideally powered without batteries or other temporary power sources [48]. Such powering can be done using many different approaches. For example, a very appealing method is to generate power from the power sources already present around us or within the body such as motions, pulse, inhalation or chemical fuel cells. However, methods to harvest power from these power sources do not provide enough energy density for small devices. For example, power harvesting using motion (e.g. walking) is utilized through three units of ceramic elements (total volume 1.2 cm^3) to harvest around 4.8 mW of power in typical walking condition [49]. Ambient kinetic energy has also been proposed as a power source. However, a BiCMOS electrostatic energy generator which works by charging vibration driven variable capacitors could only generate 86.1nW at best due to low background energy level and low efficiency [50]. Thermoelectric (TE) methods have also been proposed and a test system has been shown to generate 775uW using 1mm^3 device [51]. However, these systems need special materials and their efficiency depends on large temperature gradients which may not be possible for *in-vivo* applications. There are many other methods including Airflow energy, background RF energy, background optical energy (sun/artificial lights) [52].

All of the methods mentioned above have some limitations and therefore a practical system design needs an external source of power that can be reliable and well controlled. Hence, the most relevant

powering method is wireless powering from outside. Wireless powering can be done with mechanical waves (acoustic) or electromagnetic waves (RF, optical). Acoustic waves require bulky devices which mostly need to physically move for transduction. For example, piezoelectric transducers can act as acoustic generators and receivers. However, the transduction materials are not available in standard fabrication processes (like CMOS) and very inefficient to use in a liquid or solid media. Although other methods of creating acoustic waves do exist (e.g. surface acoustic waves), these are not suitable for power transfer due to their poor efficiency.

Electromagnetic waves, on the other hand, do not need a physically moving source and receiver. The size of the devices can be quite small if high frequency waves are used and both power density and efficiencies can be quite high for most applications. These methods have been used in past for many implant applications. For example, Near-Field inductive coupling has been used to transfer power wirelessly [53] and resonantly coupled coils (e.g. LC resonators) have also been tried since Tesla first proposed their use in 1902 [54]. Some near-field communication protocols (for example, RFID) also use this method for wireless communication over short distances. Far-Field electromagnetic powering has also been used for longer distance operations [55]. However, this approach places a limit on the size of the system since such systems normally need large receivers to harvest enough power because of the high path loss in tissue at high frequencies and low energy density of electromagnetic fields in the far field region[56]. However, since wavelength at higher frequencies are smaller, high frequency methods can have more (directional) gain if the devices are implanted very close to the skin surface or underneath the fingernail, which is possible for some applications.

If one goes to even higher frequencies, optical methods can increase the gain related with directivity even more. For example, Photovoltaic (PV) systems can be made very small compared with electromagnetics based systems. Such optical powering has been proposed to be useful for energy harvesting for many applications [57] and the resulting systems can have small footprints. It is possible to direct a concentrated energy beam (e.g. laser) to generate high output power. Furthermore, these systems can provide very stable and efficient power generation without the need of rectification. Also, sun light and/or artificial light are available in most cases whereas background electromagnetic energy may not be readily available in all cases and its energy density in the microwave spectrum is also much lower ($1\mu\text{W}/\text{cm}^2$ compared to $100\text{mW}/\text{cm}^2$). Another advantage of these optical systems is their MRI compatibility as no magnetic materials are needed in their design [58]. Hence, electromagnetic methods at different frequencies can be utilized for power harvesting. Integrated power supplies can have better performance than bonded or glued together systems as parasitic or stray elements are avoided, and chances of deboning or similar failure modes are reduced.

Communication with the implant should also be performed wirelessly. As with powering, there are different ways this can be achieved. Acoustic transducers present one choice although these are normally bulky and need large voltages to create reasonable fluctuations for high signal to noise ratios. Electromagnetic communication schemes are more suitable and can be compared in different mode for optimal design. For example, RF telemetry is commonly used for many wireless implants [59]. However, optical telemetry has many attractive properties including lower background noise, which is easier to filter and a smaller footprint [60]. For ultra-small implants, these are very appealing properties. For any method used, the interaction of the signal with body tissue has to be

well understood and a detailed comparison of different electromagnetic methods has to be made for a proper choice of communication scheme.

2.1.1 Biocompatibility

Biocompatibility is a very important aspect of the design of implantable devices and in deciding the appropriate size scales for different applications. The mammalian bodies are very good at identifying foreign material in the body and try to isolate it from the body [61]. This leads to the rejection of the foreign body (i.e. the implant) by a complex foreign body response, which is an integral part of body's defense system [62]. This response is thought to happen in two stages. In first stage (acute inflammatory response), flow of body fluids around the sensor brings protein and cells to it. Then, the proteins adsorb on the implant surface (biofouling). Later, phagocytic cells (neutrophils, monocytes, and macrophages) bind to receptors on these proteins and try to 'kill' the implant by releasing inflammatory cytokines and other growth factors. After around 3 days, the chronic inflammatory response starts and forms a fibrotic encapsulation (scar tissue) around the implant using cross-linked procollagen [62]. This thick capsule decreases the diffusion of analyte to the sensor and decreases its functionality. This lag can be compensated initially (using prediction), but as the capsule grows thicker, it becomes harder to measure body chemistry accurately or even to detect any signal. It has been proposed that the sensor chemistry is not reacted adversely as long as it does not contain some toxic agents and the explanted devices regain their decreased sensitivity[63]. Hence, the decrease in sensitivity is mostly considered due to the fibrotic encapsulation of the implant.

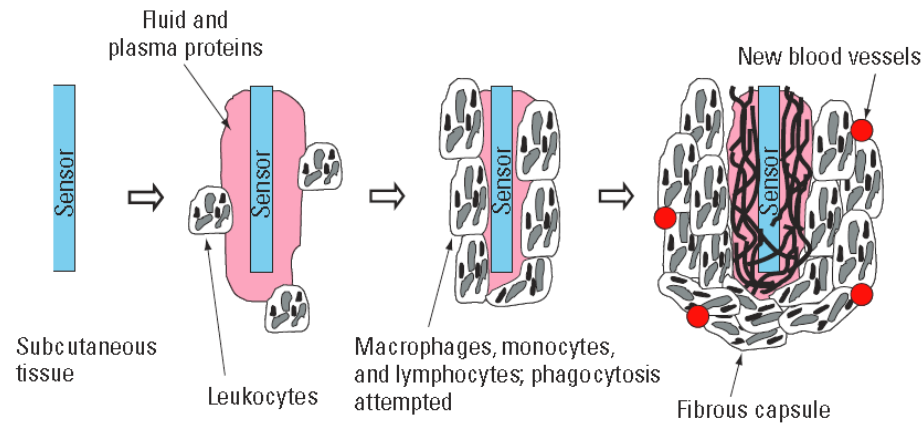


Figure 14 : Sequence of Foreign Body Response in subcutaneous Tissue [62]

Biocompatibility is mostly achieved by choosing some surface coating which does not allow the proteins to adsorb and hence stops the next steps in the entire pathway. Some commonly used materials include Parylene, implant grade Polydimethylsiloxane, Nafion, Silicones, Hydrogels (e.g. Polyethylene Glycol) [64]. To counter the chronic inflammatory response, anti-inflammatory drugs (e.g. Dexamethasone) or other anti-inflammatory agents (e.g. Nitric Oxide) are also suggested [65]. Although many biocompatible materials can slow this process down, there is no material or processing technique developed so far which stops this process completely [61]. Hence, an ideal implant has to be designed to create minimal foreign body response to begin with. The most direct method to achieve this is to decrease the implant size as much as possible [44]. Since most implants use electrical power, electrophysiological tissue irritation can also occur and can increase the foreign body reaction. However, a very small device with proper encapsulation would be expected to lead to minimal tissue irritation. Miniaturization also decreases the motion of the implant relative to the surrounding tissue which makes the implant position more stable in the tissue and is believed

to decrease the wound healing period [66]. Hence, miniaturization can help overcome some major biocompatibility issues.

2.2 Proposed Design

It is evident now that that a miniaturized integrated system with minimal post-processing will be best suited for our requirements. This means all the subsystems should be able to be implemented using the same technology. Also, the technology should be standardized to make the design repeatable, reliable and manufacturable. Probably the best fabrication technology that has been optimized for miniaturization is the CMOS technology. It provides powerful processing capabilities at very small area and power requirements. Hence, the CMOS technology was chosen as the underlying technology for our applications.

The CMOS process allows integrated power harvesting using either on-chip integrated diodes optimized as photovoltaic transducers (photo-cells) or using metallic structures (antennas) as receivers for electromagnetic energy. However, there are no optical transmitting elements available for the CMOS process. Since a small laser can be driven with the output driver from a CMOS circuit, optical methods can still be implemented, especially for ultra-small size or high data rate applications. Alternatively, metal structures can be used as electromagnetic transducers (antennas or resonators) for electrical communication as well. Furthermore, to reduce power and area, passive communication schemes are more attractive than active communication schemes. In such schemes, an incoming signal is modulated by the implant, and this modulation is read externally. Hence, there is no need to generate signals on chip.

The integrated electrodes from the CMOS process can be converted into electrochemical sensors with minimal post-processing without the need of bonding additional components. Such sensors can

provide very sensitive and selective signals at reasonably small size scale [5]. These sensors need to be functionalized with suitable chemistry to provide selective signal for a given application. Furthermore, since the need for the small size of the system calls for easy, ideally monolithic, integration of all the subsystems, use of CMOS integrated electrochemical sensors provides this advantage automatically. Moreover, these sensors can be used for many different applications by changing their surface chemistry. This enables the use of several small scale sensors for many different sensing applications forming a true body area network[67].

The microsystem design consists of a CMOS substrate with integrated sensors, power supply, and an integrated or bonded communication device. It is shown schematically in Figure 15. There are some additional elements, such as through silicon vias, which are needed if sensors are constructed on the back side of the substrate (for maximum area utilization) [68]. A hole is used to guide fluid flow through the device without any blockage.

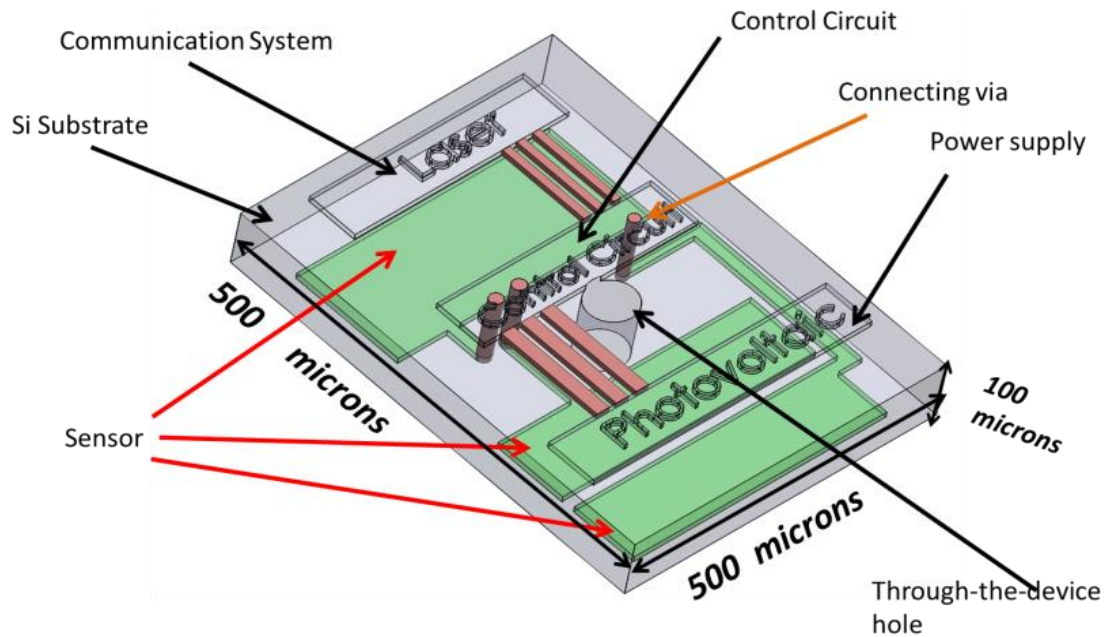


Figure 15 : Proposed Design of Integrated Sensing Platform

This system shows optical powering and communication as an example. In this work, we will present our results on both optical and lower frequency electromagnetic powering and communication and compare their performances for small scale implants. This will provide a comparison into the more appropriate choice for different applications.

2.3 Summary

In this chapter, a completely wireless and integrated (monolithically integrated in the ideal case) system design is proposed which can act as the basis for an ultra-small implantable sensing platform which can be used in a diverse range of continuous and real-time applications. The system uses standard CMOS technology as the backbone and build up the system utilizing the CMOS technology.

Chapter 3 Integrated Sensor

The sensor is defined as the component of the system which generates a signal corresponding to some physical quantity of interest. For example, a sensor is used to measure the concentration of one or more analyte of interest, usually from a mixture of many different analyte in a media e.g. body fluids (blood, interstitial fluid, etc.). There are many possible mechanisms for implementing a sensor for a particular application. The factors affecting this choice are:

- Type of analyte to be measured
- Sensitivity
- Selectivity
- Background Medium (blood, interstitial fluid, etc.)

Common sensing mechanisms utilize different means of interacting with the analyte of interest to induce a change in the response of a component or a set of components.

- Mechanical (e.g. MEMS/NEMS sensors) – Mechanical Loading of a device by analyte
- Thermodynamic (e.g. Calorimetric Sensors) – Mechanical Loading of a device by analyte
- Optical (e.g. fluorescence sensors) -- Optical Interaction with analyte
- Electrochemical– Chemical Interaction with Analyte, Electrical Output

Optical sensing schemes include fluorescence, biochemical luminescence, absorption and many other optical methods and have gained substantial interest for some time [69] . However, in-vivo use of such technologies is quite challenging as these are adversely affected by blood and other

body fluids around these. Also, few of these techniques need materials with optimized optical properties and hence are non-standard and not easy to miniaturize [37]. Nonetheless, these sensors can be used if suitable methods (e.g. filtering, surface cleaning) to deal with fluids are developed. In CMOS process, optical sensing can be done using integrated photosensitive structures for simple applications like oximetry. This would need one or more external light sources which can be used for absorption similar to regular oximetry.

Mechanical sensors (e.g. MEMS/NEMS) can also be used for very sensitive measurements in different modes (e.g. mass measurements). However, these devices need special piezoelectric materials, are difficult to read, and are difficult to integrate at small scales and are prone to mechanical failure [70]. Nonetheless, these sensors are also being improved continuously and some CMOS processes offer some simple mechanical processing for a repeatable design for some applications. Thermodynamics can also be used for determining reaction rates. Calorimetric methods have been employed in many applications. However, for small scale sensors with fluids around, it is not an easy to implement method [69].

Electrochemical sensors are quite versatile and can be used for many sensing applications. These have been used in biomedical sensing for long time. Clark Oxygen Electrode [71] and Updike Enzyme electrodes [72] are a couple of notable examples. Since these sensors employ electrodes which generate electrical detection signals, these are easiest to integrate with the signal processing circuitry while providing high sensitivity and selectivity. This avoids the need of complex post-processing requiring expensive chip area as required by the mechanical sensors. Furthermore, these sensors do not need bulky off-chip components to make the measurements and also do not need precise alignment with external devices as needed for optical sensors. Also, the materials used in

enzymatic electrochemical sensors are biocompatible [73]. A more detailed and thorough comparison between the different sensing mechanisms is given in literature [74].

For glucose sensing, electrochemical sensors are so far the only sensors which satisfy the sensitivity and selectivity criterion when compared to the bench top gold standard test given by Clark error grid [75]. Such sensors have been fabricated, in different geometries, on separate dies and bonded with control circuits using flip-chip bonding or other die bonding techniques. However, for the ultra-small size requirement, lithographic integration is the most appropriate method. Hence, we fabricated these sensors directly on CMOS dies. To understand the basic operation of such sensors, we can review some basic electrochemical concepts relevant to their operation.

3.1 Basic Electrochemistry

An Electrochemical system consists of at least one electrode (electrical conductor) immersed in an electrolyte (an ionic conductor) [76]. Depending upon the electrolyte and the electrode material (intrinsic electrochemical potentials), the electrode will either dissolve positive ions in the electrolyte resulting in a negative potential at the electrode or will absorb specie from electrolyte by giving electrons to positive ions and hence resulting in a negative electrode potential. The electrode potential depends upon the thermodynamic potential difference between ions in the solution and electrons in the conductor and can be calculated using Nernst equation ¹

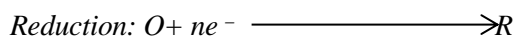
$$E = E_o - \frac{RT}{zF} \ln \frac{a_{red}}{a_{ox}}$$

¹ This electrochemical formulation follows Bard and Faulkner

[76]Allen J. Bard and Larry R. Faulkner, *Electrochemical Methods: Fundamentals and Applications*, 2nd ed.: John Wiley&Sons, Inc., 2001.

In the Nernst equation, R is the universal gas constant, T is temperature (Kelvin), z is the ionic charge, F is the Faraday's constant and a is the activity of specie (close to concentration for low concentration solutions). For standard electrolytes under standard temperature and pressure in standard solution, the electrode potentials are called standard electrode potentials (E_o) and are given in literature [76].

The reactions at the electrode surfaces are either oxidation or reduction reactions defined as



The current through an electrode-electrolyte interface when the concentration of specie everywhere in the cell is constant (initial stages of reaction or with constant stirring or flow) is given by Butler-Volmer equation

$$I = I_o \left[\exp \left[\frac{(1 - \alpha)nF\eta}{RT} \right] - \exp \left[\frac{(-\alpha)nF\eta}{RT} \right] \right]$$

Here, η is overpotential and I_o is exchange current. For mass-transfer limiting case, given C is concentration of the specie in bulk, current can be linearized as

$$I = \left[\frac{nFD}{\delta} \right] \cdot C$$

For fast voltage changes (e.g. Chronometry or Cyclic Voltammetry), current is given by Cottrell equation as a function of time and diffusion characteristics of the specie(s) of interest.

$$I = nFAc_o \sqrt{\frac{D}{\pi t}}$$

For cyclic voltammetry, time is normally replaced with scan rate. It is clear that current is a function of square root of the scan rate. Faster scan rates can provide more current even for smaller sensors. However, the charging currents (non-Faradaic currents) will also be higher in that case. Also, the fastest possible scan rate is limited by the diffusion properties of the specie(s) of interest and the kinetic properties of the reaction itself (rate of reaction).

To make an electrically meaningful measurement, at least two electrodes are needed. This basic system is called an electrochemical cell. The operation of the cell depends upon type of electrode materials and the electrolyte. Normally, one of the electrodes would preferably oxidize and the other will preferably reduce if these are made of different materials. The reactions at both electrode-electrolyte interfaces are called half-cell reactions. The complete cell reaction is a combination of the half-cell reactions. The electrode potentials of half-cells can be calculated by applying Nernst equation to each half-cell and these can then be used to determine the overall cell potential.

Due to the interface potential and the electrolyte being ionized, the electrode-electrolyte interface forms a layer of ions of opposite charges initially which attract opposite charge ions and hence make a complex multilayer structure which is known as the Helmholtz (also Stern or Debye) layer or simple electric double layer [76]. The electrode potential is dropped across this layer and the bulk of the electrolyte remains at 'ground' potential. Understanding this layer is very important in understanding most electrochemical phenomena.

3.2 Sensor Design and Operation

An electrochemical sensor is basically an electrochemical cell with the electrodes designed to serve a particular role in the detection process. One electrode is designed to have the interfacial reaction specific to the specie under detection and hence is called the sensing or working electrode (WE).

Another electrode is used to provide a stable potential reference in the electrolyte of interest and hence is called the reference electrode (RE). The third electrode is designed to complete the cell by providing a current equal to the working electrode, but in the other direction (oxidation or reduction) and is called the counter electrode (CE) [76]. For some applications, the CE and the RE can be merged especially if the sensor current is very small. However, for stable long term operation, it is appropriate to have a separate RE to provide more stable reference which is inert (no current flow) and hence does not polarize and does not get consumed during cell operation especially if the cell reaction is not completely reversible [77]. The sensor electrodes can be planar or patterned at micro and nano scale [78]. The sensor may have some surface coatings to achieve specific performance goals. A schematic of an electrochemical sensor is shown in Figure 16.

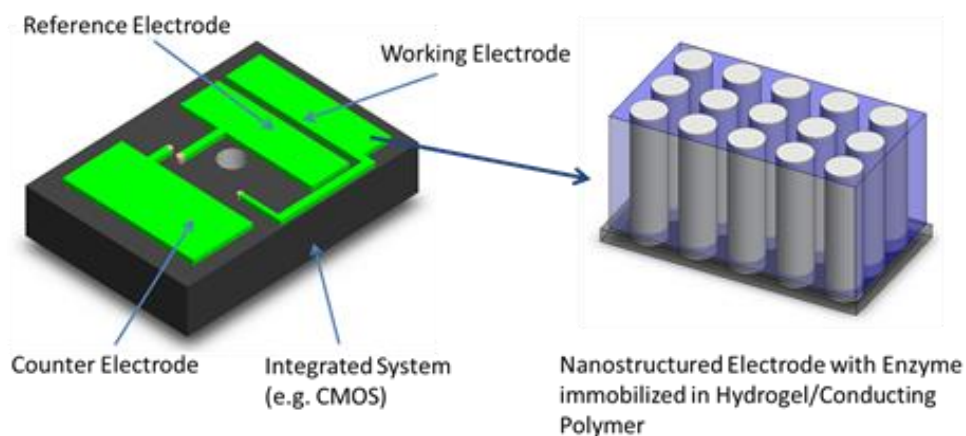


Figure 16 : Schematic of Integrated Electrochemical Sensor

The design of each system starts with a set of design constraints. For the sensor, design constraints include total die area used by the sensors, its biocompatibility and non-toxicity, desired sensitivity and selectivity, and operation time ranging from a few weeks to a few months. For our applications,

the sensors are intended for small sub-mm sized implants and the total area is limited to the size of the implant at the most. Initially, the sensor is designed assuming square dies. Later on these square CMOS dies would be shaped to other more favorable shapes for implants (e.g. rectangular shafts or circular dies).

Electrochemical sensors work by detecting the interaction of electrolyte with the electrode surface at electrode-electrolyte interface. The interface reactions depend upon the type of current-voltage mode used in the sensor operation. There are many different modes the cell can be operated in. The most common modes are explained briefly here (details in [79]).

3.2.1.1 Potentiostatic Mode:

In this mode, the current flow at the working electrode is controlled and the resulting potential difference between the working and the reference electrode is measured. One example is keeping this current zero which results in open circuit cell potential. The potential then depends upon both electrodes' materials as well on the electrolyte.

3.2.1.2 Amperometric Mode:

In this mode, the voltage at the working electrode (WE) is controlled w.r.t the reference electrode (RE) and the current flowing at the WE is measured. This current is proportional to the interfacial reactions happening at the WE. The term amperometry is normally used if the cell potential is kept fixed and the resulting current is measured. If the cell potential is varied in a predefined manner, this technique is referred to as Voltammetric techniques. Cyclic Voltammetry (CV) is the most common type in which potential is cycled between some limits. For some reactions, more elaborate Voltammetric techniques (such as square wave voltammetry) can be used to get a better signal at a

given redox potential. This is mostly useful for nucleic acid based detection schemes having some redox specie as the reaction indicator.

3.2.1.3 Conductometric Mode:

In this case, the cell conductance (or impedance) is measured at a fixed frequency or in a range of frequency for an alternating cell potential. This small alternating signal is applied (at these frequencies) on top of a large fixed cell potential and impedance or conductance is found by equivalent circuit model of the cell. These techniques are quite sensitive to interface changes and can be used to study surface properties (e.g. surface binding reactions) such as capacitance changes due to some dielectric changes in the solution or on the surface.

There are many other techniques which are defined according to their function as well. For example, when time dependent characteristics are studied using fast pulses, the technique is called chronoamperometry or chronopotentiometry.

An understanding of the interface phenomenon is necessary to understand which method should be used for a particular sensing application. The most important factors are the type of interface reaction and resulting change in cell parameters. Other variable are the range of the concentration of the specie to be detected and the transport phenomenon and kinetics of the reaction. For example, for large dynamic ranges (e.g. in H^+ concentration i.e. pH), potentiostatic methods can cover the range as the results are proportional to the logarithm of the specie concentration according to the Nernst equation [76]. Hence, open circuit potential measurements between the reference and working electrode can be used for pH measurements. For smaller ranges, Voltammetric techniques can be used as the interface current is proportional to the specie concentration. However, this current can be both linear or non-linear based upon the relationship between mass transport and

reaction kinetics. For mass-transport limited regime (fast interface reactions, slower specie diffusion), this current is proportional to transport rate which in turn is proportional to concentration gradient as given by Butler-Volmer equation [76]. For reaction rate limited cases, the current is non-linear and depends upon the rate at which the specie can be consumed at the interface. For some cases, the reaction can change form one type to other within the concentration range of the specie(s) of interest. For example, it can be transport limited for low concentrations, but reaction-rate limited for high concentrations. In this case, the rate will be linear initially, but will become non-linear for higher concentrations [80]. For studying changes in interface properties (e.g. surface binding or surface functionalization), conductometric (or impedometric) methods are more relevant.

The amperometric mode is the most widely used mode for electrochemical glucose sensors [19] because of its inherently sensitive detection. For implants, it is most relevant as it does not need an ultra-stable reference electrode as is needed for potentiostatic measurements. However, to achieve the desired performance from an amperometric sensor, it has to be designed in the mass-transport limiting regime so that the sensor current is a linear function of glucose concentration. This is especially important for autonomous sensors (e.g. implants). Hence, tight control over the sensor chemistry is needed for suitable in-vivo operation. The control includes type of functionalization technique, type and loading of enzyme and type of mediators chosen (if any).

Once the mode of operation and other design constraints are known, three electrodes based electrochemical sensors can be designed and fabricated using biocompatible materials. The design starts with electrochemical design guidelines on geometry [81]. For example, the counter electrode (CE) should be much larger than WE, and RE should be as close to the WE as possible. The CE size needs to be as large as possible so that it does not limit the WE current. We chose it to be

roughly an order of magnitude larger than the WE to achieve this while still keeping the sensor within our size constraints. The RE needs to be as close to the WE as possible to minimize the iR drop in the sensor (parasitic drop due to finite solution conductance). The RE size should be enough to maintain stability during the entire operation for long term implants. These constraints lead to various possible geometries. For large scale (macro) devices, optimizing the geometry is not very significant, although still relevant, since adequate performance can be achieved using many different types of geometries without any optimization. However for small scale devices it is very important to study all the factors that can affect sensor performance.

Integrated Electrochemical sensors can be fabricated on either the top or bottom of the CMOS substrate. An example of such electrochemical sensors (two different geometries) fabricated on the top metal layer of CMOS dies is shown here. The details of this fabrication process are included in methods chapter.

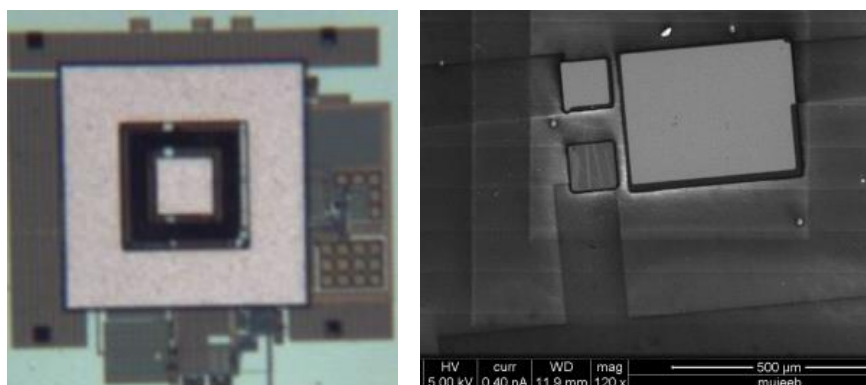


Figure 17 : CMOS Integrated Electrochemical Sensors

Alternatively, sensors can be fabricated on the Silicon area on the chip. The Silicon area can be either on the top or on the bottom of the CMOS substrate. Such sensors need special ways of

connecting these to the CMOS circuit. For example, for sensors on the back Silicon, contacts should be fabricated either using Through-Silicon vias or metal contact lines along the chip edges. Such technologies exist and can be integrated with the post-processing flow [82].

For prototyping, some example geometries were fabricated on silicon substrates as shown in Figure 18. The substrates were isolated first using thin (100nm) of either grown or deposited insulating layers (e.g. silicon oxide). The details are given in the methods chapter as well.

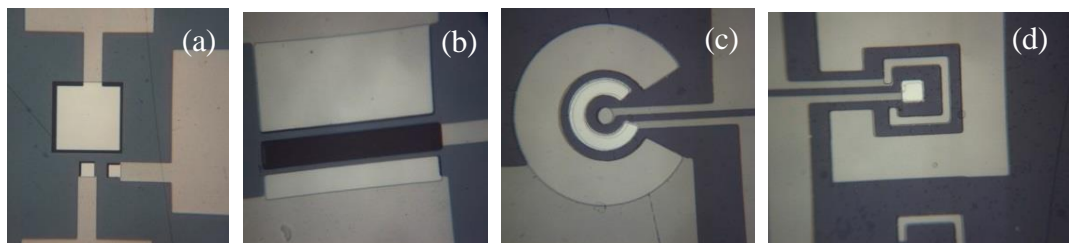


Figure 18 : (a) Design A (Pt RE) (b) Design M (AgCl RE) (c) Design G
(Ag RE) (d) Design N Ag (RE)

Rigorous analytical and numerical modeling methods can be used to compare these geometries for their performance. Some examples of simple numerical modeling are shown in appendix I. Experimental methods can be used as an alternative to these techniques, although testing all the possibilities can become tedious. We used a combination of modeling and experimental techniques. A few geometries were chosen based upon simulation results and their performance was compared experimentally. These were compared first using hydrogen peroxide testing to determine their sensitivity as it is the underlying sensing mechanism in most glucose sensors. The comparison of maximum sensor currents at 0.6V potential between WE and RE during a CV is shown in Figure 19.

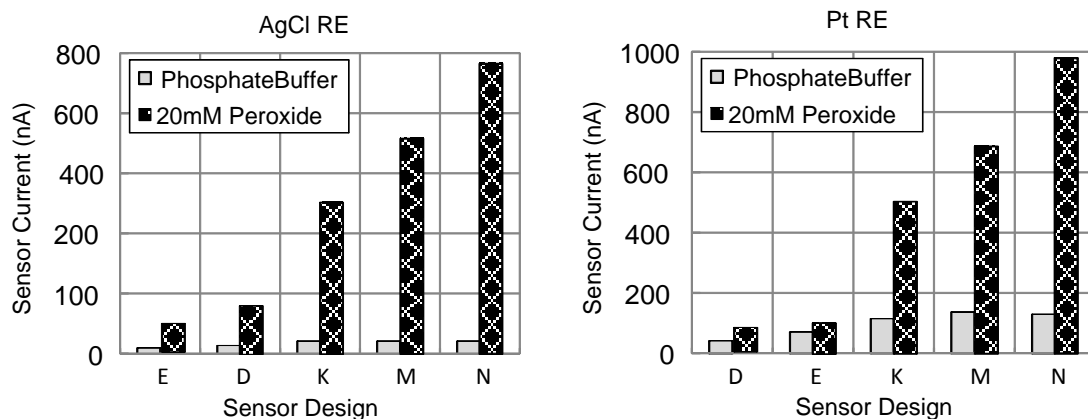


Figure 19 : Design Comparison for Sensitivity (a) Ag/AgCl RE (b) Pt RE

Other methods for comparison involve spectroscopic techniques including impedance spectroscopy and cell potential spectroscopy. These methods were used to confirm the results obtained through CV measurements. The results confirmed the same trend in electrochemical properties as shown in Figure 20 (PBS) and Figure 21 (20mM Peroxide).

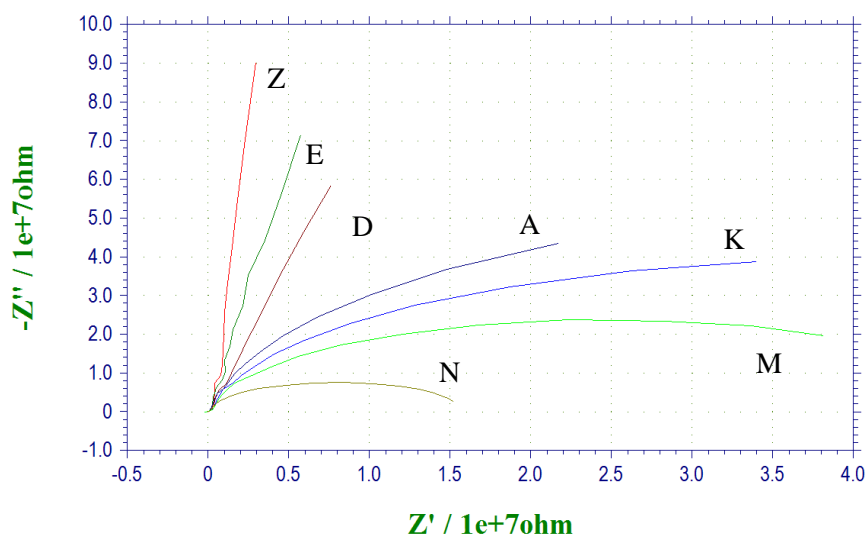


Figure 20 : Electrochemical Impedance of different sensor geometries in PBS

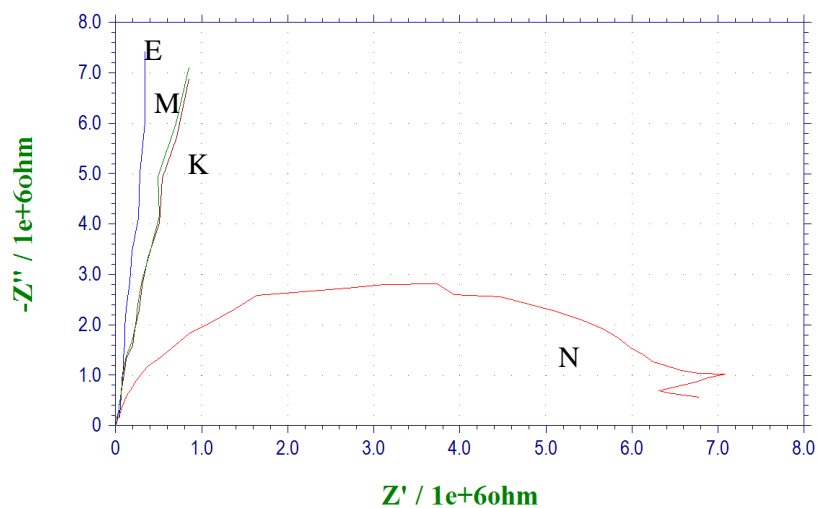


Figure 21 : Electrochemical Impedance of sensor geometries in 20mM Peroxide

The above results also suggest that the use of Pt RE if higher current is required as the overall cell impedance is lower in this case. This was also confirmed using impedance spectroscopy for different sensors. A typical comparison is shown in Figure 22.

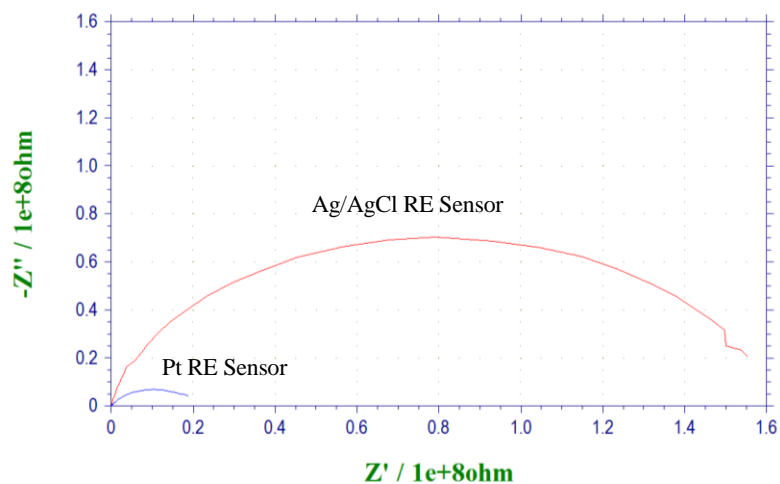


Figure 22 : Impedance comparison between Ag/AgCl and Pt RE sensors

All of these results suggest that design N followed by design M are the two most useful designs in terms of performance. We selected design N for CMOS devices because of the easy reproducibility while design M for sensor testing because of more reproducible fabrication using batch fabrication at wafer scale. We also tested few parameters regarding the design which are the spacing of the RE from the other two electrodes. The results show that the RE should be closest to the WE, as shown by the performance of design M compared to design K (which are both same design with RE being further from WE in K compared to M).

3.3 Material Aspects

After the geometrical design is completed, the electrodes have to be coated with a material which can provide the desired electrochemical interface properties. The electrode material is required to be very conductive even in thin films and needs to be chemically stable for extended life-time. At the same time, it should be not only very electroactive, but also to be able to detect the target specie efficiently and be biocompatible. Noble metals (also known as Platinum group metals) such as Pt, Au, Ir and their alloys have many favorable properties in this regard. Platinum is used for the working and counter electrodes due to its high electroactivity for the species being detected (e.g. hydrogen peroxide, oxygen) for metabolic sensing [83]. Furthermore, Platinum is chemically very inert and can keep a stable surface profile for a long time. Gold electrodes are used for DNA sensing due to the ease of attaching target probes using thiol chemistry [84]. Thin films (few 10's of nm) of these metals are adequate to provide stable operation for long-time under normal conditions. It was found experimentally using hydrogen peroxide detection that thin film Pt (same as Bulk Pt) can retain a stable interface for much longer time than Au (contrary to bulk Au), as shown in Figure 23 . The results were obtained with high concentrations of peroxide (50mM) for accelerated aging tests. Although there can be other reasons (differences in deposited films) than just the material

properties, the results were quite clear for multiple samples after reasonable attempts to isolate other effects like pinholes in films.

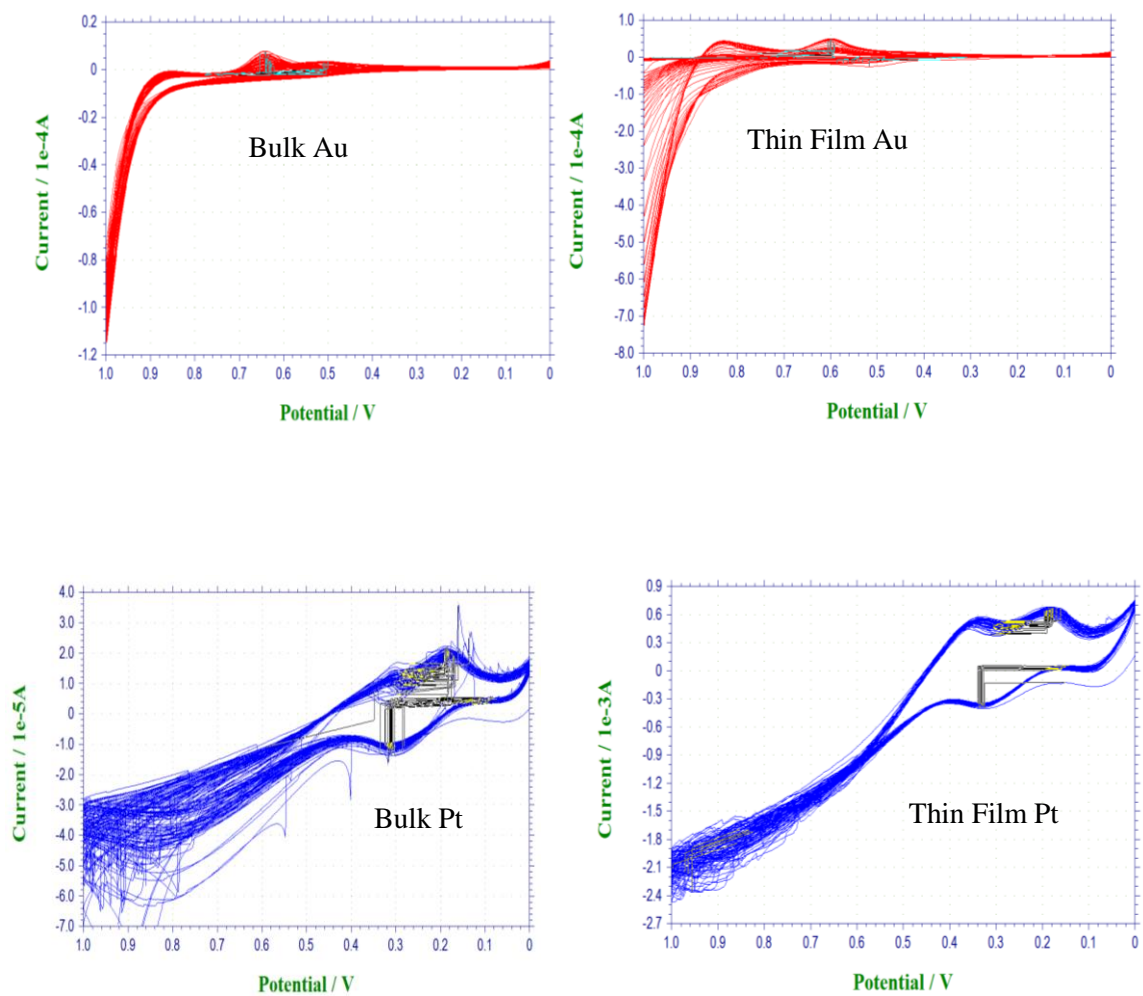


Figure 23 : Electrochemical Stability of Electrode Materials in 50mM Peroxide solution

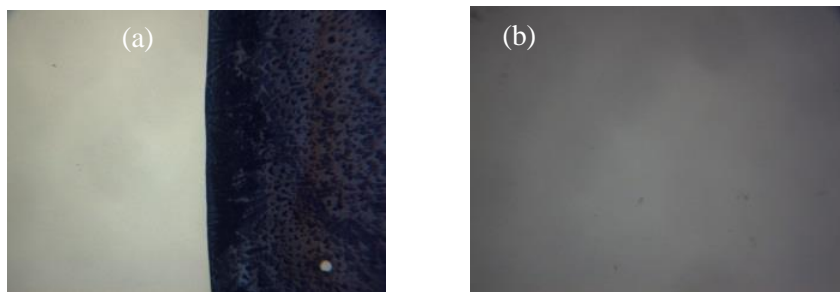


Figure 24 : Effect of Repetitive testing on electrode material (a) Au (b)

Pt

Another advantage of Pt is that direct electrochemical oxidation of glucose can occur on it at high enough potentials (around 0.6V vs. Ag/AgCl) [83]. This can be used for glucose detection with little interference rejection mechanisms. Gold, Carbon and other working electrode materials do not have this property. Although it has been reported that gold can be used in these applications, it has lower activity in amperometric mode. However, for Pulse Amperometry, it is reported to have higher activity than Pt [83]. However, in our work, we show that Pt have sufficient sensitivity which can be further increased by increasing its surface area. This, together with more long-term stability makes it more suitable as an electrode material for our applications. Hence, Pt was chosen for long-term electrochemical hydrogen peroxide sensors. For other sensing mechanisms, the comparison should be reevaluated. For example, for Nucleic Acid based sensing, it was found in the literature and in our experimental work that Au is easier to use as a working electrode material in terms of binding the nucleic acid strands (probes) using thiol bonds. The same chemistry did not show any appreciable binding to Pt. Hence, Au was chosen for such sensors as WE material.

In blood or other complex fluids, both gold and Platinum are poisoned by chloride ions and many other species (e.g. amino acids) due to surface adsorption. However, nanopatterned Pt has shown to

have high stability against these blood agents [83]. Nonetheless, since these sensors are not used in direct contact with blood, but in interstitial fluid, this is a less critical problem. For blood applications, electrodes will have to be coated with special materials for filtering (e.g. Nafion)

There are many different reference electrodes which can provide stable voltage readings in solution to form potential differences between electrodes for proper sensor operation, but the standard solid state reference electrode material is usually Ag/AgCl. Some noble metals covered with their oxide also act as pseudo-reference electrodes (e.g. Pd/PdOx, Ir/IrOx) [85]. Since we already use Pt electrodes for WE and CE, it is very desirable to test Pt-based reference electrodes and compare their performance with standard Ag/AgCl reference electrodes. The standard Ag/AgCl reference electrode is made using thin Ag deposited similar to the Pt layer. The top of this silver electrode is then converted to AgCl using different methods (dipping in strong chloride solutions, electrochemical reaction or Dry chlorine plasma) and the thickness of the AgCl layer is kept high enough for long term operation. However, not all Ag is converted into AgCl, as the sensor operation depends upon the interface between the Ag and AgCl layers[85]. The conversion was verified visually (AgCl has a brown color), spectroscopically, and through microscale structure (AgCl has a granular structure). The results of these material processing are shown in following figures.



Figure 25 : Silver based integrated Reference Electrodes

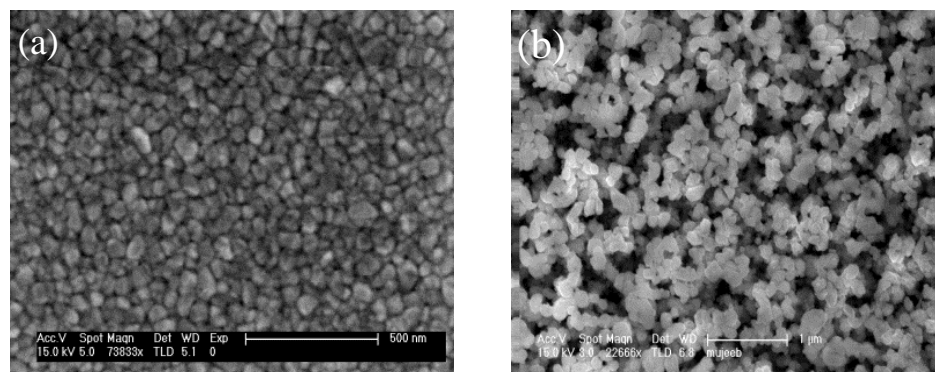


Figure 26 : Thin Film Reference Electrode Materials (a) Ag (b)

AgCl

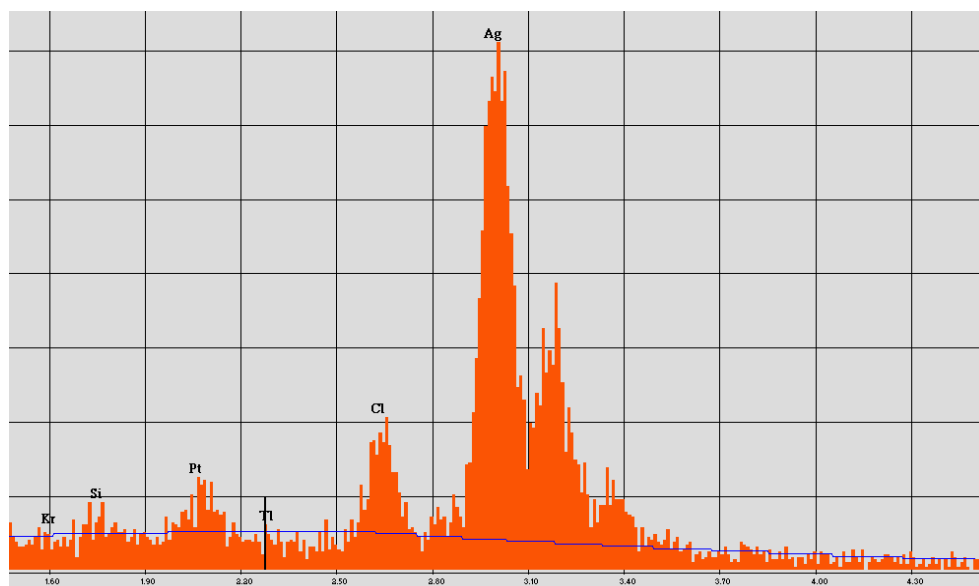


Figure 27 : Spectrum of Ti/Pt/Ag/AgCl electrode

Since Pt itself is sensitive to pH and peroxide interference, it would not be a very stable RE for glucose sensing. However, coating it with a suitable insulating layer makes it quasi-stable. For example, a somewhat inert layer of PtOx can be used to make a Pt/PtOx RE. This can be very useful since it avoids the need of having a separate material (Ag) or using other metal/metal-oxide based electrodes which need special post-processing [85] and can also be toxic. Also, Pt based reference electrodes can be used in harsh conditions where Ag/AgCl RE may not be feasible, although simple Pt may be better in such extreme conditions. Since Pt is a noble and very inert material, it is not easy to oxidize it even with strong oxidizers such as hydrogen peroxide. In this work, Pt oxidation was attempted using strong oxygen plasma as well as using strong oxidizing agents (like sulfuric acid) along with high electrochemical voltages. Oxygen Plasma exposure showed some effect on the Pt surface and the electron diffraction X-ray studies showed some Oxygen as part of the film. The films were heated to release any oxygen physically adsorbed in it. However it is still hard to confirm the chemical nature of the oxide film. Nonetheless, the resulting electrochemical stability suggested that the film had become a better reference electrode material than bare Pt. SEM's of the films are shown in the following figure.

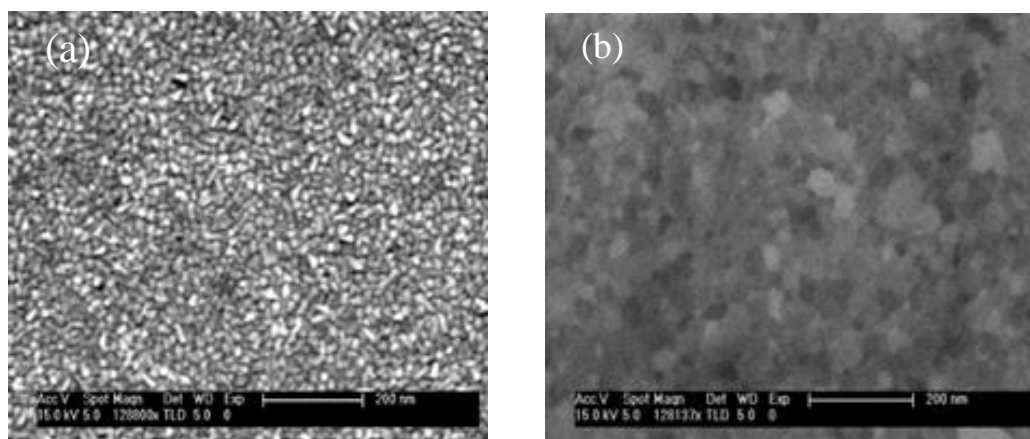


Figure 28 : Thin Film Reference Electrode Materials (a) Pt (b) 'Pt/PtOx'

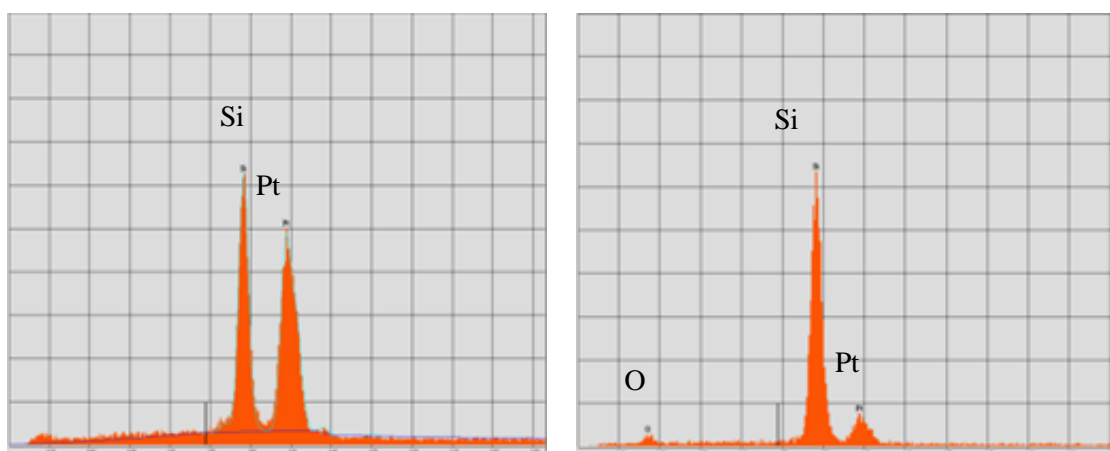
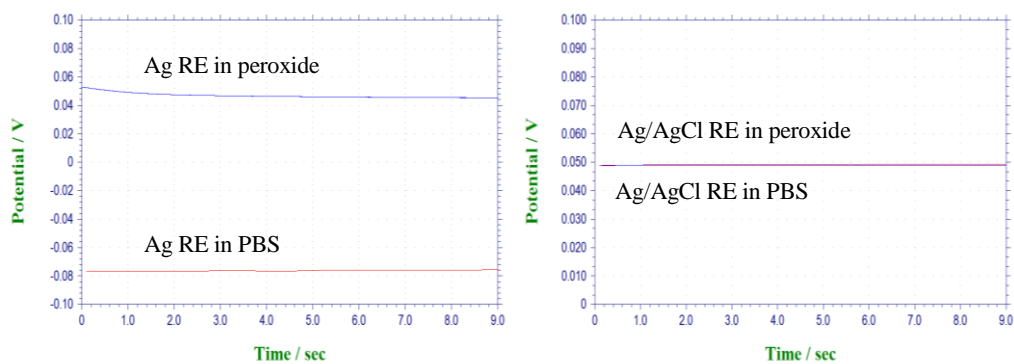


Figure 29 : Spectroscopic Measurement of Pt based RE materials (a) Pt (b) PtOx

Each sensor design was fabricated with both a Pt RE and Ag/AgCl RE. The stability of the RE was tested first by measuring its potential relative to a commercial stable RE, which in our case was Ag/AgCl RE from CH instruments. Secondly, Cyclic Voltammetric measurements were performed

using sensors utilizing either the Ag/AgCl RE or the Pt RE. Results indicated that Ag/AgCl RE proved more stable than Pt RE especially at higher reference potentials as seen in Figure 12. This is due to interference from species reacting with Pt at such potentials, most notably hydrogen peroxide. However, it also shows that a Pt RE can still be used for less sensitive applications. Although, bare Ag showed a pretty stable response, peroxide interference had some effect on it. The formation of AgCl layer on top makes it more independent of conditions in in-vivo fluids. Also, since the chloride ion concentration in body remains pretty constant [43], the Ag/AgCl RE was used without any special concentrated coatings as are used sometimes in commercial RE. The results in PBS and other body fluids confirmed that the RE could provide good enough performance in such cases. After Chlorination, AgCl became quite stable and peroxide did not have any appreciable effect on it. Bare Pt showed more serious problems regarding stability and peroxide interference. Oxidation proved to increase stability and decrease peroxide interference effects as expected.



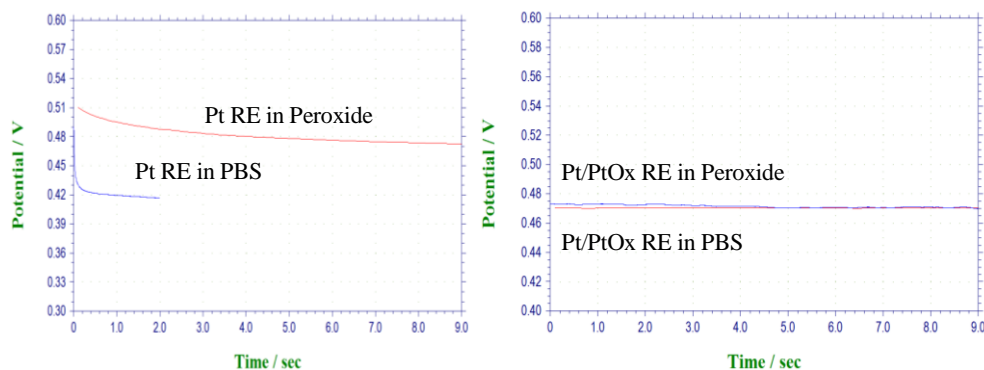


Figure 30 : Open Circuit Test for electrode Stability and Interference Effects

Table 1 Comparison of Different Reference Electrode's Performance

Electrode Material	Temporal Stability (voltage change)	Peroxide Interference (voltage change)
Ag	15mV	120mV
Pt	30mV	60mV
Ag/AgCl	5mV	3mV
Pt/PtOx	20mV	10mV

The open circuit potential difference between Pt/PtOx RE and AgCl RE was found to be a function of surface properties and cleanliness of the surface. There were some variations from batch to batch. However, this effect can be suppressed by standardized manufacturing and by performing some calibration with standard RE. Hence, the results suggest that a Pt based RE can be quite stable for some applications. Bare Pt itself can be used if the electrode is small and the interference from peroxide (or other similar molecules) is small. However, for very high peroxide concentrations, the Pt RE again showed interference effects. However, this occurs only at very high concentrations and

is only meant to demonstrate the limit of this electrode material. However, for the desired range of peroxide concentrations, this interference effect is not seen.

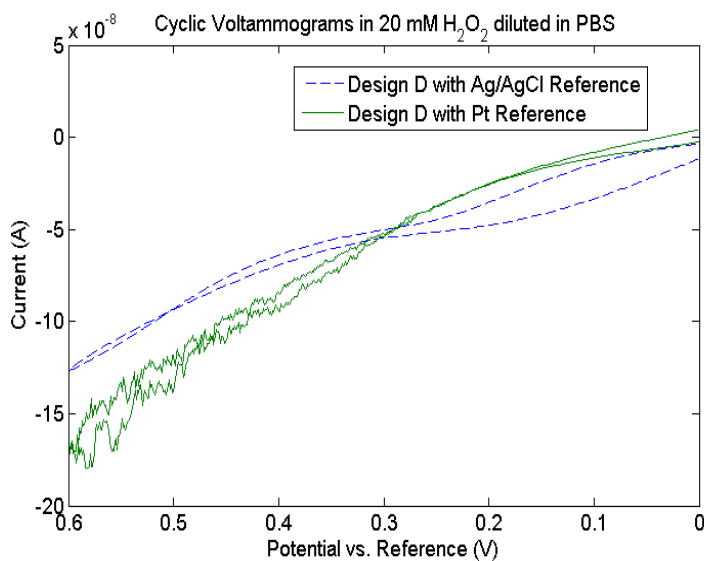


Figure 31 : Comparison of Pt and Ag/AgCl RE

3.4 Patterned Electrochemical Sensors

Micro/Nano scale structuring of electrodes has been used in sensing and energy storage for quite some time. Such structuring of electrodes can provide high output signal and enhanced selectivity [86]. Advantages also include high surface area and control of the diffusion profile near the electrode surfaces as well as stronger interaction with smaller species [86]. This patterning can also allow for much better utilization of functional coatings (e.g. enzyme coatings) on these electrodes and extend the enzyme life-time by decreasing their kinetic conformational changes [87]. However, the techniques employed for their fabrication are typically bottom-up growth (PVD, VLS or complex templates) which compromises control of their properties and robustness, leading to

uncontrolled variation in electrode properties. If the overall size of the electrode is not large enough, this leads to significant batch-to-batch variations and hence excessive recalibration of each device is needed. Also, such patterned electrodes are susceptible to failure over long term use because of limited mechanical/chemical robustness. Finally, the methods of fabricating these electrodes are not compatible with current CMOS technologies and need specialized post-processing and extra on/off chip circuitry and equipment. Intuitively, micro scale patterning is used for species which are present in high concentrations or in bigger sizes (e.g. cells) to keep the design simple. Nano patterning is used for sensing very small concentrations or for sensing molecular species which need even smaller surface geometries to interact at molecular level [88]. However, electrode capacitance and other double layer effects need to be carefully modeled for such small scale systems to optimize the size scales for different applications. For example, Pt electrodes are known to have more capacitance than Au electrodes [89]. This means high surface area Pt electrodes should be replaced with Au electrode for fast sensing applications. Similarly, overly dense structures are not good for high frequency applications and hence micro patterning may be more useful for these applications.

Such patterning has been demonstrated in the past for Platinum based sensors using many different material systems [90], [91], but we used standard Silicon and CMOS based materials and processing techniques to make high performance nano-patterned sensors as shown schematically in Figure 32. The fourth electrode shown here is optional and can be used in many different ways such as to make a differential measurement or to act as a second working electrode.

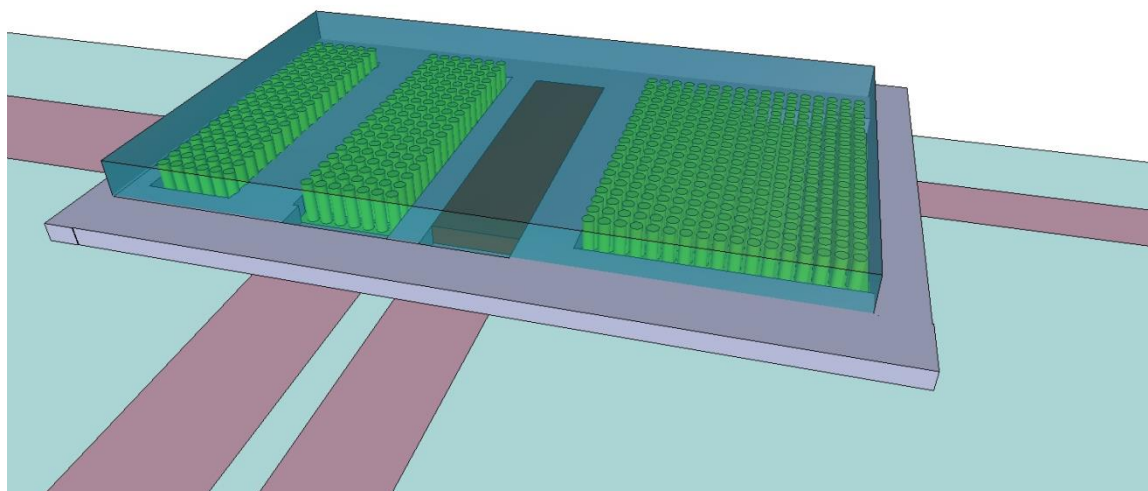


Figure 32 : Nanopatterned electrochemical sensor coated with a functionalizing matrix

For electrochemical metabolic sensing, the signal changes quite slowly and capacitance is not an issue as far as the sensor speed is concerned. Generally, the smaller the size of the patterns (e.g. pillars), the larger the sensing area and the better the sensor performance. The advantage of using patterned electrodes over planar electrodes is usually depicted by the surface area enhancement as given by following equation describing surface area of a patterned electrode (S) as compared to a planar electrode (S_0) in hexagonal packing²

$$\frac{S}{S_0} = 1 + 7.26 \left(\frac{r}{a}\right) \left(\frac{h}{a}\right)$$

Here, r is the radius of the pillars, h is the height of the pillars and a is the separation between the pillars. For a standard rectangular arrangement of pillars, the equation can be written as

² Derivation performed by Ervin Natawutt

$$\frac{S}{S_0} = 1 + 6.28 \left(\frac{r}{a}\right) \left(\frac{h}{a}\right)$$

For typical sensor parameters, the difference between the hexagonal and rectangular arrangement is not very significant. Since the rectangular arrangement is easier to layout and operate upon, we used it as the arrangement of choice in our work. These equations show that higher r/a and higher h/a give higher surface area which results in higher sensitivity and hence results in better devices. This clearly shows that electrode patterning is advantageous for performance enhancement, especially if the overall size of the sensor needs to be minimized. The exact scale of patterning depends upon the application and the cost of the processing. The height of the pillars is limited by the surface tension forces in the liquid. The pillar deflection due to these surface tension forces is given by [86]

$$\delta = \frac{Ph^3}{3EI}$$

Here, P is the capillary force, h is pillar height, E is young's modulus and I is second moment of inertia given by

$$I = \frac{\pi D^4}{64}$$

This also shows that Silicon processing can be advantageous since it provides high tensile strength. The young's modulus of Si (180GPa) and Pt (168GPa) are quite similar. However, the ultimate tensile strength of Silicon is 7000 MPa [92], as compared to around 300 MPa for Platinum. Assuming that a material with higher strength can withstand higher surface tension, Silicon nanopillars (or a combination of metals with other materials) can withstand more capillary forces than pure Pt metal. Other noble are also similar to Pt in mechanical properties. Although, the Si pillars are oxidized in some applications and coated with Pt, their properties should be better due to

the underlying core still made of silicon. Our results confirmed that these pillars were quite robust in solutions at the size scale where other pillars are reported to have mechanical issues as reported in literature [86]. The resulting sensor with nanopatterned electrodes are shown in Figure 33. Details of the fabrication procedure are given in the methods chapter.

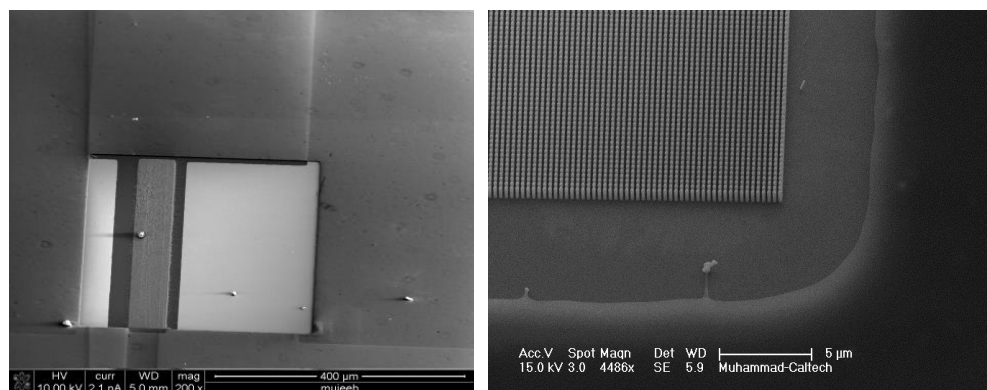


Figure 33 : Integrated Nanopatterned Electrochemical Sensors

The patterning methods used in this work do not need special materials, non-vacuum based processing (e.g. liquid plating methods), or complex porous templates which are difficult to replicate. This is a standard fabrication process and can even be integrated in the CMOS fabrication process to make it even more controllable and repeatable. Our novel patterning process can allow designers to design high performance electrodes for other applications apart from electrochemical electrode preparation where impedance poses a limitation.

3.5 Electrochemical Measurements

Electrochemical measurements can be made using different modes as discussed before. For implantable glucose sensing, we chose amperometric measurements which produce current output proportional to the reaction rate on the working electrode. This is more suitable to an implantable

sensor scenario since the reference electrode potential will not be very stable (due to changes in ion concentrations, temperature and other factors) [81]. Constant potential amperometry also minimizes the contribution of non-Faradaic currents to the overall sensor response, which improves the signal to noise ratio. However, Cyclic Voltamograms can be used to identify a host of different phenomena during the sensor operation. Although it suffers from charging current and hence is not the best analytic method, it was used extensively to characterize the sensors in different aspects. Chronoamperometry depends upon short pulsed measurements of the electrode current and has similar problems as it measures. Although there are charging currents as well as Faradic currents, it was also used as a test case for pulsed mode operation of the sensor.

3.5.1.1 Electrochemical Spectroscopy

There are different techniques which are used in electrochemistry to perform spectroscopic analysis over different variables, with frequency being an important one. Electrochemical Impedance Spectroscopy (EIS) is a technique of measuring the cell impedance (or conductance) across a range of frequencies around a set cell potential [76]. It is a very important tool in characterizing electrochemical systems in terms of their behavior in the solution and help understand and design such systems [93]. It involves biasing the electrodes at a known cell potential, sweeping the frequency of a small (few mV) ac signal on top of the bias and measuring the resulting cell current [94]. The resulting curve can be plotted as the imaginary versus real impedance (Nyquist Plot) or real and imaginary components of the measurement (either current or impedance) as a function of frequency (Bode plot). Results from EIS show the behavior of resistive and capacitive components of the cell impedance (including WE, RE and CE and solution resistance). If the system is properly designed (CE much larger than WE, inert RE with negligible current flow and solution with reasonable ionic conductivity) then the impedance mostly reflects the impedance of the WE which

is most interesting. It also helps in finding the equivalent electrical circuit of the sensor which is required for designing the control circuit for proper sensor operation.

It is important to emphasize that EIS measurements only reflect the cell impedance at the given cell potential as is used in the experiment. Sometimes, it is very difficult to do the EIS measurements at the desired cell potential due to large signal changes happening at the interface (e.g. during electrode polarization step). Hence, EIS is done at zero bias and is used in conjunction with other methods (e.g. cyclic voltammetry) to completely characterize the system response. Also, EIS results are the aggregate impedance results and there can be many different impedance networks which can result in same EIS response. Hence, the results are normally fitted to the predicted EIS models in theory to find the value of the different components of the already known model. This fitting can be done using custom written codes or using Frequency Response Analysis (FRA) software. Since the electrochemical cell is a non-linear system, it requires the use of non-linear FRA tools and methodologies.

We also used other electrochemical spectroscopic methods to further characterize our sensors. One such method is sweeping the potential between the electrodes and measuring the sensor current, all on a constant frequency. We call this Potential scan Spectroscopy. It helps compare different designs in terms of their impedance at different biasing potentials. The frequency of the input signal was swept from 100KHz to 10mHz, a range which is typically available range in commercial Potentiostat. The impedance can be matched to different electrochemical models to understand the electrode phenomenon. We considered the Randles model of an electrochemical cell which includes the impedance of the electrodes and the solution modeled as a combination of impedances.

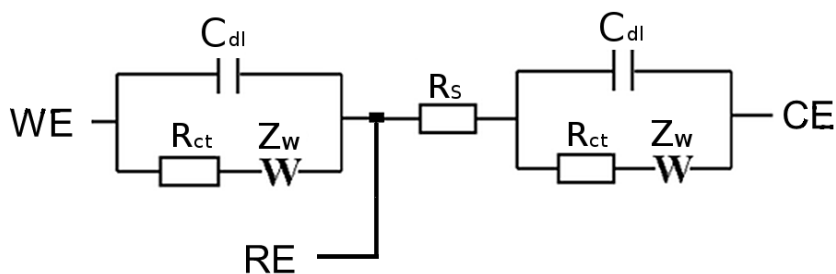


Figure 34 : Randles equivalent electrical model of an electrochemical cell

In this model, C_{dl} is the double layer capacitance at the electrode-electrolyte interface. R_{ct} is the contact (charge transfer) resistance between the electrode and the electrolyte. Z_w is the diffusion limitation (Warburg impedance) from the bulk to the electrode-electrolyte interface and R_s is the series resistance of the bulk solution between the electrodes. The double-layer capacitance is a nonlinear capacitance and hence is difficult to model. Its value depends upon many parameters including applied potential, temperature, ionic concentrations, types of ions, insulating layers, electrode roughness, impurity adsorption and so on [76]. Charge transfer resistance (R_{ct}) is the resistance to current flow at the electrode when the electrode potential is moved away from its Nernstian value. For a given electrode with surface area A , these parameters can be calculated as

$$C_{dl} = K \cdot A \quad (8)$$

$$R_{ct} = \frac{kT}{zq} \left| \frac{1}{i_T} \right| \quad (9)$$

A typical value of K is $10\text{-}100\mu\text{F}/\text{cm}^2$ for most materials and it is different for different materials. The numbers from different studies do not exactly match, but mostly fall within this range. The solution resistance can be calculated from its resistivity (ρ) and electrode spacing (L)

$$R_s = \frac{\rho L}{A} \quad (10)$$

The charge transfer resistance dominates the diffusion impedance (Warburg impedance) at low frequencies. Hence Warburg impedance can be ignored in such slowly varying metabolic sensors. This is one of the simplest electrochemical models, but is still more complex than normal impedance models. For example, the impedance due to the double layer capacitance mostly acts as constant phase element (CPE) rather than simple capacitor. Also, all impedances are non-linear and are frequency dependent. Warburg impedance represents the impedance corresponding to diffusion of specie to or from the electrode surfaces. It is frequency dependent and is also difficult to model. For simple models, it can be ignored, but for modeling of the diffusion effects on the cell performance, it has to be accounted for through numerical modeling. The usefulness of EIS is illustrated here by measuring the change in electrode impedance for planar versus nanopatterned electrodes as shown in Figure 35.

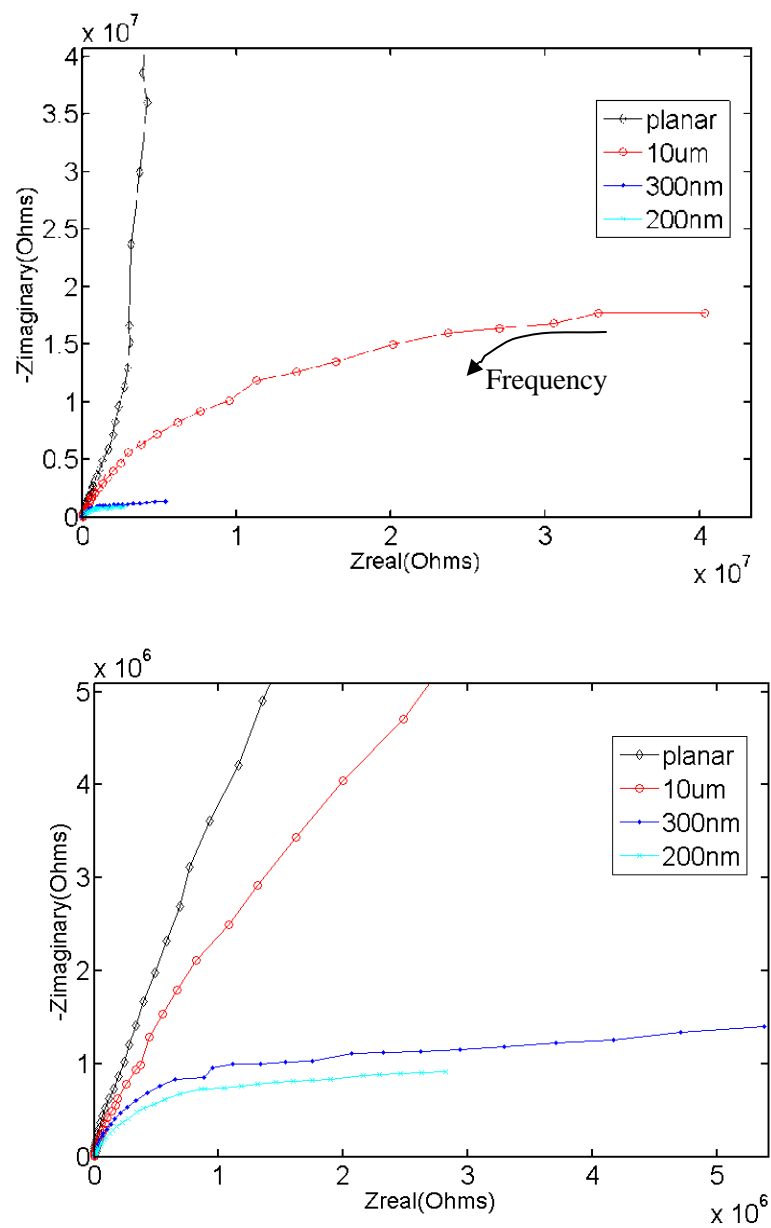


Figure 35 : Impedance Comparison between Planar and Nanopatterned Electrodes

Since the solution resistance in Randles model is the same for all the cases (the solution was PBS for all the sensors), the results clearly show that as the pillar diameter is reduced (and hence the

number of pillars is increased) the impedance of the sensor at a given frequency goes down. We also observed that both the charge transfer resistance and the double layer impedance decrease as both the real and imaginary impedances for nanopatterned electrodes are reduced with decreasing pillar diameter. The improved reduction in impedance between the electrode types is more pronounced at low frequencies which are the more critical range for most sensing mechanisms in biomedical applications. This was further confirmed by measuring the impedance difference between fully integrated planar and patterned sensors. This result confirmed the same trend for the entire sensor as was noticed for individual electrodes as shown in Figure 36.

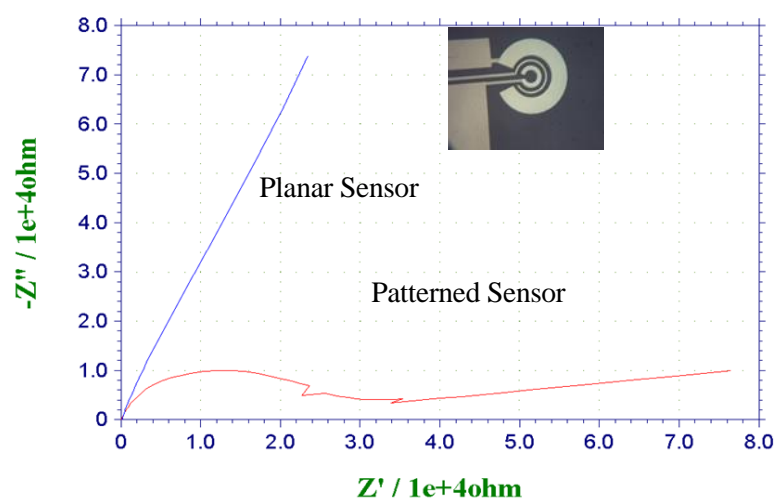


Figure 36 : Comparison between Impedance of Planar and Patterned Sensor

For almost all measurements, the decrease in impedance due to patterning is larger than that predicted by theory. However, it is important to point out that this trend will change at very small electrode spacing due to the overlap between the electric double layers. Hence, the enhancement in overall effective surface area (electrochemical equivalent surface area) will be lower than that in

device surface area. This happens at nanopillars spacing comparable to the electric double layer thickness which depends upon the electrolyte in the relevant study. For typical electrolytes, the double layer thickness is less than 1 nm [76]. Hence, the effect does not come into play unless the pillar spacing is comparable to this dimension.

3.6 Surface Functionalization

The electrochemical sensor needs to be coated with different chemistries to operate in selective environments for sensing selective species in a process called functionalization. Different types of functionalization methods have been developed for electrochemical sensors. For ultra-small devices, *in situ* functionalization provides the most flexibility with the process while still allowing high yields. In this work, functionalization is achieved either through immobilization (fixing a specie to stay near the electrode surface is called ‘immobilization’) or by direct chemical binding (e.g. Nucleic acid binding using thiol chemistry) based upon application. For example, for sensing glucose levels in body fluids, the sensor needs to be able to produce a signal proportional to the glucose level in the body. This signal has to be selective to the presence of other similar molecular species like ascorbic acid, acetaminophen, urea, and even other types of glucose and higher saccharides (e.g. Maltose). This selectivity can be obtained by different methods. Since glucose does not have a significant electrochemical signature, the most sensitive method is to use chemistry which can convert it into some electrochemically active specie which can be sensed selectively compared to other interfering species. These enzymes have to be kept close to the electrode surface for sensitive detection. Immobilization can be achieved using different methods including direct binding (van der Waals linking, ionic bonding, covalent bonding), encapsulation (hydrogel, conducting polymer), cross-linked aggregation [95] or some special support materials (e.g. titania sol-gels). Direct entrapment in different types of hydrogels is a simple yet efficient method although

without enzymatic crosslinking, the enzyme loss occurs very rapidly and the sensor cannot function for long time [96]. Immobilization in a hydrogel along with cross-linking with that hydrogel increase enzyme entrapment (decrease leakage) without affecting its properties much [97]. Electropolymerization is an alternative to hydrogels and involves entrapment of enzymes while a monomer is being polymerized electrochemically in a polymer[98]. This method allows very fine control on the thickness, enzymatic loading, and diffusion properties of the immobilization matrix. The most commonly used materials for both of these entrapment methods are organic hydrogels (e.g. BSA hydrogel, PVA hydrogel, Chitosan) and inorganic polymers (e.g. Silica, Conducting Polymers like Polypyrrole) [98]. Another benefit of immobilization is that it increases the enzyme life-time and enables repeated use for long-term detection. This is supposed to be due to lower unfolding of the enzyme which decreases the chances of its denaturing [97]. It also decreases the denaturing by increasing the temperature at which enzyme stops working. For example for Glucose Oxidase, immobilization in hydrogel has been shown to keep the enzyme stable at as high as 70°C [97]. In our experiments, Glucose Dehydrogenase appeared to be stable for almost the same temperature when immobilized under same conditions in same material.

Table 2 Comparison of Functionalization Methods

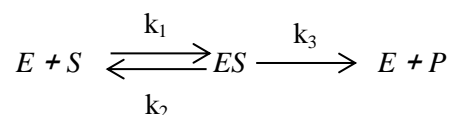
Method	Complexity	Effect on Enzyme	Leakage	Control variables	Applicability
Adsorption	Simple	Native State (Less Stability)	Strong	pH, surface dependency	Enzyme, Surface Specific
Covalent Link	Moderate	Changed(may affect reactivity)	Small	Presence of inhibitors, pH	Enzyme, Surface specific
Chemical Entrapment	Moderate	Increased Stability	Moderate	Mixing Ratio	Universal
Electrochemical Entrapment	Complex	Increased Stability, Transduction	Moderate	Electrical Parameters, Concentrations	Moderate
Crosslinking	Complex	Decreased Activity	Moderate	Amount of Enzyme	Wide

Typically, lithography is used to pattern and define the functionalization matrix [99]. However, this involves the use of high energy (Ultraviolet) light or electron beams and also exposes the enzyme to organic solvents (e.g. acetone). These factors are known to affect enzymatic activity. Hence, we used a physical in-vivo functionalization method by forming a controlled well-like structure around the sensor and later on filling it with a hydrogel solution which gels at room temperature without the need of any complex processing. This eliminates any damage to the enzyme, even if it is minimal.

3.7 Enzyme Kinetics

The enzyme kinetics are important to understand sensor operation and also to design the optimum enzymatic loading for different applications. The theory of enzyme kinetics is described by Michaelis–Menten theory [80]. This theory assumes that the enzyme works by first forming an

enzyme-substrate complex which then decomposes. Part of it forms product and some part goes back to the actual substrate and enzyme. In terms of chemical reactions, this can be written as



The Michaelis-Menten constant K_m is equal to the substrate concentration at which the catalytic rate is half of its maximum value. Hence the reaction rates can be described as follows

$$V = V_{max} \frac{\{S\}}{[S] + K_m}$$

$$K_m = k_2 + \frac{k_3}{k_1}$$

The apparent K_m is found by fitting the reaction curve (catalytic rate versus substrate concentration) to the Michaelis-Menten equation. For high enzyme activity in immobilized form, the reaction is substrate diffusion rate limited and for low activity, it is enzyme activity limited. Hence, in former case the apparent K_m from curve fitting is larger than K_m of free enzyme in the solution and in the latter case it is closer to the K_m of free enzyme in solution under ambient conditions. For reaction rate limited by other factors (e.g. mediator concentration), the apparent K_m can actually be lower than the K_m of free enzyme in solution. An example of a linear fit for one of the sensors is shown in Figure 37. As seen, linear fitting of the entire curve will result in larger K_m than actually measured.

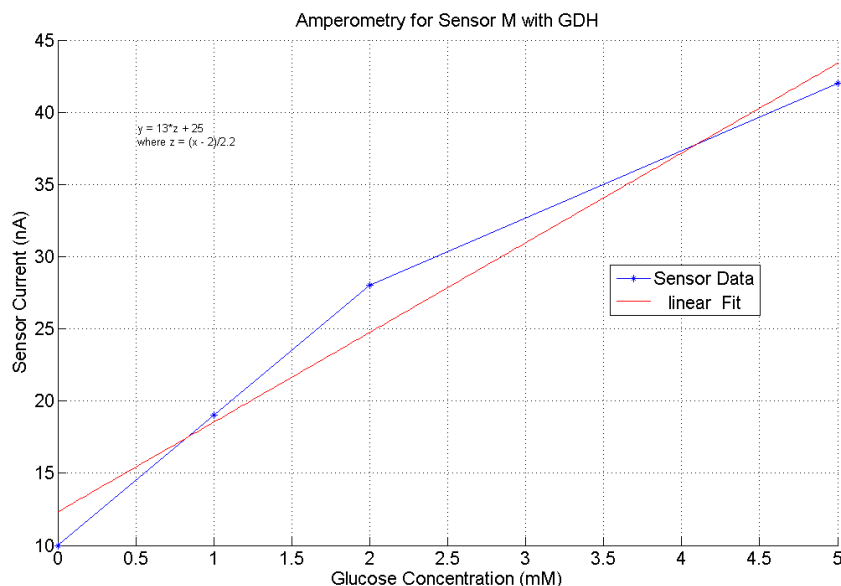


Figure 37 : Fitting sensor response for Enzyme Kinetics

Modeling of the currents for enzyme electrodes has been performed extensively in the literature for many practical cases [100]. For the special case of thin film sensors, the current equation is modified and solved numerically. The closed form analytical solutions under some assumption is given as [101]

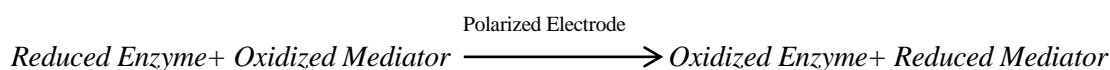
$$\frac{nFA\alpha}{i_{obs}} = \frac{K_m}{k_{cat} \cdot K_s \cdot s_{\infty} \cdot \mathcal{E} \cdot l} + \frac{1}{k_{cat} \cdot \mathcal{E} \cdot l} + \frac{1}{k \cdot K_A \cdot a_{\infty} \cdot \mathcal{E} \cdot l}$$

Here, n is number of electrons transferred in the reaction, F is faraday constant, A is electrode area, i_{obs} is observed hydrogen peroxide detection current, k_{cat} is apparent catalytic constant of immobilized enzyme, K_m and K_s are apparent Michelis-Menten constants for enzyme and substrate, k is the rate constant for reoxidation rate of mediator, l is the thickness of the immobilized layer, s_{∞} and a_{∞} are the bulk concentrations of substrate and mediator, \mathcal{E} is enzyme

concentration in immobilized layer, α is between 0.5 and 1 and represent the balance between the oxidation of reduced mediator to the bulk and to the electrode surface. The above equation can be used by fitting the sensor response to it which can yield the values of different parameters. Another approach uses numerical simulations to solve for different cases. We used COMSOL software's physical modeling tool to model the reaction-convection equation and solved some simple scenarios to see the effect of different system parameters on its performance. Afterwards, we used an experimental approach for the system design.

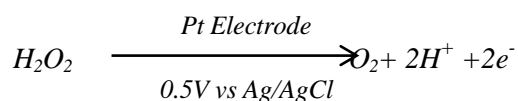
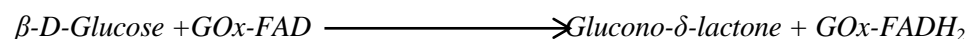
3.8 Glucose Sensing

Glucose sensing is one of the most important applications of electrochemical sensors. There are three generations of electrochemical glucose sensors defined in literature, each with different methods of transduction of electrons to the underlying electrodes [83]. Glucose itself is not electrochemically active and does not have a strong electrochemical signature. However, nanopatterning increases this weak signal on Pt and some other special alloy electrodes for solid-state sensing. However, the achieved performance is not selective enough for implant applications [83] and therefore, for selective detection of glucose, the electrodes are functionalized with glucose selective chemistry. Enzymes are the most commonly used materials for this purpose and are the basis of almost all clinical glucose sensing available currently. In general terms, an enzyme can convert a selective molecule (substrate) into other molecules in the presence of suitable environment, as shown by following equations. Such enzymes are called oxidoreductases and are normally in their oxidized (natural) state.





More specifically for glucose, these enzymes mostly oxidize it into glucono- δ -lactone (which hydrolyses in water to gluconic acid). The most common mediator in in-vivo solutions is dissolved oxygen molecule (O_2 and is reduced to H_2O_2). This reaction can be described by following chemical equations



At the CE, some reduction takes place to balance the WE current. The most common reaction is thought to be the reduction of O_2 .



This results in a net current flow in the external circuit which can be used to measure the reaction rate and eventually glucose concentration.

In this work, glucose was successfully sensed³ using both GOx and GDH based sensors in PBS, mouse serum, and mouse blood. Results show that the sensor has very sensitive response to glucose in the metabolic concentration range (0-10mM). The sensors were more sensitive at lower concentration, which is important for detecting hypoglycemic events that can be very dangerous if not detected in time. At high concentrations, the sensor showed some saturation effects and the

³ This work was done by Muhammad Mujeeb-U-Rahman and Mehmet Sencan

response becomes a bit non-linear (enzyme limited region). If needed, this response can be tuned to a specific sensitivity by controlling the enzyme concentration in the immobilization matrix or by controlling the glucose flux into the immobilization layer. A typical response of a sensor coated with hydrogel with immobilized gold is shown in Figure 38. The sensor in this case consists of a planar thin film electrode as a WE using off-chip RE and CE.

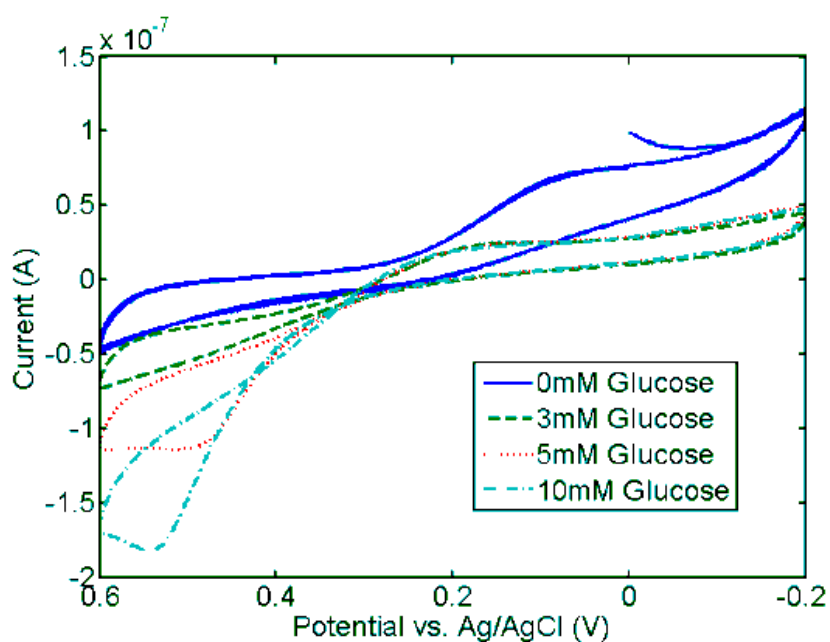


Figure 38 : In vitro sensing of Glucose using electrode immobilized w/ GOx

Another set of experiments were carried out using fully integrated sensors with on-chip WE, RE, and CE. Same geometries were used to compare the enzymes; results are shown in Figure 39. It seems from the results that GDH-FAD is more sensitive compared to GOx. This means that lower quantities of enzyme can be used for detection. This is very relevant to the implants since the

enzymatic loading decreases with time and longer operations are possible with enzymes which can provide more sensitivity even when present in small amounts.

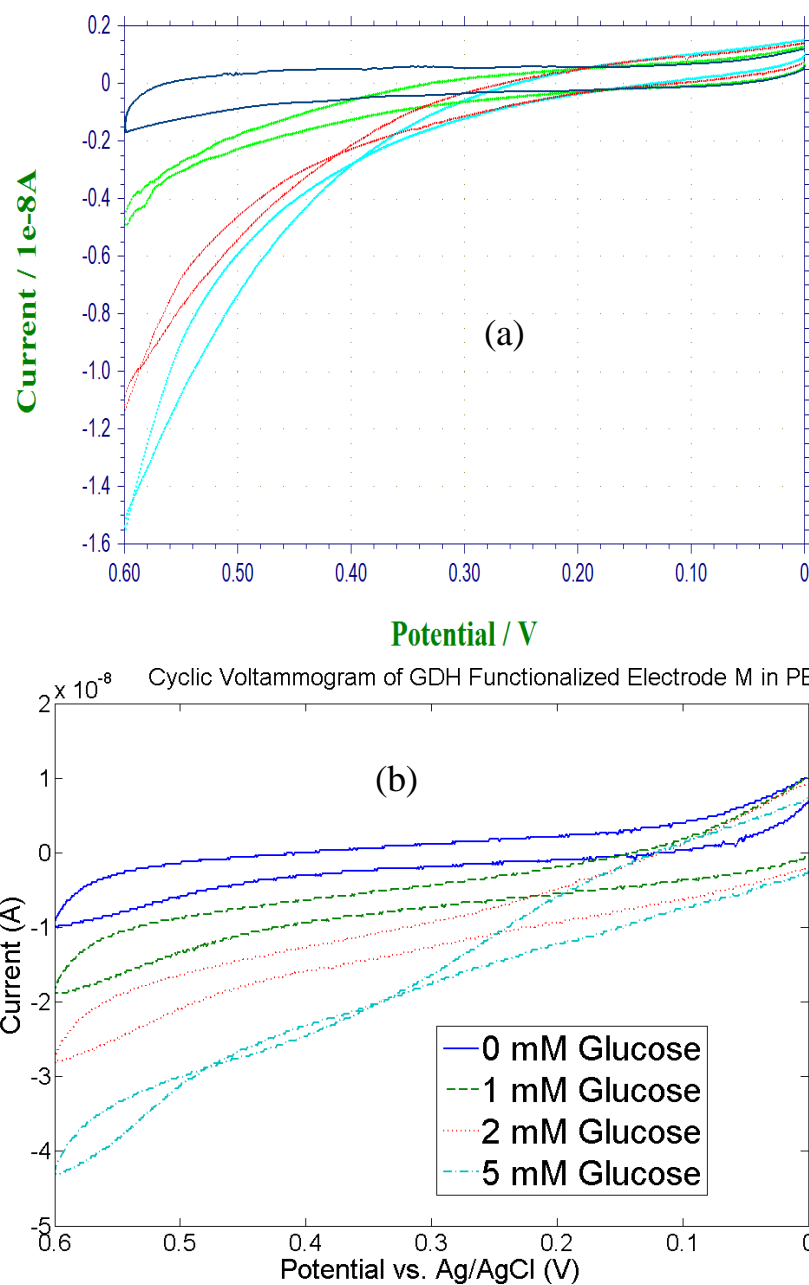


Figure 39 : Glucose sensing using integrated sensors with (a) GOx (b) GDH

A nanopatterned sensor with similar functionalization provided an order of magnitude improvement over these sensors as shown in Figure 40. It is good to note that the response seems similar to the simulation results of nanopatterned sensors in terms of narrow cyclic voltamograms as shown in appendix I. The sensor shows improvement over the planar sensors in many ways. It has higher current as well as higher linear region of detection. This proves that the performance of small integrated sensors can be controlled precisely by the control of their surface geometries and can be tuned to many applications where traditional planar sensors may not be able to provide sufficient performance.

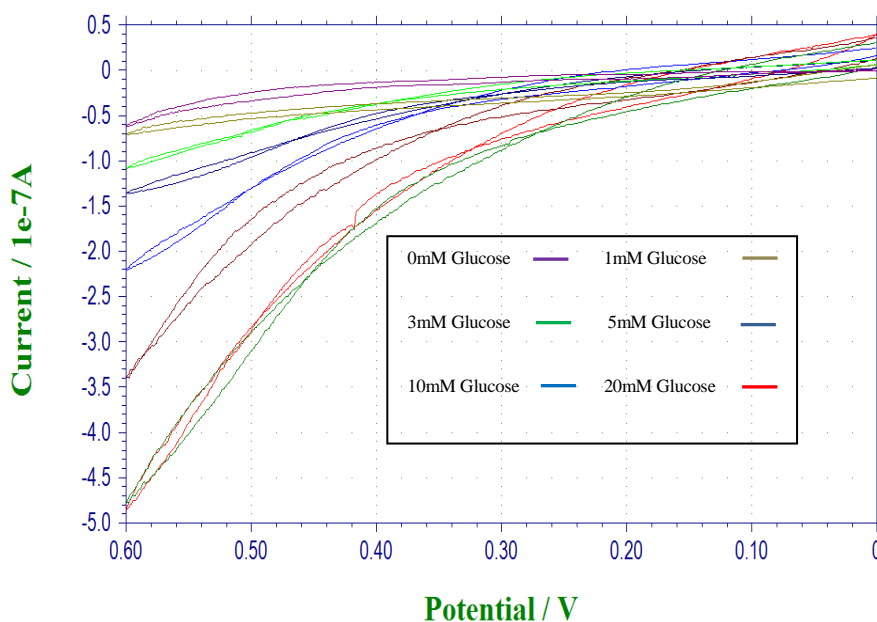


Figure 40 : Nanopatterned Glucose Sensor performance

A comparison of the nanopatterned electrode with the planar electrodes provides insight into the performance enhancement provided by Nanopatterning.

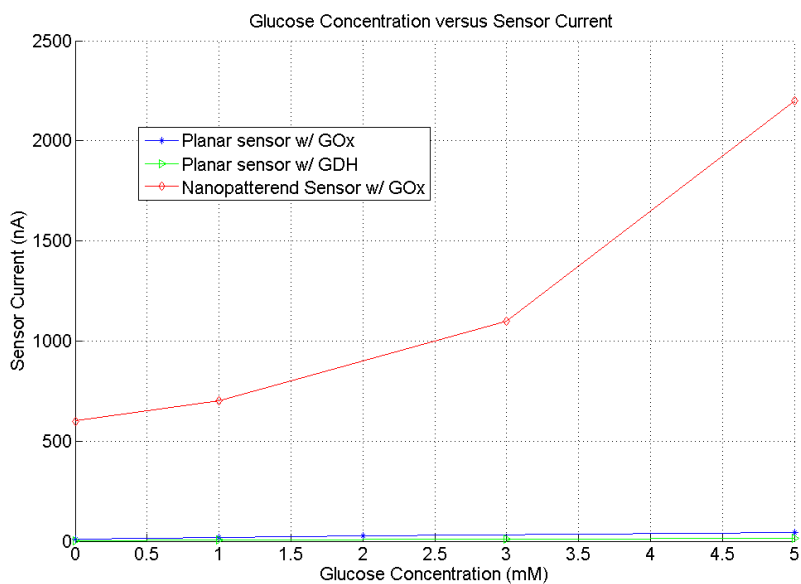


Figure 41 : Comparison of Nanopatterned and Planar Sensors

Coulometry is the measurement of charge involved in the reaction and is the most direct method of making reaction measurements. Chronocoulometry does this for short pulses and the following graph (Figure 42) is an example after 3 weeks of a sensor under pulsed testing.

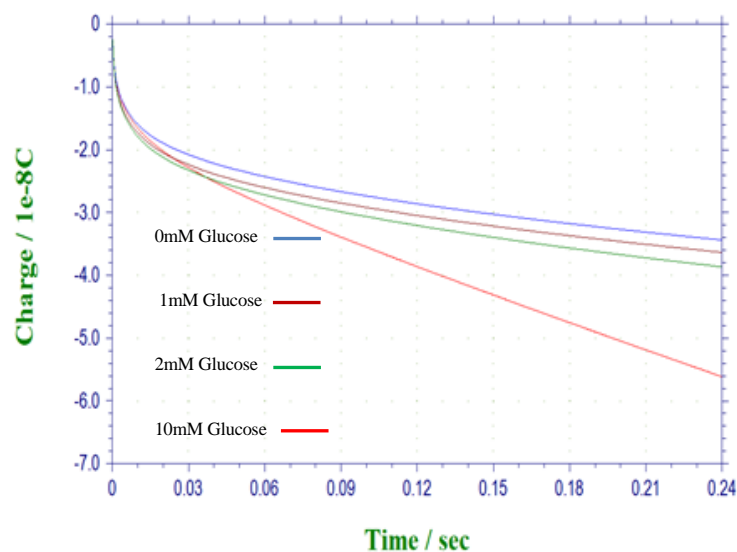


Figure 42 : Chronocoulometric Sensing of Glucose in PBS

Repetitive pulsing shows that this technique is valid for ‘continuous’ measurements if the pulses are separated by a short time period. The pulses just need to be sufficiently separated to allow glucose diffusion and enzyme reaction to equilibrate completely (reach steady state) which are both pretty quick phenomenon as glucose is a small molecule and hydrogel consists mostly of water. For more detailed analysis of this system, numerical modeling using ‘transport through porous media’ can be used in the regime.

Constant potential amperometry was also used to characterize this sensor because of its potential of continuous measurement as well as less background noise compared to the Chronoamperometric and Cyclic Voltammetric methods. The WE was kept at 0.6V vs. Ag/AgCl RE for this measurement. The results are shown in Figure 43.

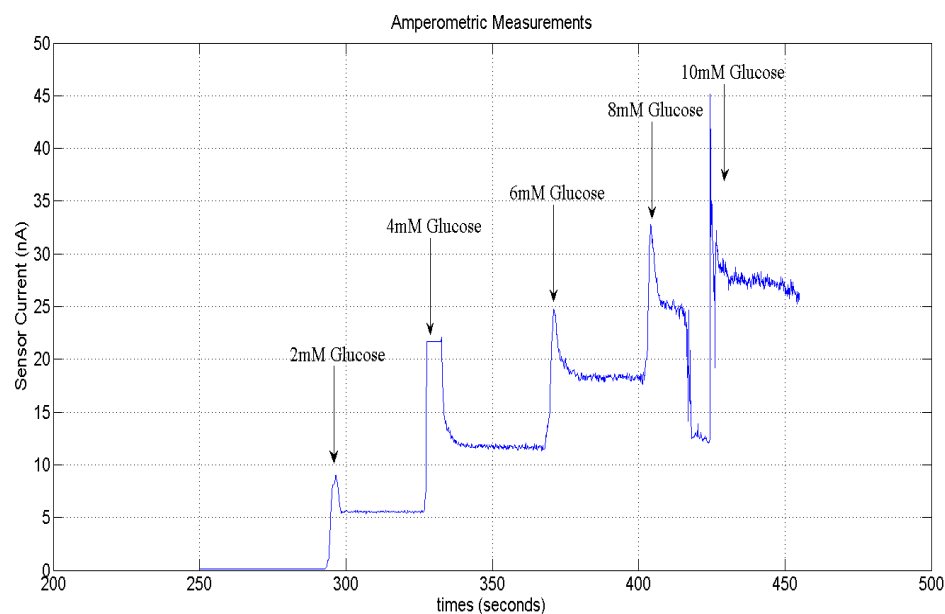


Figure 43 : Amperometric Glucose Sensing using an integrated planar sensor

3.8.1 Testing in Body Fluids

Testing in blood is quite challenging due to the active degradation by the enzymes and other components of the blood. In commercial strip sensors, elaborate filtering mechanisms are used to avoid these effects. In implantable sensors, the need of repetitive use limits the type of filtering mechanisms that can be used. However, the hydrogel (or other immobilization matrices) provides some inherent filtering. Both CV and Chronoamperometry were used to characterize the sensor response in mouse serum first, as shown in Figure 44. The sensor currents decreased from their value in PBS. However, the response was still detectable, and signal processing (e.g. integration) could be used to extract signal with high enough fidelity.

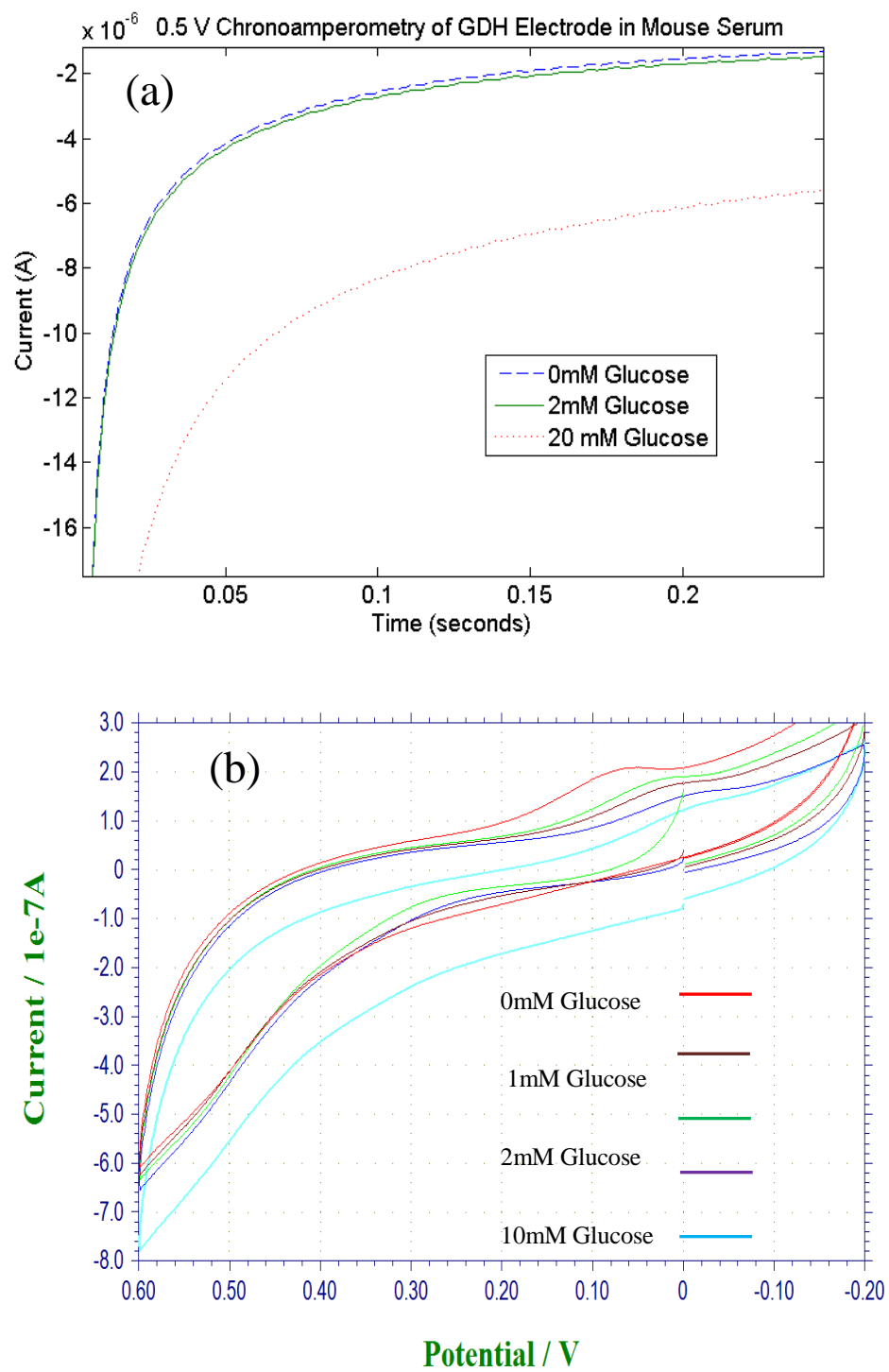


Figure 44 Glucose Detection in Serum using (a) Chronoamperometry (b) CV

The sensor response in blood was even more suppressed than that in serum. This can be explained by the blockage of hydrogel sites with blood cells or other blood components. However, sensor still showed adequate sensing after couple of days of incubation as shown in Figure 44.

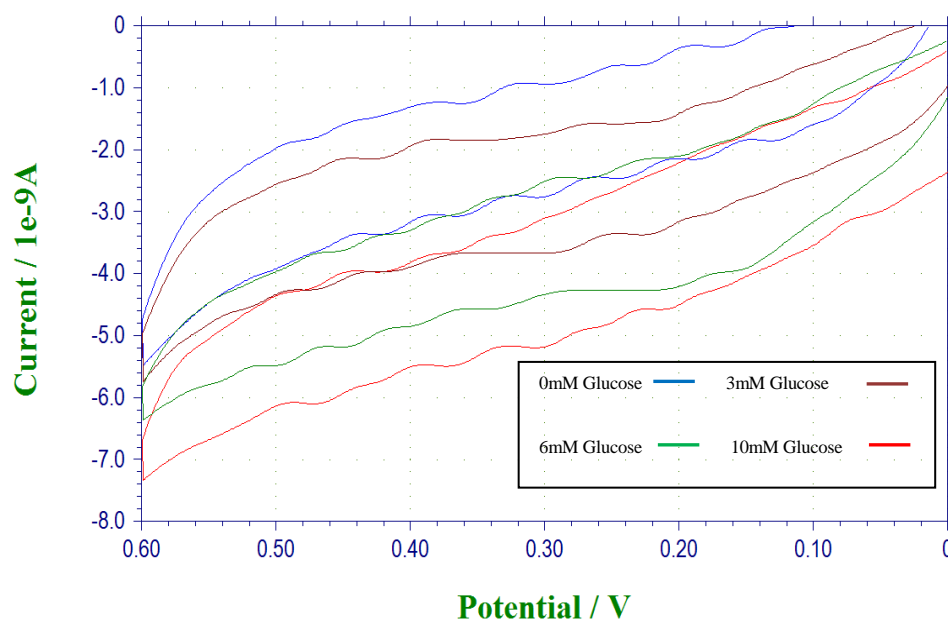


Figure 44 : Sensor w/GDH, test in mouse blood

As seen here, the current and sensitivity both have decreased. However, Signal processing could be used to recover sensitivity again. Furthermore, for many applications, operation in interstitial fluid can suffice, which is quite close to the serum in chemistry. Hence, direct testing in blood is not needed. If such devices are needed, some blood filtering (e.g. dialysis membranes) methods should be used to increase sensor life-time as well as to get higher signal levels for better accuracy.

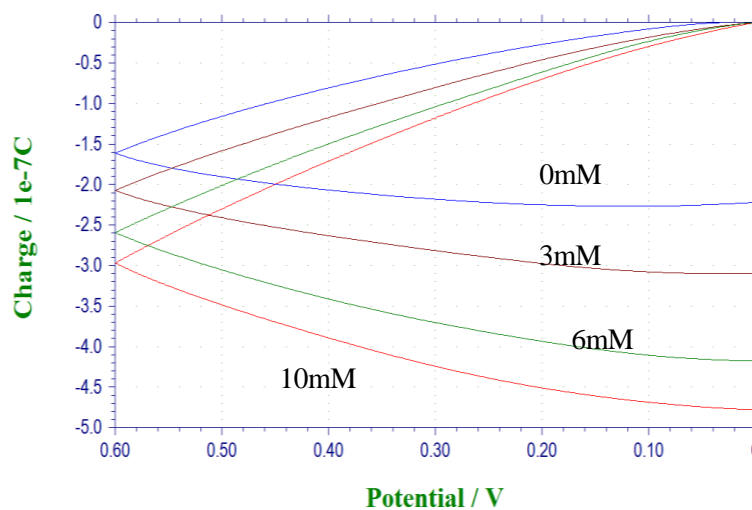


Figure 45 : Improving Sensitivity using Signal Processing

These results show that such sensors can be used in complex body fluids. However, use of filtering mechanism can improve their response and extend their life-time for long term use.

3.8.2 Interference Issues

Interference from other species is an important concern for sensors in complex environments e.g. *in vivo* sensors. For glucose sensors, the most problematic interference is from acetaminophen, ascorbic acid, and urea [3]. This happens when high potentials (near 0.6V) are used for glucose sensing. The interfering species also oxidize around this potential on Pt electrodes and hence cause noise signals. As an example, a thin film Pt sensor with repeated tests in PBS shows very little deviation (noise). However, with 0.1mM Acetaminophen (AA) in the solution, the interference level increases significantly, as shown in Figure 46.

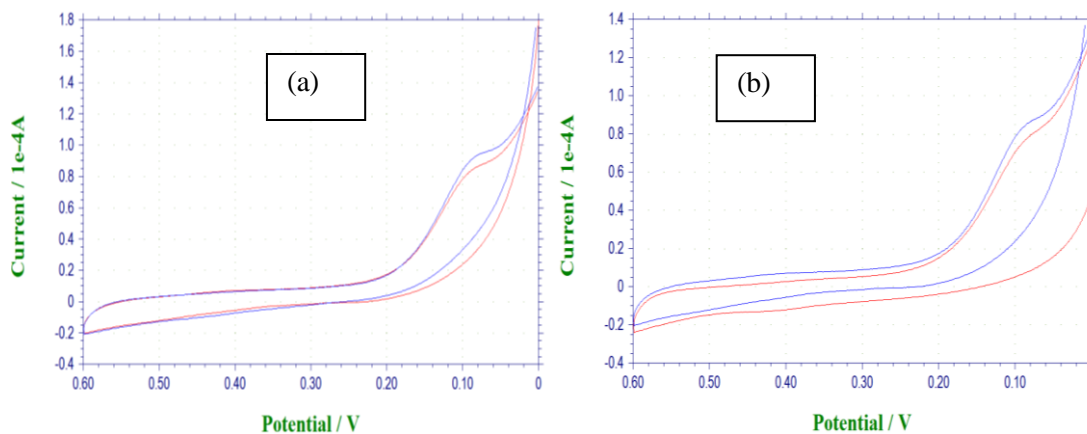


Figure 46 : Interference on Pt electrodes (a) in PBS (b) with 0.1 mM AA

Thin films of dense polymers like polyphenol (PPh) can be used to limit interference as well as immobilization of enzymes [101]. Such coatings are effective because these do not limit the smaller molecules which are being detected while filtering the larger interfering molecules. As very thin coatings (e.g. 10nm) can be very effective in interference reduction, their effect on sensing smaller molecule (like peroxide) can be negligible as shown in Figure 47. It shows that the change due to AA is negligible compared to the change due to peroxide detection. Hence, PPh acts as a very good interference rejection layer without affecting the peroxide sensing as it is much smaller molecule compared to the interfering molecules.

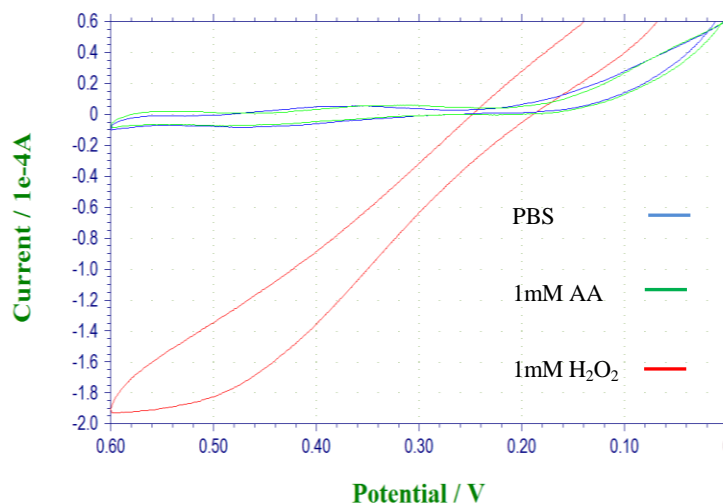


Figure 47 : Effect of PPh on Peroxide Detection on Pt electrode

Another method to get rid of interference is to use lower potentials or even negative potentials to keep these species from creating a signal. However, using lower positive potential for peroxide detection decreases the sensitivity, although it is still adequate for accurate detection. This method is more suitable for detecting oxygen consumption in the glucose enzymatic reaction and converting that information into oxygen concentration after adjusting for the background oxygen levels in body fluids. This approach was used in first bench top glucose sensors and is also used in some modern research due to its excellent interference rejection properties [35]. Alternatively, detection at low potentials can also be achieved if the enzymes being used can transfer the electrical charges easily to the underlying electrodes. In this case, the detection mechanism is direct charge transfer from enzyme to the underlying electrode which depends upon conduction properties of the enzyme and the immobilization matrix. For example, Glucose Dehydrogenase-FAD enzyme has a cytochrome-c entity as a part of its synthesized version from some sources [102]. This entity is known to help the tunneling of electrical charge from biological molecules [103]. This can be even more pronounced

at the nano scale where the enzyme molecules can be in much closer proximity to the electrode than the planar sensor. Hence, lower potentials can be used to detect glucose and the interference issues can be avoided. This is actually observed in our devices using Glucose Dehydrogenase as measurable glucose signal detection start happening around 0.1V, which is low enough to avoid interference from the above mentioned species. Further optimization can be performed to increase the transduction by having conformal layers of enzyme coated directly on the pillars. A historic example of this direct conduction (also known as ‘wiring of enzyme with the electrode’) is the use of osmium based PVP polymer which allows the reaction to happen at lower overpotential (near 0V) and hence reduces interference effects[104]. Normally, mediators are used in sensors to accelerate the electron transfer from the enzyme and hence decrease the dependence on dissolved O₂. Ferrocene and its derivatives are the most widely used mediators [105]. However, previous work on osmium complexes showed that in the presence of proper transduction from the enzyme to the electrode, the O₂-dependence of the detection can be minimized. Since mediators are toxic and can leach from membranes, avoiding their use is the best policy for a long term implant applications [104]. Hence, redox hydrogels or polymers are very attractive for these sensors. We tested the use of such polymer for peroxide detection using horseradish peroxidase. The synthesis of this polymer for glucose based enzyme would allow us to use it for glucose sensing as well. However, due to toxicity of osmium, more work remains to be done before its use in implantable applications.

Another method is direct transduction without the need of any supporting chemistry. However, enzymes are large and complex molecules and the reaction centers are mostly located deep inside their structures. Hence, to be able to tunnel the electrons from these to underlying molecules, either very small mediator molecules or redox-mediator based hydrogels are needed [106] unless the enzyme molecule is engineered to have some electron tunneling structure (e.g. heme) [103].

Glucose Oxidase based detection is known to have high sensitivity towards dissolved oxygen. This was tested by bubbling air through the solution (which increases O_2 concentration as measured by a commercial dissolved oxygen sensor). Results are shown in Figure 48 and clearly indicate relatively large change due to O_2 concentration change. However, secondary effects like enhanced diffusion after bubbling can also have secondary effects in such experiments.

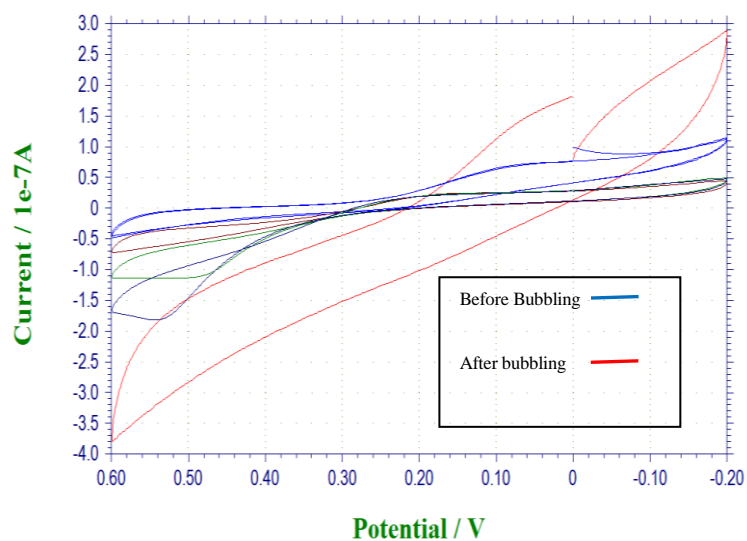


Figure 48 : Effect of O_2 bubbling on GOx Sensor

On the other hand, GDH based detection showed much reduced O_2 dependence, as depicted by Figure 49. This is due to the O_2 independent pathway that GDH takes for glucose oxidation.

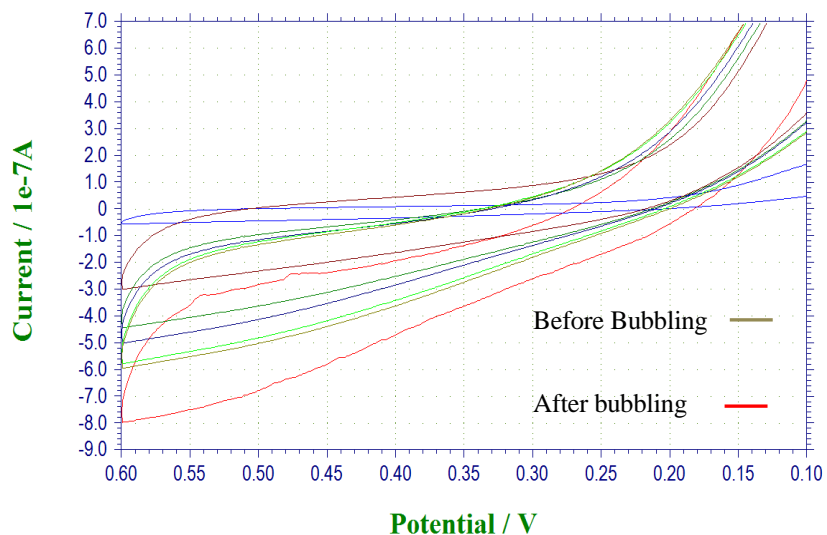


Figure 49 : Effect of O₂ bubbling on GDH Sensor

Another method to minimize interference uses multiple working electrodes to measure glucose through hydrogen peroxide and oxygen sensing mechanisms. The same enzyme can be used for this purpose along with same working electrodes. This method involves measuring at negative potentials for oxygen sensing using two electrodes, one of which is not coated with enzyme hydrogel and the other is coated with the enzyme. The difference in their oxygen measurement is proportional to the glucose concentration. Also, this does not involve interference from species which oxidize at positive potentials and has been used for glucose sensing by itself for long time [35]. However, for very small electrodes, this may become a challenging measurement since the dissolved oxygen concentration is very small in the body fluids. Together with the hydrogen peroxide sensing mechanism, this method can generate useful results; nano-patterning of the electrodes for optimum oxygen sensing can improve dissolved oxygen sensing to make this measurement even better.

3.8.3 Lifetime and Repeatability

Longevity of these devices is crucial for meaningful implant applications. Longevity was tested by sensing for a few days to a few weeks. It was thought to provide an insight into the time response of these sensors to design appropriate calibration algorithms. Different solutions of PBS and pH buffers were added as control solutions, but did not create any appreciable change in the sensor response. This demonstrates that these sensors have very good signal to noise ratio. Also, these devices exhibit good longevity. The sensors were also measured using different hardware platforms (CHI 7051D as well as Metrohm450) and different laboratory settings to test their robustness. These were also shipped back and forth between different labs and showed very stable and repeatable results. A comparison between the sensor responses over 3 weeks is shown in Figure 50.

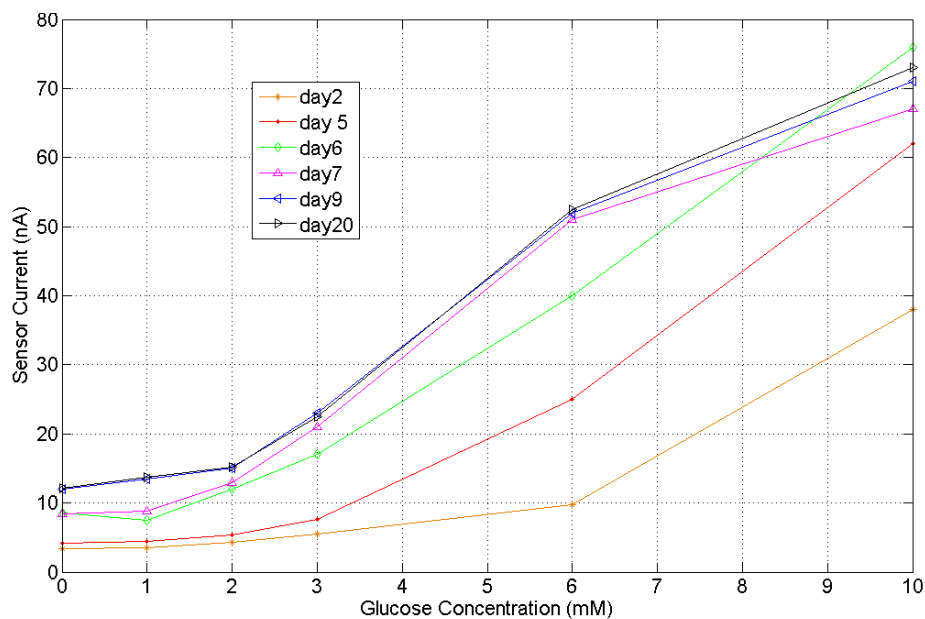


Figure 50 : Response of a Glucose Sensor over 3 weeks

This test also showed that the response was not very stable. This is assumed to be a result of the functionalization matrix not completely free of unbound material. As the differences decreased with time, this argument seems quite plausible. Storing these sensors for some time before their use should decrease this effect substantially. Also, Chronocoulometric measurements showed much lower variations. We think this is because these methods are more limited by diffusion of specie rather than the gel properties. Also, larger signal and integration decreases effect of current variations somewhat.

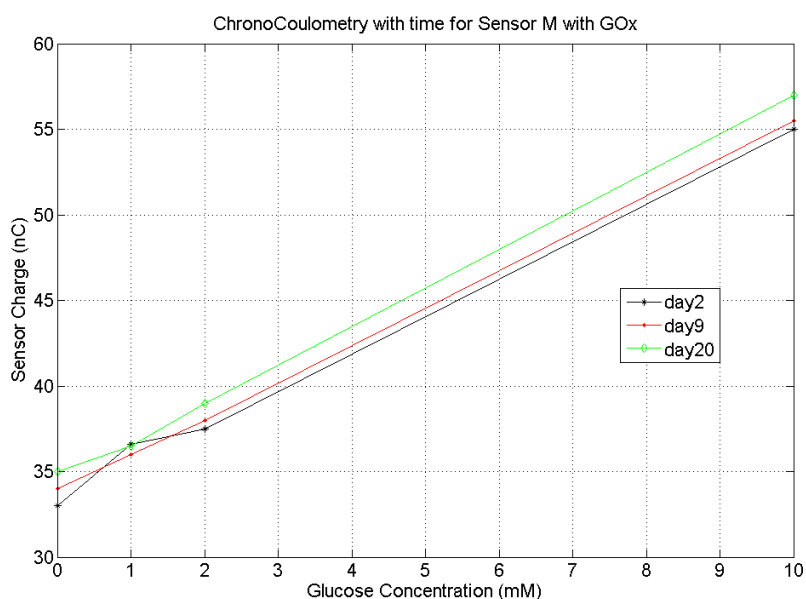


Figure 51 : Chronocoulometric Response of a Glucose Sensor over 3 weeks

Sensor to sensor variation is another important constraint in realizing repeatable results from microsensors. Since these sensors were meal coated using manual processing, there were variations in the overall sensor structure from one sensor to another. Even in immobilization performed

manually, variations in process and chemicals conditions could occur. Hence, it was difficult to compare devices over different fabrication and immobilization runs. However, devices within the same fabrication and immobilization runs could be compared. For example, a batch of 8 devices was selected in the same fabrication and immobilization run for comparison and for the working devices in this batch, the sensor response showed very little (less than 5%) variation. This shows that if these sensors are fabricated under more controlled environments (e.g. an automated fabrication line), these can provide very repeatable results and calibrating individual sensors may not be necessary. The response curves are shown in Figure 52. The Pt RE based sensors showed more variance than the AgCl based RE, although both were within the error tolerance. Simple analysis shows that these devices have good signal to noise ratio (around 10). Hence, the required accuracy could be achieved and the exact allowed tolerance can be found by measuring glucose levels in the same solutions with a gold standard device (e.g. benchtop instrument from Yellowstone Instruments) and plotting the results on the Clark Error Grid which is the clinical standard for allowed variance in glucose readings [43].

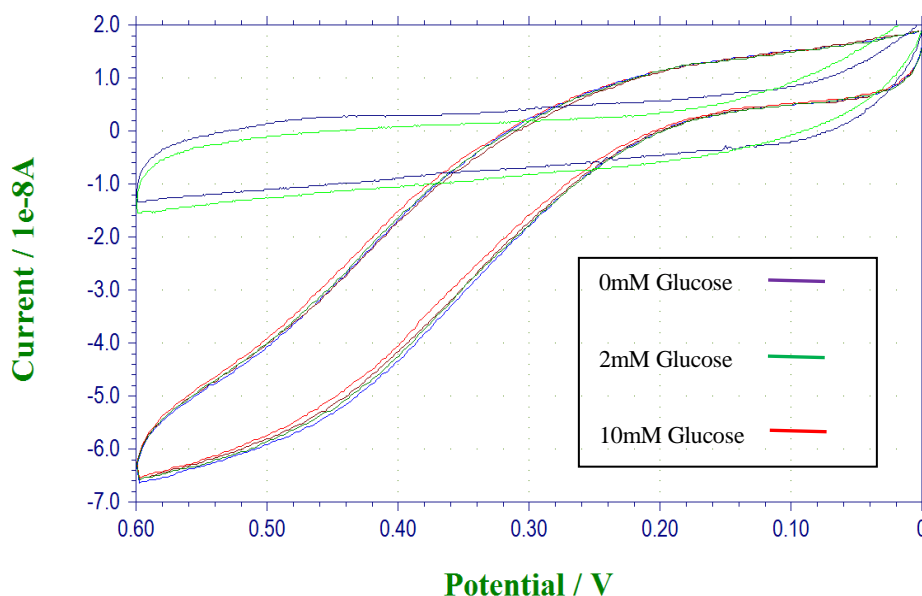


Figure 52 : Sensor to Sensor Variation within a batch

Electrochemical noise and interference (ENI) is defined as the noise due to inherent electrode processes and interference from other species due to reaction with enzyme or directly with the electrode. Noise processes on electrodes are quite complex and depend upon the type of electrode processes (Faradaic versus non-Faradaic). Thermal noise is always present in all systems and random adsorption/conduction reactions can also occur at the electrode surface. A detail of the electrochemical noise processes is given in literature [107]. A practical approach we used was to perform statistical characterization of the sensor and then use change in current (δI) as a measure of electrode noise. This change is statistical and would better model noise if a large number of measurements are taken. Also the average current (I) was used to normalize the change ($\delta I/I$) and the normalized change was found to be less than 5% in most of the cases. In these cases, the total noise of the measurement depends upon external noise sources (circuit noise, electromagnetic

noise) rather than the internal electrode noise. However, for very small sensors, the simple ($\delta I/I$) test should be repeated to see this. At some point, the electrode noise will start dominating the external noise. The clinical accuracy levels for implantable glucose levels allow 5% error. Hence, these sensors can be used for clinical applications [19].

3.8.4 Optimization of Sensor Response

In order to optimize the sensor (e.g. to extend the sensor lifetime), the functionalization chemistry needs to be optimized carefully. For example, optimal enzymatic loading should be used in the immobilization matrix to keep the sensor in mass-transport limited regime (for linear current output) for the entire concentration. On the other hand, to extend the sensor life-time, high enzymatic loading should be used as the enzyme degrades with time (due to peroxide 'bleaching', thermal effects, statistical protein death, etc.). Hence, the sensor response may not be linear initially. In such cases, a mass-transport limiting membrane is normally used to extend the linear range of the sensor. Different materials can be used for this purpose. Polyurethane is a typical example of this. For harsh environments (e.g. blood), Dialysis membrane and Nafion are also used as both a protective and a filtering layer [43]. We coated Nafion on our sensors using both physical deposition as well as electrochemical coating. Our results with Nafion coating showed that the sensor kept its sensitivity and the linear range got extended a bit, most probably due to the filtering effect of Nafion. Overall, current decreased a bit, possibly also due to the filtering effect. However, it has been mentioned in the literature that Nafion is not suitable for long term implantation due to calcification. There are other materials (e.g. Humic Acids) which can provide better alternative for longer operations [108].

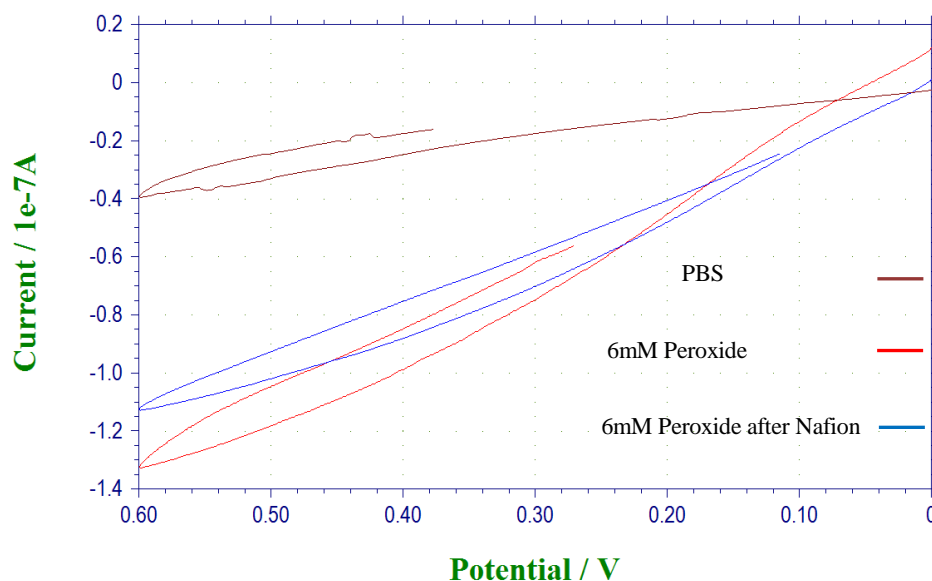


Figure 53 : Effect of Nafion coating on Peroxide Detection

Another method is to again use multiple working electrodes with similar coating, but using one at a time. The electrodes can be coated with materials that degrade at a programmable rate (e.g. PLGA) and only one electrode is under use at a time. The electrodes can be switched at either a pre-programmed rate or through an external command. External sources like light, local heating, etc. can also be used for the purpose of exposing a particular electrode at one time [68].

Another optimization parameter is the choice of enzyme. The most commonly used enzyme for glucose sensing is glucose oxidase (GOx). It has been well-studied and has good sensitivity and selectivity for glucose. The most common cofactor is FAD and is the part of the enzyme (reaction center) where the glucose reaction actually happens. An issue with glucose oxidase is that it uses oxygen as a mediator for the glucose reaction. In fingerprick devices, this is overcome by using mediators. However, most of the mediators are small and toxic and are not good for implantable

devices [37]. Glucose Dehydrogenase (GDH) is another type of enzyme which can be used for such devices. GDH with FAD cofactor is also quite sensitive and selective towards glucose. Our experiments indicated that GDH-FAD is more sensitive towards glucose than GOx and is also less sensitive to dissolved O₂ concentration compared with GOx (Figure 39). It can detect smaller levels of Glucose compared with GOx which is important during hypoglycemia. It also has a wider dynamic range of detection than GOx owing to its higher activity [109]. Also, although GOx can be engineered to have an electrical transduction element, some versions of GDH-FAD naturally appears to have one [102]. The only disadvantage of GDH-FAD is that its xylose sensitivity is higher than GOx. It is reported that xylose level gets high in the body right after eating (plant based food) and it is not absorbed much, but is quickly excreted [110]. One advantage of GOx is that it has been well studied and engineered to have better stability as compared to GDH. However, with research focus on implants and hence on GDH, this difference may diminish soon. Hence, GDH-FAD appears to be the better enzyme than GOx for implantable applications. Further protein engineering can be used to decrease its xylose sensitivity and to make it even more suitable.

There are some non-enzymatic chemistries as well that are being explored for their use in glucose sensing. Boronic Acid is a common example. It has the problem of high sensitivity towards other saccharides as well [83]. Active work has been going on for improving its properties as it provides a very attractive alternative for long term applications.

A detailed comparison of different enzymes used in glucose sensing based upon literature[109] and our results is given in table 3. It seems that GDH is a much better choice than GOx.

Table 3 Comparison of Different Glucose Sensing Enzymes

Enzyme	Activity	Interference	Cofactor	Longevity	Transduction	ENI
GOX-FAD	Low	O ₂	Integrated	Yes	No	Moderate
GDH-NAD(P)	Moderate	-	Separate	No	No	High
GDH-FAD (Fungal)	Low	Xylose	Integrated	Yes	No	Moderate
GDH-FAD (Bacterial)	High	Maltose	Integrated	Yes	Yes	Low

3.9 Nucleic Acid Sensing

Nucleic Acid (DNA/RNA) sensing has many applications in biomedical measurements including disease diagnostics, gene detection etc. Electrochemical Nucleic Acid sensors are capable of very sensitive and selective detection of DNA strands and mutations [111]. We used DNA hybridization for the detection of single stranded DNA (ssDNA) target strand using a complimentary ssDNA as a probe. The chemistry used was based upon Bard et al [112]. Our protocol is given in methods chapter.

3.9.1 Sensor Design

Three electrode sensors were used for Nucleic acid based sensing. For surface functionalization, we used thiol binding as Au was used as the WE material. A standard Ag/AgCl electrode was used as reference electrode. For CE, both Au and Pt RE were tried. Geometries used were similar to the ones used for glucose sensors in this work.

3.9.2 Functionalization

Sensors were functionalized with specific nucleic acid sequences for detecting complementary strands through hybridization. A methylene blue redox probe was attached to the probe strand. After

hybridization, change in the nucleic acid morphology creates a change in the redox current and that change is proportional to the quantity of probes hybridized with the target. Careful surface cleaning and electrochemical profiling was done to make sure there were no redox peaks before the nucleic acid attachment. Surface properties at each step of the process were tested by electrochemical means by running a square wave voltammetry from 0 V to -0.6 V at different frequencies (near 100Hz) versus the Ag/AgCl reference electrode. Tests showed that the actual voltage of redox peak depends upon the type of the CE material as well as sensor environment and the frequency of detection. For sensors with Au CE, the peak position seems to be a bit shifted (from the redox potential of the methylene blue probe) towards the higher potential. The peak was also more broadened than the sensors with Pt CE. The peak position appears to be a function of frequency for Au CE sensors, but not for Pt CE sensors as shown in Figure 54. This demonstrates that Pt or other noble metals should be used as CE material for these sensors. Also, control of surface morphology at each step is very important for a successful sensor based upon surface chemistry.

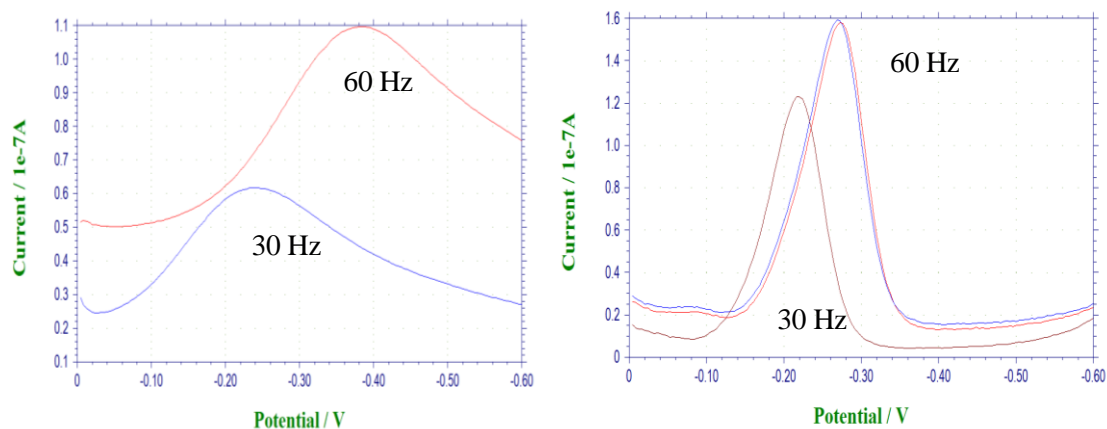


Figure 54 : Frequency Dependence of MB Redox Peak

The difference in the peak current corresponds to the decrease in redox current of the methylene blue probe which corresponds to change in the morphology of the probe strand due to hybridization.

3.9.3 Results

For DNA sensing, functionalized sensors were immersed in a beaker containing PBS and tested using different Voltamograms (e.g. CV and square wave voltammetry). Hybridization was tested by either dipping the electrode in a complimentary ssDNA solution or by adding the ssDNA solution into the test solution itself. The first method was used for commercial electrodes (3mm diameter) which were dipped in the complimentary solution with concentration of 2micromolar DNA. However, the integrated planar and nanopatterned electrodes were tested by spiking the background solution with 2microliters of 2micromolar target solution and measuring the decrease in redox current as a function of hybridization time. The results showed that these sensors have very good sensitivity towards the target DNA, despite their small size. The current levels of the planar integrated sensors were lower than the big commercial sensor. The nanopatterned sensors showed even more current than the commercial planar electrodes. Hence, it can be concluded that nanopatterning increased the signal level by decreasing the electrochemical impedance overall as well as by increasing the hybridization efficiency by increasing the number of target sites. The experiment was repeated with a control DNA and the results did not show any appreciable hybridization. The results are shown in Figure 55.

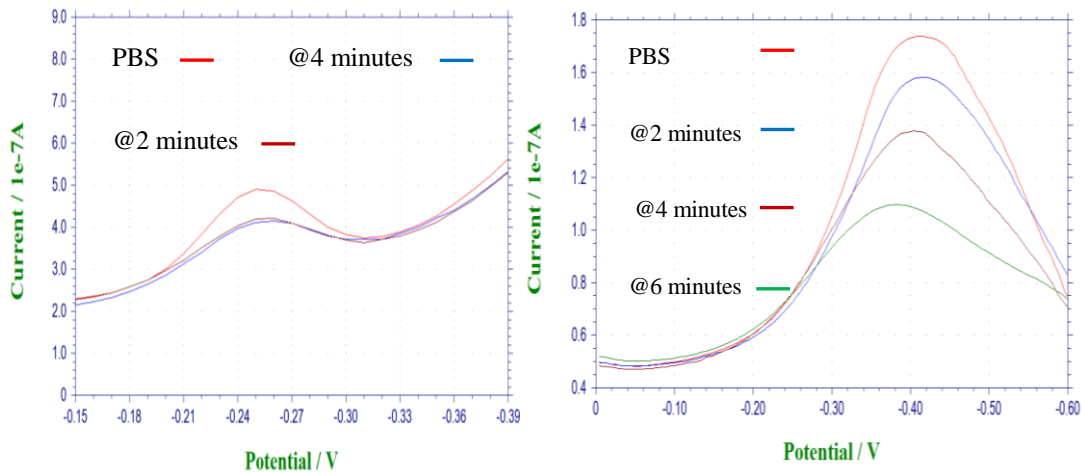


Figure 55 : Comparison of Macro and Micro Planar Sensor as function of Hybridization time

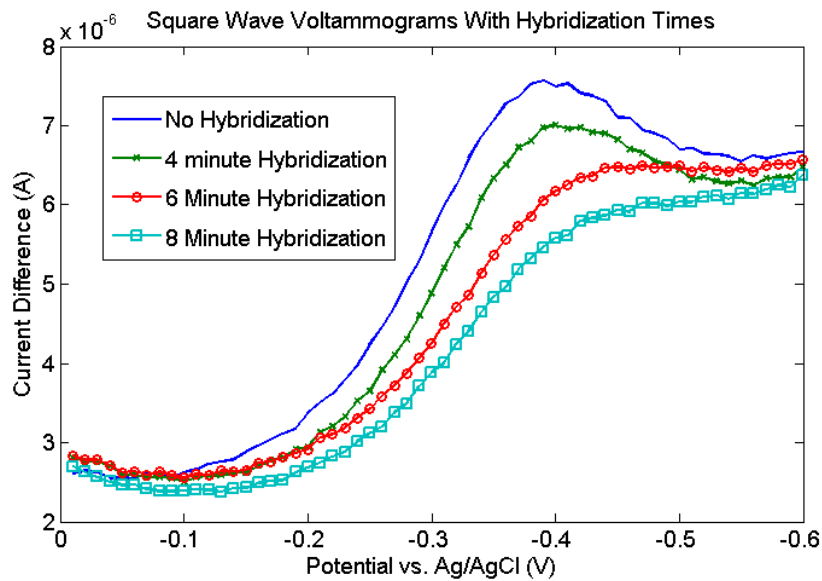


Figure 56 : Hybridization Detection using Nanopatterned Sensor

These sensors showed detection of nucleic acid in near-picomolar (100 picomolar) concentration within ten minutes. The background signal remained quite stable for several days in the dark at room temperature. The exact detection range and current on each sensor was a bit different due to lack of precise control on the probe coverage in our functionalization procedure. However, this can be overcome by normalizing the sensor signal according to the background signal after it is allowed to stabilize in the background solution. Hence, such sensors need at least one normalization step for clinical use. This can be avoided again by automating the functionalization protocol and by improving the probe coverage either through lithographic or chemical methods. Also, while CV could detect these reactions, square wave voltammetry provided more sensitive signals due to the accumulation of signal over the redox potential. Hence, square wave voltammetry was used in this case. The parameters of detection (e.g. frequency) depend upon the system design and optimal parameters were found through regressive testing and analysis.

These results showed very fast and sensitive response for such hybridization processes which can be beneficial for many applications. Patterning can be used to make devices for field applications where traditional electrochemical sensors were not traditionally considered due to their slow response time, but can cut the cost for such applications.

Sensor to sensor variation was larger for the DNA sensors as compared to the glucose sensors. There can be many reasons for this. First, the chemistry to backfill the electrodes surface is not very repeatable and this changes the background currents. Also, it is hard to control the surface coverage of probe molecules. Hence, these sensors would mostly need some calibration procedure prior to their use in tests. Simple background currents in buffer solutions may be an adequate calibration

depending upon applications. Also, the chemistry and fabrication procedures can be standardized to make these sensors more reproducible.

3.10 Protein Sensing

Proteins are some of the most important candidates for measuring the health of a person. There are different traditional methods to measure proteins (e.g. antibody binding tests and western blotting tests). Electrochemical sensors can provide good performance to these methods and can be more suitable choice for integrated operations [113]. Recently, Aptamer based protein sensing has gained much interest. Aptamers are segments of nucleic acids which can be designed to provide sensitivity to select proteins and can be more stable than traditional antibodies. Specific aptamers are selected to detect a specific protein using Systematic Evolution of Ligands by Exponential Enrichment also known as SELEX [114]. An alternative is to use segments of nucleic acids found empirically. For example, the Insulin Linked Polymorphic region is known to be part of the insulin gene and has been shown to be selectively sensitive to insulin by Jennifer et al. [114].

In this work, Insulin was sensed because of its importance in the metabolism as well as its relevance to the long-sought closed loop glucose sensing and regulation system. Details of the protocol used are described in the methods section. Due to chemical selectivity of aptamers, these sensors can have higher selectivity compared to non-functionalized sensors (e.g. those based upon metal oxides without any functionalization).

3.10.1 Sensor Design and Testing

Integrated planar sensors similar to the one used for DNA hybridization experiments were used for this study. Sensors were tested using same AC Voltammetric technique as used in hybridization testing since the redox specie was same (methylene blue). The insulin-sensitive aptamer was used

instead of the ssDNA probe. Solution was spiked with different concentrations of human insulin dissolved in hydrochloric acid. Results showed the sensor provided adequate sensing up to 0.4 μ M human Insulin and adequate selectivity compared to other proteins (Bovine serum Albumin and Human Serum Albumin). Typical results are shown in Figure 57.

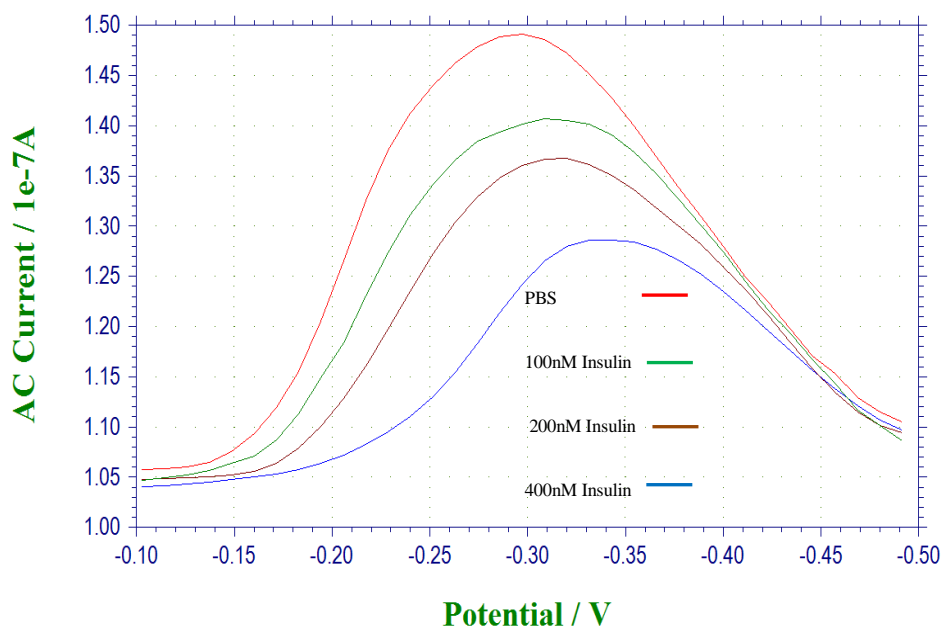


Figure 57 : Electrochemical Insulin Detection using
Aptamer

These sensors showed near micromolar detection range for insulin which covers the range in humans (normally picomolar). The sensors can be made more sensitive by further optimization of the chemistry and by protecting the probes from any surface binding or inhibiting factors that may be present in the experimental setup. Hence, these sensors can be used in in-vivo conditions. Also, use of nanopatterned sensors can increase the sensitivity and range of detection.

Similar to DNA hybridization tests, these sensors showed fast response (around 10-20 minutes for detection signal to become stable) but poor repeatability which can be solved proper coating procedures as well.

Finally, the combination of Aptamer based assays with enzymatic chemistry can provide very sensitive detection for many proteins. Such sandwich assays have been developed for sensing complex proteins like Thrombin [115]

3.11 pH Sensing

pH of blood or interstitial fluid is another important indicator of health. Variations in pH can disturb the metabolism and can result in a severe problem for people already at risk (e.g. diabetics). Normally, blood pH stays in a very controlled and narrow range near 7.4. Large changes in this affects many chemical reactions and can be very detrimental to body functions. pH sensing traditionally has been done using pH sensitive coatings (e.g. pH sensitive hydrogels) on ISFETs or electrodes. Solid state pH electrodes can be useful for long term use. Furthermore, noble metal oxide electrodes (e.g. Pd/PdO and Ir/IrO) have also been used for pH sensing. Since we use Pt as electrode material for our sensors, it was quite desirable to be able to sense pH using Pt electrodes. Bare Pt electrodes are not suitable for these applications due to interference from other species. However, forming an inert layer on these electrodes can decrease these interference effects while allowing these electrodes to attain stable potentials as a function of solution pH.

Different electrochemical methods can be used for pH sensing. We used open circuit potential measurements to minimize the interference from other sources (e.g. hydrogen peroxide) while being able to measure orders of magnitude difference in hydrogen ion concentrations owing to the logarithmic relationship of Nernst equation. Open circuit measurements depend upon the type of

electrode as well as the solution properties. If the electrodes are fixed, the change is only due to the solution properties. To enable measurements without the need of Ag/AgCl or other reference electrodes which cannot be used in some harsh environments, it was desirable to test if both electrodes could be Pt based. It seemed plausible that two Pt/PtOx electrodes (each oxidized to a different degree) can be used to make measurements. This would also minimize hydrogen peroxide interference on these electrodes. This interference can also be minimized by physical placement of pH electrodes away from glucose or similar hydrogen peroxide sensing electrodes. Results for a pH sensor are shown in Figure 58.

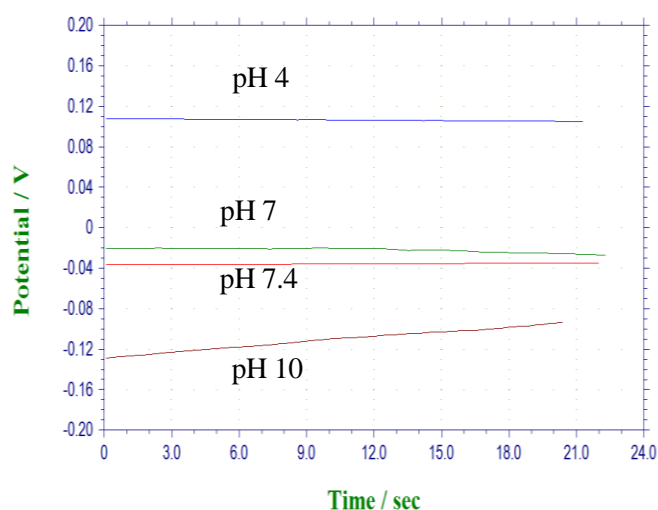


Figure 58 : pH Sensing using open circuit potential of Pt/PtOx vs. Ag/AgCl

Similar to the DNA sensing, this sensing is also a strong function of surface properties (e.g. surface cleanliness). This results in sensor to sensor variations, but the use of thoroughly cleaned electrodes shows pretty stable and repeatable response. Also, suitable coating materials (e.g. polymers, polyelectrolytes) can make these pH sensors more stable for long term use.

3.12 Simultaneous Sensing of Multiple Analyte

Multiple working electrodes can be used to sense multiple specie while sharing the same CE and RE. For example, simultaneous sensing of glucose and insulin can be very helpful in controlling medication of diabetes. Glucose measurements in the brain can also be very useful for diabetic patients. The same sensors can be used to measure neural chemistry as it is also a good indicator of personal health [116]. Similarly, continuous oxygen measurements, as well as pCO₂ and ionic measurements, can be very useful for continuous health monitoring.

3.13 Comparison of Electrochemical Measurement Techniques

We showed with examples that different electrochemical methods can be employed to characterize the response of different sensors. The following table compares these methods.

Table 4 Comparison of Electrochemical Testing Techniques

Method	Test Time	Accuracy	Signal Level	Selectivity
CV	Long (10's of seconds)	Medium	Medium	Medium
Amperometry	Short (couple of seconds)	High	Low	High
Chronoamperometry	Short (Fraction of second)	Low	High	Medium
Chronocoulometry	Short (Fraction of second)	Medium	High	High
Impedance Spectroscopy	V. Long (minutes to hours)	High	High	Low

3.14 Summary

In this chapter, design of micro/nano scale integrated electrochemical sensors for different sensing applications was discussed. It was shown that such devices perform very well for many applications

which were chosen as suitable examples here. However, the scope of these devices goes much beyond these applications. This provides the flexibility to use these sensors under a variety of conditions and environments.

Chapter 4 Wireless Powering

As discussed in Chapter II, wireless power transfer using power harvesting is the most appropriate method for small scale implants. This can reduce the size of our integrated system significantly since batteries are often their largest components. There are different possible methods which can be used to achieve such wireless power transfer. These can be classified as

(i) Mechanical (e.g. Acoustic) methods

(ii) Electrical (e.g. RF) methods

(iii) Optical Methods

The acoustic methods make use of relatively low frequency (up to MHz) longitudinal waves for energy transfer. Such waves are normally generated with some vibrating body (for example, a micro-resonating structure) and intercepted by another structure designed for this purpose [117]. Although these systems can be miniaturized to small scale, there are many technical challenges (non-standard materials, processing and power requirements) which need to be resolved before these devices can be used at the small size scale [118] desired.

The electromagnetic methods (both electrical and optical) make use of high frequency transverse waves. The useful frequency range spans from near Mega Hertz (MHz) to Tera Hertz (THz) and hence resulting structures can be quite small. The electrical methods use lower frequencies (RF and Microwave frequencies) where the interaction of electromagnetic waves with matter can be explained using electrical models whereas optical methods use high frequency where waves and matter interaction happen according to the optical properties of matter.

In this work, we used both optical and electrical powering methods and compared their performance. Both methods were optimized for ultra-small scale integrated applications. Electrical or RF methods have traditionally been used for wireless power transfer [48], but for ultra-small systems, optical methods can provide a better option due to the shorter optical wavelengths. Also, for miniaturization of power harvesting subsystem, high energy focused beams have to be used to transfer power to the system. As optical beams have the attractive ability to focus to micron scale resolution, optical devices can be made smaller than electromagnetic devices [119]. Another important design consideration is the efficiency to absorb most of this energy and provide it to a load. Optical power conversion efficiencies can be higher than electromagnetic power conversion efficiencies for ultra-small devices. Furthermore, optical systems do not need larger metallic structures which make these compatible with the low frequency electromagnetic medical instruments like MRI [120]. However, the interaction with tissue is much stronger near visible wavelengths than for lower frequency electromagnetic methods. Hence, an overall comparison will be needed to compare the two systems. In general, for very high optical frequencies, the response is mostly particle based whereby scattering and absorption are the most relevant phenomena. For lower electromagnetic signals, it is mostly the electric (dielectric and conductive) phenomenon which dominate the response [121]. For even lower frequencies, relevant to magnetic induction, the magnetic properties of the tissue are more relevant. We will compare these methods in rest of this chapter.

4.1 Optical Properties of Tissue

The optical spectrum of interest in our application involves frequency bands near visible wavelengths. This includes, Ultraviolet (UV) region which includes wavelengths below 400nm. This region can cause damage to the skin and other tissues. The visible region is 400-720nm and

causes less damage, but scatters and absorbs very strongly. Infrared (IR) region is considered from 800nm to 1000nm and near infra-red (NIR) is 750nm to 2200nm [122].

For optimum performance, the wavelength of the optical signal has to be chosen to minimize absorption and scattering in the biological media (skin, tissue) and maximizing absorption in the power harvesting subsystem without heating either of these. The NIR region is very suitable for such applications [122] due to the presence of a region of low tissue absorption (so called therapeutic window) which overlaps with suitable wavelengths that can be absorbed in silicon photovoltaic devices without creating lots of phonons and heating the silicon substrate.

The skin tissue has quite intricate structure as shown in Figure 59. There are basically two main parts, the epidermis and the dermis. The epidermis is the top of the skin, is pretty thin (hundred microns) and is subdivided into different layers: Stratum corneum is the top most layer and has refractive index of 1.55 and thickness near 10's of microns [123]. The lower layer is called the dermis and is a few mm thick (2-4mm usual) and variable. The dermis has order of magnitude less absorption and scattering than the epidermis. Subcutis (or Hypodermis) is below the dermis and also has variable thickness in the mm range.

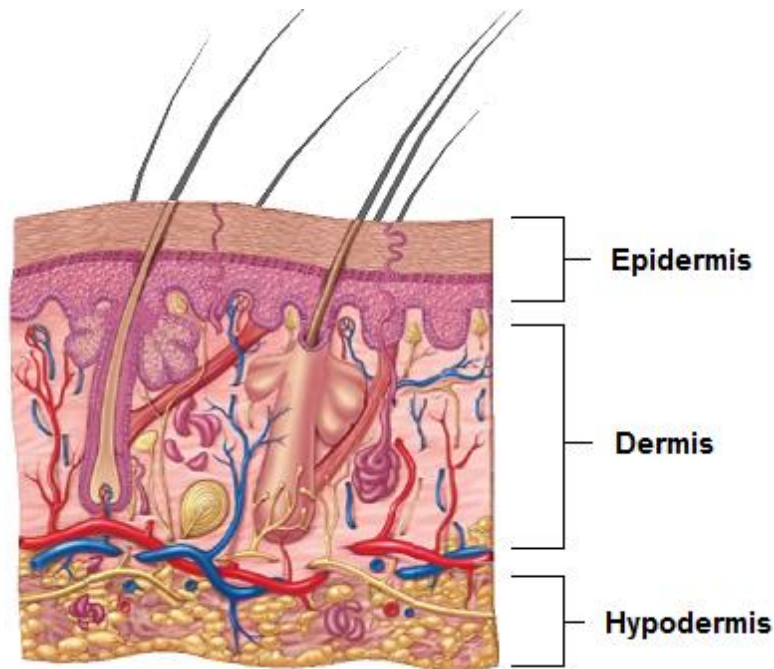


Figure 59 : Anatomy of Human Skin [124]

This complex structure leads to different optical phenomena such as absorption, scattering, and reflection in different layers. In general, the top layers have higher absorption and scattering coefficients which decrease as we go to the lower layers. For skin in NIR, overall absorption is normally much lower (e.g. 3dB) compared to scattering (e.g. 30dB) [125].

In the near IR, the differences in different type of skin are minimal as the dominant effects are from water and hemoglobin [126] . This allows us to use a general analysis approach without having to go into all different skin types. Figure 59 also depicts the non-homogeneity of the skin tissue which shows that it is hard to model with homogeneous parameters like the absorption coefficient. However, in practice, each layer is assumed to be uniform and the entire tissue is modeled as a stack of all these different layers. In general, the muscle tissues are simpler and are modeled using similar

schemes with lower number of layers than those needed for skin [127]. Pigmentation of skin (Melanin) and blood absorption (water and hemoglobin) are important components towards absorption. Absorption of light in NIR region in human skin is shown in Figure 60 [128].

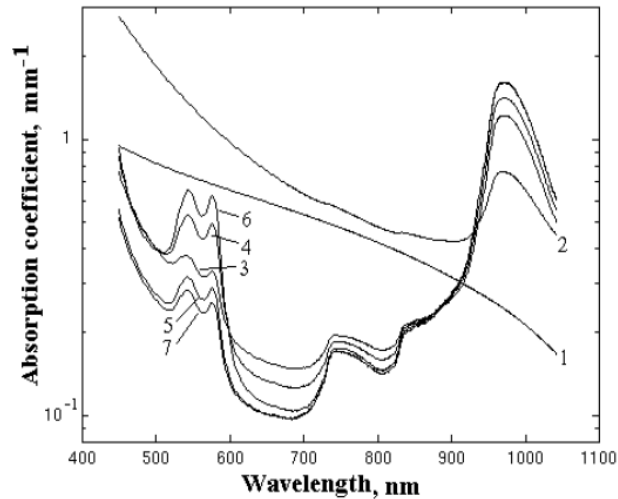


Figure 60 : Wavelength-dependent absorption of different components of human skin (-stratum corneum,2-living epidermis, 3-papillary dermis,4-upper blood net dermis,5-reticular dermis,6-deep blood net dermis and 7-subcutaneous fat)

Scattering is another important optical phenomenon for such systems as it also reduces the number of photons reaching from source to destination and hence can be treated as a loss mechanism. Scattering is mainly due to the microstructure of skin due to cells, their fine structure (membranes, lipids), large molecules (proteins (e.g. collagen)), and small molecules (water), etc. Scattering from small elements is Rayleigh like and from bigger ones is Mie like. Scattering in skin in near infra-red region is shown in Figure 61 [122].

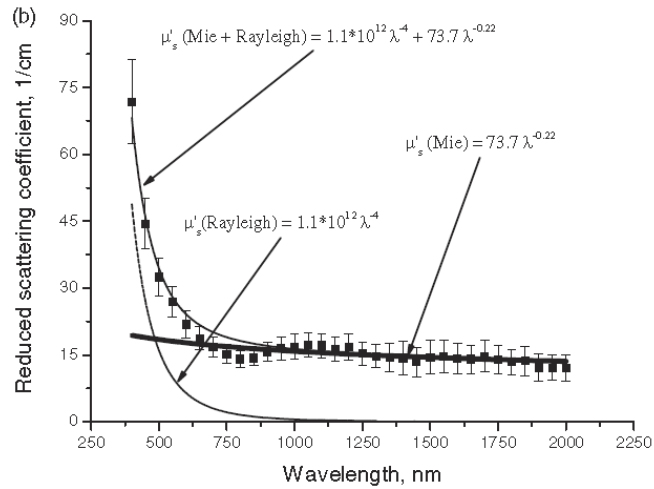


Figure 61 : Scattering coefficients of different layers of the skin tissue, and fitting results from Mie and Rayleigh theories [122]

It is evident from Figure 61 that scattering increases with a decrease in wavelength and hence is low at longer wavelengths of NIR region. Hence, NIR window is quite suitable in terms of minimal scattering as well.

Reflectance is also another important aspect. It depends upon skin type and wavelength. A typical results is shown in Figure 62 [129]. It shows that reflectance is less variable in the infra-red region around 800nm. This can further be reduced by using index matching substances between the skin and the device.

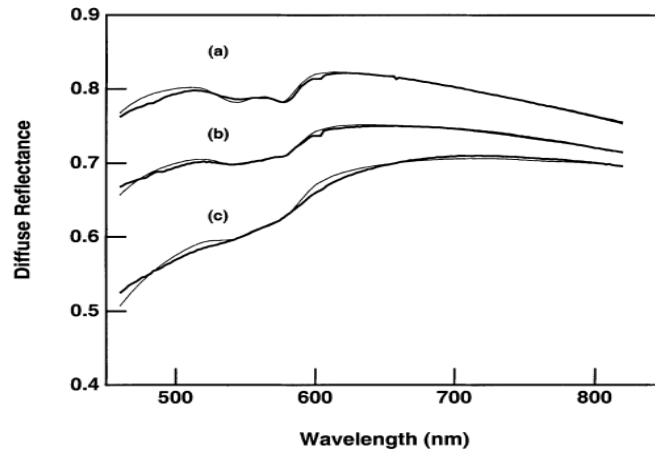


Figure 62 : Reflectance as a function of wavelength in skin (a) White Caucasian (b) Japanese and (c) black African [129]

4.2 Modeling Light Transport in Tissue

For our applications, the mode of operation is far-field optics which allows us to use conventional geometrical optics based analysis. For a material (e.g. tissue) which is illuminated with an incident light intensity of I_0 , the amount of light energy at thickness x inside the material can be modeled using Beer-Lambert Law

$$I(x) = I_0 e^{-\alpha(\lambda)x} \quad (4.1)$$

Here $\alpha(\lambda)$ is the absorption coefficient of light in the material (tissue) in units of inverse thickness (mm^{-1}). It is defined as the distance where at least e^{-1} or 37% light can reach (rest 67% is absorbed in that much thickness). This shows that large tissue thickness or higher absorption coefficient in the tissue leads to exponential decrease in the amount of the incident light that reaches the power harvesting system. Scattering deviates light from its straight path and hence is considered loss for

line-of-sight models. The scattering coefficient (μ_s) is the parameter defined to mathematically include scattering effect as a loss mechanism as in the Light transport equation.

$$I(x) = I_o e^{-[\alpha(\lambda)+\mu_s]x} \quad (4.2)$$

‘Reduced Scattering Coefficient’ is defined to include the effect of anisotropy of scattering properties of tissue. A parameter g is added to the model which is called the coefficient of anisotropy and varies between 0.69 to 0.99 for biological tissues ($g=0$ for isotropic media) [130]

$$\mu'_s = (1 - g)\mu_s \quad (4.3)$$

The value for absorption and reduced scattering coefficients for different skin and tissue layers can be found in literature [127]. These numbers can be used to calculate the expected loss of optical signal to and from the implant.

Due to the multilayer structure, multiple reflections happen at multiple interfaces in the skin. However, the effect of net reflection can be captured using a properly defined reflection coefficient under suitable conditions. Hence, the transmission equation for light can be written as

$$I(x) = \Gamma I_o e^{-[\alpha(\lambda)+\mu_s(1-g)]x} \quad (4.4)$$

Here, Γ captures the percentage of light that goes into the tissue and is later either absorbed or scattered and is not reflected. More sophisticated methods that take multiple reflections into account also exist [131]. In our case, total loss (both absorption and scattering) for Skin in NIR are calculated (appendix III) to be 8.5dB/mm.

There are different numbers in literatures as the absorption and scattering coefficients are reported to be different possibly due to different experimental setups. A typical example is 20dB/mm [120].

The wavelength difference between sunlight and monochromatic light can also be a reason. It is also important to note that the scattered light can still be gathered by large enough photocollectors and hence the efficiency of light transfer can be better than what is predicted by equation 4.4 above. This also shows the significance of using a collimated light source so that the pattern after scattering is still such that most of the light can actually be collected by the photocollectors. Also, this shows that advantage can be taken by focusing light inside the tissue using techniques similar to the ones used in deep tissue imaging using external scattering elements to conjugate tissue scattering [132].

4.3 Design of CMOS Power Harvesting System

The cost and size criterion of the system calls for using integrated photovoltaic systems using same material set and fabrication process as used for CMOS integrated electronics. This is by far silicon although other materials (e.g. germanium and compound semiconductor materials) are also used in some applications [133]. A CMOS based integrated power harvesting system using these Si Photodiodes and an external power source (e.g. laser) is shown in Figure 63. The exact number and type of the Si Photodiodes (PD) depends upon the design requirements and system capabilities.

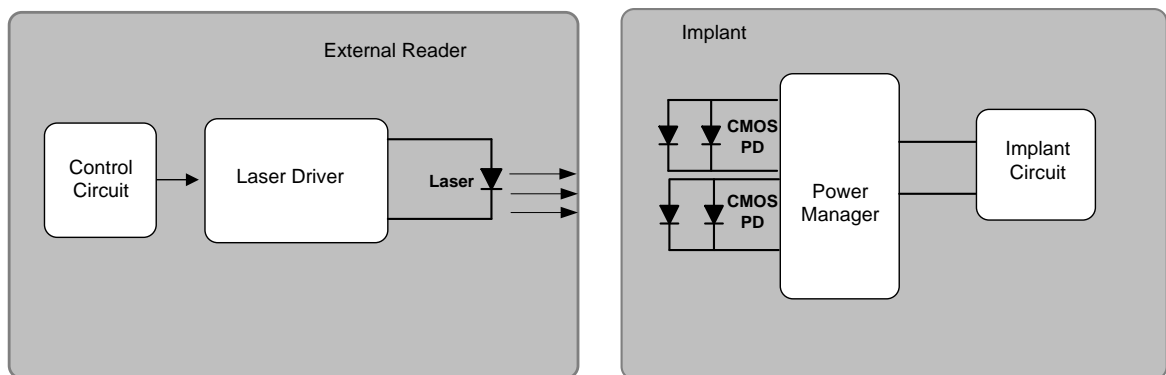


Figure 63 : CMOS Integrated Photovoltaic Power Harvesting System

Si is an indirect bandgap material with bandgap energy of 1.1 eV. It can absorb photons of almost 1.1 μm and smaller wavelengths. The absorption depth of light in visible and infra-red region is shown in Figure 64 [134].

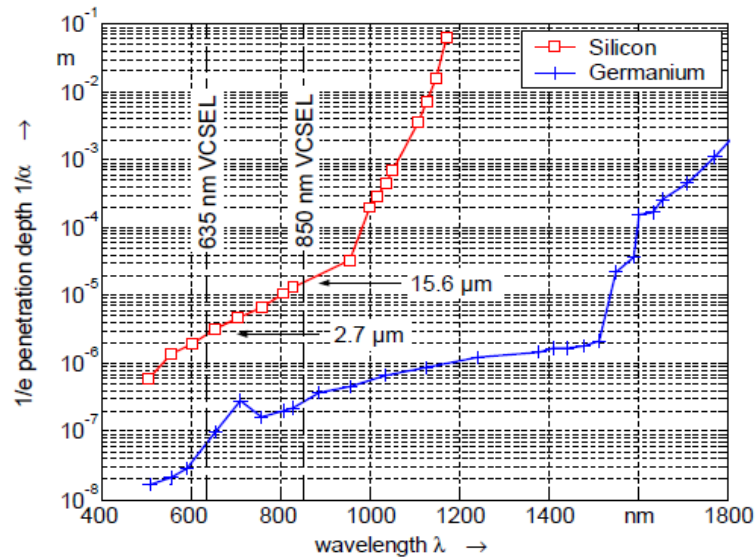


Figure 64 : Penetration depth in Si and Ge as a function of wavelength [134]

The photogenerated current inside a material depends upon the intensity of light at the particular depth as well as the efficiency of the material in converting that light into photocurrent. This efficiency is called quantum efficiency. External quantum efficiency (opposed to internal quantum efficiency) is the relevant term as it is the one that captures the light conversion efficiency[135]. The intensity of light at a particular depth in Silicon also follows Beer-Lambert law. For the infrared region, the absorption depth is in the order of few microns to few 10's of microns as shown in Figure 64. The photogenerated current density from a p-n junction photovoltaic device is the current

density due to electron-hole pair generation by light. For a monochromatic light, this is theoretically given as [136]

$$J_{ph}(\lambda) = qNQE(\lambda) \quad (4.5)$$

J_{ph} is Photocurrent density⁴, q is electronic charge, N is density of incident photons (=Incident Optical Intensity/Photon Energy), and QE is quantum efficiency. This equation proposes that to achieve high photogenerated current, high light intensity as well as material with high quantum efficiency at the particular wavelength is required. External quantum efficiency depends upon absorption coefficient and hence is a function of wavelength of light. It is basically the conversion efficiency from number of photons hitting a surface to the number of electron-hole pairs generated. For Silicon, the quantum efficiencies are wavelength dependent. For actual CMOS system, many different types of devices are possible based upon different types of p-n junctions. Each of these devices exhibits different quantum efficiency [137] which can be found through experiments or using efficiency calculations for different wavelengths [138].

For most cells with small parasitic resistance (small leakage currents), short circuit current density and photogenerated current density are almost equal. In this case, the short circuit current density can be determined from following relationship

$$J_{sc} = q(L_n + L_p + W_d)G = qNQE(\lambda) = J_{ph}(\lambda) \quad (4.6)$$

The QE in this equation is external quantum efficiency which is a measure of efficiency of electron-hole pair generation and collection to form device current. The main design

⁴ Here, it seems more appropriate to work with current density (current per unit area) to avoid confusion with light intensity which also uses I as the symbol.

consideration in our implementation is maximizing the region where photons are absorbed and resulting electron-hole pair can be collected efficiently without being absorbed again in the material. This region includes the depletion region of the p-n junction devices (W_d) as well as diffusion length of minority carriers in p (L_p) and n (L_n) regions for the total area of the photovoltaic cell (A). In equation (4.6), G is the rate of photogenerated electron-hole pair generation. For vertical junctions, G changes with depth as light intensity changes with depth and is found by differentiation of light intensity (rate of change of light intensity). For cells with efficient absorption, it can be assumed that all absorbed photons generate 'captured' electron hole pairs and hence contribute to cell current. Hence, total current density is an integral from the surface to the actual thickness of the PV cell. The current density can be calculated using simple photogeneration equations as follows

$$G(x) = \alpha N(x) \quad (4.7)$$

$$J_{sc} = q \int_{x=x_s}^{x=x_e} G(x) dx \quad (4.8)$$

$$J_{sc} = q\alpha N_0 \int_{x=x_s}^{x=x_e} \exp(-\alpha x) dx \quad (4.9)$$

Where $N_0 = I_0/h\nu$ and x_s and x_e represent the depths where the electron-hole pair generation and collection starts and end (these are found by adding depletion widths and minority carrier diffusion lengths on both n and p side of the p-n junction).

This formulation can also be used to calculate the external quantum efficiency as following

$$QE = \frac{q\alpha N_0 \int_{x=x_s}^{x=x_e} \exp(-\alpha x) dx}{qN} = \alpha \int_{x=x_s}^{x=x_e} \exp(-\alpha x) dx$$

The open circuit voltage of a p-n junction photovoltaic device depends upon the short circuit current density found through equation (4.9) and is given by following relationship

$$V_{oc} = \frac{nkT}{q} \ln \left[\frac{J_{sc}}{J_o} + 1 \right] \quad (4.10)$$

Here, J_{sc} is the short circuit current density which in this case is equivalent to photogenerated current and J_o is the reverse saturation current density of the p-n junction. This shows that to maximize the photogenerated voltage of one junction, good junction quality (n) and high light intensities are required. Also, the reverse saturation current density (J_o) should be as low as possible. Normally, n is higher for crystalline Silicon (as in CMOS) than in commercial polycrystalline Silicon solar cells. For a loaded photovoltaic device, only a portion of J_{sc} can be provided to a load for a non-zero voltage V_{loaded} across the device as the rest flows through internal (intrinsic junction diode). This value is found by following equation [136]

$$V_{loaded} = \frac{nkT}{q} \ln \left[\frac{J_{sc} - j_{load}}{J_o} + 1 \right] \quad (4.11)$$

In theory, maximum available output power can be given by product of maximum output voltage (open circuit voltage V_{oc}) and maximum available current (short circuit current I_{sc}). However, practically operating at this maximum is not possible (due to loading effects). In practical cases, a fill factor (FF) is defined to illustrate the effect of load on the cell. It is given as

$$FF = \frac{J_m V_m}{J_{sc} V_{oc}} \quad (4.12)$$

Here, J_m and V_m are output current density and output voltage at maximum power point. This FF is often used to define the maximum cell output in terms of cell characteristics as

$$P_m = FFV_{oc}I_{sc} \quad (4.13)$$

The maximum power point is the point when cell is loaded by its characteristics load impedance

$$R_{ch} = \frac{V_m}{I_m} \quad (4.13)$$

This shows that maximizing the FF is as important as maximizing V_{oc} and I_{sc} to get higher cell output power. FF is maximized by maximizing loaded voltage and current by decreasing the amount of photogenerated current not converting into cell output. This requires optimizing cell geometry as discussed in next section. Finally, we can define conversion efficiency at maximum power point as

$$\eta = \left(\frac{P_m}{P_{in}} \right) 100$$

This analysis shows that to achieve maximum output power, designer should try to maximize the FF, open circuit voltage V_{oc} and short circuit current I_{sc} . The wavelength and device material should be chosen to have maximum quantum efficiency to achieve this.

4.4 CMOS PV Design

A photodiode generate photocurrent when illuminated by light of right photon energy. The equivalent circuit of a diode under illumination is shown in Figure 65.

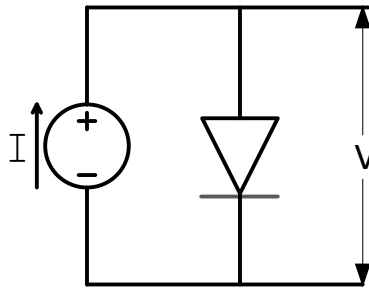


Figure 65 : Simple Equivalent Circuit of a Photodiode

The current source represents the photogenerated current. The diode represents the intrinsic junction diode with drift and diffusion currents due to the built-in potential and the thermal kinetic energy. At open circuit, all the photogenerated current flows through the intrinsic diode in the forward bias direction and generate an open-circuit potential determined by its I-V characteristics. At short circuit, all of the current flows through the short and no current flows through the internal diode. At an intermediate level, some of the current flows through external terminals through the load and some flows through the internal diode (equation 4.10).

The design of the CMOS PV devices involves optimizing the junctions which are designed for electronic use such that these can provide best possible photovoltaic response. The types of junctions are both lateral and vertical in standard CMOS and only lateral in most SOI CMOS processes. Some standard CMOS processes have only basic N and P wells, whereas others have both standard and deep N and P Wells [45]. Optimizing the Photovoltaic power harvesting for different applications needs different design methodology. For example, maximizing current requires maximizing the photogenerated electron-hole pairs and collecting these efficiently before recombination can happen. This normally means utilizing maximum area for device which is

normally achieved using one device to avoid any wasted space between devices. However, maximizing voltage calls for using best photodiode junctions and stacking these in series. Furthermore, it is also important to match these to have similar characteristics which require having multiple smaller devices than one large device. For CMOS, the materials are chosen by the foundry, the user can only make the suitable choices of structure design for maximum possible efficiency. However the wavelength selection here is limited by the optical properties of the tissue. Given this limited range, the designer must choose the wavelength with maximum quantum efficiency to get maximum efficiency of the PV cell. Alternatively, if the wavelength is fixed, we should choose the right p-n diode structure to get maximum conversion from incident photons to electrical current. The optimum structures for the Photovoltaic devices were custom designed since the CMOS process did not have any suitable layouts.

Also, the CMOS devices have a stack of insulators and metals on top of the actual Silicon area. These metals are used for interconnects while the dielectrics are used for insulation and planarization of each layer [45]. In our designs, the metal contacts are optimized to cover a minimum area since the photocurrents are normally small and hence the metals do not face electromigration problems. Secondly, the top insulation layer was removed during the CMOS fabrication process from some devices while it was kept on some others to see its impact. This can affect the interference pattern from the dielectric stack and appears as a ringing in measured quantum efficiencies [138]. Results showed that the devices without the top insulation performed better (higher currents). Since the device will be coated with some biocompatible polymer at the end and also the diodes are pretty robust, this does not create any issues for the photodiodes.

The types of photodiodes available in a standard CMOS process along with approximate junction depths are shown in Figure 66 and their equivalent circuit in Figure 67.

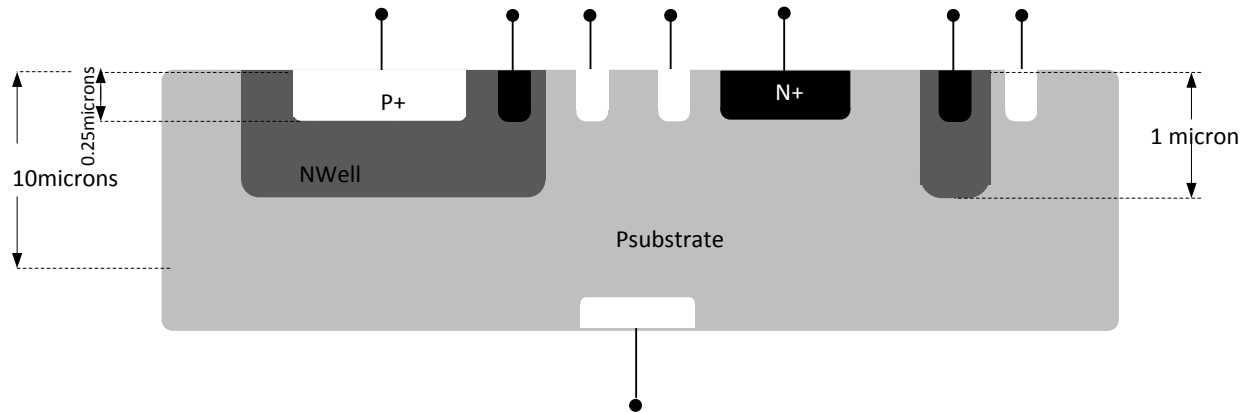


Figure 66 : Types of Junctions in Standard CMOS

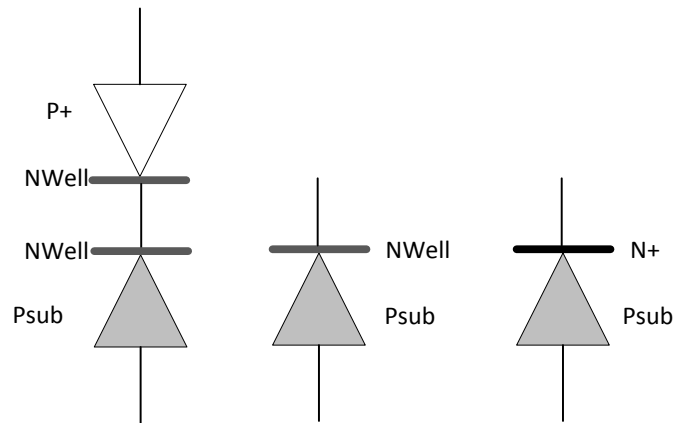


Figure 67 : Types of Junction Diodes in Standard CMOS

This shows that there are different devices available in the CMOS process and careful selections need to be made for optimal performance. In general, the n-p diodes are expected to have better

spectral response compared to the p-n diode due to higher electron mobility and lower hole mobility [136]. Also, low doped regions have low recombination rates (larger minority carrier diffusion lengths) and should perform better than highly doped regions. Furthermore, each type of junction is expected to have slightly different quantum efficiency and hence different responsivity (Amps/Watt) to light. A comparison between different photodiodes from literature is shown in Figure 68. It seems that for maximizing current, the nwell-p structure is the best option.

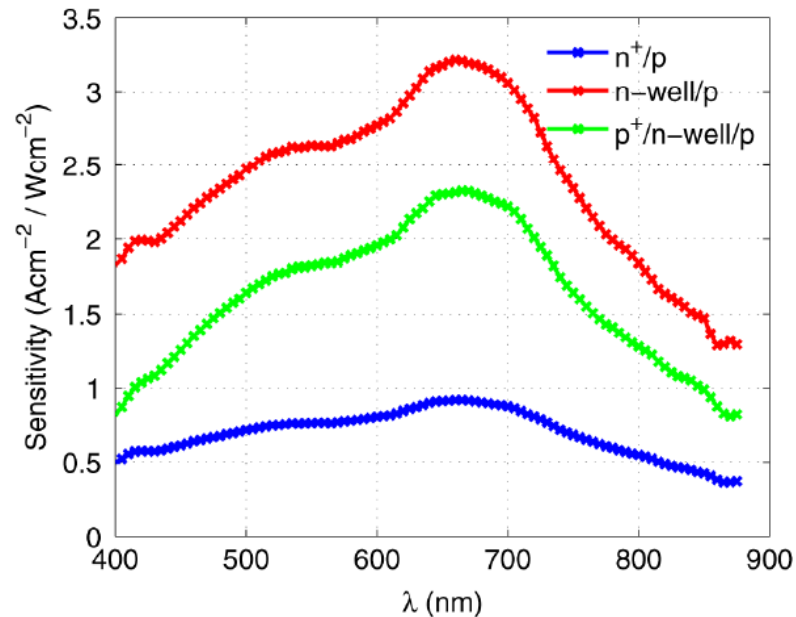


Figure 68 : Photoresponsivity of different p-n diodes in CMOS [139]

An issue with this type of standard CMOS in achieving higher voltage is the common substrate that causes problems in stacking photovoltaic devices. For series stacking, none of the possible n⁺/p-substrate, n-well/p-substrate and p⁺/n-well diodes can be used due to the parasitic buried diode structures as shown in Figure 69. Here, an important point to note is that the CMOS substrate is

normally p-doped and hence has to be connected to lowest potential in the circuit for proper operation of the transistors.

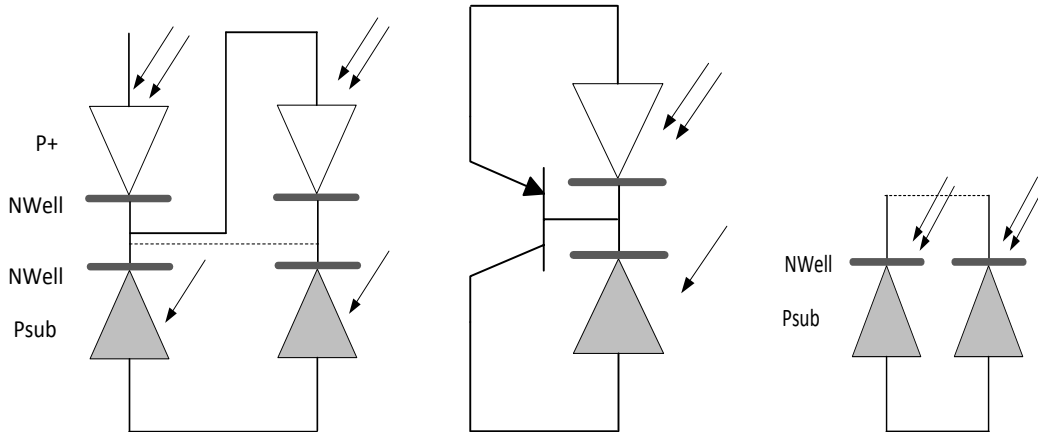


Figure 69 : Effect of Parasitic Devices on Diode Stacking

Different solutions have been proposed, including the use of extra devices to compensate for the substrate leakage[140] or the use of DC-DC converters to boost the voltage[141]. However, most of these methods take too much area or use complex circuitry, which increases system complexity and area requirements. We decided to use the deep well type structures since these are used to electrically isolate different parts of circuits from each other by isolating their substrates for RF application [45]. Furthermore, such wells can also provide more p-n junctions which make it possible to stack more devices in series for high voltage operations. Deep Wells are becoming more available in the CMOS processes and hence are standard design components in our applications. For a standard CMOS process with deep n-well, different types of doped regions are available as shown in Figure 70.

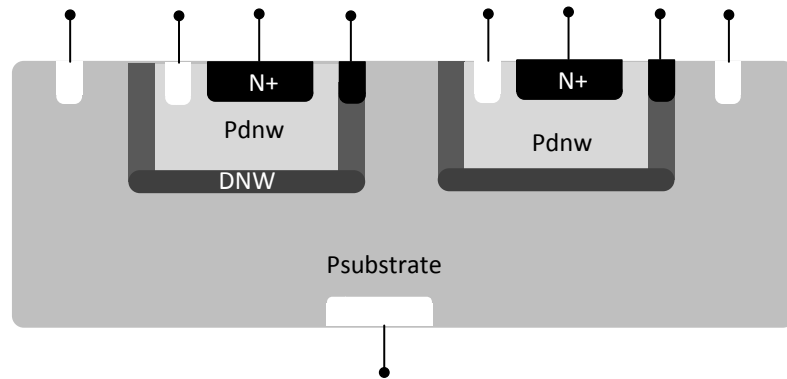


Figure 70 : Types of Junctions in Deep N-Well CMOS Process

In general, P substrates should be connected to the lowest potential in the circuit which would be the cathode of the last photodiode in the series. With this constraint, stacking of two diodes could be arranged using different topologies. However, as we wanted to drive a vertical cavity surface emitting laser (Chapter 5) with the CMOS PV, we wanted to generate more than 1.5V and hence two diodes stacking wasn't sufficient. Since deep N-wells create electrical isolation between devices, the part of substrate inside the wells acts as a body terminal for the MOSFETs inside the well and hence these need to be connected to lowest potential available in the system. Hence, the entire P substrate no longer needs to be connected to the lowest potential and can actually be used as part of the photocollectors. The circuits are designed inside isolated wells and their corresponding wells become their body contacts. Preliminary test on a simple ring oscillator in this technology showed good isolation as desired. However, it is important to measure the effect of such topology on circuits to see if the isolation is enough or not for the desired application. Hence, three diodes could be obtained using the topology shown in Figure 71.

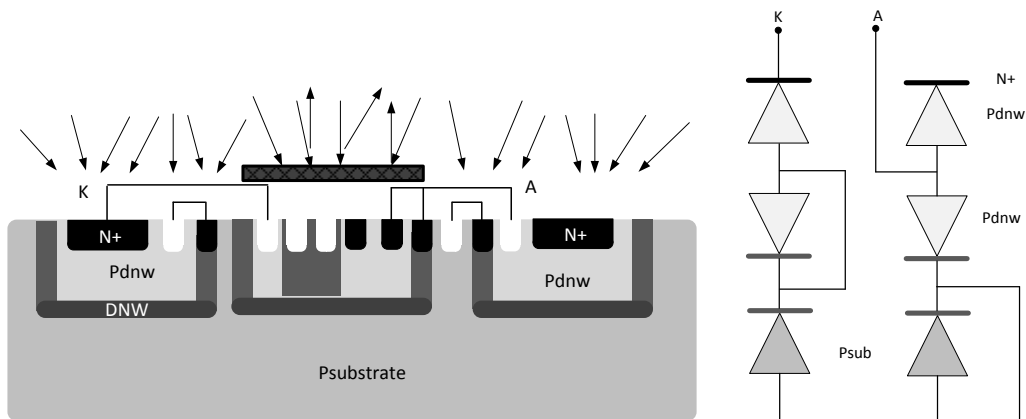


Figure 71 : Connections and equivalent circuit of three photovoltaic cells powering integrated circuit

The actual die diagram of this implementation in TSMC 0.25 microns process is shown in Figure 72

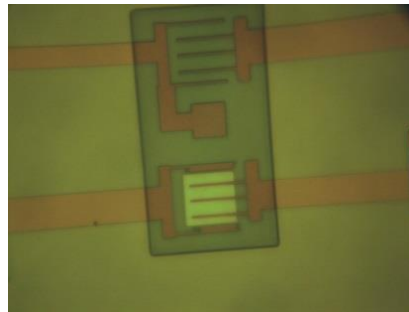


Figure 72 : CMOS photovoltaic on die utilizing deep n-well based devices

Optical testing under laser illumination revealed that the optical output voltages generated were pinned to around 1.5 V after stacking these deep well devices. From these results, we developed a revised model which takes into account the effect of stray (Parasitic) devices, as shown in Figure 73

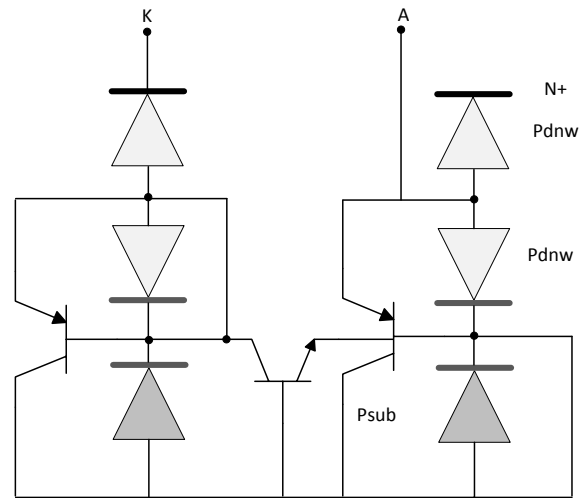


Figure 73 : Parasitic BJTs in deep N-Well CMOS

The most important realization here is to take the parasitic BJT structures (both vertical and lateral) into account. An important result is that these BJTs leak current to the substrate and decrease the percentage of photocurrent available to load. Hence, substrate leakage is still an issue even with deep N-well based CMOS processes as it drains the current away from these devices. Substrate leakage also appeared in limiting the current of the stacked devices even when large photocollectors were used. This is because increasing the area of the actual diodes also increases the area of the buried parasitic devices as well. Achieving very large currents is not possible with this topology for reasonably sized diodes, and the best solution is decreasing the wavelength so that light does not reach the stray elements and hence these stay off. However, since we have to operate in the NIR region and since the parasitic junctions are not very deep in Silicon; this is not a viable solution. Also, metals or other structures cannot be used to block light as these parasitic devices exist underneath the actual photodiodes.

Another problem exists in stacking the photodiodes in series to get high optical power output. Since these devices are similar to current sources, their currents have to be matched for a proper series connection. Otherwise, the lowest current forces other devices away from their maximum power point. However, different diodes connected in the stack have different leakage issues and it is hard to design these to have equal current *a-priori* as the actual photogenerated current that they produce is not simply proportional to their area. This can be solved by doing an array of designs each time for dynamic (run-time) matching, but is not very practical. Another method can be to only stack similar types of devices, but this is not possible as shown with the model before. Recursive designs enables us to achieve sufficient matching between the devices to achieve enough current to power the electronic system wirelessly.

4.5 Testing and Results

The load curve was measured by using a Keithley source meter as a sink to draw variable amount of current from the PV device and measuring the resulting voltage as well. The results for single diode as well as for the stack are given in table 5. The devices showed the exponential behavior of illuminated diodes as expected. Summary of the Open Circuit Voltage and short circuit currents for different diode structures as well as their series stack are given in table 5.

Table 5 Illuminated characteristics of Stacked CMOS Photovoltaic Devices

Diode	Open Circuit Voltage	Short Circuit Current (d1)	Short Circuit Current (d2)	Short Circuit Current (d3)
Deep N-Well	0.75V	50uA	200uA	500uA
Substrate	0.6V	250uA	1mA	1.5mA
Surface	0.7V	40uA	150uA	375uA
2 Diodes	1.1V	30uA	110uA	230uA
3 Diodes	1.5V	25uA	75uA	120uA

Here, d1 denotes surface diode of 35umx25um, d2 represents surface diode of 100umx100um, and d3 represents a surface diode of 500umx500um. The I-V characteristics of the stacked photodiode were used for FF and efficiency calculations. It is important to emphasize here that the cells are not always used at the maximum power point. These are used depending upon the requirements of the load which can be low current, high voltage or high current, low voltage, etc.

The current mismatch effect also manifested during testing. The laser focusing location for maximum voltage and maximum current were slightly misaligned from each other, which is most probably due to the fact that the smallest diode has to receive most light to be able to provide high current. However, the maximum voltage point represents lower current from the system which

pushes other diodes close to their open circuit potentials. This mismatch can also be due to the incident laser which did not have a nicely collimated beam. Use of a better laser or a power LED can be better in this scenario. We have recently acquired a power LED along with a driver circuit to do testing with it for a comparison. There are other NIR powering systems which can be used as well for comparison.

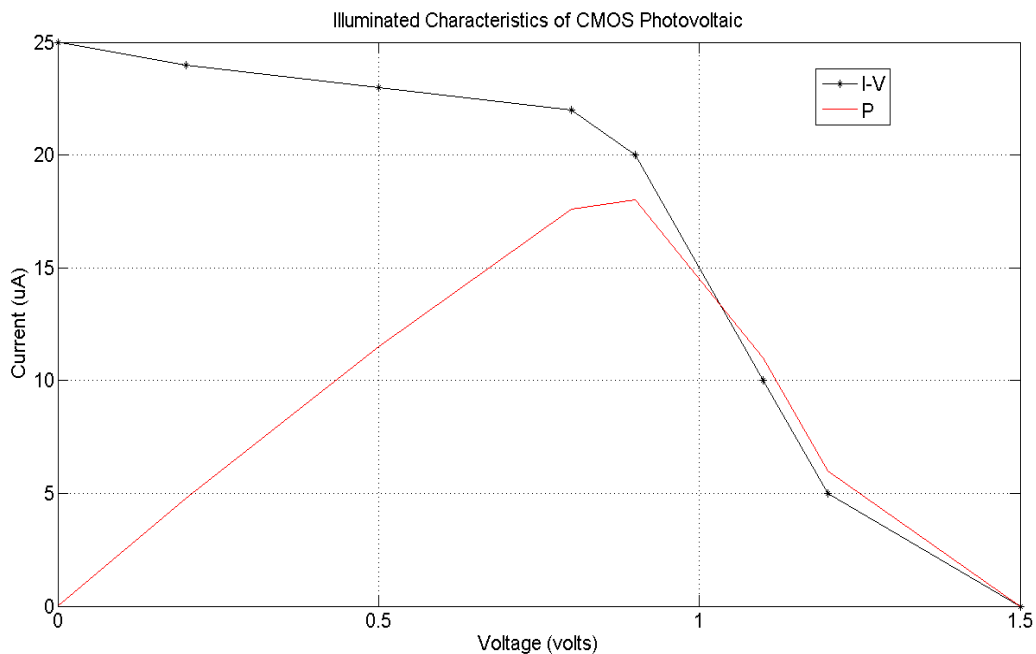


Figure 74 : I-V Characteristics of stacked Photodiode (d1)

The FF for the entire device comes out to be around 48% and efficiency around 13.5% (appendix III). This efficiency calculation was done based upon the area of the PV system. Although these numbers are lower than what is expected from silicon PV devices (FF can be as high as 80% and efficiency around 30%), these devices need top metal for contacts and are also suffering from leakage and mismatch effects. Keeping these limitations in mind, these devices actually performed

pretty well and the resulting power is sufficient of most low power circuits. These devices provided highest reported voltage for integrated PV devices without the need of DC-DC converters.

It is important to emphasize that the received power (not the efficiency) can be increased by focusing the light more. The results by focusing the light are given in Table 6. It was noticed that further enhancement was also possible, but the intensity was high enough to cause damage to tissue as was noted by damage to different dielectrics (e.g. thin FR4 strips) used for testing.

Table 6 Effect of Laser focusing on performance of stacked PV system

Diode	Open Circuit Voltage	Short Circuit Current (d1)
Deep N-Well	0.8V	70uA
Substrate	0.6V	350uA
Surface	0.7V	65uA
2 Diodes	1.1V	45uA
3 Diodes	1.5V	35uA

Another test was done to compare the photodiodes with different geometries to achieve the optimal geometry from the different possible geometries shown in Figure 75. It is evident that the distributed structures with higher peripheral areas around the p-n junction provide higher current

due to higher percentage of electron-hole pair being able to be collected at the device terminals.

This also shows that using the library diodes as photovoltaic structures will result in sub-optimal performance. Finally, it should be noted that further optimization using rigorous mathematical modeling using the CMOs process parameters is also possible and can increase system efficiency even more.

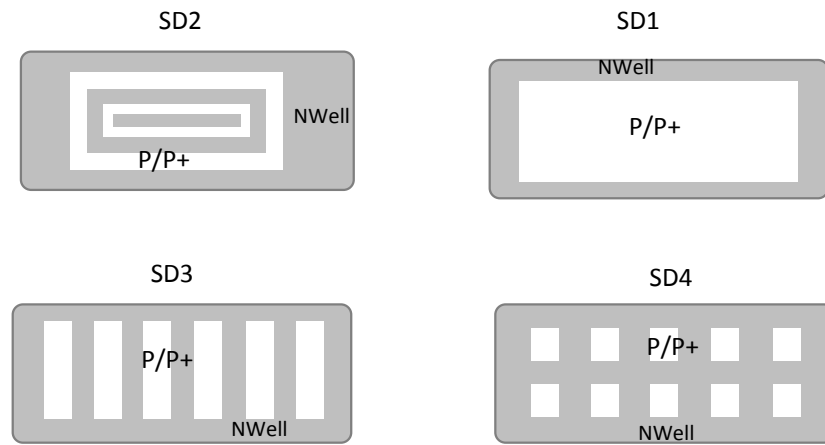


Figure 75 : Different Photodiode Geometries

The results from the comparison are listed in Table 7.

Table 7 Photodiode Geometry Comparison

Diode	Open Circuit Voltage	Short Circuit Current
Surface (SD1)	0.7V	35uA
Surface (SD2)	0.66V	41uA
Surface (SD3)	0.63V	44uA
Surface (SD4)	0.6V	50uA

4.6 Effect of Tissue on Power Transfer:

A piece of chicken skin and tissue (around 3mm thick) was placed between the CMOS chip and the power laser to see its effect on the received power. It was evident that tissue absorption, scattering, etc. will have a negative effect on the performance of the photovoltaic cells. This was observed from the results as well. It is difficult to relate these measurements with tissue parameters of human skin as described earlier in this chapter. However, it was evident that introduction of tissue substantially reduced the power output of the system (around 70% reduction in performance). However, it is also important that the experiment was done in an extreme case (2mm thick skin along with 1mm thick tissue). Also, the larger diodes showed lower percentage reduction than the smaller diodes. This is possibly due to the reduced effect of scattering on bigger diodes than on smaller diodes. It is also important to note that these readings are consistent with the transcutaneous data reported in literature [142]

Table 8 Effect of Tissue on Performance of PV System

Diode	Open Circuit Voltage	Short Circuit Current (d1)	Short Circuit Current (d2)	Short Circuit Current (d3)
Deep N-Well	0.65V	20uA	80uA	190uA
Substrate	0.45V	100uA	600uA	750uA
Surface	0.55V	15uA	60uA	130uA
2 Diodes	1.0V	12uA	40uA	90uA
3 Diodes	1.2V	7uA	25uA	60uA

It was also observed that a thicker piece of tissue had more effect than a thinner slice. Furthermore, tissue with skin had more effect than bare tissue. However, the PV system still showed adequate performance for most of the applications if appropriate low power electronics can be designed. Moreover, this effect can be minimized by using some integrated focusing mechanism and also by using wavefront shaping to improve the focus inside the tissue.

4.6.1 Thermal Effects

Since the photons used have energy higher than Silicon bandgap, the extra energy is converted into heat. For high illumination levels, this can increase the temperature of the photodiodes which increase the intrinsic diode current and can decrease the load current. The change in silicon diode's built-in potential is noted to be $-2\text{mV}/^\circ\text{C}$ [136]. This was observed in our experiments by continuous

testing of the photodiodes for long time (few hours). However, in actual applications, the illumination will be for short durations and hence this effect may be negligible. Also, the tissue around the device cools it down to body temperature if the temperature is not elevated too much.

4.6.2 Effects of Non-uniform Illumination

For PV systems with non-uniform illumination, any diode receiving minimal energy becomes the performance limiting point. However, as our devices are quite small and as tissue scattering spread light, the possibility of this happening is lower in our case. Hence, it wasn't observed directly in our case. However, it was observed that the focus for maximum voltage and maximum current outputs from the stacked devices was different from each other. This was possibly due to current mismatches between devices resulting from non-uniform illumination as well as inherent leakage phenomenon as described before. Our power laser had a non-uniform output beam and replacing it with a laser with more uniform beam can also decrease this effect. Use of an LED can also help as long as the viewing angle can be small to focus maximum energy on the implant. Also, for high power LEDs, caution must be used to avoid constant UV irradiation of the skin.

4.7 Compound Semiconductor Photodiodes

Direct bandgap materials can absorb/emit light just by absorbing/emitting photons. Hence, these are more efficient for both light absorption and production. GaAs is a direct bandgap material and hence is more efficient for photovoltaic power generation than Silicon. Commercial GaAs photodiode arrays from ULM Photonics [143] were tested as PV cells. These devices were assembled into multiple diode assemblies⁵ on chip carriers using wirebonding. Although, these

⁵ Assembly performed by Akram Sadek and Muhammad Mujeeb-U-Rahman

devices provided high open circuit voltage (1.8V from each diode), their voltage dropped very quickly when a load current was drawn. It seemed that these devices were designed as efficient photodetectors rather than efficient Photovoltaic devices and their I-V characteristics were not suitable for powering applications.

4.8 Silicon-on-Insulator (SOI) based Power Harvesting System

SOI technology provides inherent isolation using trenches created during the CMOS fabrication (shallow trench isolation). Hence, series stacking of diodes is not a problem as long as the resulting voltage is below the dielectric breakdown for the trench isolation material (much higher than the voltages needed in implant applications). However, the Si absorption area is smaller due to the very thin nature of the top active Silicon in such processes. Also, only lateral junctions were used since vertical p-n junctions are not available in such technologies due to too thin Silicon device layer. One method will be to increase the path length of light in Si by scattering and/or reflecting it. SOI devices were designed in a 130 nm process from ST Microelectronics provided through the CMP service.

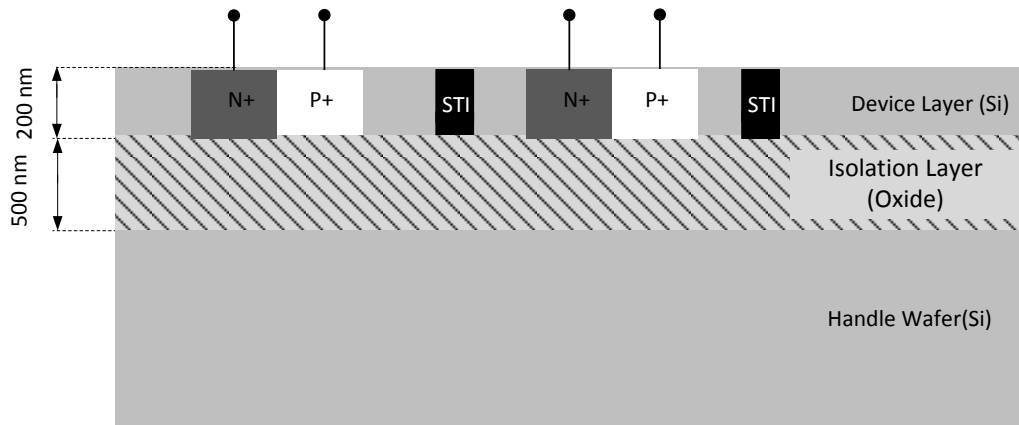


Figure 76 : Different regions in Silicon-on-Insulator CMOS

The top Silicon is only around 200nm thick in the process. Hence, photo-absorption would be very low. However, some light-trapping methods can be used to further increase device efficiency. A simple method is using the top metal structures as bottom reflectors and using backside illumination. For this, the thick handling substrate on the back of the devices needed to be etched. Etching was performed using aligned backside lithography and gas phase etching (using Xenon Difluoride). The silicon oxide insulation layer was used as etch stop. The resulting structures are shown in Figure 77.

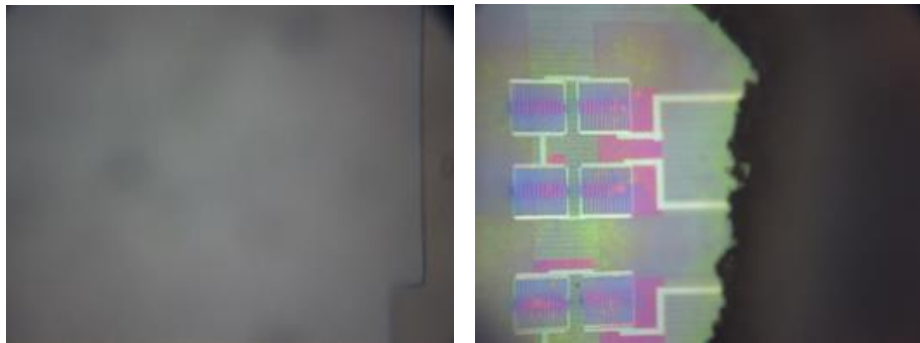


Figure 77 : Backside view of SOI-CMOS after Etching

The devices were tested using backside illumination and front electrical contacts. Due to thin structures, bigger photodiode arrays (250 micron x 250 micron) were used to achieve high photocurrents. Optical measurements were done⁶ on these devices using the same power laser as used for standard CMOS. However since these devices were very thin, heating due to permanent exposure caused damage to the devices for highly focused power laser. This was mitigated by using

⁶ Measurements done by Dvin Adalian

pulse mode testing employing a Newport electromechanical shutter (open for 40 milliseconds every 1 minute).

The maximum voltage from a stack of four diodes was found to be 2.95V and maximum current 215 microamperes for pulsed operation and 2.91V and 51 microamperes for continuous mode, both in air. Efficiency was calculated to be around 9.6% for constant exposure and around 10.1% for pulsed mode operation. Efficiency is low for these devices because of the thin silicon absorption region. Also, the effect of tissue hasn't been tested, but can be assumed to be the same for same power source as in standard CMOS. As new SOI technologies are emerging with more and more Silicon thickness, this process can easily achieve higher efficiency and can be used in many applications especially neural implants where high data rates are needed, but only when actual neural activity happens so continuous communication may not be needed.

An important observation was made from the SOI devices is that similar post-processing can be done to isolate the different structures in standard CMOS. This can provide thick light absorbing regions which are isolated from each other. This can result in both high voltage and high current and is currently being pursued. RF coils were also designed in this SOI technology for performance comparison. However, presence of fill layers from the fabrication process has created difficulty in testing and we are currently trying to find methods to test these structures.

4.9 Safety Issues

Both irradiative and conductive heating can happen in these systems. Human cells are known to sustain up to a 4°C temperature change (up to 41°C) but higher temperatures will increase the likelihood of cell death through necrosis [144]. IEC 60601 standard indicate that cells can withstand 41°C for long durations, 42°C only for eight hours, and 43°C for four hours [145].The actual

temperature rise depends upon the location, as some parts of skin are cooler than others. The American National Standard Institute's standard ANSI Z136.1 has Maximum Permissible Exposure (MPE) guidelines for exposure to optical fields of different wavelengths [146]. For reference, total NIR exposure in sunlight is 50mW/cm² (out of total 100mW/cm²). The maximum permissible exposure (MPE) in NIR region depends upon area of exposure (eye or skin) and duration of exposure. A graph of the MPE allowed by this standard is shown in Figure 78.

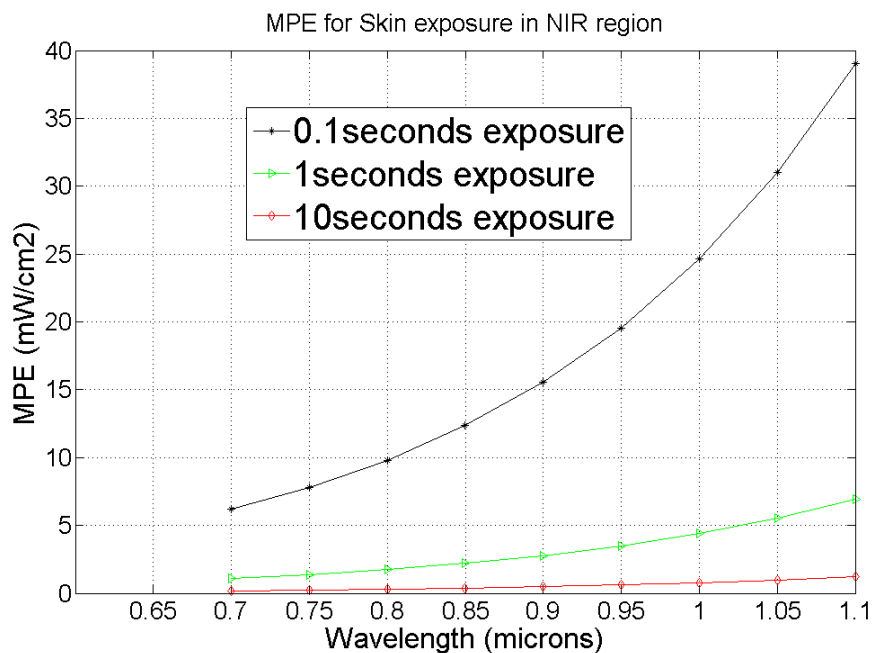


Figure 78 : MPE guidelines for Skin exposure in NIR

It is important to note that this standard is a guideline for keeping the temperature below 41°C in all conditions and has large safety margins. However, it does not take into account the cooling mechanisms for in-vivo tissue (e.g. blood perfusion) if the exposure is on a small area. For example, a 789 nm laser diode using a 1mm diameter optical fiber was shown to heat 1mm thick in-vivo

tissue at $2.95 \times 10^{-4} \text{ }^\circ\text{C}/\text{mW}/\text{cm}^2$. For the 4°C safety range, one can use intensity as large as $13.5 \text{ W}/\text{cm}^2$ compared to the MPE value of $316 \text{ mW}/\text{cm}^2$ [144]. We performed a numerical simulation to test the effect of $800 \text{ mW}/\text{mm}^2$ for a short duration of 1 second. This simple COMSOL simulation showed that the temperature rise was within the safe limits as shown in Figure 79.

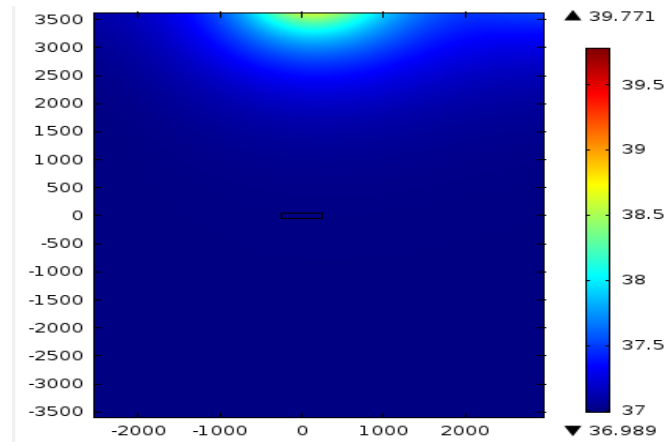


Figure 79 : COMSOL simulation of tissue heating due to laser exposure

Also, pulsing can be used to keep the temperature increase within the safety limits. The other form of heating is due to the thermal contact (hence conductive heating) between the optical emitter and tissue during the emitter operation. This can be easily avoided by using proper packaging of the junction so that it does not come in direct contact with the tissue. For external power laser (or LED), this limits the distance the closest the device can be brought to the skin surface without increasing the local temperature beyond 4°C safety limit.

4.10 Electrical Power Transfer

Electrical power transfer can provide an alternative to photovoltaic powering. The circuit model for an electrical power transfer system is shown in Figure 80.

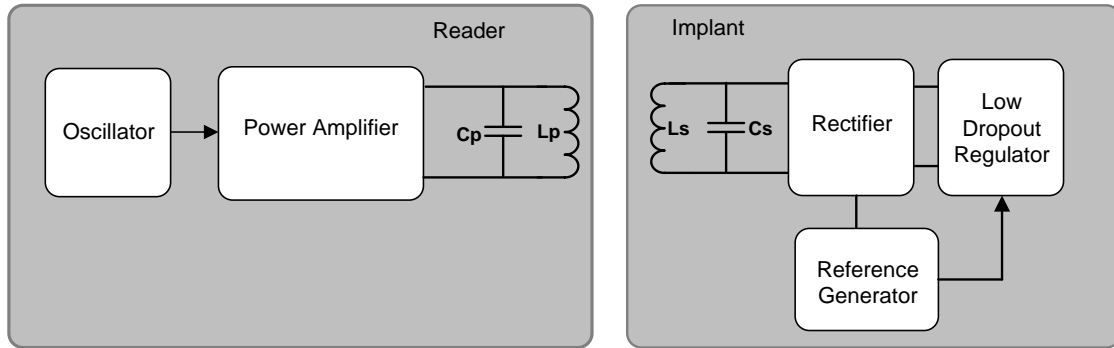


Figure 80 : Electrical Power Transfer System

Electrical power transfer using lower frequency electromagnetic waves is classified based upon the distance between the source and the receiver into following three categories :

- (i) Near Field (Non-Radiative) Mode
- (ii) Midfield (intermediate) Mode
- (iii) Far Field coupling (Radiative) Mode

The near field mode uses strongly coupled systems in close proximity to each other. It can be done by electrodynamic (magnetic field) coupling, electrostatic (electric field) coupling or evanescent wave coupling. The field from the source is strongest in the near-field region and hence most efficient energy transfer is possible. The exact relationship between Electric and magnetic fields as a function of distance is complex in the near-field region. Both the electric and magnetic fields vary very rapidly ($1/r^3$ to $1/r^2$) and hence the electromagnetic energy varies very rapidly as a function of distance from the source[147]. Due to the physics of electromagnetic induction, this method is also a strong function of alignment between the transmitting and receiving structures [148]. In the far field, electric and magnetic fields decay linearly with distance and hence the Poynting vector (field

energy) decays as square law. Hence, the exact distance is less critical than near-field. However, the energy transfer is lower due to the smaller energy density related with the fields far away from the source. The far-field methods are a bit more tolerant in terms of alignment between transmitting and receiving structures. In the mid-field region, field energy and alignment requirements are intermediate between near and far field.

Far-Field methods are more suitable when efficient antennas can be designed at the wavelength of interest to have high directivity; otherwise the efficiencies of power transfer are relatively low. Due to the higher frequencies involved, the on-chip area required for implementing far field methods (e.g. antennas) can be smaller than that needed for near and mid-field coils. However, higher frequency also results in lower efficiency due to high tissue loss [149]. Such high frequency far-field methods provide very low power even if relatively large (but still sub-wavelength) antennas are used for even slightly deep implants. For example, a 1/8 wavelength antenna (8.6cm in MICS band, 433MHz) and a half-wavelength (30.5cm) antenna could transfer only -60dBm between them in air. In tissue the situation will be even worse [150]. Hence, RF powering is only viable for implants which are situated close to the skin surface. However, the advantage of existing infrastructure at these frequencies, along with low-power circuit design, can be a very interesting combination and is being explored currently.

Normally, near and mid-field coupling based methods are more efficient than far field based methods for ultra-small scale implant applications. For near-field methods, frequencies near or below 10MHz are normally used due to low tissue-loss [151]. The near-field power transfer methods have high efficiency if strong magnetic coupling can be achieved as is the case in transformers and sufficiently large coils can be made to intercept the magnetic field energy.

However, in small implants, such inductive coupling has very low efficiencies due to small coils and low coupling resulting from non-ferrite core (air and skin) in implant applications. Efficiency enhancements are possible if the coils can be resonantly coupled [152]. Such resonant coupling based methods have been increasing in popularity in powering consumer electronics and even vehicles [153]. They can provide good performance when the conditions are not suited for simple magnetic coupling [147]. A comparison of these different methods is provided in Table 9.

Table 9 comparison of Electrical Power Transfer Modes

Method	Frequency	Off/On Chip	TX Size (Diameter)	RX size (Diameter)	Power Transfer	Efficiency
[152] Inductive	~1MHz	Off-Chip	4 cm	2 cm	242mW	30%
[149] Inductive	8.75MHz	Off-Chip	5.9cm	3cm	80mW	20%
[59]Resonant Coupling	20MHz	-	1.4cm	0.4mm	0.46mW	-
[154] RF	50MHz	Off-Chip	7.6cm	12 cm	5.6mW	11%
[55] RF	2.4GHz	Off-Chip	-	5mm		1.1%

To understand the tissue response to electrical powering, it has to be modeled using an electrical circuit model. Tissue is electrically modeled as a lossy dispersive medium as it has both dielectric and conductive properties. The commonly used model for such media is the Debye relaxation model [121] and is given as

$$\varepsilon = \varepsilon_r(f) - \varepsilon_r(\infty) + \frac{\varepsilon_r(0) - \varepsilon_r(\infty)}{1 - i(2\pi f\tau)} + i \frac{\sigma}{2\pi f\varepsilon_0} \quad (4.14)$$

Here, f is operating frequency (Hz), σ is tissue conductivity at that frequency, ε_r is relative dielectric constant of the tissue, and τ is the relaxation time. These parameters are available in the literature [155]. From the model, it is evident that low frequency losses are mostly due to conductivity,

whereas high frequency losses are mostly due to dielectric phenomenon [156]. Similar to the optical power transfer, a model for wave propagation inside tissues can be made. The dielectric constant in equation (4.14) allows this model. However, the analytical solutions are quite complex and numerical simulations (e.g. FDTD) are mostly done to find the absorption depth and power inside the tissue.

For resonantly coupled power transfer, the operation of the system can be explained by the theory of simple coupled resonators [157]. A simple lumped element analysis is followed to understand the system better. Replacing the simple matching schemes with high frequency matching networks can help use the results of this analysis for high frequency systems as well.

A passive electrical resonator consists of two different energy storing elements, i.e. , an inductor and a capacitor. Practically, there is always an energy dissipating element (resistor) due to finite conductivities of materials used. These elements can be connected in series or in parallel. A series circuit being powered with an AC source is shown as an example in Figure 81.

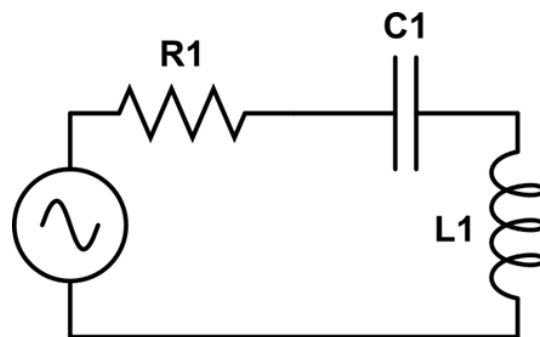


Figure 81 : A typical series RLC Resonator circuit

The current in this circuit depends upon the frequency due to the frequency dependence of capacitive and inductive impedances. A typical response is shown in Figure 82.

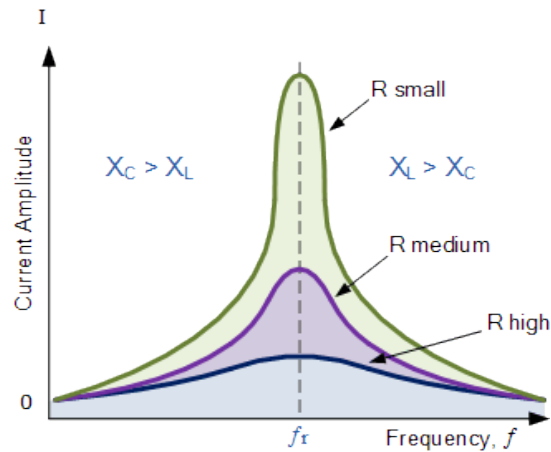


Figure 82 : Current in series RLC resonator as a function of input frequency

The frequency for maximum current amplitude corresponds to resonance condition given by

$$f_r = \frac{1}{2\pi\sqrt{LC}} \text{ (Hz)} \quad (4.15)$$

The height and sharpness of the peak (selectivity) is given by a dimensionless quantity described as the quality factor (Q). It is the ratio between the reactive impedance (either inductive or capacitive)⁷ at resonance and the resistive impedance of the system. It is basically a measure of stored versus dissipate energy in the system or the bandwidth of the system.

⁷ At high frequencies or for other topologies, the expression is different and can be derived analytically using ratio of energy storing over energy dissipating factors using S or Y parameters.

$$Q = \frac{X_L}{R} = \frac{1}{R} \sqrt{\frac{L}{C}} \quad (4.16)$$

This shows that the magnitude of driven resonant frequency depends upon the value of frequency dependent parameters, i.e., capacitive (X_C) and inductive (X_L) impedances. The quality (i.e. height) depends upon the energy dissipating element i.e. the resistor as well.

The theory of coupled resonators proposes that the transfer of electromagnetic energy from one resonator to the other is maximized when these are resonantly coupled. This means that the primary (external) and secondary (implant) circuits should be matched to have the same resonance frequency.

$$fr(primary) = \frac{1}{2\pi\sqrt{LpCp}} = \frac{1}{2\pi\sqrt{LsCs}} = fr(secondary)$$

There are four different configurations possible regarding the series or parallel arrangement in the primary and secondary circuits. A series resonant circuit is mostly used in the primary and we also used it for simple PCB based design. However, a parallel topology is better for matching networks for high frequency[158]. For the secondary circuit, a parallel configuration is also better since it increases the effective resistance of secondary when seen through primary which increases the power transfer efficiency [158]. Simple capacitive matching is optimal on the CMOS chip due to higher quality on-chip capacitors compared to on-chip inductors. For external devices, more sophisticated L, π or other matching networks can be used based upon design requirements of bandwidth, area, etc. [156].

The coupling between the primary and secondary circuits is quantified using the coupling coefficient. The ratio between actual coupling (also known as mutual inductance) and maximum possible coupling is called the coupling coefficient. For optimal power transfer, the coils need to be critically coupled and the coupling coefficient has to be large, but not very close to 1.

$$\kappa = \frac{M}{\sqrt{L_p L_s}} \quad (4.17)$$

Our analysis of the resonant system assumes simple lumped element model for simplicity and follows the analysis in [159] and [160]. The model used for this analysis is shown in Figure 83.

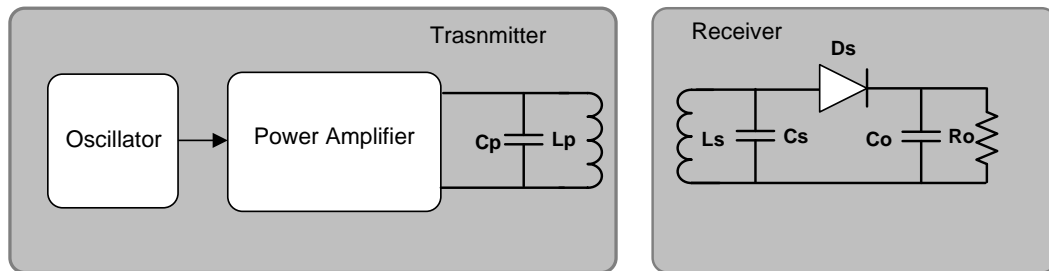


Figure 83 : Circuit Model for Resonant Power Transfer

The Voltage transfer ratio is a function of inductance of coils as well as the quality factors

$$\frac{V_s}{V_p} = \frac{M}{L_p} \cdot Q_p \cdot Q_s \quad (4.18)$$

Mutual Inductance is a function of coil geometries, number of turns, and the magnetic permeability of the medium (μ).

$$M = \mu \frac{\pi}{2} N_p N_s \frac{Y_s^2}{Y_p} \quad (4.19)$$

Here, Y_p and Y_s are diameters of primary (transmitting) and secondary (receiving) coils. N_p , N_s are number of turns in transmitting and receiving sides. For AC power, the resistance after the diode (R_o) is replaced by a resistor with equivalent power dissipation. Assuming rectifier with 100% efficiency, $R=R_o/2$ (rms value). Including the effect of resonance, load resistance is given as

$$R_L = \frac{(\omega L_s)^2}{R} \quad (4.20)$$

The total resistance in the secondary circuit (R_s) is then the sum of internal resistance of the secondary inductor (R_2) and the load resistance R_L . The power transfer efficiency is then calculated from power ratios in the primary circuit with equivalent reflected resistance of secondary as shown in following equations

$$R_e = \frac{(\omega M)^2}{R_s}$$

$$\eta = \frac{\kappa^2 Q_p Q_s R_2 R}{[(R + Q_s^2 R_2) + (1 + \kappa^2 Q_p Q_s)R + Q_s^2 R_2]}$$

The best case efficiency is achieved for optimal load given by

$$R_{o(opt)} = 2R_2 \frac{Q_s^2}{\sqrt{1 + \kappa^2 Q_p Q_s}}$$

$$\eta_{opt} = \frac{\kappa^2 Q_p Q_s}{[1 + \sqrt{1 + \kappa^2 Q_p Q_s}]^2} \quad (4.21)$$

It is important to emphasize that the actual efficiency depends upon the actual load and can be much lower than the optimal efficiency. Also, efficiency will be higher for more coupling and narrower

resonance (high Q 's) as the energy transfer at the resonance will be highest. This also signifies that without resonant coupling, efficiencies will be very low in standard inductive powering (low Q). For the complete system, the efficiency is further reduced by multiplying with the efficiency of next blocks in the power management system (rectifier and regulator).

4.11 Optimizing Electrical Power Transfer

There are many factors which affect the system performance and needs to be carefully selected. The distance between coils and their relative position affects the amount of coupling. For optimum operation, the receiver coil should be placed as close to the transmitter as possible and should be within the maximum field regions of the transmitter based upon its field pattern. For example, for planar spiral coils, it should be within the circumference of the transmitter rather than in exact coaxial alignment [159]. Angular misalignment between the coils also affects the link efficiency [148] due to field interaction with the receiver structure. As noted before, high Q 's are good for high efficiency. However, lower Q provides better performance in case of mismatches between the external and internal coils. Of course, too small Q values make the receiver voltage dependent upon the changes in the load resistance [161]. In integrated circuit coils, Q 's are normally low (around 10) [162] due to limits on metal thickness and other losses which make the design challenging, especially at very small scales. Since the system should be resonant in presence of complex biological media, optimum tuning can be performed by dynamic matching implemented at both source and load [163]. However, a simple approach is to incorporate the effect of mismatches due to tissue in the external device to make the implant design easy. This can be done during the implant read out experimentally by changing the matching capacitor in the external device and hence keeping the internal device simpler. We use this approach and our results show that reasonable matching can be achieved using this method, even when the device is inside tissue.

4.12 Implementation of Electrical Powering

Electrical powering was tested using different devices to get more insight into the tradeoff involved in the system design. The purpose of these tests was to learn about the optimization parameters which can then be applied to the on-chip design to obtain maximum efficiency. This is described in the following section.

4.12.1 Proof-of-Concept using Discrete Coils

Discrete coils made of a 20 AWG wire were used to test the system parameters and the effect of saline solution on its performance⁸. An Agilent function generator was used to drive the primary and an oscilloscope was used to read the secondary. Resonance frequencies near 20MHz were used as the system was quite big. Discrete capacitors were used to tune the LC circuit. The coils were tested in both air and in salt water to test the effects of alignment and power efficiency inside conducting media. The series and parallel configurations were also tested to compare their performance. The results from a typical test are shown in Figure 84.

⁸ Done by Muhammad Mujeeb-U-Rahman and Sith Domrongkitchaiporn.

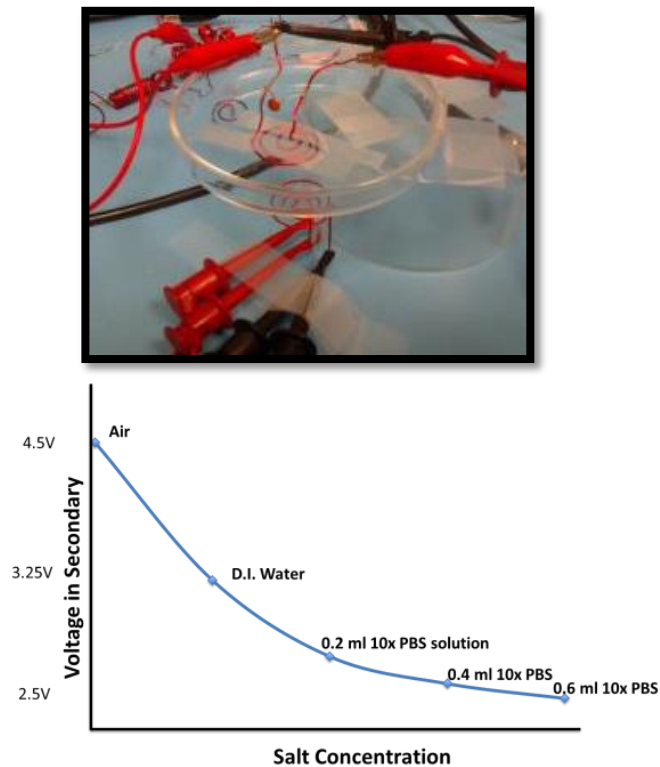


Figure 84 : Testing Resonant Coupling using Discrete
Coils

The results from these system showed that resonance based coupling is needed for air core and water core coils for reasonable power transfer efficiencies because simple magnetic coupling had very low efficiencies for such loosely coupled coils. Furthermore, there was substantial change in received voltage in going from air to DI water. As DI water should not have much loss, this was considered due to loss of resonant coupling between the coils. It was assumed that these wires have thin insulators which couldn't isolate their fields from water completely. When PBS was added to DI water, the voltage transfer ratio dropped by 50% at maximum salt concentration. This was

assumed to be due to the change in parasitic components of the RLC circuit which affected its resonance and hence decreased the voltage in secondary.

4.12.2 PCB based Design

We also tested coils in PCB technology as a model system for the integrated coils, as shown in the schematic in Figure 85. The PCB technology was chosen to enable fast turnaround times for testing.

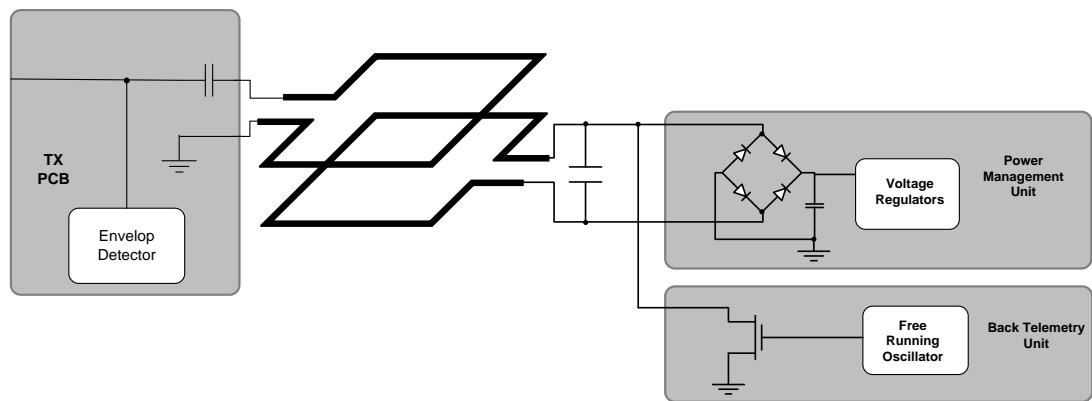


Figure 85 : PCB system for testing resonant coupling

Since bigger coils were possible, the frequency range similar to the discrete coils was used in this case. The ‘implant’ PCB was 5mmX5mm in size and contained one and two layer inductor. The inductor was designed using the planar inductor calculator available online [164]. One and two layer inductors were designed. Regular FR-4 substrate was used for simplicity and the resonance frequency was chosen at around 20 MHz to compare planar coils with discretely wound coils. An on-board capacitor was used to tune the resonance and a larger external PCB was constructed as the external reader and power source. A test board and an integrated board was made for testing power harvesting efficiency and complete system operation.

The results indicated good power transfer in air. An input power of 1W (30dbm) at primary resulted in a power of 5mW at secondary and the power transfer efficiency is estimated to be around 0.5%. Although it is quite low, it was enough to run the entire system. Given that this was a very basic design with no optimization, the results were quite promising and showed that wireless powering using sub-wavelength coils can provide enough power even in the presence of conducting and dielectric medium such as tissue in between. Also, it was found that efficiency was higher for peripheral alignment rather than when the device was in the center of the transmitter coil, which is in accordance with literature [159]. Furthermore, the feasibility of backscattered communication as a means of communication from the secondary to primary side was also verified (chapter 5).

An important point here is that although these systems were designed to study the coil design and the effects of misalignment, etc., if designed on proper biocompatible substrates with enough flexibility (e.g. flexible polyimide), these could actually be used for some applications where extreme miniaturization is not required. Since thicker copper layers are possible in these technologies, higher Q's can be achieved as well as higher inductances, which can allow operation at lower frequencies that are more tolerant to misalignment and can communicate for longer distances as well (due to longer wavelengths).

4.12.3 Silicon Based Custom Designs

Major differences between the PCB based system and on-chip systems are the conducting silicon substrate, thin metal films (hence lower Q) and smaller coils. These effects were studied using simple inductors on oxidized Silicon substrates (with bottom oxidation removed). The inductance of a planar spiral coils is given by modified Greenhouse formula [162].

$$L = \frac{\mu n^2 d_{avg} c_1}{2} \left[\ln\left(\frac{c_2}{p}\right) + c_3 p + c_4 p^2 \right] \quad (4.22)$$

Here, d_{avg} is the average diameter of inductor, n is number of turns, p is fill factor and c_n are functions of geometry. d_{out} and d_{in} are outer and inner diameters of inductor. It has been shown empirically that this formula overestimates the inductance value by 26% [162]. The coefficients for this inductance formula for different shapes are given in [162]. A comparison of inductances for different shapes (diameter of 1mm) is shown in Figure 86.

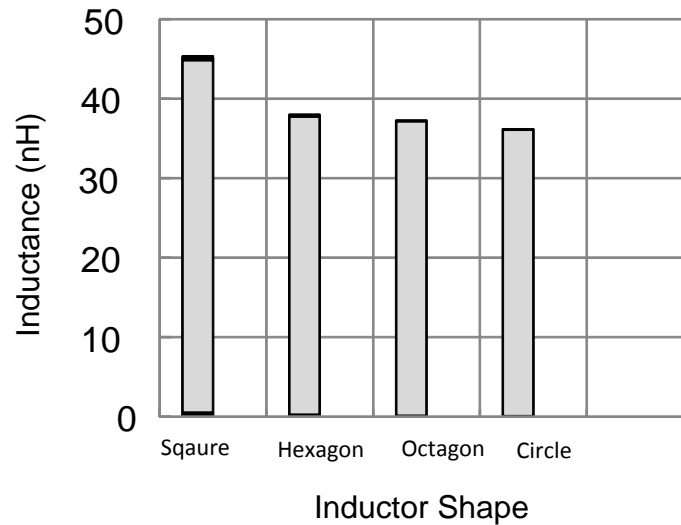


Figure 86 : Effect of Geometric Shape on Inductance value

Due to the extreme sub-wavelength nature of these coils, both planar coil models [162] and simulations using COMSOL software were used to test the effect of different parameters on coil design. The inductance of a conductor was calculated in COMSOL using following relationship

$$L = \frac{2W_m}{I^2}$$

Where W_m is the magnetic energy around the inductor calculated using Maxwell's equations. The simulation results are shown in appendix I. For understanding the inductor from circuit's point of view, it is modeled as lumped elements. There are different models reported in literature. Simple two port π -model for inductor is given in [165] and model for CMOS type lossy substrates is given in [166]. The π -model can work for most of the cases and verified using simulations. It is shown in Figure 87 . Here, C_p is the parasitic (self) capacitance of the coil, R_s accounts for overall ohmic losses in metal, R_{si} accounts for overall ohmic losses in Si substrate, C_{ox} represents parasitic capacitance between metal and substrate through intermediate dielectric, C_{si} is capacitance of substrate due to its semiconductor properties (induced polarization effects)).

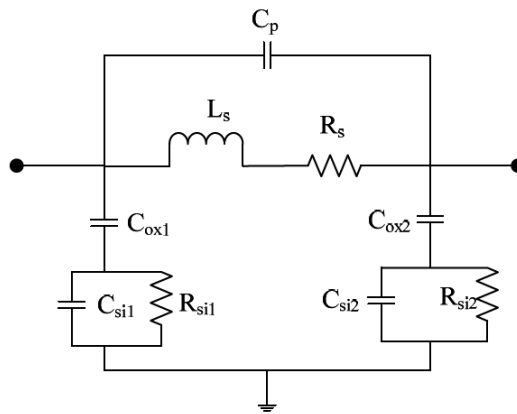


Figure 87 : Simple Electrical Model of On-Chip Inductor [166]

All these values can be found analytically from process parameters (metal thickness, substrate resistivity, etc.) and their closed form equations are given in [167]. In our experiment, a High

precision LCR meter (Agilent 4404A) was used to measure the approximate resistance, self-inductance and self-capacitance of the on-chip, custom fabricated coils after detailed calibration procedures were done to decouple the probes. From the results, it was noticed that the last (small) turns do not add much inductance to the coil, but only increase its resistance. It was also noted that the stray capacitance to substrate can be decreased by using thicker oxides. Hence, processes with thick dielectric layers can decrease substrate coupling effects and would provide a better choice. A typical custom designed coil on oxidized Si is shown in Figure 88.

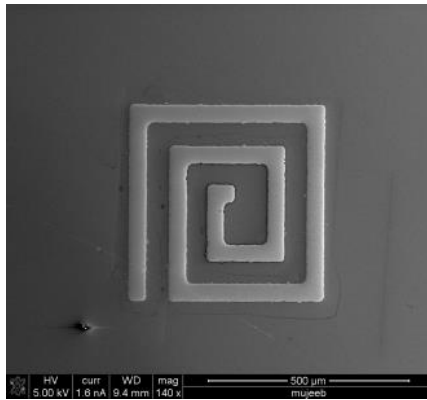
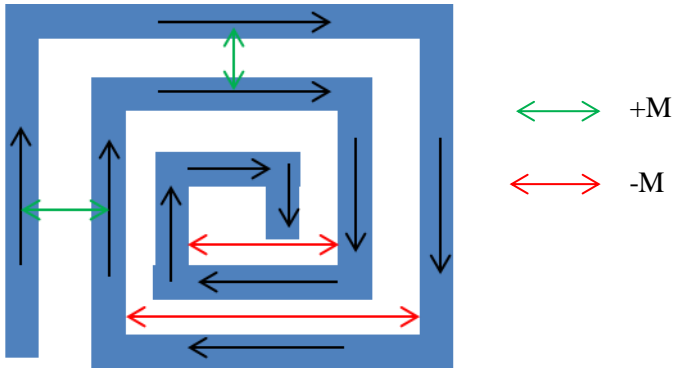


Figure 88 : A Silicon Coil Design for Impedance Testing

Multi-layer simulations in COMSOL showed the effect of current direction on inductance (appendix I). As shown in following schematic, the direction of current in a spiral coil affects the overall inductance of the coil.



$$L = \sum_{i,j,k,o,p} (L_i + M_{j,k} - M_{o,p})$$

The results from discrete coils testing indicated that a higher number of turns (longer coil), higher frequency of operation and smaller conductor width (to allow for more turns) are general trends for a good design in air. For multilevel coils, these should be designed to have maximum positive mutual inductance (same direction of current in adjacent conductors). Another important realization was that the Self-Resonance Frequency (SRF) should be much higher than the desired resonant frequency to avoid the ‘negative inductance’ phenomenon. This was especially important for system operation in water and tissue as it affects the self-capacitance which affects the SRF. One way is to simulate this effect and incorporate it into the design, but an accurate simulation is difficult. Another method uses thick top insulators to isolate the resonator from changes in its local environments. As thick top dielectrics are not available in CMOS, this means that special thick top dielectric layers need to be coated by post-processing. These layers can also serve the function of biocompatibility and hence do not necessarily add to system complexity.

4.12.4 Integrated Coil Design

The integrated coil design starts by choosing the optimum frequency and mode of operation. The choice of optimum frequency depends upon tissue response as well as size and power requirements. For small (mm scale) implants, the optimum wavelength for transmission through the tissue is around 1GHz [163]. We chose 900MHz as it lies in the ISM band which allows high power operation without much restrictions. The relative permittivity of skin is around 41 [168] at this frequency, which results in a wavelength of around 50mm at 900MHz. For the small size requirements of around 1mm, we had to design an optimum sub-wavelength coil structure. It was shown in [159] that sub-wavelength systems can harvest enough power if proper matching (tuning) between primary and secondary side is done. Hence, we⁹ chose to design a resonantly coupled system for wireless power harvesting.

As discussed before, the quality of the resonance depends upon the quality factor of the system. For integrated coils, a process with thick top metal is desired since it will reduce the parasitic resistance of the coil and hence improve its quality factor. The thickness should be at least more than the skin depth at the frequency of operation. Skin depth is defined as the depth of the conductor where current density falls to 1/e percent (37%) compared to the value at the surface. It depends upon material and frequency of operation and is given as [121]

$$\delta = \sqrt{\frac{2}{\sigma\mu\omega}}$$

The effect of skin depth on resistance is normally included in resistivity as given by

⁹ Designed by Meisam Honarvar Nazari and Muhammad Mujeeb-U-Rahman.

$$\rho = \frac{1}{\sigma\delta}$$

For Aluminum (most common top metal in CMOS), the skin depth at 900 MHz is around 2.8 μ m. Hence, a process with metal layer thickness near this value would be helpful in realizing good quality coils. Another important aspect about quality of the coil is proximity effect as changing fields in nearby conductors can affect the field in the coil. Hence, we designed the coil at sufficient distance from other metal structures (e.g. the sensor) found through numerical simulations (using Ansys HFSS software). The design could also be tested for its real impedance using the same techniques used for custom fabricated coils. However, it was realized that this testing would be difficult due to very small values and the absence of appropriate calibration structures at that scale in the current fabrication run. Nonetheless, the system provided adequate performance in power transfer and hence simulations are considered very accurate in this scenario and are extensively used for design optimization. It was also found through simulations that large number of turns are not very suitable for internal coils, especially as it will degrade Q a lot and since the Q values are already low in the CMOS processes (around 10-20 for most cases [162]), it was decided to design a four turn coil for our application. Only top thick metal was used as it provides much higher Q than lower layers.

It is also important to note here that careful layout can reduce the effect of proximity conductors and also decrease the negative effect of opposite currents in the coil design itself. Detailed Layout improvement techniques are listed in [169]. Differential excitation can also help as given in [170]. Also, suspending the inductor can also minimize the coupling losses to lower layers. This can be achieved using undercutting of insulation layers [171]. However, for mechanical stability reasons, this was not used. Processes with lower substrate conductivity would be better if such options are

available. Multilevel inductors can also provide better performance if thick enough metals are available in more than one level [172].

High frequency design and analysis was done with the help of Ansys HFSS software. The system geometry was designed and simulated in it. Resulting s-parameters were used in Cadence to calculate the coupling and power transfer efficiency. The CMOS process chosen was the 0.18microns process from TSMC offered through MOSIS, offering a thick (4.6 microns) top metal. A 4turn, 1.3mmX1.3mm coil was designed in the top metal layer and an on-chip MIM capacitor was used to tune the system to 900MHz [173]. Detailed parasitic extraction was performed in Cadence to achieve this tuning in the presence of stray elements (L and C) in the system.

4.12.4.1 CMOS Results

The power source for CMOS system is the on-chip integrated LC resonator. The output of the resonator is fed to the CMOS power management unit consisting of a three stage self-driven synchronous rectifier (completely MOSFETs based) followed by a low drop out regulator. The power transfer to the chip was tested using an external LC resonator as the wireless power source. The outputs at different points in the power management system were measured using an oscilloscope and external load resistor. Successful power transfer through air, water, PBS, isopropyl alcohol and chicken skin and tissue (5mm thick) was achieved, as shown in Figure 89.

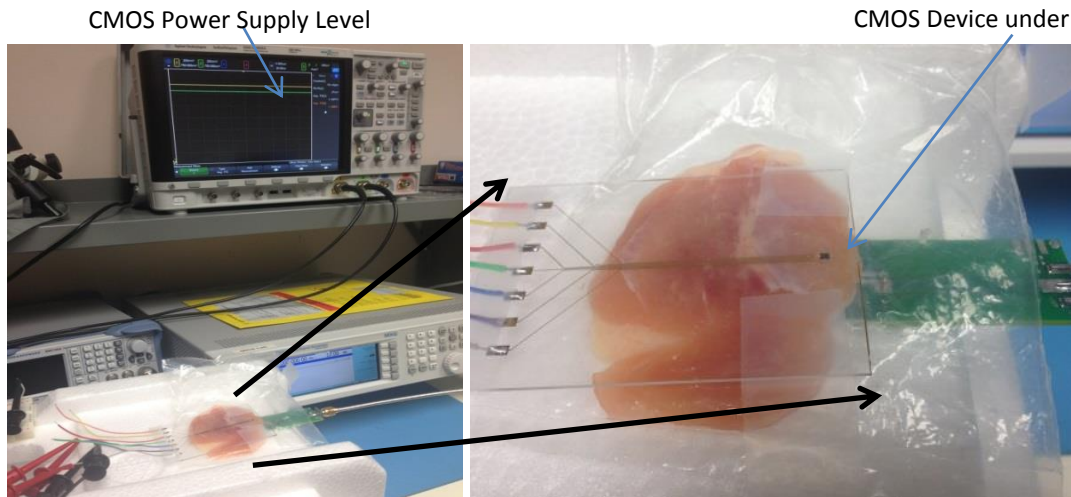


Figure 89 : Wireless Power Transfer to CMOS chip using Resonant Coupling

The system showed around 3mm alignment tolerance on either side (from the center of the external PCB) which is more than that required for optical power transfer. However, misalignment tolerance can be improved by using different approaches [174]. For example, by distributing the coils as much as possible, especially the transmitter coil to generate even magnetic field [175] or by using lower frequency (if possible), more robust powering is possible.

A stable supply voltage of 1.2V was achieved using around 16dbm of power in air and 19dbm when the devices were immersed in water and 22dbm for device inside 5mm thick tissue. The currents drawn in each case were around 8 microamps. Hence, the efficiency in air is around 0.25%, in water is 0.01%, and through tissue is around 0.006% (appendix III). Also, this efficiency is the relevant efficiency for load as it includes the effects of rectification, filtering, and regulation in it. Although the efficiency is low, the transferred power was enough to run all the subsystems on the CMOS chip.

In the past, electrical powering has been shown using custom fabricated MEMS coils [176], wound wire inductors [177], Printed (PCB) inductors [178] or off-chip coils [179]. An on-chip inductor is designed in 90nm RF process in [180]. However, no data was provided on power transfer efficiency of that system and hence a comparison cannot be made. To the best of our knowledge, this work is the first example of using small-scale on-chip resonators to power a functioning microsystem.

4.12.5 External (Reader) Device

The external powering device was designed to be a 900 MHz PCB with a matched coil to couple the energy to the implant and to read the backscattered signal. That system was also designed in HFSS. The external coil is larger to enhance the mutual inductance by increasing both its diameter and its quality factor. Our external PCB was characterized using a vector network analyzer to verify its resonance properties. The PCB was connected to RF signal generators and oscilloscopes for powering and communication. Input power levels (at the primary coil) were measured using a directional coupler and RF power meter. Output power from the on-chip power harvester was measured using different load resistors to draw variable current from the power harvesting system's output regulator.

4.13 RF Safety and Regulatory Issues

From a communication point of view, the electromagnetic methods are more restrictive in terms of regulation compared to the unregulated optical methods. The regulations are stricter for minimizing interference in other electromagnetic systems compared with the allowed levels for safe operation. However, using ISM and other approved bands (e.g. MICS, SRD, WMTS etc.) allows some freedom in terms of regulatory control on power levels. For the ISM band near 900MHz, FCC

allows a maximum EIRP of 36dbm while maximum power fed into an antenna can be 30dbm [181]. These levels are pretty high and our device operated within these levels. However, the other concern of using high electromagnetic energy is biological safety. These energies can cause heating in the biological tissues beyond the safe limits [182]. Both near and far field energy transfer can also heat up the biological tissues by both conductive and dielectric losses. The quantity that relates the electromagnetic field levels to energy absorbed in the body is called Specific Absorption Rate (SAR) and has units of mW/Kg.

$$SAR = \int_{body} \frac{\sigma |E|^2}{\rho}$$

Here, σ is conductivity, E is electric field intensity, and ρ is density. It has to be done over the relevant part of the body that will be exposed to the electromagnetic energy. For localized exposure, IEEE guidelines seem to allow up to 200W/m^2 between 300MHz and 3GHz. Also, for localized exposure, SAR is allowed to be as high as 20 W/Kg [183]. However, FCC has also set the exposure levels based upon the frequency band. For example, the 900MHz cellular band is limited to 1.6W/Kg SAR [184]. However, for localized exposures as in our case, the SAR needs to be calculated and simulated to carefully understand the risks involved. For example, it can be done to see if the temperature increase in any area is exceeding the 4°C safety limit for substantial time periods. Fortunately, full human body models are available and can make these simulations simple.

It should be pointed out that some other modes of damage from electromagnetic power are also sometimes reported (e.g. from microwave auditory effect). However, these are still ambiguous and are not regulated or documented properly. Our experiments did not create any such effects and

hence can be considered safe. Also, with iterative designs, the required power level can be further decreased and efficiency increased making these systems even safer.

4.14 Comparison of Power Harvesting Methods

A comparison of the different wireless powering methods is provided in Table 10. It shows the advantages of both electrical and optical methods. This shows that both can be used for such systems based upon specific requirements (e.g. size, safety etc.).

Table 10 Comparison of different methods to power wireless implants

Method	Size	Disadvantage	Tissue Loss	Longevity	Power Density	
Battery	Big (cm ³)	Toxicity	-	No	10uW/mm ³	[30]
Inductive	Medium (cm ²)	Interference	Negligible	Yes	1.6mW/mm ²	[152]
Resonant-low freq. (~10MHz)	Small(mm ²)	Interference	-	Yes	3.6mW/mm ²	[59]
Resonant	Small (mm ²)	Interference	0.5dB/mm	Yes	10uW/mm ²	This work
RF	Small(mm ²)	Interference	2dB/mm	Yes	12uW/mm ²	[150]
PV	Small(sub-mm ²)	Scattering	10dB/mm	Yes	20uW/mm ²	This Work

Table 11 Comparison between integrated power transfer methods

Method	Voltage Output	Current Output	Tissue Effects	Size	Efficiency in Tissue
Optical	No., quality of photodiodes	Area, QE	More Severe	Very Small	0.001%
Resonant	No. of turns,	Area, Q	Less Severe	Small	0.006%

	Rectifier Design, Q				
--	---------------------	--	--	--	--

4.15 Summary

In this chapter, we provided our results on wireless power harvesting using optical and electrical methods. It was shown that there are many challenges involved in obtaining high voltages from the CMOS integrated photovoltaic power harvesters. The electrical powering results showed that this is less of a problem for the resonantly coupled systems. However, results showed that optical power supply can provide high currents while electrical powering schemes can provide lower current. Realistic testing was performed using chicken skin and tissue to compare these methods in a realistic environment. Results from Silicon-on-Insulator based PV systems showed that these can provide high voltages due to inherent isolation, but low currents due to thin silicon absorbers.

Chapter 5 Wireless Telemetry

Wireless communication between the sensor and the outside reader is called Wireless Telemetry. This communication ideally needs to be done in both directions; from the implant to outside (forward link) and from outside to the implant (reverse link). The type of device used for this telemetry depends upon design factors which include data rate, size, and power requirements. In the case of implantable devices, the size and power need to be as small as possible. The actual data rate depends upon the type and number of sensors. For example, for single glucose sensor, the data rate is very low (bits per second). On the other hand, for neural implants, the data rate can be very high (Mbps) based upon number of channels being measured.

Both active and passive communication schemes can be used for implants with slow data rates. In active communication, a signal is generated on chip and is transmitted outside carrying the data. In passive communication, a signal is transmitted from outside and is modulated by the sensor circuitry. For high data rates, active communication has the advantage of high Signal to Noise ratio since signal has to travel through the tissue only once. Passive communication has the advantage of low on-chip power consumption since no signals need to be generated and hence overall size becomes small.

The options for wireless communication are similar to those available for powering and the challenges are similar. For example, acoustic telemetry has been used for some implantable applications [117]. However, such links normally need high voltage (for proper transducer operation) and special materials. Also, although the devices can be miniaturized in principle, there are still some technical challenges which need to be resolved before this can be achieved [185]. On the other hand, Telemetry using low frequency electromagnetic waves has been used in many

applications [58]. Both active and passive modes can be employed for such communication. In the passive format, the fact that any change in electrical parameters in one coil affects the other coil through their mutual interaction is used to communicate between the coils. For example, change in current (impedance) in the secondary coil generates a back EMF (change in reflected impedance) in the primary coil which changes the potential and current in the primary circuit which can be detected. Even for weakly coupled coils, this can be used for reliable communication at low data rates, especially if digital communication schemes are used. Arraying techniques can be used to increase the robustness of this technique by increasing the coupling to the small coil inside the body. For weak and scattered signals in back telemetry, some equalization techniques can be used for faster data rate communication. The near-field communication schemes make use of low frequencies to achieve high signal levels at short distances. Tissue loss is also lower for low frequencies.

At higher frequencies (GHz range), telemetry is done by far-field propagating fields between some radiating antenna structures. There are many windows in the electromagnetic spectrum which can be used for radiative transfer of data. For small implants, these antennas are normally sub-wavelength and hence are sub-optimal. However, adequate signal to noise ratio can still be achieved for sufficiently small implants located near the skin surface [55]. The allowed frequency bands for RF communication are MICS band and ISM bands (Short Range Devices, SRD in EU) due to regulatory issues [181]. Even within these bands, RF links are susceptible to interference from other systems using same frequency bands (e.g. WiFi, Bluetooth). Also, high frequencies suffer from high tissue absorption [186]. An advantage though is the existence of abundant communication protocols to make the communication network implementation quick.

Optical Telemetry has many useful properties suited for wireless sensors [187] like lower electromagnetic noise and smaller footprint. The optical spectrum is also unregulated and hence there is no bandwidth limitation, except the fundamental limit of transmitter and receiver designs. Moreover, background noise can be easily filtered using optical filtering. Furthermore, equalization is also less critical as optical signals are not limited by tissue scattering until very high data rates (Gbps) compared to RF where this effect starts at much lower data rates [188]. Since channel bandwidths are high, simple on-off modulation can be used which keeps power requirement low since multilevel coding schemes are not required [189]. However, optical communication suffers from high tissue loss and the need to integrate extra components capable of emitting or manipulating optical signals on the implant.

In this chapter, we will compare these two methods (Optical and Electrical) for their performance in communicating through tissue and discuss the results.

5.1 Optical Telemetry

Optical telemetry uses electromagnetic waves near the visible spectrum. Design of optical telemetry consists of designing the transmitter at the implant side and the receiver on the external reader. The general design includes a modulator and laser driver with an optical transmitting element and a receiver with some filtering/focusing optics, a detector and electronics as shown in Figure 90.

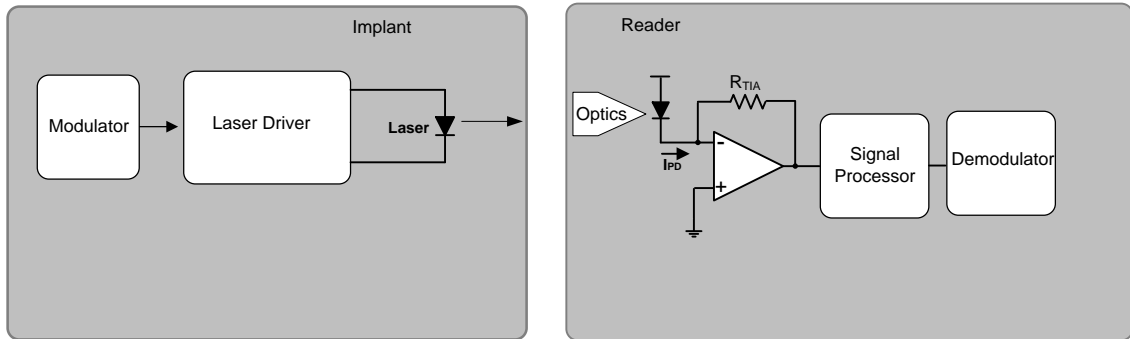


Figure 90 : General Optical Telemetry Link for Implants

5.2 Optical Telemetry Link Design

Optical link design starts with choosing an optimal communication wavelength similar to what was done in optical powering. If the power laser is also used to pump the implanted communication laser, the communication wavelength has to be longer than power wavelength. Longer wavelengths also scatter less than shorter wavelengths. In this case, a detector with starting wavelength higher than the power wavelength is used for easier filtering of background signal from power laser. Alternatively, communication wavelength can also be lower than power wavelength so a detector with cutoff wavelength lower than the power wavelength can be used. This can be advantageous as the responsivity of the detector is normally higher for shorter wavelengths in the NIR.

5.2.1 Optical Transmitter

The next step is choosing the right light emitting device. Luckily, there are many types of materials and devices available for this wavelength range. Both Silicon and compound semiconductor materials can be used for this wavelength region. Silicon is an indirect bandgap material and hence is less efficient for such applications. Compound semiconductor materials (e.g. GaAs) are direct

bandgap materials and hence are more efficient emitters and absorbers of light. Optical Telemetry links based upon Light Emitting Diode (LED) [190] and Laser Diode (LD) [191] structures have been demonstrated in literature before. In this work, we test the use of compound semiconductor based Vertical Cavity Surface Emitting laser (VCSEL) from ULM photonics [143] as a light source. Luckily, the VCSEL was available within the therapeutic window's transmission wavelength range (@850nm). VCSEL was selected as it can be more efficient than micro LEDs and Laser diodes for many reasons. These VCSELs offer very small threshold currents and one of the smallest threshold voltages for devices which emit in the desired wavelength range. Another advantage of laser is higher spectral efficiency. Hence, a low power laser can be used to reduce the power consumption. As a consequence, this would allow smaller power harvesting system. These devices have lower power dissipation which increases their efficiency and keeps local tissue heating low. Finally, their output beam is narrow and hence more light can reach a detector with a limited angle of incidence. An 850nm VCSEL from ULM is shown in Figure 91.

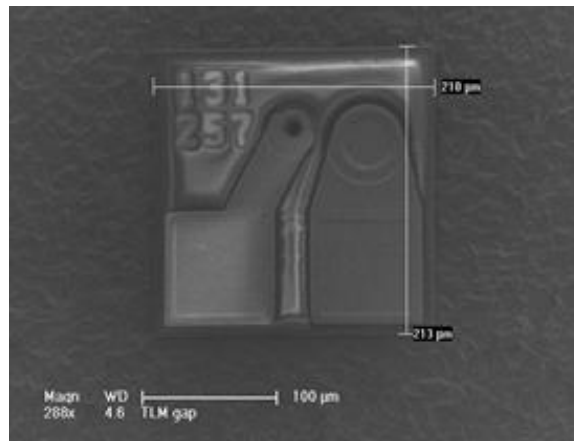


Figure 91 : SEM image of VCSEL chip from ULM [143]

We tried to improve the VCSEL by etching¹⁰ away the bottom substrate using wet chemical etching. This would also help in bonding as it would make it much thinner. The VCSEL characteristics before and after etching are shown in Figure 92.

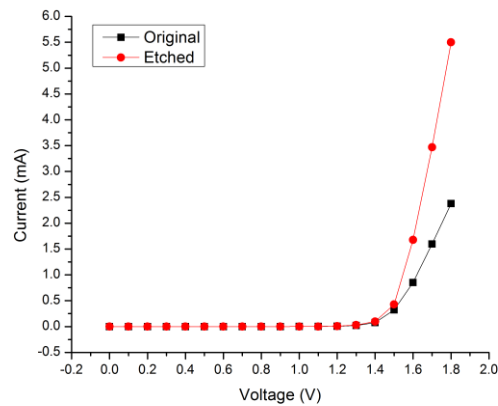


Figure 92 : Effect of substrate etching on VCSEL properties

5.2.2 Optical Receiver Design

The quality of detected signal on the receiver side depends a lot on the quality of the hardware and signal processing used. High quality low noise amplifiers and filters can improve the system performance a lot. The choice of proper detector is also important. There are different types of detectors including p-n diodes, p-i-n diodes, avalanche photodiodes (APDs), Photomultiplier Tubes (PMTs), and Schottky diodes [192]. APDs need very good filtering (due to high intrinsic gain) and

¹⁰ Etching was performed by Chieh-Feng Chang

large bias potentials while PMTs are bulky. Hence, p-i-n photodiodes are the best choice considering quantum efficiencies, responsivity and bandwidth. [193]. Both regular (no amplification) Si detectors (CMOS imager), compound semiconductor (InGaAs), and Amplified Si p-i-n photodetectors were used and their performance was compared. The compound semiconductor detector (InGaAs) and amplified Si p-i-n detector showed adequate performance, but the simple imager showed poor detection. However, the amplified photodetectors came with built-in high gain, low noise electronics. Hence, this may also be due to the electronics which was part of the package to amplify the detected signal. As an example, the dark state noise level of the amplified Si detector is stated as -120dBm and noise equivalent power is $3.2\text{pW}/\sqrt{\text{Hz}}$ [194] which is much higher than simple CMOS or CCD imager.

For the actual integrated receiver design, the receiver circuit needs to be custom designed. However, it is quite straightforward to use off-the-shelf components to achieve this. A low noise high gain Transimpedance amplifier (TIA) can be used to convert the photodetector signal into a voltage signal. If the use of multiple components increases noise, a custom IC can be designed for this purpose. Since the data rates are low here, the design is much simpler than those required for high speed optical communication links. Hence, a simple low-power custom design can suffice.

Good receiver optics can also help receive maximum communication signal. It was found that simple focusing lenses improve the capturing area by focusing the incoming photons to the relatively small detector. For integrated operation, this can be achieved using integrated lenses. Also, an array detector can be beneficial in terms of noise performance than a single big detector. Another important aspect of detector optics is filtering the reflected power laser. For in-vitro experiments, it was found that this was not needed as the reflected signal got diffused due to larger

distance used in the experiments. However, when these devices would be placed closer to the implants, it would be necessary and physical filters can be made by coating the detector with thin layers of appropriate materials. Alternatively a color filter with low absorption at communication wavelength can also be used.

5.3 Optical Link Capacity

The link capacity describes how much data rate can be transmitted with a given error rate limit. Calculation of link capacity is done by applying information theory concepts to the link and calculation of signal and noise levels is fundamental for determining the link capacity. There are many different noise sources in our system including noise from background light and noise from the receiver itself (e.g. dark current, electronics noise). Statistical or shot noise of the detector also adds to noise by random photocurrent generation in the detector. Thermal noise in the detector creates thermal current and leakage (dark) current which also adds to the detector noise. Thermal noise from the electronics itself also becomes a noise source. Similar to other communication links, an optical link is characterized by its impulse response [189]. It depends upon the wavelength, signal power and tissue properties. This impulse response can then be used to find the response of the system for arbitrary waveforms. We can formulate this using some basic communication theory. If the receiver collects incoming optical signal using a planar absorber of area A having a responsivity R at the wavelength of detection having a noise current density J_{noise} , the signal to noise ratio at the receiver can be defined using the system parameters

$$S = AR \int H_{rcv}(x, y) I_{tx}(x, y) H_{tissue}(x, y) d(x, y)$$

$$N = AR \int H_{rcv}(x, y) I_{noise}(x, y) d(x, y) + A.J_{noise}$$

Here, H_{tissue} represents the tissue transfer function found by Laplace transformation of the impulse response [189]. H_{rcv} represents the effect of receiver design (receiving detector and receiver optics and electronics). A general closed form of the transfer function for different tissues may be hard to find due to many non-linearities. However an experimental approach can be used to measure it. We used this approach by sending in a known pulse through the tissue and measuring the response as a function of coordinates at the receiving end. A detailed experiment for different tissue types and resulting responses have been reported in literature [60]. They determined that the transfer function takes the form of a Gaussian function for most tissue types. In our experiment, the line of sight signal was weaker and hence the shape appeared to be skewed Gaussian, but this may be due to refractions at the tissue –air interface. H_{tissue} would be flat for a tissue with no scattering and would only capture the effect of absorption. However, for most tissues, scattering is an issue and H_{tissue} would capture the effect of pulse widening by behaving more like a filter with finite bandwidth. This can lead to inter-symbol-interference (ISI) as in wireless communication channels suffering from multipath impulse broadening. While ISI can be a problem for multipath channels, short tissues do not have lots of delay between different scattered paths and hence it is not a major problem [195]. For deeper implants, the situation may be different. In Chapter IV, we experimentally found out that transmittance was around 25% for few mm (around 3mm) thick chicken skin and tissue for optical signals in NIR region. We also found that transmittance was inversely related to thickness. Hence, body locations with smaller skin thickness are more favorable for optical telemetry as the transmitter in this case is small and power limited. Also, very deep implants are not easy to design with this technique. Furthermore, larger optics is useful to compensate the effect of scattering. Also, detectors with lower dark currents would be better to improve the signal to noise ratio. Filtering of background signal (I_{noise}) can also help in this process.

Once signal and noise levels are determined, capacity can be calculated using bandwidth and the Signal-to-Noise ratio (Shannon Theorem [189])

$$C = BW \log_2 \left(1 + \frac{S}{N} \right) \text{ bits/second}$$

However, Nyquist sampling theorem dictates that the maximum channel capacity cannot be more than twice the channel bandwidth (BW) which means

$$C = 2BW \text{ samples/second}$$

The two theorems are related together by channel encoding schemes employing M encoded waveforms to carry the data from the channel

$$1 \text{ sample/second} = \log_2(M) \text{ bits/second}$$

Hence, for low signal to noise ratio (SNR) channels, encoding schemes with high number of levels can be used to achieve high data rates. However, if the SNR is high, simple coding schemes can be used and still high data rate can be achieved. The first case normally applies to RF channels whereas second one applies to optical channels. As there are no regulatory bandwidth limitations for optical communication and optical devices can switch fast, the BW of the channel is normally limited by the bandwidth of the transmitter receiver electronics. Channel bandwidths are also normally quite high and tissue scattering starts limiting link capacity only at very high data rates.

5.4 Alignment in Optical Telemetry Links

Optical alignment is important for achieving good signal to noise ratio at the receiver. Using maximum possible power at the transmitter and a well-designed optics at the receiver provides some misalignment tolerance. Scattering also plays a role in spreading out the signal. Pulse based

modulation (e.g. PWM) instead of amplitude modulation at the receiver provides some decorrelation from the signal amplitude. Highly sensitive front end at the receiver (e.g. a good LNA) can help in amplifying the small received signal. For such low signals at the receiver, signal to noise can be improved by Minimizing background noise and by using low noise (e.g. dark current) detector. Correlation based detection using a lock-in circuit can also help differentiate the signal from the background noise.

5.5 Optimum Modulation Scheme

As optical channels have very high bandwidth, simple amplitude modulation can be used where the amplitude of the optical signal is proportional to the information being transmitted. However, since the signal is quite small, any change in tissue scattering and absorption and misalignment between transmitter and detector can affect the reading. While Automatic gain control (AGC) similar to AM radios can be used to compensate for some effects, its design is quite challenging for such applications. Frequency modulation based techniques in general are more robust since the information is not encoded in the signal amplitude, but in signal timing. Analog frequency modulation would require somewhat complex circuitry to generate a continuous carrier waveform and to modulate it with the actual signal.

Digital modulation schemes on the other hand do not need a continuous carrier wave, but still can encode the information in signals' timing. The circuitry needed to convert the analog signal into digital signal can be as sophisticated as required by the compromise between power and performance. Different pulse modulation schemes can be used which encode information in relative timing between pulses or in relative change in pulse duration compared to a standard pulse. The first type needs slightly more circuitry for timing and relies on short pulses which need more

sophisticated receiver and post-processing (due to tissue scattering) to extract the information.

However, their benefit is low power operation. The second type consumes more power as the laser pulses are wider now, but it can use simpler encoding and decoding circuitry. We used the simple pulse width modulation scheme in this work.

5.6 Optical Telemetry Circuit

Once the device (VCSEL) was chosen and its characteristics understood, a telemetry link needed to be designed to drive the VCSEL to send data through it. The CMOS circuit was designed to get some data from the on-chip sensor circuitry in electrical form (either a current or a voltage) and converts it into a digitally encoded pulse stream. The digital modulator consisted of a simple ring oscillator with either current input or voltage input controls for modulation. The ring oscillator was designed by only utilizing the active devices (CMOS transistors). This yields repeatable and reliable performance without the need of passive components (e.g. capacitors) as used in some designs. For simple N stage ring oscillator, oscillation frequency is a function of the oscillator design and is given as

$$f = \frac{1}{2NRC}$$

Where R is the equivalent resistance and C is the equivalent capacitance of each stage. Hence, RC is the (charging/discharging) delay time for each stage. Its value depends upon the process parameters and transistor sizes and can be found from simulations of process transistors [133].

This is a free running circuit with constant oscillation frequency at constant processing conditions, within the limits of jitter and noise. A control circuitry is required to modulate the oscillation frequency of the free running circuit according to the data being transmitted. The actual type of

control circuitry depends upon the type of control variable. For voltage input, this can be achieved by introducing another transistor in the inverter stage to modulate the equivalent resistance of the inverter stage and hence the charging and discharging times of the intrinsic capacitances which control the overall time response of the stage and hence the VCO frequency as shown in equation 1. Both NMOS and PMOS control stages were used to couple different types of inputs to the basic oscillator stage. This also helps to maximize the modulation ratio of the oscillator output to achieve high signal-to-noise ratio. The circuit is shown in Figure 93.

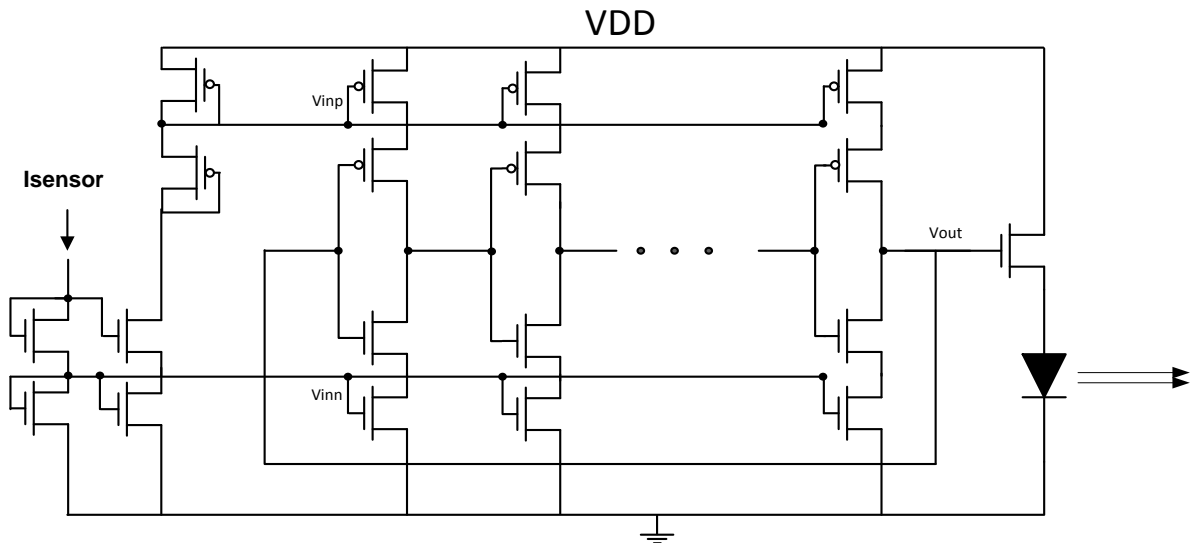


Figure 93 : Pulse Width Modulation Circuit for Optical Telemetry

For these controlled oscillators, the oscillation frequency becomes a function of input current as well as the oscillator design as shown in literature [196]

$$f = \frac{I_{sensor}}{2NV_{osc}C}$$

For current inputs, the control circuitry can consist of a current to voltage converter stage followed by the voltage fed design. Alternatively, current can be fed directly to the VCO as well. However, this results in some variation in output signal amplitude (voltage) as well as the desired pulse width modulation as predicted by the simulations. This extra modulation can create some difficulty in demodulation, especially at low SNR. Transistor sizes were chosen so that the free running oscillation frequency is kept low enough to minimize dynamic power consumption as it is proportional to frequency [133]

$$P_d = C_L V_{DD}^2 f$$

This range of frequencies was chosen to minimize power consumption of the circuit (e.g. 50 KHz, 100 KHz and 150 KHz). The number of stages used was limited to seven to ensure lower variations due to change in process and temperature. The diagram of the PWM circuit is shown in Figure 94.

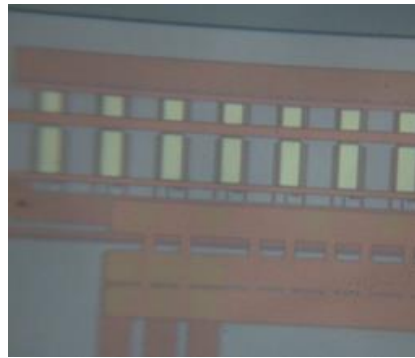


Figure 94 : PWM circuit utilizing seven stage voltage controlled oscillator

The pulse width modulated (PWM) data is fed into the output VCSEL driver. Normally cascaded buffers with successively increasing sizes are used to minimize the loading of the output driver to the oscillator using the method of logical effort design [133]. However, in this work, a simple

single transistor based driver was used to save area and power since the data rates were not particularly high. The effect of the loading of this large transistor on the PWM stage was included in its design through cadence simulations. Since the output device (laser) is a threshold based device, this loading was not expected to affect the system performance. The CMOS technology used is 0.25um 1P5M process from TSMC provided by the MOSIS service. The VCSEL was epoxy bonded¹¹ on a dummy top metal which also acts as a filter to protect the underlying circuits from the laser radiations. The electrical connections were made to the VCSEL by wire bonding it to the circuit pads. The assembly was optionally sealed in a non-conducting implant grade and hermetic (water-tight) epoxy. The VCSEL was also epoxy bonded on a chip carrier and wire bonded to it. The connections between the circuit and the VCSEL were made through the PCB.

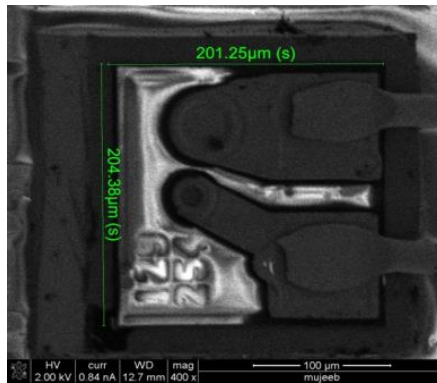


Figure 95 : VCSEL with bonding wires

The circuit was simulated using the electrical model of the VCSEL as series connected diodes and a resistor. The model was optimized to result in similar I-V characteristics as provided by the VCSEL

¹¹ Bonding performed by Akram Sadek.

manufacturer and measured using a semiconductor parameter analyzer. This technique essentially resulted in an equivalent circuit model of the VCSEL. The rest of the circuit was simulated using standard transistor models provided in the process design kit. Process and condition corner simulations were performed. The circuit was initially powered through an external power source and its output frequency was measured as a function of input current. The waveforms showed some loading effects from the large capacitance of the output stage (large rise and fall times). However, the frequencies were a function of the control voltage (input current or voltage as desired). Since the VCSEL is a threshold based device, this loading was considered to have minimal effect on system performance. An example result showing the current versus frequency for one of our readout circuits is shown in Figure 96.

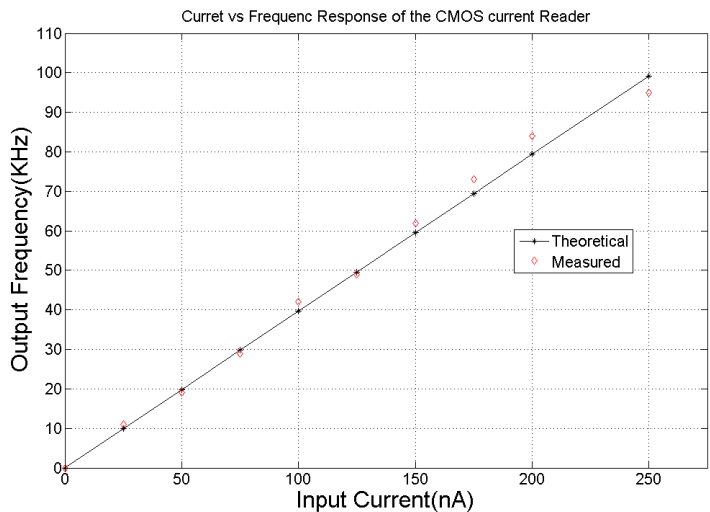


Figure 96 : Current versus Frequency Response of the Telemetry
Circuit

Next, the output of the readout stage was connected to the VCSEL and the optical signal was detected on the other hand. Both Voltage and Current input version were tested. Without any external modulating signal, the unmodulated carrier was detected on the receiver end as shown in Figure 97. There was some edge rounding but overall the response appeared fine.

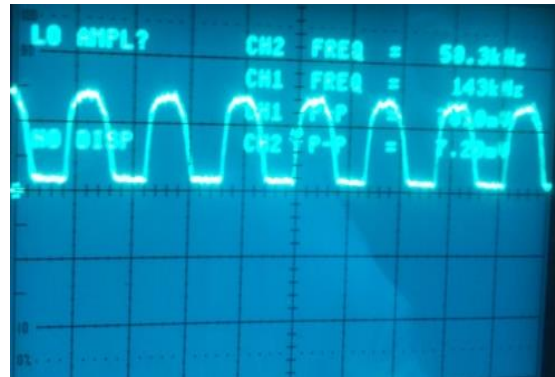


Figure 97 : Unmodulated Data from the Optical Telemetry Link

Then a modulating signal (100Hz frequency) was fed into the circuit and the modulated output from the circuit was used to drive the VCSEL. The transmitted signal was detected on the other end. An RF Lock-In amplifier from Stanford Instruments showed the actual data confirming successful data communication as shown in Figure 98.

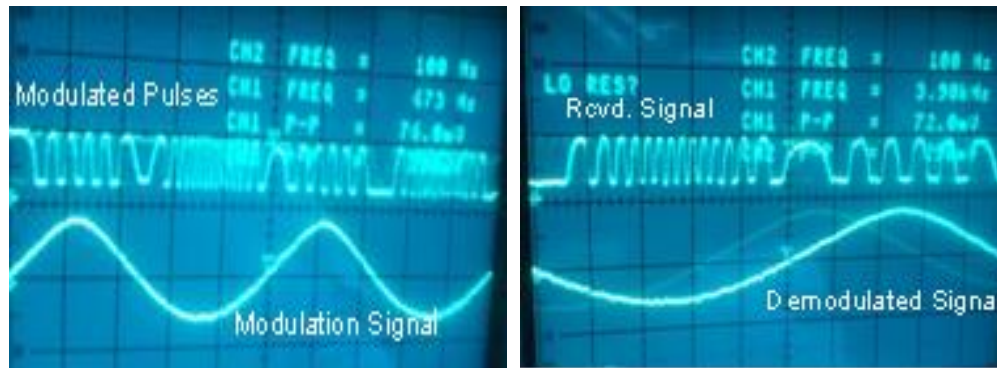


Figure 98 : Results of Optical Telemetry Using VCSEL

5.7 Communication through Skin and Tissue

In this case, a piece of chicken skin and muscle tissue was inserted between the VCSEL and the detector. The piece was soaked with saline solution throughout the experiment. The setup¹² is shown in Figure 99.



Figure 99 : Optical Telemetry through an ex-vivo tissue

¹² Setup was done by Akram Sadek, Muhammad Mujeeb-U-Rahman and Elizabeth Schroder.

The experiment was carried out using simple sinusoidal signals transmitted through the biological sample for easy visual inspection. The results initially showed extreme distortion on the receiving side. However, integrating the signal several times (4x integration) helped improve the detection substantially. This showed that although scattering is an issue, its effect can be compensated using simple techniques. The results are shown in Figure 100. Since large distances were used in this case, the effect seemed worse than what it can be for actual applications where the reader is placed very close to the VCSEL and ideally VCSEL should be kept inside the tissue.

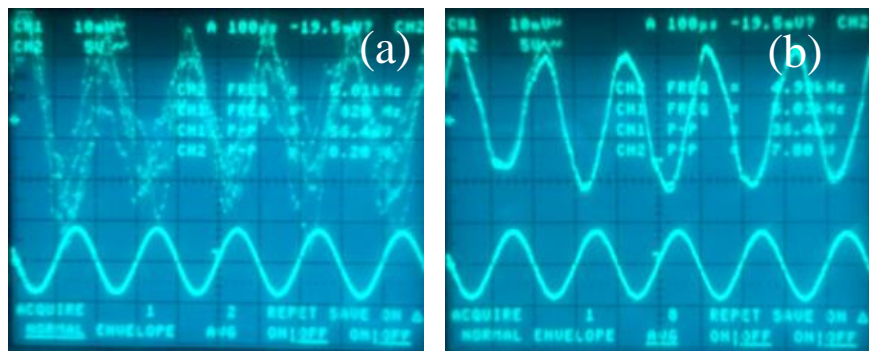


Figure 100 : Optical Telemetry through Tissue (a) Raw Data (b)

Results after 4x Integration

This experiment showed that a properly designed optical telemetry link can work quite well for implantable applications for communication through tissue. Using good optics and electronics on the detector can provide good performance. This can be more useful for implants which need high speed telemetry (e.g. neural implants).

5.8 Effect of Power Laser

As described in Chapter IV, a high power (0.8W) laser is used to power the integrated photovoltaic power supply. Due to scattering in the skin and tissue, some of this high power laser also illuminates the VCSEL. Experiments were performed to find the effect of such high intensities on the low power optical telemetry link. The experimental setup was modified to incorporate the high power laser. The power laser was initially turned off and the experiment was performed as usual. Then the power laser was turned on and the effect on the communication laser was noted. The power laser was left on for some time to see the effect of continuous illumination. It was also modulated using a mechanical shutter to see the effect of pulsating illumination.

The power laser seemed to increase the signal amplitude without affecting the modulation and showed no negative effect on communication system's performance. It is speculated that the increase in signal amplitude is due to the optical pumping of the VCSEL by the laser. This does not increase the signal level to very large extents because of the front mirror in the VCSEL design which reduces the actual intensity that reaches the active medium. This also shows that a high power laser of appropriate wavelength can be used to optically pump the VCSEL which can then be modulated electrically to consume lower on-chip power.

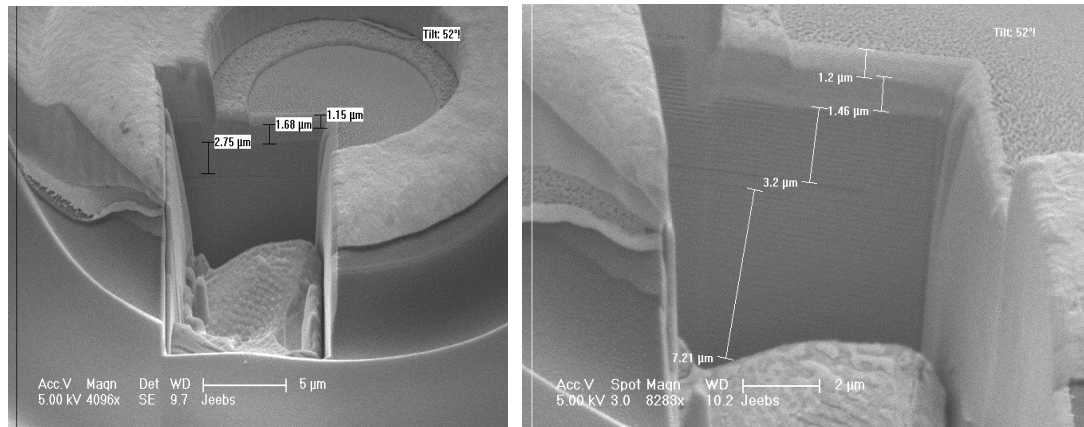


Figure 101 : Cross section of the VCSEL Structure showing Mirrors

5.9 Reverse Link Design

Optical techniques can be used for the reverse communication link by utilizing the different types of P-N diodes in the CMOS process which are sensitive to different wavelengths. This spectroscopic data can be used for forward communication as a digital communication scheme. This communication can be used to send data or commands from outside to the implant. It can also be implemented by modulating the power signal itself with a known sequence. In this case, an extra laser can be used to send signal at different wavelength compared to the power signal. The effect can be enhanced using extra filtering layers added to filter out the power laser from generating a false signal on these photodiodes.

5.10 Optical Communication Results

The optical telemetry link using a VCSEL and a CMOS modulator and driver showed adequate performance in both free space communication and communication through skin and muscle tissue. The Unmodulated (free running) pulse stream showed that the oscillator design was successful in

controlling both the operation of the oscillator (providing stable oscillations) as well as the frequency of operation. After modulation with a sinusoidal signal, the data stream showed pulse width modulation effects as expected from the design. The detector showed appropriate detection performance as the signal at the detector end was comparable to the transmitted signal. After passing through skin and muscle tissue, the received signal was decreased in amplitude and also showed effect of scattering. The optimal reception was not at line of sight, but found to be at an angle (around 10 degrees) from the transmitter. This angle was found to be dependent upon many factors including skin and tissue properties and laser properties. Line of sight was the direction of maximum received signal without the skin and muscle tissue in the path. The received signal strength as a function of angle appeared to be a skewed Gaussian function. The signal shape was recovered after several waveforms were integrated to result in a smooth signal at the receiving end. This can also be achieved with the use of a proper front-end filtering and back end signal processing as well. When actual modulated signal was transmitted through skin and tissue, the result showed an attenuated and distorted signal due to absorption and scattering. The signal was still recoverable though after integration was used to integrate waveforms. Long term performance of the telemetry link was tested by leaving the setup on for few days. The system showed very little variation and hence the overall scheme appears stable enough for long term use.

However, an issue with the active optical telemetry link is too high power consumption. Although the VCSEL is the most efficient optical signal generator at the micro scale, it still requires around 1.6V and 400microamps of current to work. This is too high for most small scale power harvesting schemes. The best possible mechanism at the small size scale seems the use of a power laser to pump a small laser and then modulate it with the telemetry circuit. This was tried in our group with some custom laser designs, but no successful design could be obtained. An alternative is to use on-

chip power storage and then use the VCSEL in pulsed modes for communication. This is possible, but needs large on-chip capacitors which take lots of area. Due to these problems, it was decided to explore other communication mechanisms for our low data rate applications.

5.11 Electrical Telemetry

Electrical telemetry (low frequency electromagnetic communication) is the most prevalent form of telemetry for most implantable application [152]. Such telemetry can be established in both forward and reverse directions. Similar to powering, it can be done in near, mid and far field regions.

Far Field communication can be used by employing special sub-wavelength antennas in these small implants. However, integration of these antenna and relevant feed structures on CMOS at ultra-small scale is quite challenging. These structures take significant area even for optimized cases. An interesting method is dual purpose use of metal structures and can allow the design of ultra-small systems in special situations [197].

Near field communication is much more versatile and has been used in many areas for example RFID[198]. Such communication schemes have also been implemented in cell phones and other devices and their use is also regulated in the ISM band [199]. Passive Telemetry using Load Shift Keying (LSK) or backscattering also employs similar communication between two resonantly coupled systems [149]. This scheme can use the same coil which is used for powering and hence does not need extra chip area [151]. The simple circuit model used to illustrate this scheme is shown in Figure 102. Here a switch in the secondary circuit modulates the load seen by the primary and creates a change in the current in the primary circuit which can be read as a change in voltage across the primary inductor.

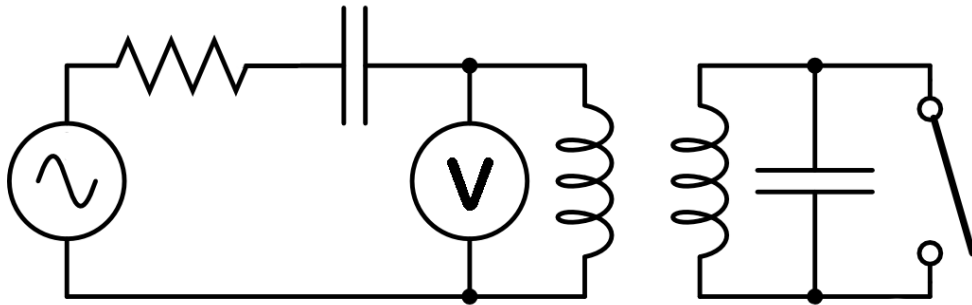


Figure 102 : circuit Model for Load Modulation Telemetry

This method has been employed before for some implants including retinal implants [200] and neuromuscular stimulators [201]. The circuit used in our design is simply a transistor switch in parallel with the receiver resonator and the switch is used to pulse width modulate the incoming signal from the external device which is shown at the external device through backscattering. It is detected using an envelope detector at the transmitter side. The reflected impedance depends upon frequency and mutual inductance as follows.

$$Z_p = \frac{(\omega M)^2}{Z_s}$$

The LSK scheme uses the same coil as used in powering. The extra circuitry needed is minimal and does not consume any static power. A schematic of the circuit used is shown in Figure 103.

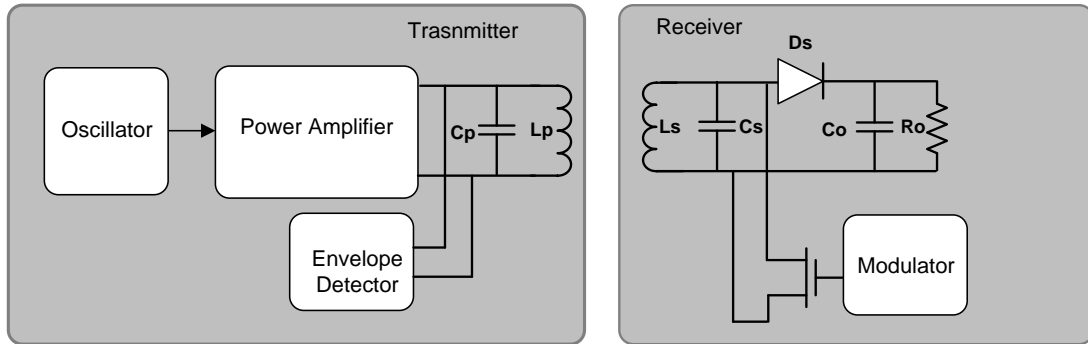


Figure 103 : CMOS circuit for Backscattering Communication

The equivalent AC load resistance in the secondary circuit is a function of frequency and inductance and is given by [160]

$$R_L = \frac{2(\omega L_s)^2}{R_o}$$

The equivalent resistance of secondary circuit as seen on the primary side is given as

$$R_e = \frac{(\omega M)^2}{R_s + R_L}$$

Here R_s is the series resistance of the secondary coil. Equation (5.) shows that a change in the load resistance (R_L) in the secondary circuit creates a change in the resistance in the primary circuit through a change in the reflected resistance (R_e). This phenomenon is called load shift keying or backscattering. To get high modulation, the transistor in the backscattering modulator should be designed to have minimal resistance compared to R_L so that their parallel combination has minimum resistance which maximizes the change compared to the case when the transistor is open.

5.11.1 Electrical Link Capacity

Resonant based coupling schemes can provide enough bandwidth for low data rate communications through tissue. Unlike the optical telemetry link, the bandwidth of these channels is limited and is dominated by the higher quality factor which is mostly the external coil and the resonance frequency as given by [202]

$$BW = \frac{f_0}{Q_p}$$

For high power transfer, coils with highest possible Q's are designed. This means that the system bandwidth will be low resulting in low data rate according to the Shannon theorem. For high data rates, compromise on power efficiency will have to be made to decrease Q. An SNR requirement will set the fastest possible data rate for a given distance between transmitter and receiver according to Shannon theorem.

$$C = BW \log_2 \left(1 + \frac{S}{N} \right)$$

As an example, for an SNR of 3 (received signal power is 3 times higher than background noise) at ISM band of 900MHz and typical Q of 20

$$C = \frac{900\text{MHz}}{20} \log_2(4) = 45 \text{ Mbps}$$

Practically, this high data rate may not be easy to achieve, but it shows that this system is capable of providing sufficient data rates for most metabolic sensing applications. Noise in this telemetry scheme is mostly dominated by the electromagnetic interference from other systems using the same bandwidth. Filtering is possible by use of specially designed external device housing and by reading

very close to the receiver coil. The telemetry system has to be designed to work in worst possible EMI (or RFI) situations.

5.12 Electrical Telemetry Designs

Similar to electrical powering, electrical telemetry was tested using different models of the system for better understanding. The results from these different models are given below.

5.12.1 Discrete Coil Design

Discrete coils were used to test this communication scheme using the same coils used for power transfer. The configuration used was similar to one shown in Figure 100. Different topologies (series, parallel) of the resonant system were compared. Also, both active and passive schemes were tested. In the active scheme, an actual signal was used to power the secondary which creates a field that links to the primary and create a change in it. In the passive scheme, this change is created by only modulating the resistance seen by the primary. The best topology was found to be series in primary (providing isolation between input and output for easy detection of backscattered signal) and parallel in secondary to create maximum changes in load resistance. The larger the secondary coils was, the more was the change in reflected signal. Also, good alignment was needed similar to powering and the results are shown in Figure 104.

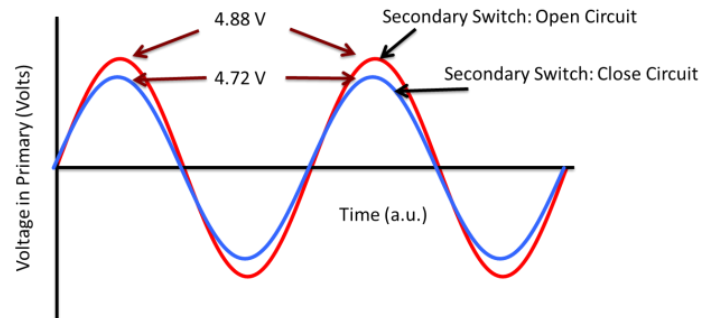


Figure 104 : Load Modulation Results for Discrete Coils

5.12.2 PCB Design

This telemetry scheme was also implemented using PCBs for rapid prototyping of integrated systems. The PCBs used for power transfer experiments also had the functionality to send the data using load shift keying. The results from testing the PCBs showed clear changes in the backscattered signal on primary side. An oscilloscope was used for detection. For integrated receiver design, this data can be extracted by using an envelope detector.

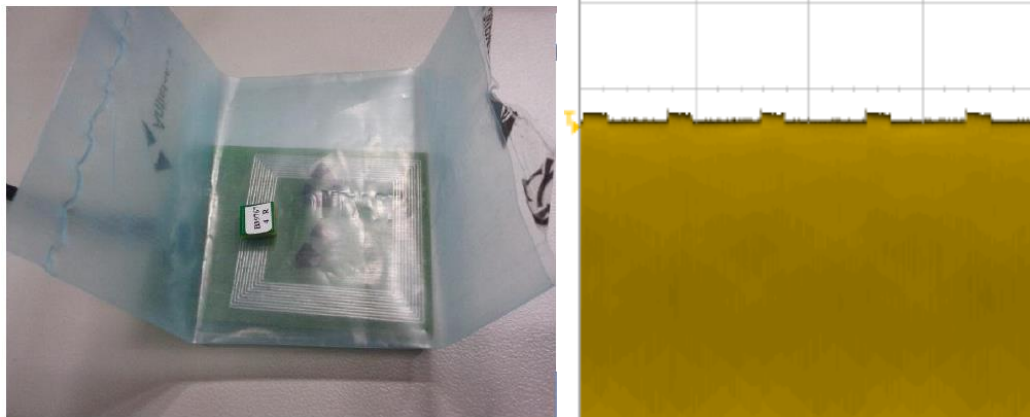


Figure 105 : PCB testing of Load Shift Keying based Communication

5.12.3 CMOS Design

Our system¹³ consists of integrated resonant circuits on both primary and secondary sides and a switch to modulate the load impedance seen by the primary [173]. The system was tested for communication through air, water, and chicken tissue. The data on primary side was read using an envelope detector. A typical set of results is shown in Figure 106.

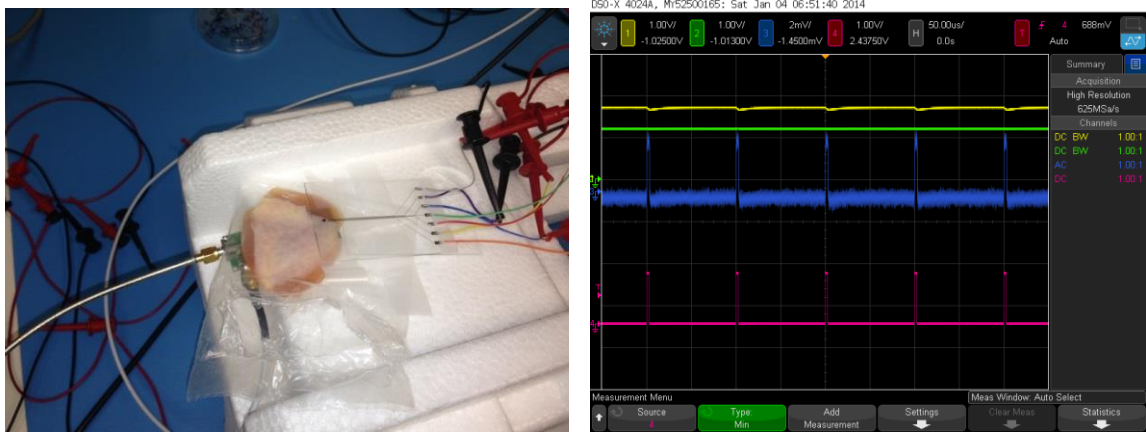


Figure 106 : Load Modulation using CMOS circuit

5.13 Reverse Telemetry

Reverse telemetry can be done by modulating the power carrier to send a specific signal to the implant. Modulation is designed to occur at very low rates to avoid a significant decrease in power transfer efficiency[151]. We used this method to perform reverse telemetry to send data to the implant. An envelope detector on the CMOS side detects and decodes this signal.

¹³ Designed by Meisam Honarvar Nazari and Muhammad Mujeeb-U-Rahman.

5.14 Comparison of Telemetry Schemes

A comparison of different telemetry schemes is given in Table 12. It shows that both electrical and optical methods can be useful depending upon application. It also shows that passive methods are in general more suitable for low data rate applications due to smaller size and power requirements.

Table 12 Comparison of Telemetry schemes for implant applications

Method	Size	Power Requirement	Bandwidth	Noise	Tissue Effect
Inductive Coupling	Large (cm)	Small	Small	Small	Small
Resonant Coupling	Small (mm)	Small	Medium	Medium	Small
RF	Small (mm)	Medium	High	High	Medium
Optical (Active)	Very Small (sub-mm)	High	V. High	Medium	Large
Optical (Passive)	Very Small (sub-mm)	Small	High	Low	Large

5.15 Summary

In this chapter, we discussed the wireless telemetry using optical and electrical methods. First it was shown that optical telemetry can work if a small communication laser is driven through the CMOS circuit. It was also shown that this communication can even work through skin and tissue. However, the required power was too high for the small power harvesting system designs shown in Chapter IV. Hence, passive electrical telemetry was tested and results showed that it can work through tissue without needing too much power. It was shown that good power transfer limits the bandwidth of this communication scheme and for very high data rates (e.g. for neural implants), optical communication may be a better choice.

Chapter 6 Control Circuit

An on-chip circuit is required to control the sensor operation. This circuit is designed to be robust and completely autonomous as it needs to be able to work in completely automatic mode. It also needs to measure the sensor response and process it for the communication system which transmits it to the external device. The basic goal in this circuit design is to keep it simple, low power and have the smallest footprint possible, yet providing enough capability as required by the application.

The operation of most electrochemical cells depends on controlling electrode potentials with respect to the ionic potential or solution potential thus allowing one or more reactions to happen preferentially. This potential is known as redox potential for particular redox specie. When an electrochemical cell is connected to a control circuit, some currents flow through the electrode-electrolyte interface and the electrode potentials change from their initial (or idol) values as predicted by the Nernst equation. Hence, a feedback based control circuit is needed which can adjust the cell potential to the desired operating point. This circuit, controls the potential difference between the WE and RE by controlling the current flow through the CE by adjusting its potential w.r.t fixed RE potential [76]. It is known as a Potentiostat. The function of the Potentiostat is shown schematically in Figure 107.

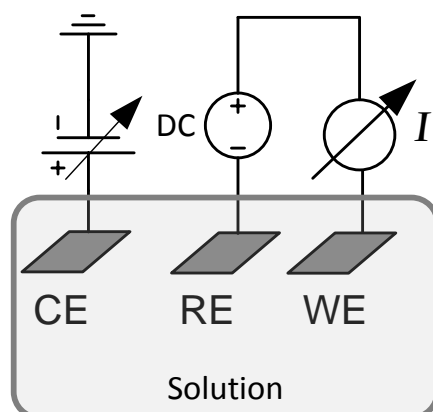


Figure 107 : Schematic representation of a Potentiostat

The classical Potentiostat which is commonly used is based upon the circuit shown in Figure 108. As evident, this design consists of at least two op-amps, one working as a control amplifier which is followed by another one working as a Transimpedance amplifier (TIA) [76].

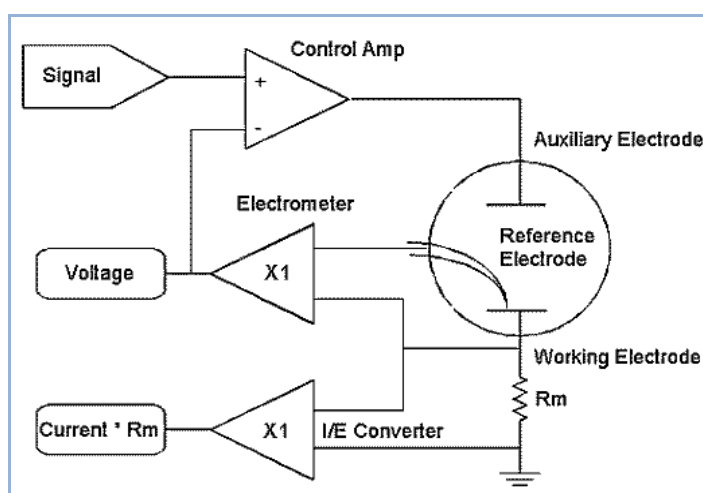


Figure 108 : Classical Potentiostat Circuit [76]

This Potentiostat has a large footprint and power consumption. Also, it needs large resistors for high TIA gain. Although large resistors are possible to miniaturize in the CMOS process, it takes large chip areas and their values are difficult to control¹⁴. Moreover, the working electrode terminal in this design is not at any fixed potential which makes it vulnerable to noise and interference issues. Nonetheless, this circuit has the advantage of high bipolar swing and wide dynamic range and hence can be used for many electrochemical methods including cyclic voltammetry and amperometry. We used this design as a reference for other Potentiostat designs for comparison.

6.1 Low Power Potentiostat Design

Exact design of the Potentiostat circuit depends upon the type of sensor. Our glucose sensor works by oxidation of H_2O_2 on the WE, which means the sensor current (conventional sense) flows from the WE to the CE, and hence WE is kept at higher potential than the CE. Also, this reaction happens around 0.5V vs. Ag/AgCl RE. Therefore, the WE has to be kept at higher potential than the RE as well. In our design, the WE is kept at highest fixed potential which is VDD (which acts as AC ground for noise). For O₂ based detection, this would be opposite (sensor current flows from CE to WE) and WE would need to be kept at the lowest potential (either ground or VSS). The RE potential is controlled to control the potential difference between WE and RE. Hence the CE is the floating electrode in our applications. Furthermore, since material consumption of the reference electrode can degrade its performance with time, a design

¹⁴ If designs can be based upon ratios of resistors in close proximity to each other, the error can be much smaller.

with very low input current in the RE terminal is needed [77]. This means that the RE should only be connected to the gate terminal of a MOSFET.

There are many possible topologies that can be used to implement the desired Potentiostat [203]. The topology selected in this work was the fixed WE to minimize noise because of small sizes of electrodes and resulting current. Many Potentiostat circuits are published in literature including fully differential designs [204] and shared amplifier based designs [205]. In our work, we used the current conveyor based design [206]. This circuit uses a transistor to act as current conveyor [207] which passes it to other circuit elements for further processing as shown in Figure 109.

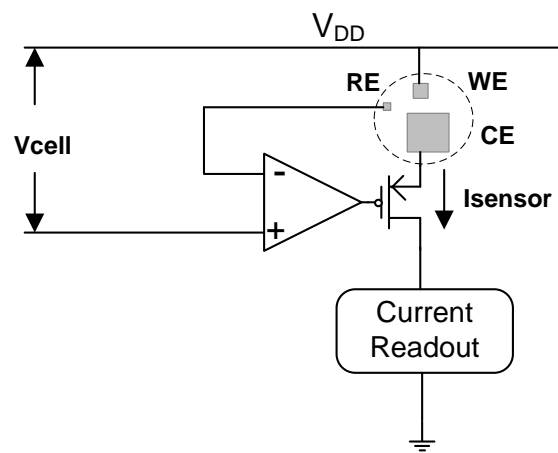


Figure 109 : Current Conveyor based Potentiostat Design

As shown here, the RE is connected at the input of an op-amp. This means it can be kept unpolarized (or at its standard potential) given the input impedance of the op-amp is quite large. For CMOS designs, this is straightforward due to high gate impedances, especially at low frequencies. The output transistor should act as current conveyor. Since the sensor current can change over a wide range during the operation, design of this transistor is very critical to keep it within its proper

operating range. For too large current variations, more than one transistor may be needed and appropriate transistors can be selected during device operation using some circuit which keeps an eye on the current through the transistor. However, for most practical sensors, a single transistor can suffice. To keep the input impedance of the transistor low (so that it does not load the CE node), a PMOS is selected over an NMOS in which case the CE feeds to the source terminal and impedance seen is r_m (or $1/g_m$), which is quite small compared to r_o of MOS transistors. Also, the cell potential in this case is the potential difference between WE and RE. Hence, the V_{cell} should be $V_{DD} - V_{redox}$ to have V_{redox} between the WE and RE. Similar adjustments should be done in other topologies, if needed.

In order to prevent the rest of the circuitry, most importantly the modulator, to affect the Potentiostat operation, it is isolated from that circuitry as much as possible [208]. This is achieved by copying the current using current mirrors before it is used in other parts of the circuit (e.g. in the readout circuit). It is also possible to isolate the power supply of the switching components of the circuit from the analog components (DC and AC power supply). However, to keep the circuit simple with minimal components, a single supply based design is used which can later be replaced with multiple supplies by using multiple voltage regulators.

The current mirror isolates the actual sensor operation from the modulating circuitry. In our design, cascode topology was used to increase the isolation and also to improve the current mirror functionality [45]. Furthermore, the transistors used in the current mirror were designed to have longer gate length than the minimum gate length to be less affected by channel length modulation.

The control amplifier is the most important component of the Potentiostat design and it should have a large gain, low input offset voltage, large bandwidth and low input referred noise and large gain

and phase margins for stability. The stability of the design depends upon the stability of the feedback loop in the control amplifier. Since the resistance and capacitance of the electrochemical cell vary considerably during the system operation (e.g. from being non-powered to turning on the power), it is difficult to design the system with exact values for these parameters as is normally done in circuit design. The approach we used was based upon the assumption that the most dominant elements in the Potentiostat response are contributed by the cell. For example, the electrode capacitances are assumed to be larger than transistor capacitances. Furthermore, the solution resistance is assumed to be much smaller than electrode resistance (verified experimentally). Under these assumptions, the analysis given in [208] can be used as the circuit topologies are quite similar. However, a point of importance here is that our electrodes are much smaller than used in their work and the assumptions needed to be verified numerically before we could use their formulation. Their analysis showed that the dominant poles are the pole due to WE (it is at AC ground) and the pole at output of control amplifier. For good stability, the poles are pushed away from each other. Hence, the output node of the control amplifier is designed to have small capacitance by not having too large second gain stage in it. We chose a PMOS based stage compared to the conventional NMOs based design to have large voltage swings to compare the sensitivity of detection over a wide range of cell potentials. NMOs based designs were also done as a reference. A typical PMOS based design is shown in Figure 110.

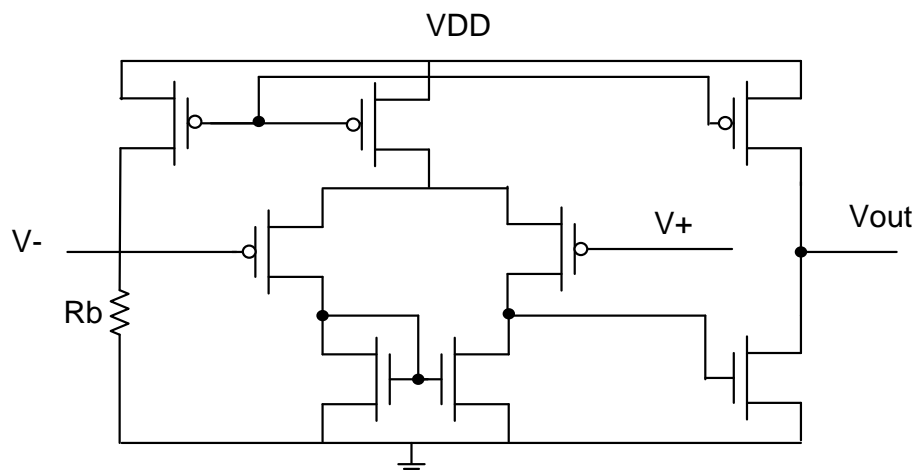


Figure 110 : PMOS based Control Amplifier Design

More sophisticated designs using fully differential amplifier along with common mode feedback adjustment circuits can be used for fully differential designs, if needed.

6.2 Potentiostat Readout Circuit

The control circuit not only controls the cell operation, but should also be able to provide an output corresponding to the cell operation. This will be voltage in Potentiostatic mode and current in Amperometric (Voltammetric) mode. Again, this can be implemented using different topologies. The simplest method would be to add a resistor in the current path and read the corresponding voltage. This resistor can be added at either WE or CE. The resulting voltage can be read using some low noise amplifiers [209]. However, this method is prone to noise and interference. In such cases, a Transimpedance Amplifier (TIA) can be used to convert the current into a voltage reading with enough gain. The TIA can be implemented using standard resistor in the feedback path or switched capacitors [210]. The feedback element (resistor or capacitor) value can be changed to get a wide dynamic range. For capacitive circuits, the capacitor needs to be discharged before the next

reading can be made. Normally a parallel switch is used to achieve this. These two topologies are shown in Figure 111.

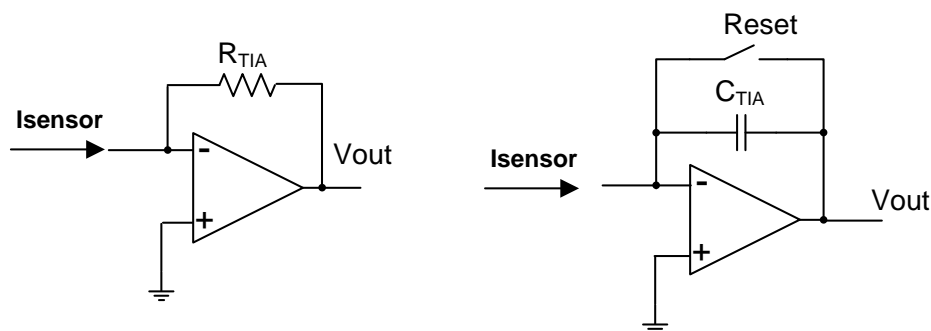


Figure 111 : Common TIA topologies using resistive and capacitive feedback

In more sophisticated designs, the current can be fed directly into current input Analog-to-Digital converters such as a dual-slope ADC [211], a sigma delta converter [212], etc. In other cases, this current can be fed into a modulating circuit which may generate other variables proportional to it (e.g. a current to pulse width converter [196], a current to frequency converter [207], a current to time converter [213], etc.).

In our first design, current was read using a low power pulse width modulator (PWM) circuit. This is one of the simplest implementations using few components and very low power consumption. Since the frequency of the sensor current is very low, the simple PWM circuit can work directly without the need of any sample and hold circuit. Hence, the final circuit consists of a low-power integrated Potentiostat to control the three electrode electrochemical cell which forms the sensor. The Potentiostat output is fed into a current mirror to replicate the sensor current. This is followed by a PWM circuit to convert the current into a pulse stream of varying widths. The output of this

circuit is fed to an output driver which can drive the output element, a VCSEL or other micro-laser, for example. The circuit was designed with different scales and different versions consume from $100\mu\text{W}$ to $20\mu\text{W}$. The resulting circuit diagram is shown in Figure 112.

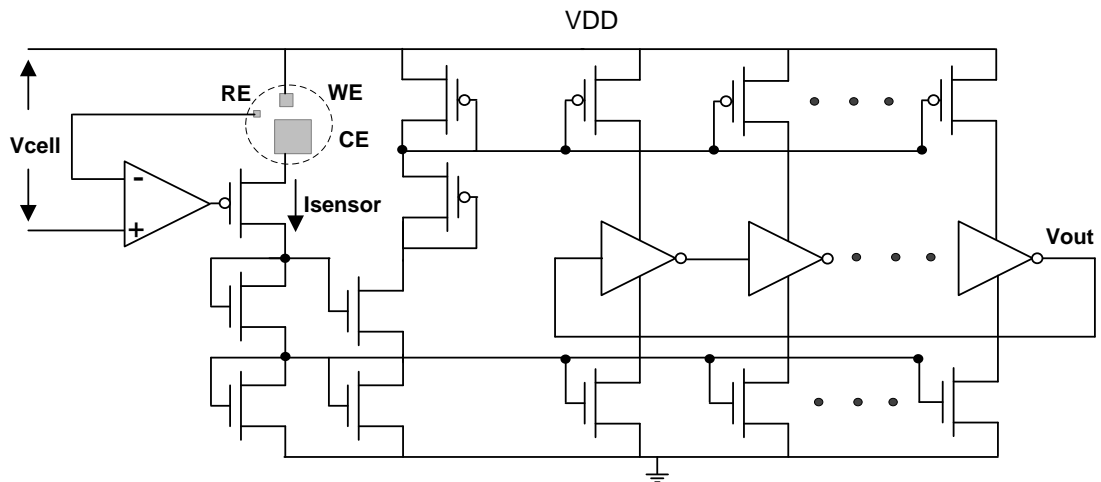


Figure 112 : CMOS Potentiostat with isolation and readout circuit

The CMOS process used was the $0.25\mu\text{m}$ process from TSMC offered through the MOSIS service.

The diagram of the CMOS Potentiostat on the die is shown in Figure 113.

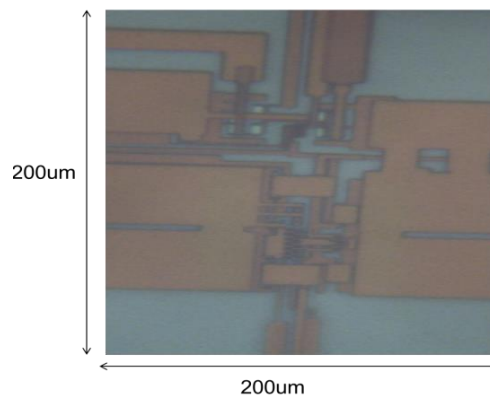


Figure 113 : A picture of one of the Potentiostat on the CMOS die

6.3 Reference Voltage Generation

The Potentiostat needs a reference voltage to be used as the working cell potential. For peroxide based sensors, a voltage near 0.5V is mostly used, although our cyclic Voltamograms suggest that the range can be much wider. The simplest method to generate this voltage is using the output voltage of a single Photodiode, as was used in our first design. For arbitrary and more controlled voltage, a supply independent reference voltage generator can be designed [45] and this was used in the second version. A potential of 0.6V was used to obtain high sensitivity for the small on-chip sensor without too much interference.

6.4 Control Circuit Testing

For design and simulation purposes, the Randles model of the sensor was used. Parameter values were extracted from EIS experiments as described in Chapter I. For testing, the Potentiostat was connected with the lumped element Randle's circuit. The control potential was swept for the entire range of operation and the reference electrode potential and counter electrode current was measured. A variable WE resistor was used to emulate the change in sensors current. The Potentiostat circuit showed very good response with fast and accurate control on the RE potential as compared to the WE potential. The results are shown in Figure 114. The results showed the Potentiostat worked according to the design whereas it could control the potential of the WE node relative to the RE node in the range of 0 to 0.7V. The results also showed that the potential difference between the RE and the WE could be maintained for the desired range of currents as per different designs. A typical range is 0nA to 250nA.

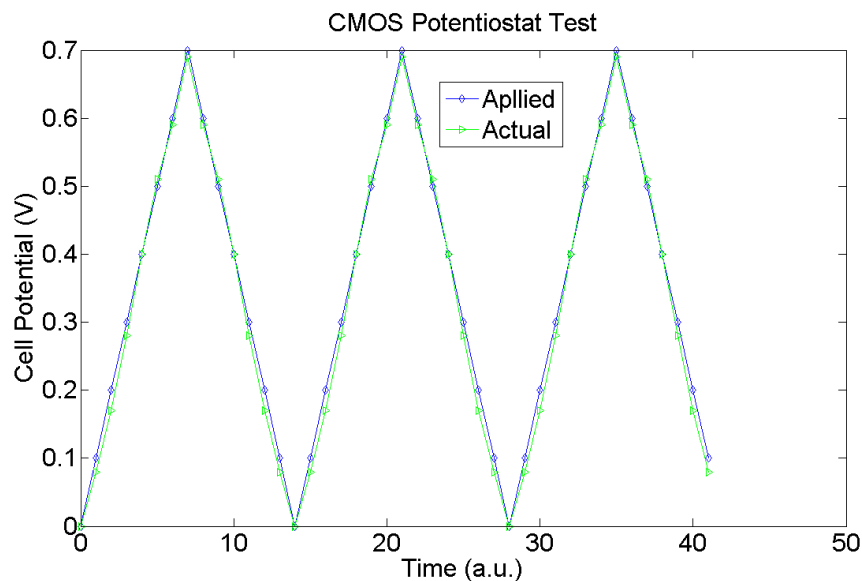


Figure 114 : CMOS Potentiostat testing using Dummy Electrical Cell

Actual sensors were also connected to the Potentiostat and their responses in amperometric mode were measured. The results showed that the Potentiostat worked fine in amperometric mode. However, electrode polarization time was around two minutes (compared to instantaneous for the resistor model tested) for the actual sensor. The reason may be the small size of the conveyor transistor which increases the time to flow initial settling currents that are larger than those during actual sensing. Also, the sensors with background current smaller than 1nA could not be polarized successfully due to noise issues. However, for the sensors with area in the considered range (500umx500um), the circuits worked as designed. Furthermore, for smaller sensors, nanopatterning can be used to increase their current so that these can also be tested with these circuits. A typical result of hydrogen peroxide sensing using this Potentiostat is shown in Figure 115.

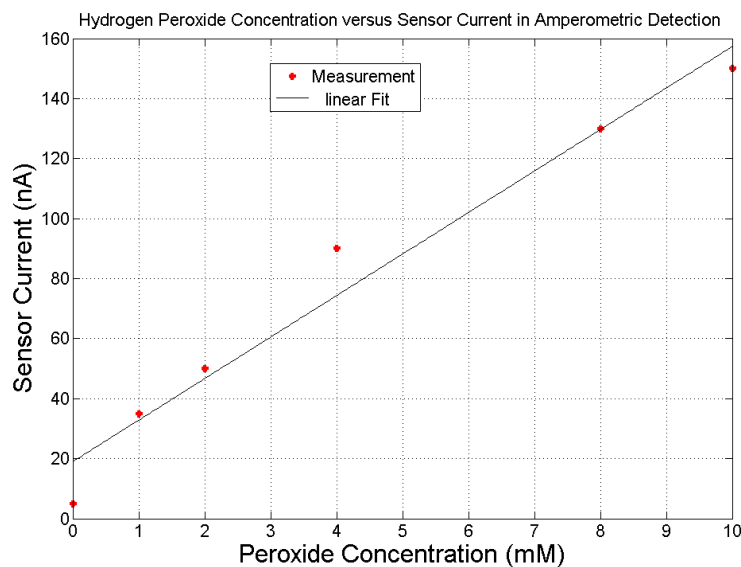


Figure 115 : Peroxide Detection using integrated
Potentiostat

The classical Potentiostat was also designed on the same die to compare its performance to the current-conveyor design. Similar electrical measurements on it showed similar response in its working. However, this design is capable of doing CVs due to the bipolar current between WE and CE, which is not possible in the current fed design due to its topology. Nonetheless, amperometric mode provides less capacitive noise and is actually the more appropriate method to be used in vivo detection for many reasons [81]. The classical design requires large area due to large integrated resistors. Even moderate resistors of 50Kilo-Ohm occupy a large chip area. Hence, this design is not ideal for actual implants.

6.5 Ultra-Low Power Control Circuit

The second version of the control circuit was designed¹⁵ to decrease the power consumption of the circuit to be able to power the implantable system based on electromagnetic powering and communication schemes. Quite a few relevant useful functionalities are also added to this circuit to make the implantable system more flexible. A supply independent reference voltage generator is used to control cell potential. A TIA with a capacitor with programmable switch rate is used to measure current. An ADC is used to digitize the current [173]. The block diagram of the system is shown in Figure 116.

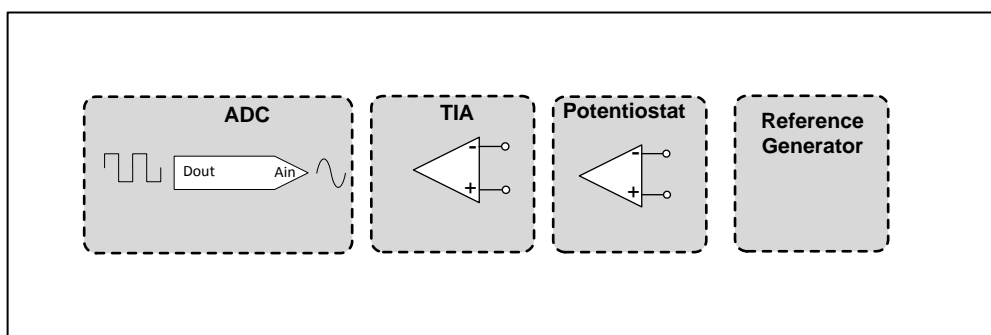


Figure 116 : Control Circuit Design-Version-2

This system was designed in 0.18 μ CMOS technology from TSMC offered through the MOSIS service. The system showed improvement in many factors compared with the version 1. The Potentiostat readings for glucose sensing are shown in Figure 117. The Potentiostat compared very well to a commercial Potentiostat while consuming much less power (3 micro Watts) compared to version 1 (20 micro Watts minimum).

¹⁵ By Meisam Honarvar Nazari and Muhammad Mujeeb-U-Rahman.

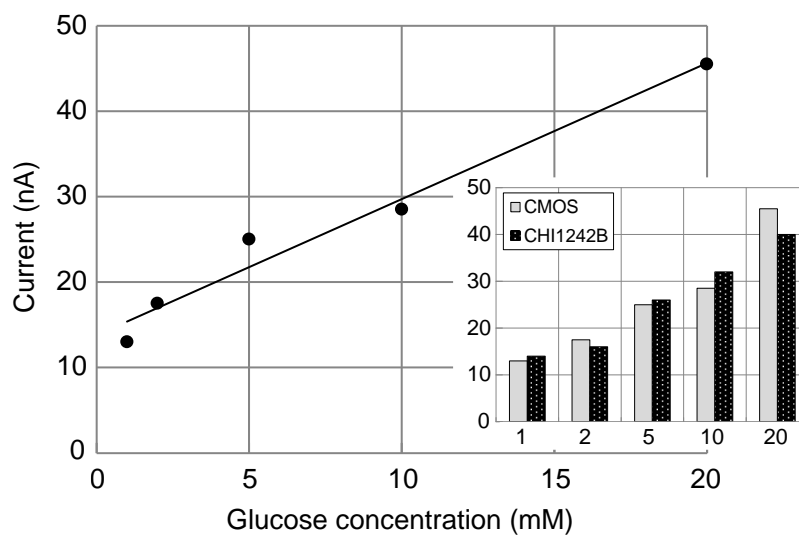


Figure 117 : Glucose Sensing using CMOS and a commercial Potentiostat

6.6 Summary

In this chapter, the design of the sensor control circuit is discussed. The control circuit consists of a low-power Potentiostat and a readout circuit. For completely integrated systems, a reference voltage generator is also needed. Two different low-power designs and their successful operation are discussed using ultra-small electrochemical sensor measurements.

Chapter 7 Conclusion and Future Directions

The requirement of designing a CMOS based integrated system lead us into testing different options for achieving different functional subsystems. The subsystems discussed in previous chapters were all integrated in different manners to achieve this. The design progression with time is shown by different versions of the integrated system.

7.1 Fully Integrated Systems

The actual design goal for this work was to create miniaturized fully functional integrated sensing platforms. The subsystems discussed in previous chapters were all integrated in different manners to achieve this. The integration in the beginning was crude but was refined with time. The progression of the integrated systems is shown by different versions that were made during this work.

7.1.1 Version 1

Initially, sensors were fabricated using standard Silicon based processing on separate dies and CMOS designs were done using standard commercial CMOS process. Integration was achieved by bonding these components together using epoxy and wire bonding. The resulting system is shown in Figure 118. This bonding was used to test if the individual subsystems perform adequately after integrated to other subsystems in the complete design.

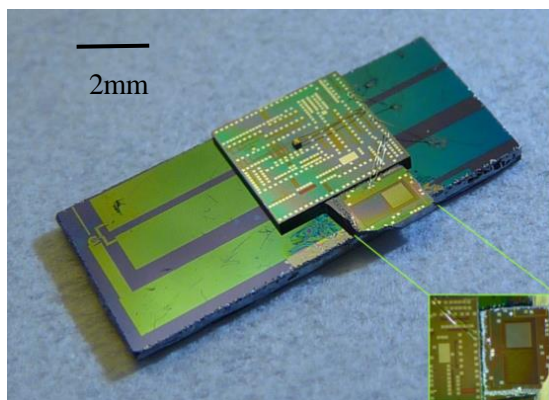


Figure 118 : Integrated Sensing Platform -Version I

7.1.2 Version 2

For this version, fully integrated systems were designed using a CMOS process. The system consists of a Photovoltaic power harvesting system, electrochemical sensor, sensor control and readout circuit, modulator and output driver as shown in Figure 119. Some electrical pads were still there to debug the system as well as to make connections with the VCSEL. The VCSEL had to be epoxy bonded on top of the dummy metal covering the circuit (to protect it from laser) using epoxy and was connected to the circuit using wire bonding. This system could be packaged afterwards by depositing thick biocompatible insulators to cover the bonding wires. The circuit was covered with top metal to minimize the effect of laser irradiation on transistor operation.

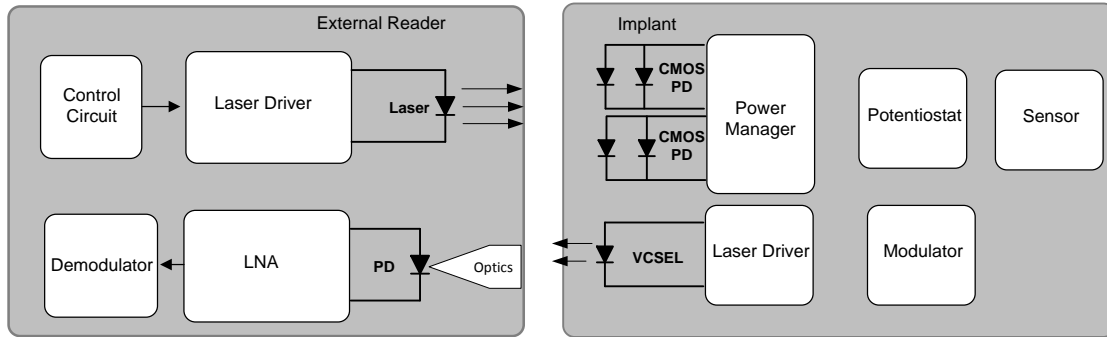


Figure 119 : schematic of Integrated System -Version II

The entire circuit takes less than 1mm^2 area which can be optimized even further. The die diagram is shown in Figure 120.

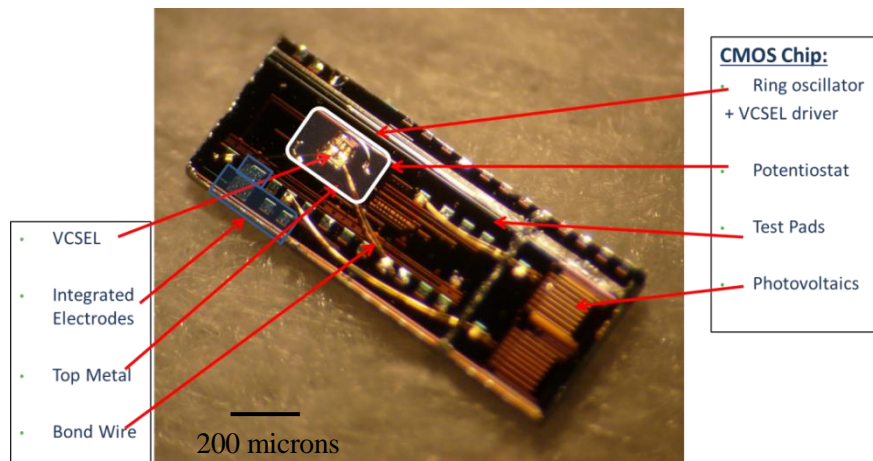


Figure 120 : CMOS integrated system-Version II

On this design, all the subsystems worked fine. However, the VCSEL was consuming too much power and needed an external power supply to run. This can be resolved by having on-chip capacitors for power storage and doing short pulses for data communication (while leaving the sensor always on to protect enzyme degradation). The other method can be to optically pump the VCSEL using a shorter wavelength laser and modulate it using its electrical contacts. For very slow data rates as in our application, this can be feasible. However, since the required data rates are very slow for most health sensing applications, we decided to replace the optical telemetry link with an electromagnetic link and use simple passive communication to save power.

7.1.3 Version 3

This system used electromagnetic resonant coupling for powering and communications. The system uses efficient on-chip power management (using CMOS based rectifiers, filtering and voltage regulation) , on-chip sensor, sensor control and readout circuit and forward and reverse telemetry using integrated resonator [173]. There are no off-chip components in this design. The CMOS circuit was designed with both wired (for testing) and completely wireless systems. The wired system was tested to test the functionality of individual subsystems. Since all the subsystems worked as per design, the wireless system was tested next and performed satisfactorily. System schematic with all integrated subsystems is shown in Figure 121.

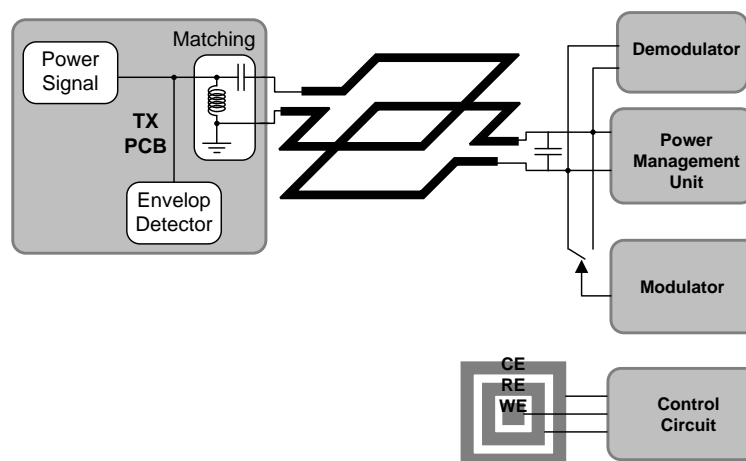


Figure 121 : Schematic of the Integrated System-Version

III

The system worked as per design and completely wireless operation was achieved using the passive backscatter communication scheme. The system was tested in water, isopropyl alcohol, PBS, and chicken skin and tissue (5mm thick). Post-processing was done to cover on-chip sensor electrodes with suitable materials (Pt, Ag) for electrochemical detection of metabolites. Post-processing was also used to coat the on-chip inductor was an implant grade insulating epoxy to prevent the degradation in system performance due to shift in its self-resonance frequency in high dielectric media (e.g. water, tissue). *In-situ* functionalization was used to obtain electrochemical glucose readings. A typical wireless measurement sequence is shown in Figure 122.

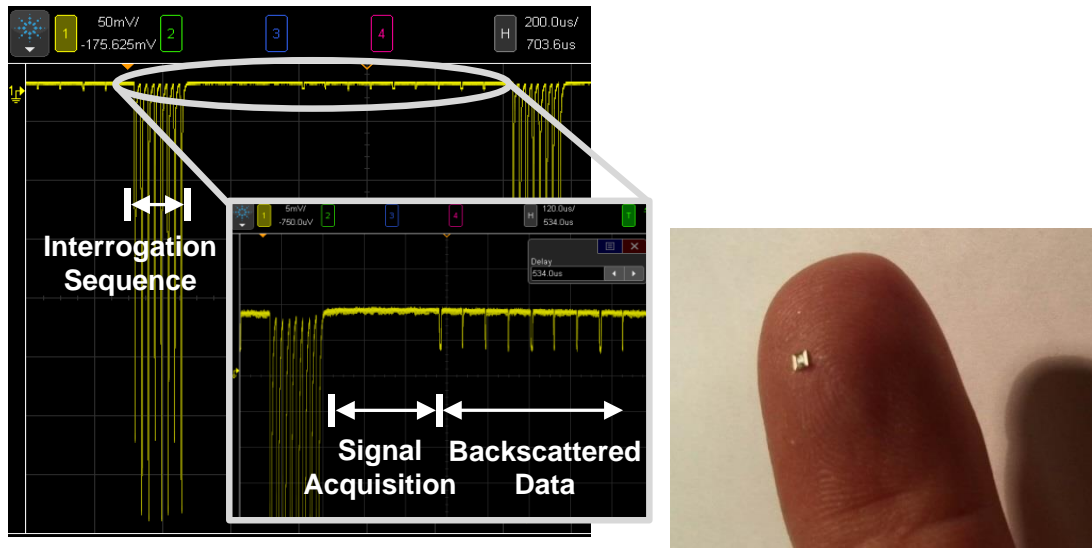


Figure 122 : Wireless Operation of the Integrated System

A comparison of our design with other works is provided in Table 13.

Table 13 Comparison with State-of-the-Art Implantable Glucose Sensors

Parameter	Design Version III	[41]	[21]
Power Consumption	6 μ W	110 μ W	3 μ W
Size	1.4mmx1.4mmx0.25mm	8mmx4mmx1mm	1cm diameter
Communication distance	1cm (5mm tissue, 5 mm air)	4cm (air)	15cm (air)
Glucose Range	0-20mM	0-40mM	0.05-1mM
Sample	Interstitial Fluid	Blood	Eye fluid
Signal Frequency	900 MHz (ISM band)	13.56MHz	1.8GHz
Fully Integrated*	Yes	No	No

* No off-chip components

7.2 Design Evolution

The design of the integrated system evolved during the course of this work, based upon different system level design optimizations. The design is evolving towards smaller and smaller implants

with shapes easier for implantation (e.g. cylindrical). Such shapes are better for implantation using needle based methods instead of surgical procedures. Higher frequency based designs can help towards achieving optimal performance for these shapes (e.g. by taking advantage of the largest dimension in the system). Furthermore, a combination of optical and electrical methods provides the toolset to select the right system for a particular shape and application. Hence, the techniques developed in this work can provide very useful tools for the future evolution of these systems for a diverse set of applications.

7.3 Conclusion

In this work, we showed the feasibility of building a miniaturized and completely wireless sensing platform for chronic applications *in-vivo*. Different options to achieve this goal had to be designed and tested as no data was available for device design at such small scales. The performance of different subsystems utilizing different techniques was compared under realistic conditions and trade-offs in designing such systems were discovered. At the end, a completely wireless platform has been realized which achieves fully wireless operation in *in-vitro* solutions and *ex-vivo* tissue. The devices have been implanted and would soon be tested for *in-vivo* performance. We believe this system can become the basis of improved personal health care whereby personal health could be monitored continuously.

7.4 Original Contributions of this work

The original contributions of this work can be summarized as follows:

- To the best of our knowledge, this work is the first example of a completely integrated wireless sensing platform for health monitoring at the mm size scale.

- To the best of our knowledge, this work is the first example of CMOS integrated electrochemical sensors with in-situ functionalization for different applications.
- To the best of our knowledge, this is the first demonstration of optically powered integrated monitoring systems at this size scale.
- To the best of our knowledge, this work is first demonstration of electromagnetically powered fully integrated systems without any off-chip components, with mm dimensions, utilizing electromagnetic communication.

7.5 Work in Progress

There are many aspects of this research which are in progress to help expedite its applications for real-world applications. A brief overview of this work is given here to provide a perspective towards the future development of this technology.

7.5.1 Special Shapes

For making implantation easier and for some special applications, it is desirable to make the sensor in special shapes which are not conventionally available in standard CMOS process. These include rectangular and circular shapes as well as other polygonal shapes. This needs designing special antenna structures which can communicate more efficiently near the mm size scale. We are also working on laser cutting to be able to separate these odd-shaped designs from the main die.

7.5.2 Compensating lag between ISF and blood values

It has been shown that under most conditions, ISF measurements can be used to have a direct measure of blood glucose levels [214]. Under some very rapid changes, there can be a slight lag [215] which is reported to be as low as 5 minutes and as high as 15 minutes [215]. However, this can be mostly corrected using predictive algorithms. The further the device will be from the blood

supply, the greater will be the delay. However, due to the size scale of capillary bed and of our device, it will always be sufficiently close to the blood supply. Different models to compensate this lag have been discussed in the literature [216]. It has been shown that simple first order prediction can compensate for this. We are working on an adaptive algorithm which uses a basic mathematical model and then adapts itself with time based on user feedback. This is thought to help make the model suitable to a variety of people each having different metabolism and slightly different relationships between the ISF and blood glucose level.

7.5.3 Optimal Implantation Site

Selection of an appropriate implantation site is important to achieve full functionality of the implant. Usually, sensor size and the sensing application dictate where the sensor can be implanted. Understanding physiology is important to make an intelligent decision on this. For example, first implantations should be carried out in regions of minimum skin thickness so that the skin loss is minimal and alignment with the sensors can also be made easily. For glucose sensors, subcutaneous tissue is considered a good location and the commercial CGM systems' probe is inserted in subcutaneous tissue. The actual implantation procedure depends upon the location as the thickness of subcutaneous tissue varies for different parts of the body [217]. A comparison of different possible implantations is given in Table 14.

Table 14 Comparison of Different Implantation Sites

Site	Accuracy	Implantation	Lag	Risk	Reference
Intramuscular	Medium	Difficult	Medium	Low	-
subcutaneous	High	Normal	Low	High	CGM systems
subcutaneous	High	Easy	Low	Low	Wireless CGM
intravenous	V. High	V. Difficult	V. Low	V. High	-

7.5.4 Implantation Procedure

Initially, simple incision and placement procedures can be used for proper orientation of the implant to make alignment with external reader simpler. Later on, special location monitoring techniques can be used and implant can be simply injected similarly to a normal subcutaneous tissue.

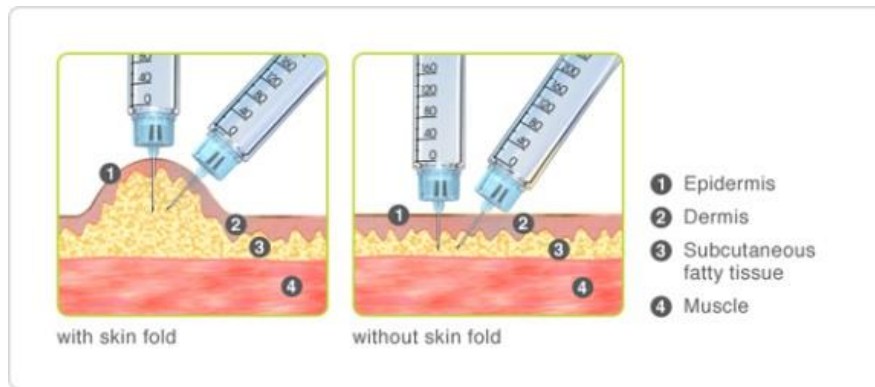


Figure 123 : Subcutaneous Injection Procedures [218]

Special procedures and special needles can be used to keep the desired orientation in the process. The technology for much bigger implants using this method has already been approved and these have been used for some time now (1-2mm diameter needles).



Figure 124 : Subcutaneous Implantation System [219]

7.5.5 Body Powered Implants

Glucose based biofuel cells are an active research area and were proposed to be able to power the implants using body's glucose supply [220]. Although, the generated voltage and power density are quite low for small scale device [221], Nanotechnology can be used along with cascading small cells to improve the technology and this may become a suitable technology soon. This, together with ambient powering (e.g. light), can be made to keep the sensor operational (can be optimized to near micro-watt range). Power harvesting can still be used for reliable operations if needed. Another method can be to power the implants using consumer electronics (e.g. cell phones). Both optical and electrical powering can be done this way, although this would need these devices to be in close proximity of the power source.

7.5.6 Enhancing Biocompatibility

The small size of our device decreases the foreign body response, as is evident from preliminary results from an in-vivo study of silicon dies (Figure 125) as only very thin microencapsulation was observed in both intramuscular and Intradermis implantations.

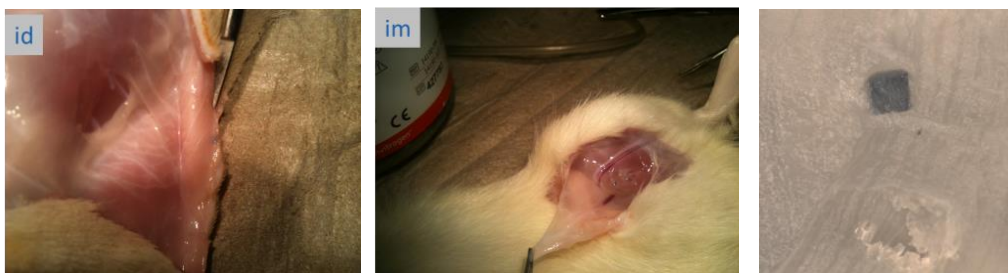


Figure 125 : Intramuscular and Intradermis implantation for 7 weeks in Wistar Rat

More active measures can be taken to improve biocompatibility. It has been reported before that the techniques of increasing vascularization can overcome the adverse effects (time lag and decrease in

analyte diffusion) due to foreign body response[222]. The effect of inflammation on changes in local tissue environment can be decreased by increasing vascularization near the device [223]. Neo-Angiogenesis has been shown to reverse this effect to some degree[224]. Another interesting point in literature is that foreign body reaction to porous implants is lower than that to solid implants[44]. Hence, we propose to create holes in the structure in any available area as shown in Figure 126.

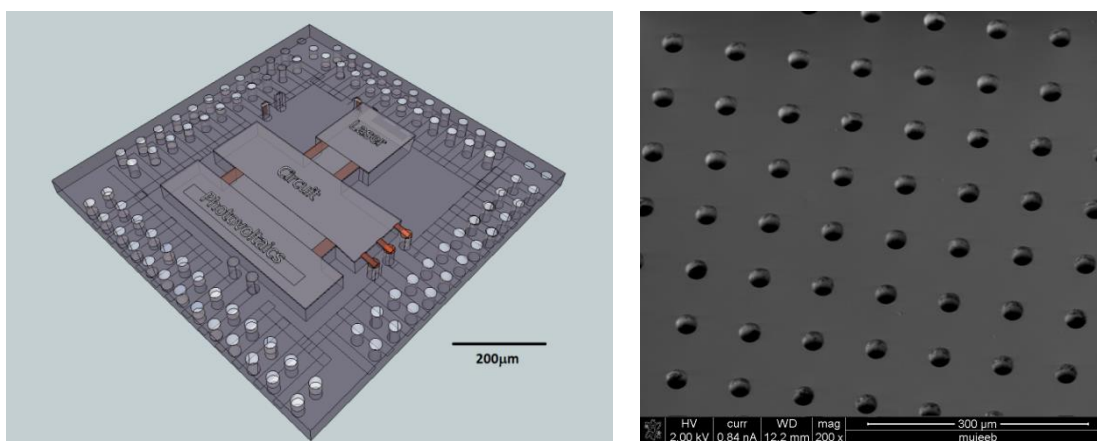


Figure 126 : Device with holes for improved Biocompatibility

We have also proposed an advanced method growing capillaries through the device to have vascularization through the sensor [225]. It has also been reported in literature [226] that local and controlled chronic heating can enhance angiogenesis as the body tries to increase blood perfusion in the area. Using our devices in-vivo within the safety limits actually makes this heating process natural and may help in achieving angiogenesis near the implant which improves the sensor functionality as discussed before. Also, optical methods can be used to enhance this angiogenesis by more controlled local heating. A combination of chemical and thermal angiogenesis may be very useful in applications using localized heating.

7.5.7 Sterilization

The implants have to be completely sterilized to avoid any adverse infectious reactions in the body. It has been shown in literature that a combination of chemical sterilization (e.g. in hydrogen peroxide), along with gamma irradiation, provided enough sterilization but only thermal method could achieve desired clinical sterilization [227]. Hence, pre-functionalization sterilization followed by clean processing is possibly the most practical method.

7.5.8 In-vivo Testing

In-vivo stability is more challenging than in-vitro stability [63] and presents a unique set of challenges. Careful design of experiment studies have to be done to get meaningful results. Some of the wireless sensors have recently been implanted in rats and no adverse inflammatory response has been noted in first 3 weeks. A detailed study would reveal the in-vivo system performance and will lead to iterative optimization. It has been shown that the implant behavior is quite unstable right after implantation until a thick encapsulation is formed around it in almost two weeks and then response becomes stable [228]. However, the small size can help make this process faster due to less local injury and less tissue irritation due to relative motion.

7.5.9 Future Applications

These integrated sensing systems can be used for many applications, both point-of-care diagnostics as well as long term applications [229]. Electrochemical detection in PCR can reduce the system complexity and cost and the use of nanopatterned electrodes are a very promising technique to eliminate the problems associated with the use of electrochemical sensors for conventional PCR based point-of-care systems. Also, a simple change in enzymatic chemistry allows tuning these systems for different applications. Table 15 shows some of the common applications.

Table 15 Some Common Enzymes and their Sensing Applications

Enzyme	Substrate	Application
Lactate Oxidase/Dehydrogenase	Lactate	Physical Stress Measurement
Cholesterol Oxidase	Cholesterol	Cholesterol Measurement
Alcohol Dehydrogenase	Alcohol	Alcohol Level Measurement

Also aptamer based detection scheme allows the use of these sensors for many applications where conventional sensing (e.g. antibody based sensing) have limited applicability. This opens a whole new area for these sensors for different applications.

7.5.10 Sensor Calibration

Calibrating the sensor is important as it relates the sensor output to actual levels of blood glucose. Single point calibration and multipoint calibration methods can be used for our devices. For completely linear sensors, single point calibration may suffice, but for most sensors, a multipoint calibration results in more accuracy. Moreover, as the sensor chemistry degrades (loss of enzymatic activity) with time, calibration is needed for accurate readings. Once calibrated, the sensor would be able to work for some time before recalibration is needed. Self-calibration is also possible whereby more than one sensor is implanted and the sensing software uses readings from all sensors to adjust the overall reading.

7.6 Software Development

A software based work engine is being developed which would allow easier data processing from sensor results to create calibration curves and to compare results with gold standard Clark error grid method. Similarly, software for readout subsystems is being developed for computers, tablets and smart phones to manage handling, display and processing of the results at different levels.

Chapter 8 Experimental Methods

This chapter is meant for providing details on the experimental techniques used in this work. This includes sensor fabrication, functionalization, and testing procedures.

8.1 Fabrication

In this section, details on sensor fabrication are provided both for planar and patterned sensors.

8.1.1 Planar Sensors

Planar electrochemical sensors can be fabricated on both substrate Silicon as well as any CMOS metal layers (most commonly the top metal layer). Substrate thinning was performed using a simple lapping machine along with SiC and diamond films. An Oxford HD ICP-CVD system is used to perform plasma enhanced chemical vapor deposition (PECVD) of thin silicon oxide layers. Operating parameters for this system are 350° C table temperature for isolation. Photolithography was performed using either an image reversal resist AZ5214E with inward tapered sidewalls or using lift-off resist LOR10A in conjunction with a positive resist such as S1813, after adjusting their viscosity to obtain desired resist thickness. Also, Microchem's spray photoresist were also used to obtain better coverage of non-planar CMOS surfaces. Electron beam deposition of metals was performed in an ebeam evaporator (either a CHA evaporator or a TES evaporator) to deposit a thin (10nm) layer of Ti followed by a relatively thick (100 nm) layer of Platinum (Pt). Heated PG Remover was used to perform lift-off. Aligned lithography was performed for Ag deposition (350nm) on one half of the samples (Pt reference electrodes are used in the other half of devices). Final photolithography was then performed using SU8 to insulate the contact lines from the solution and form a well for hydrogel immobilization later on. For sensors, on top metal layer, no SU8 insulation was used (CMOS provides inherent insulation), but SU8 wells were formed for

functionalization. Chlorine Plasma in a Unaxis RIE system was used to form a thin layer of AgCl on top of the Ag film without the need of complex wet processing. Alternatively, dipping in strong chloride solutions was also found to be effective in achieving chlorination by electroless radical displacement reaction. Simple Pt RE was also used for some sensors. X-ray analysis was done using EDAX in an FEI-Sirion SEM to verify the chemical nature of this structure. The integrated sensors on CMOS are shown in Figure 127.

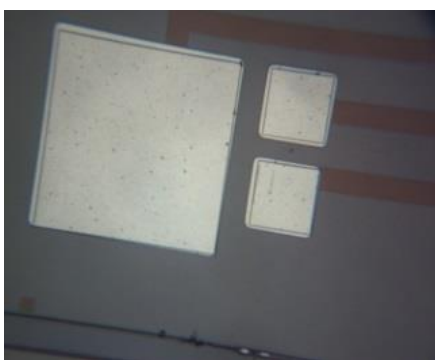


Figure 127 : An example integrated sensor on CMOS (Pt RE)

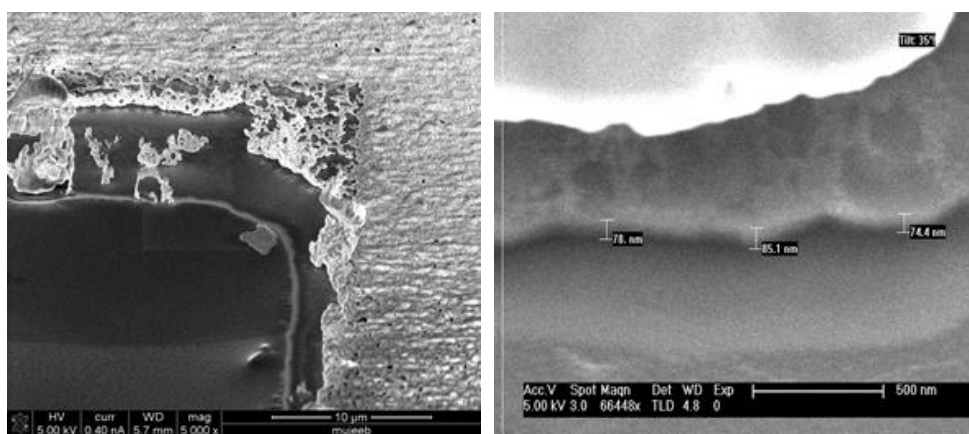


Figure 128 : SEM of AgCl/Ag RE interface

Electrochemical Oxidation of Pt to get Pt/PtO_x RE was performed using concentration Sulphuric Acid solutions and Cyclic Voltamograms to 2V vs. Ag/AgCl RE, as shown in Figure 129. The decrease in current was used as a measure of surface passivation. Experiments were repeated to find the validity of the process.

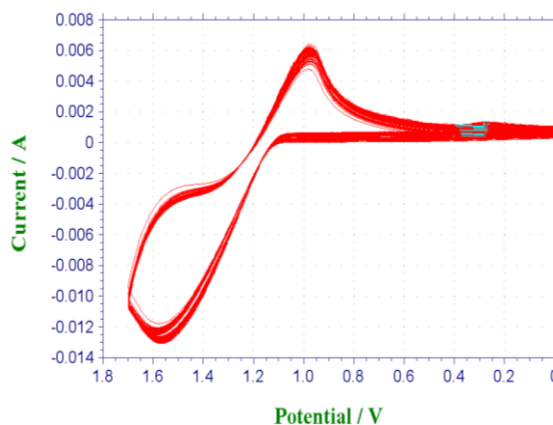


Figure 129 : Electrochemical Oxidation of Platinum in Sulphuric Acid Solution (0.1M) in PBS.

8.1.2 Micro/Nanopatterned Sensors

We used a CMOS compatible fabrication method using simple lithographic and vacuum based techniques which are carefully optimized for fabricating very high surface area nanopatterned electrodes with very precise control on the electrode properties. A step-by-step detail of fabrication process is provided for interested reader.

8.1.2.1 Lithography

For nanoscale patterning using electron-beam lithography, PMMA 950 A4 was used to achieve clean lift-off while still achieving the required resolution. The resist was spun at 4000 rpm for 1 minute, followed by a 180° C bake for 5 minutes. A dose of 1200 μ c/cm² was then used to write the pattern in a Leica EBPG5000+ system. Patterns were developed in 1:3 solution of MIBK and IPA

for 20 seconds followed by a deionized water rinse. A 50nm alumina mask was sputter coated in a Temescal TES BJD-1800 DC reactive sputter system by depositing Aluminum in presence of Oxygen plasma for 5 minutes. Mask liftoff was performed in dichloromethane in an ultrasonic bath for 2 minutes. Alternatively, ma-N resist was also used for electron beam lithography. Deep-UV lithography is also a viable alternative to avoid the use of high energy electron beams which can cause damages to the underlying substrate which may have other system elements e.g. circuits on the same substrate.

8.1.2.2 Etching

The room-temperature silicon plasma etch recipe described by Henry et al. [230, 2009 .34] was iteratively optimized to achieve uniform etch depth for all pillar widths and uniform sidewall roughness as shown in Figure 130.

Table 16 ICP-RIE Parameters for Si etching

Temperature (C)	ICP Power (Watts)	RIE Power (Watts)	Chamber Pressure (mTorr)	SF6 Flow rate(sccm)	C4F8 Flow Rate(sccm)
15	1300	23	10	32	53

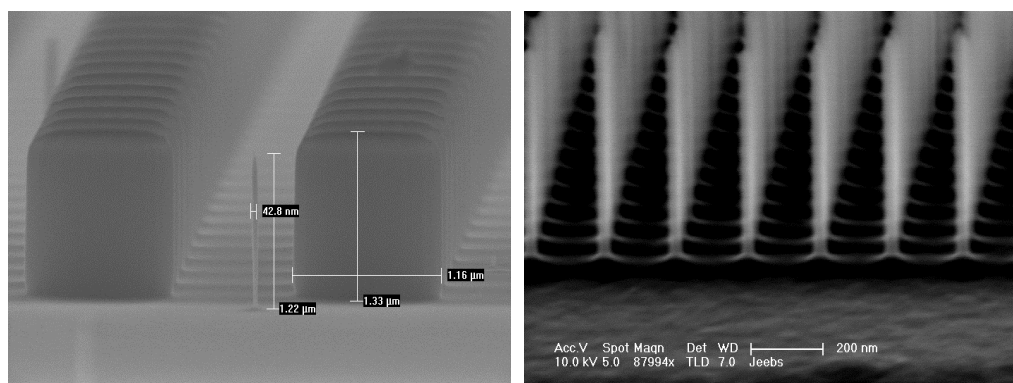


Figure 130 : SEM image of ICP-RIE plasma-etched Si nanopillars

Repetitive liquid testing was done on these devices to test their mechanical strength. This showed no destructive effect on these devices and these retained their shape. For devices with higher aspect ratios (more than 20), we observed bending and fracturing of the pillars as shown in Figure 131.

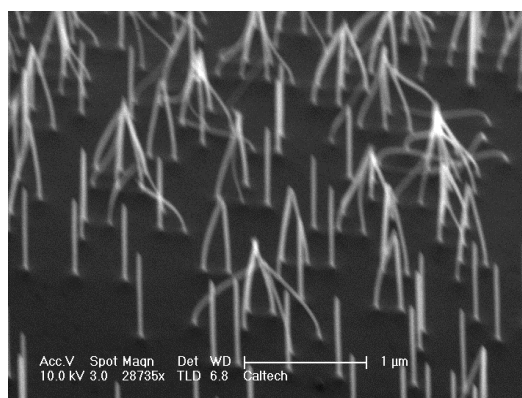


Figure 131 : Si Pillar bending due to capillary forces (aspect ratio of ~25)

8.1.2.3 Insulation

Both Thermal and PECVD deposited oxides showed conformal coverage and electrical insulation.

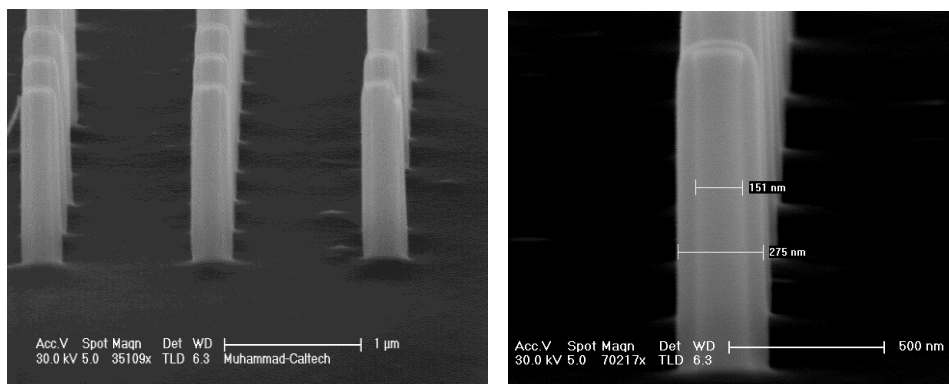


Figure 132 : Nanopillar Array after thermal oxidation

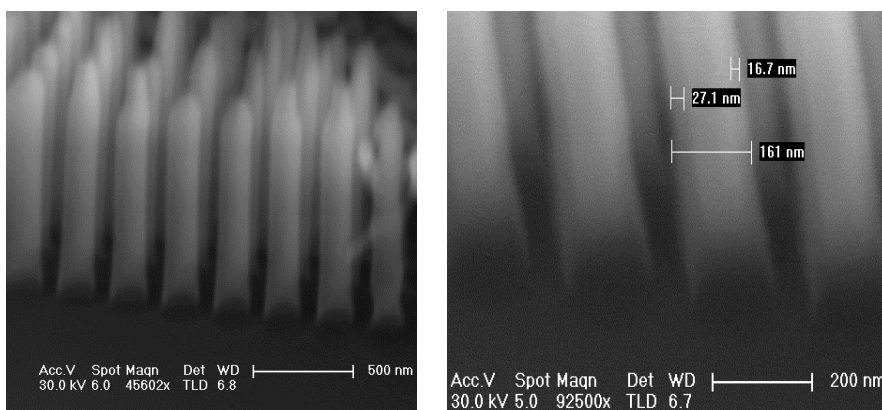


Figure 133 : Nanopillars after PECVD Passivation coating

8.1.2.4 Metal Deposition

Electron beam deposition was performed on a CHA electron beam deposition system at 2×10^{-6} torr. The sample substrate was placed on a rotating stage and various low impedance metals such as Au and Pt were used as material sources. A 5 nm Ti adhesion layer was evaporated at 0.5 \AA/s and subsequently an Au or Pt layer of 50 nm or 100 nm was evaporated at 1 \AA/s .

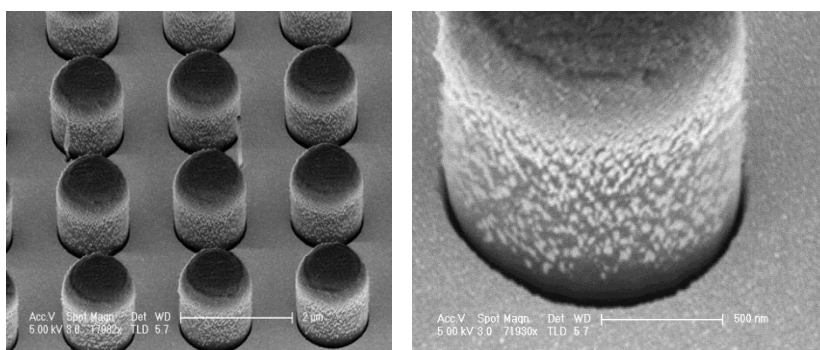


Figure 134 : Nanopillars after electron beam evaporation metal coating

Sputter deposition was used to obtain more conformal coatings. High density Argon plasma of 20 millitorr was used to increase the isotropy of the deposition. Again a 5 nm Ti adhesion layer was first DC sputtered and then 50 nm or 100 nm Au or Pt films were DC sputtered. The thin film layer grew a consistent thickness on the top, side, and base of the pillars and substrate as show in Figure 135 and 136.

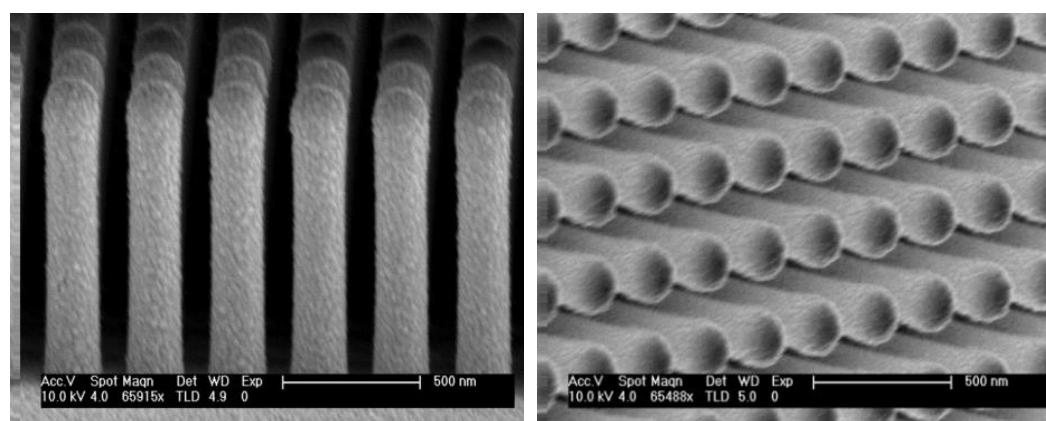


Figure 135 : Nanopillars after sputter coating of 50nm of Au

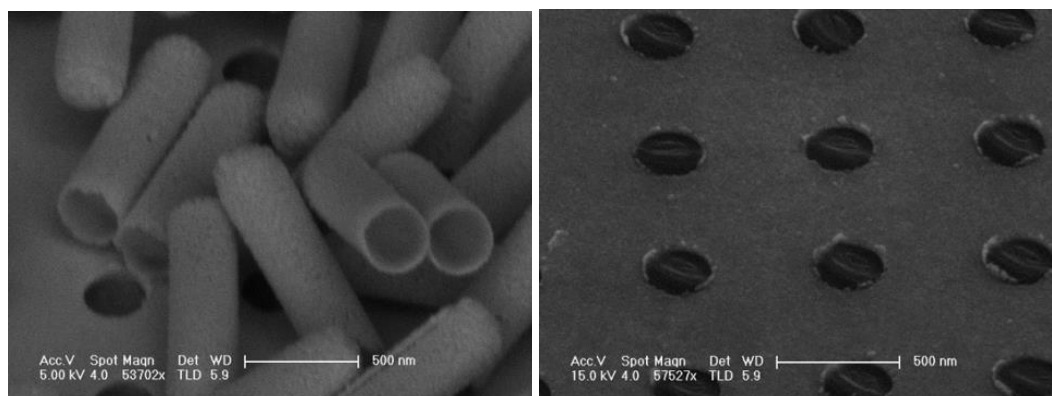


Figure 136 : Confirmation of coating on pillars' interface with the planar surface

Ion beam induced deposition of Pt was also performed using an FEI Nova 600 Nanolab ion beam source. 100 nm thick depositions were aligned directly over the pillar array electrodes. EDS analysis in an FEI Sition 200 SEM/EDAX machine was used to confirm the composition of deposited layer.

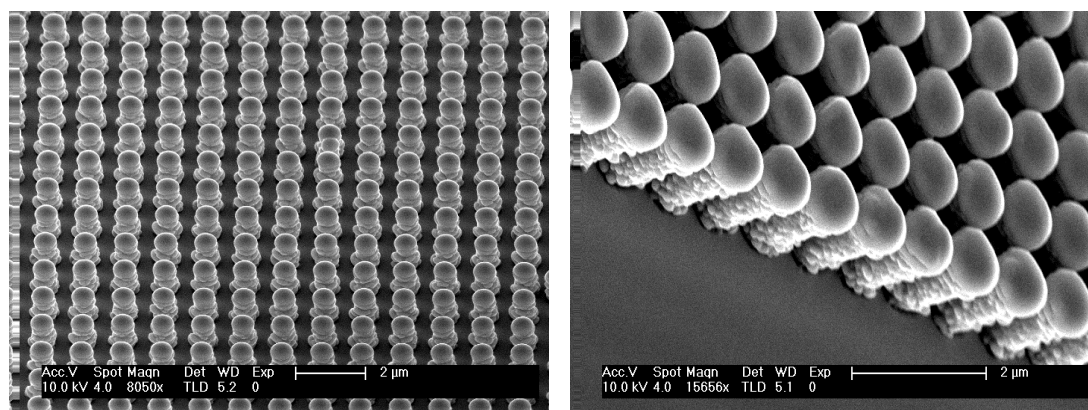


Figure 137 : Nanopillars after ion beam induced metal coating

8.1.2.5 Polymer Encapsulation

This polymer layers allow a well structure for immobilization of the sensor chemistry. Thin (approximately 2 μ m) SU8 for this purpose was used and the results are shown in Figure 138.

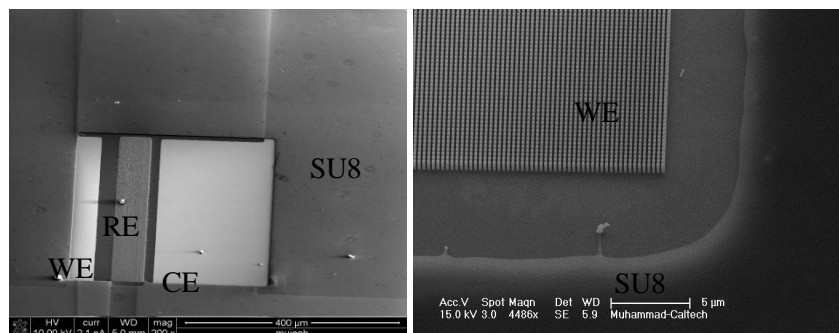


Figure 138 : SU8 Encapsulation around sensors

8.1.3 Nano sensors on CMOS

The Pad structure of the CMOS device was studied to find the thickness of different layers as the data was not available from MOSIS on this particular process. The results are shown in Figure 139.

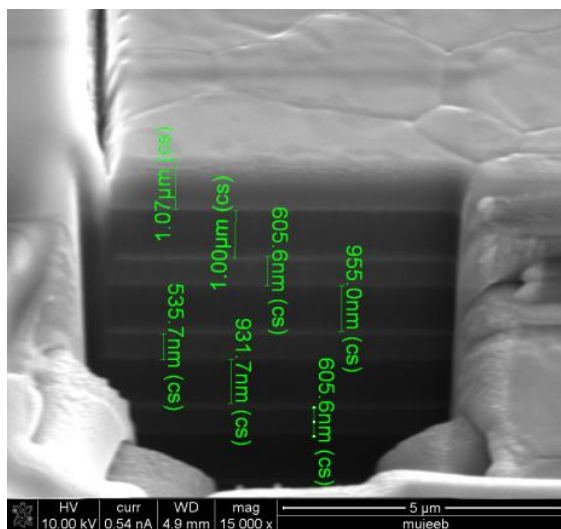


Figure 139 : Pad Stack in TSMC 250nm CMOS Process

Afterwards, nanopatterning was performed on the CMOS pillars using electron beam lithography over a wide range of aspect ratios. Etching was performed using a combination of dilute bases (e.g. TMAH) and Chlorine based plasma (Cl_2 : BCL_3). More recently, we started developing a hydrogen

bromide based etch with CH₄ passivation for better sidewall roughness control in an ICP-RIE Plasma instrument.

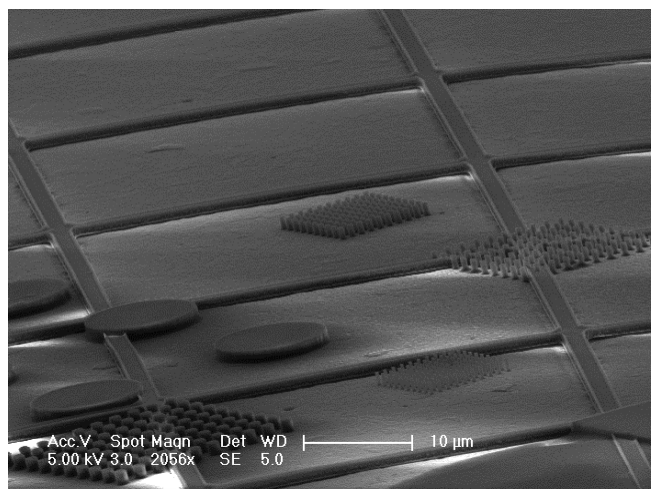


Figure 140 : Nanopyllar Arrays on top Aluminum Pads of CMOS

8.2 Sensor Functionalization

Sensors were functionalized by encapsulating the enzymes in a Bovine Serum Albumin (BSA) based hydrogel coating on the sensor electrodes. This immobilization was done in situ using techniques by adopting the protocol in [99]. The enzyme solution was made in PBS of pH similar to blood (7.4). The hydrogel used was based upon Bovine Serum Albumin (BSA). Glutaraldehyde (25% solution) was further diluted in PBS and used as a crosslinking agent for the hydrogel. BSA solution was made in PBS and the enzyme solution was added to it. Nanodrop 2000c was used to confirm the concentrations of enzyme in the resulting solution. Glutaraldehyde solution was added to this solution and the resulting mixture was pipetted carefully on the electrochemical sensor. The device was left at room temperature for five minutes to let the gel form and was constantly observed

under a microscope during this process. The sensor was then soaked in PBS for an hour to let any unbound enzyme and BSA dissolve and result in stable gel chemistry.

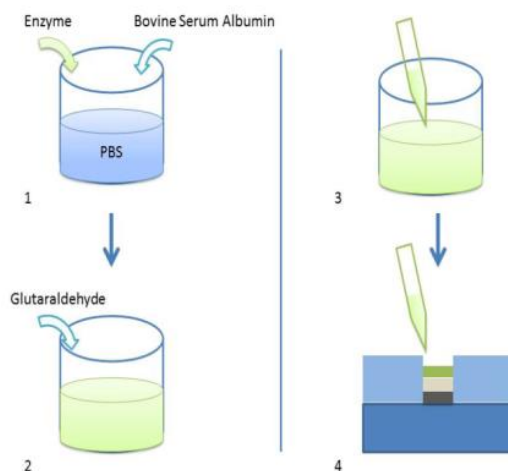


Figure 141 : Hydrogel Immobilization Procedure

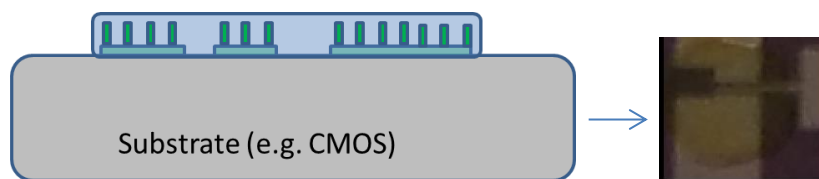


Figure 142 : Sensor Functionalization using Hydrogel

8.3 Sensor Cleaning

Rigorous cleaning of the sensors was found to be very helpful in providing more repeatable and stable results. It was important for both Pt and Au based sensors. Electrochemical and Chemical cleaning procedures were performed using Acids (Sulphuric Acid), Bases (NaOH) and Salts (KCl, PBS). As an example, there were some random peaks in the Au sensors before any DNA was

attached to the surface. However, after rigorous cleaning, those peaks disappeared and DNA immobilization provided very clear and distinct redox peak due to attached methylene blue.

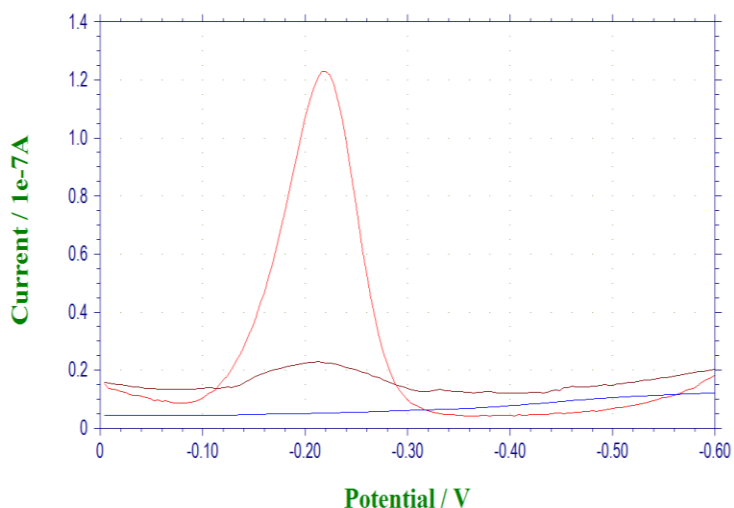


Figure 143 : Electrochemical Cleaning of Au Electrodes

8.4 Nucleic Acid Functionalization

DNA sensors were functionalized by soaking the electrodes in the appropriate solution (e.g. thiol and methylene blue functionalized single stranded probe DNA) or by pipetting the solution on the electrodes covered with a glass coverslip to minimize evaporation. The probe DNA consisted of 17 strands and have a methylene blue redox molecule attached at its 5' end and a C6 thiol at its 3'-end similar to the one used in [112]. The protocol was modified a bit for our application. The ssDNA probe was dissolved in PBS solution (pH 7.4) and its concentration was measured using a Nanodrop 2000c spectrophotometer. Tris(2-carboxyethyl)phosphine (TCEP) solution was also made in PBS and was mixed in the DNA solution to reduce any disulfide bonds in the DNA solution. The

solution was left at room temperature for 30 minutes to complete this reduction. The DNA was then diluted with PBS to achieve proper probe concentrations (typically 100nM.) The sensors were then immersed in this solution for three hours. Then the sensors were immersed in a 2mM mercaptohexanol solution for six hours to form a back-filling self-assembled monolayer (SAM) to minimize the formation of direct bonds between any target DNA and gold electrodes. Finally, these electrodes were used in the standard electrochemical cell for testing. Target DNA solution was made by dissolving it in PBS, measuring the resulting concentration and diluting it to get a concentration of 2 μ M. Controlled amounts (100 μ l) of this target DNA solution were then added to the background PBS solution to result in the overall target concentration to be 100 nM in the total solution. Square Wave voltammetry was performed before and after hybridization. For Protein (e.g. Insulin) sensing, the same procedure as above was used with the Nucleic Acid sequence (aptamer) given in literature [114]. 1mM Human Insulin solution was made using 1mM HCl as the background medium. This lower concentration of acid was used to minimize its effect on the solution pH during testing. For short term Insulin storage (at -20C) and testing, this solution provided adequate performance. Again sensors were used in electrochemical cell and solution was spiked with insulin for detection.

8.5 Sensor Testing

Sensors were assembled into different formats including a standard USB adaptor or on PCBs or flexible wires which could be connected to the USB adaptor for easy connection (Figure 144)

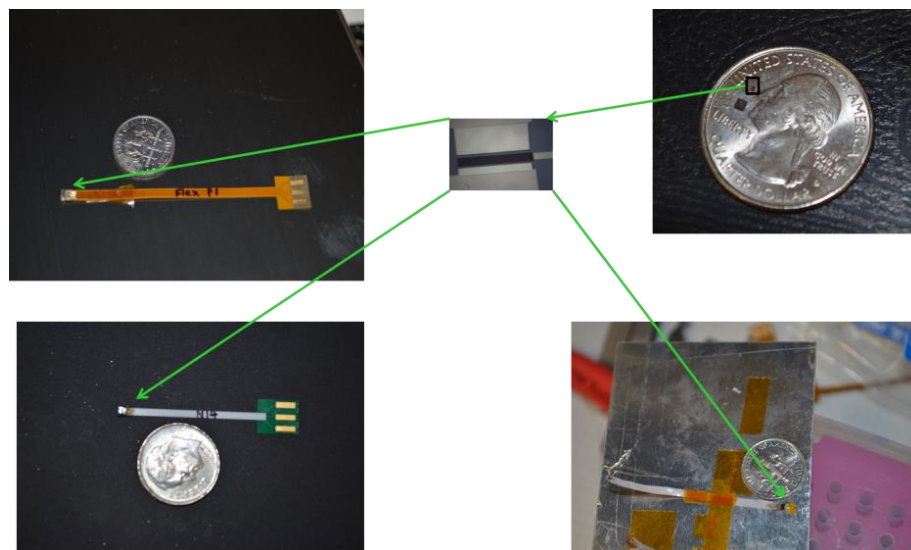


Figure 144 : Sensor Packaging for Wired Testing

Sensor assembly was then immersed in a beaker for electrochemical testing. Alternatively, solution droplets were placed on the sensor area for detection as well. In initial versions, sensors themselves were designed on silicon to have contact pads which could fit in a standard USB female connector.

Sensors were connected to a CH Instruments (model 7051D or 1242B) potentiostat or a custom CMOS integrated potentiostat to make the measurements. The electrochemical test setup consisted of a glass cell with a cell stand on a programmable hot plate/stirrer. The sensing part was then immersed in a solution or a droplet was placed on the sensor. A computer-controlled syringe pump (NE-300) was used to introduce small volumes of test solutions in the cell. The solution was spiked with different concentrations of test samples and electrochemical data was measured (using many techniques including cyclic voltammetry, chronoamperometry, impedance spectroscopy, constant potential electrolysis, and impedance-potential curves). For some experiments, this was done on a

hot plate to get measurements at body temperature. Phosphate Buffered Saline was used as background solution. Experiments were also carried out using serum and whole blood from mice.

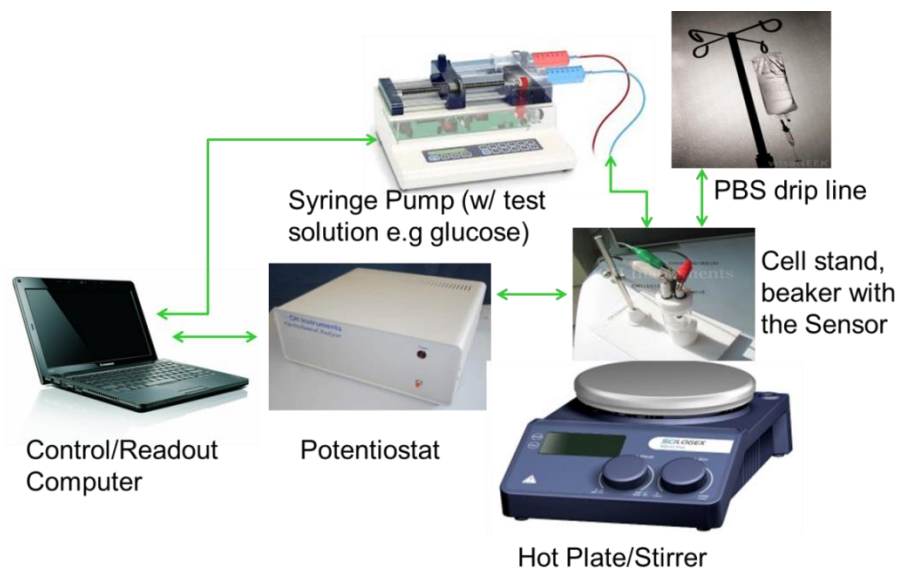


Figure 145 : Sensor Testing Setup

Packaged sensors were used to do simple implantation studies as a reference for advanced studies.



Figure 146 : Implantation Study in Rats

The study provided useful insights into the testing procedures and the test setup is currently being pursued for more detailed studies in coming weeks.

APPENDIX I COMSOL Simulations

Effect of different electrode geometries was simulated using electrochemistry and Chemical Reaction toolboxes of COMSOL¹⁶. Result of a typical simulation with a sweep of working electrode sizes is shown in Figure 147.

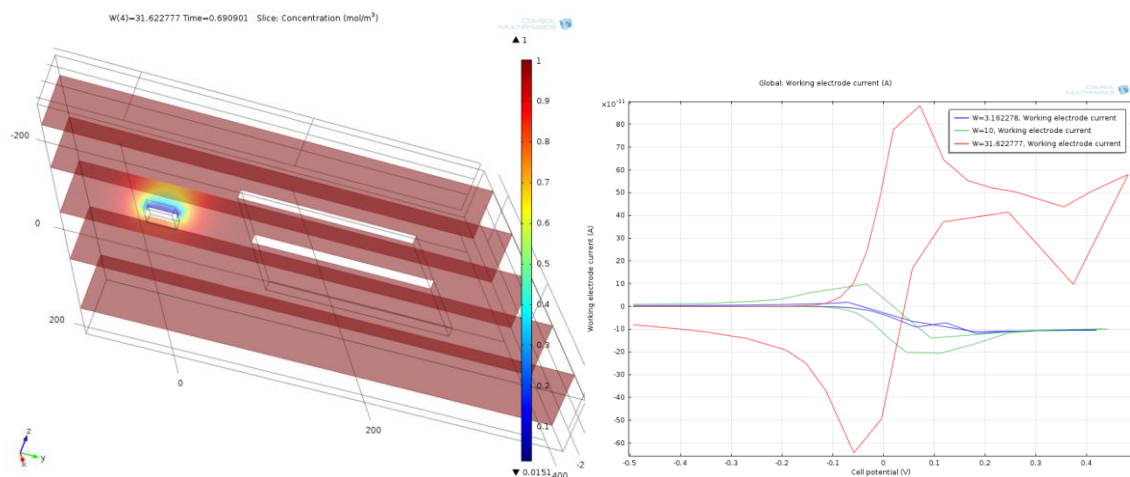


Figure 147 : Simulation of Planar Sensors of Different Geometries

Simulations were also performed for nanopatterned sensors to compare their performance and for understanding the role of pillar packing in sensor response. Results of one such simulation are shown in Figure 148. Results show that the nanopatterned sensors have less ‘hysteresis’ in their CV and the response is sharper. Later experimental work showed that this is indeed the case (Chapter 3).

¹⁶ Done by Muhammad Mujeeb-U-Rahman and Mehmet Sencan.

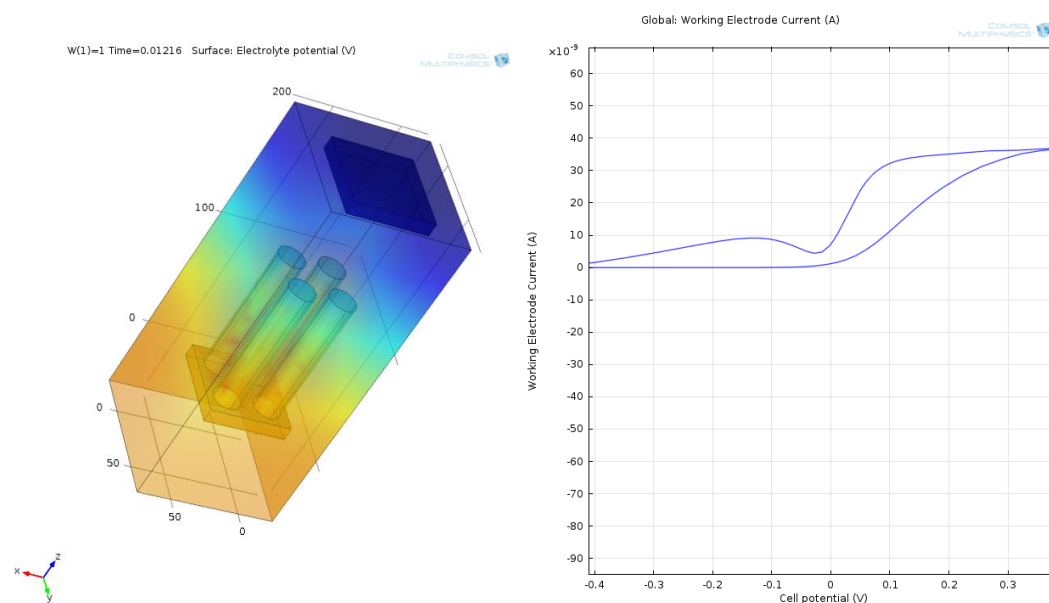


Figure 148 : Pillar array and corresponding CV, in COMSOL

Inductor Design was also studied using COMSOL modeling¹⁷. Results for one layer (case a, $L=1.6\text{nH}$), for two layers with currents in opposite directions (case b, $L=0.85\text{nH}$), and for three layers (case c, $L=1.61\text{nH}$) are shown in Figure 149.

¹⁷ Study done by Muhammad Mujeeb-U-Rahmand and Cipriano Romero.

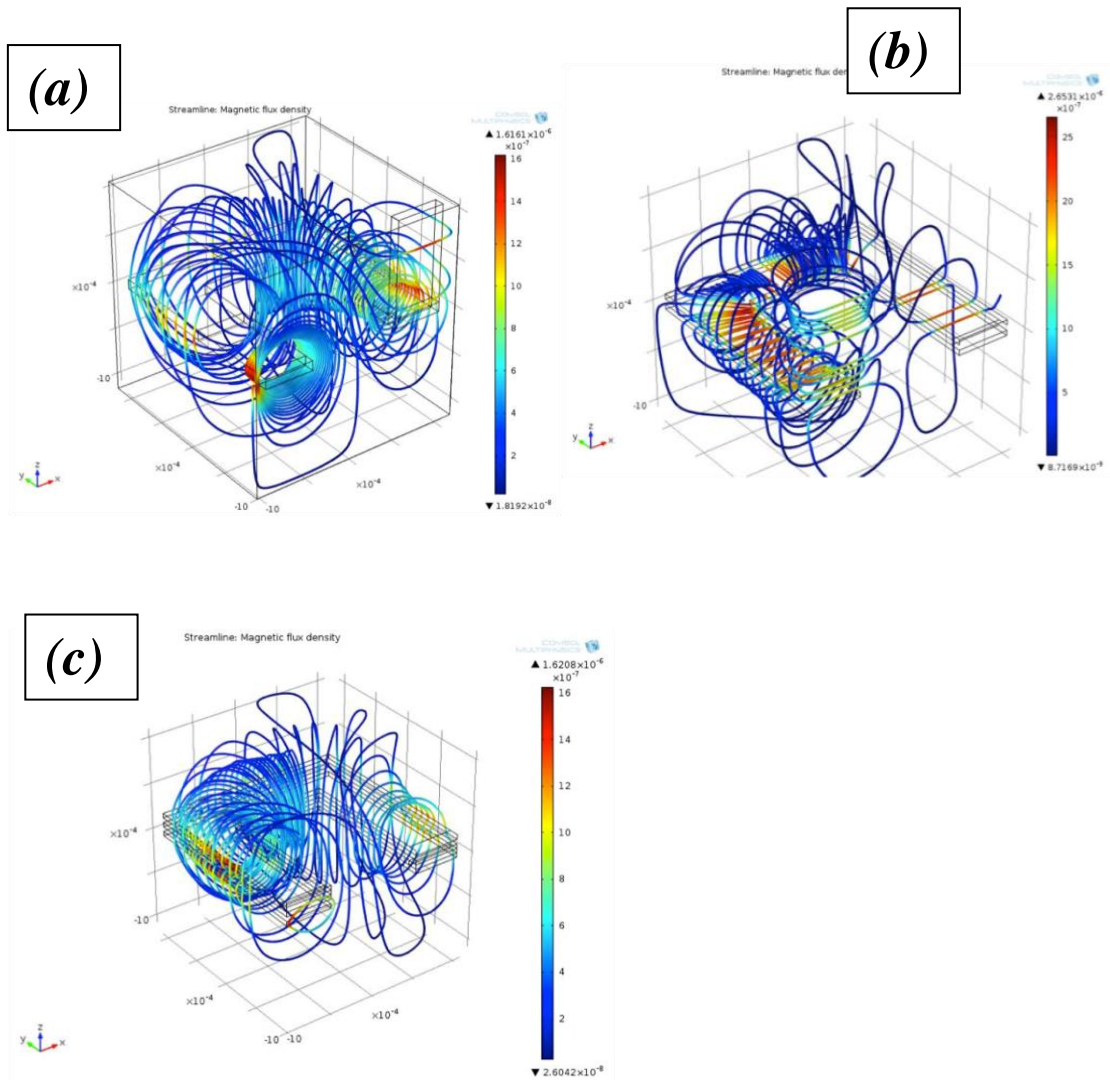


Figure 149 : COMSOL Simulations of Planar Inductors

Magnetic coupling simulations revealed that more number of turns (long coil), higher frequency, and just sufficient width (to allow for more turns) are desired (in air).

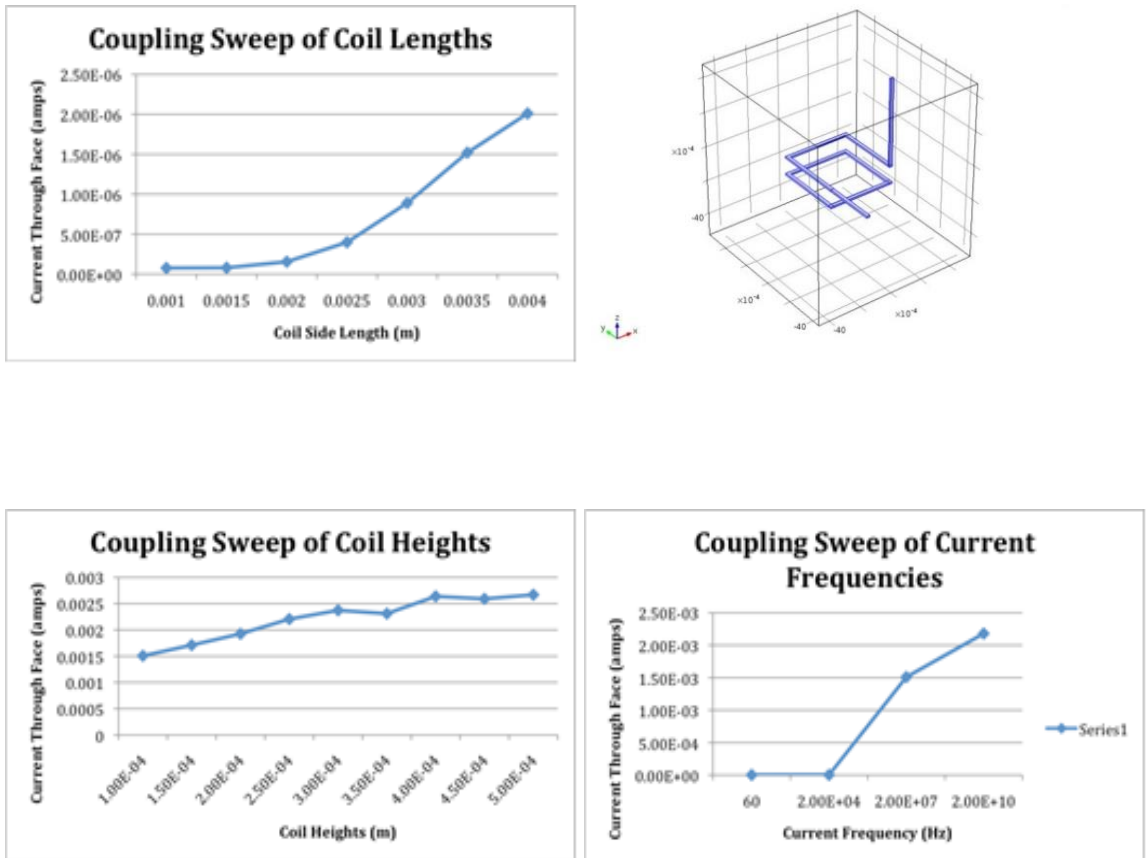


Figure 150 : Simulation of Coupling between two coils

APPENDIX II IMMOBILIZATION

Experiments were performed with both GOx and GDH and the functionalization chemistry at each step in the functionalization protocol was tested to make sure the enzyme stays active during the entire process and afterwards. Spectrophotometry was used extensively for this purpose.

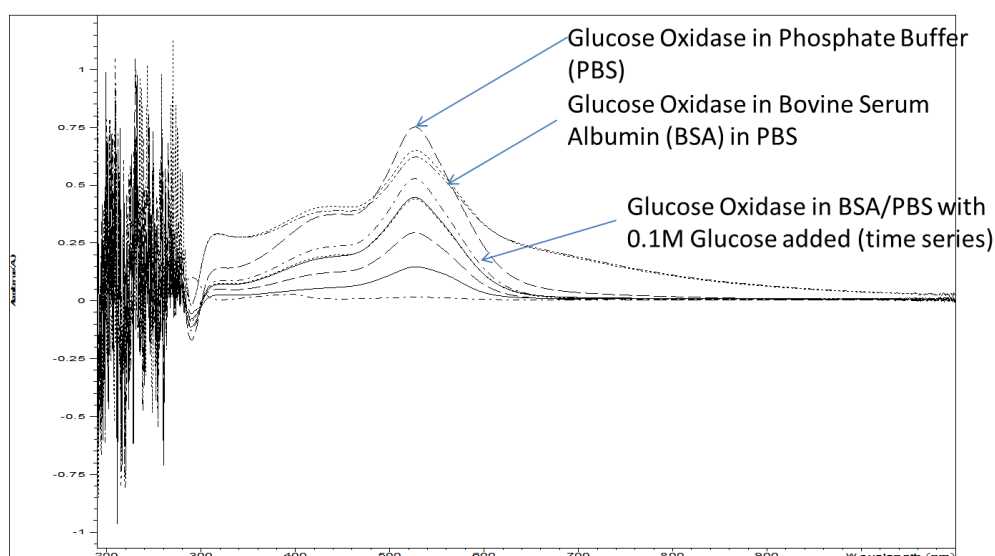


Figure 151 : Spectrophotometric Testing of Immobilization Chemistry

This data was used to optimize the immobilization procedure by keeping all the conditions within the safe limits for the immobilization chemistry.

Data on thermal stability of GOx is available in literature, but not for GDH. Hence, thermal cycling and longevity tests were conducted for GDH. Our results suggested that GDH-FAD is pretty stable for wide temperature range and also stays active for a long time (total 6 months testing duration was used) and the spectrophotometric results are shown in the following figures.

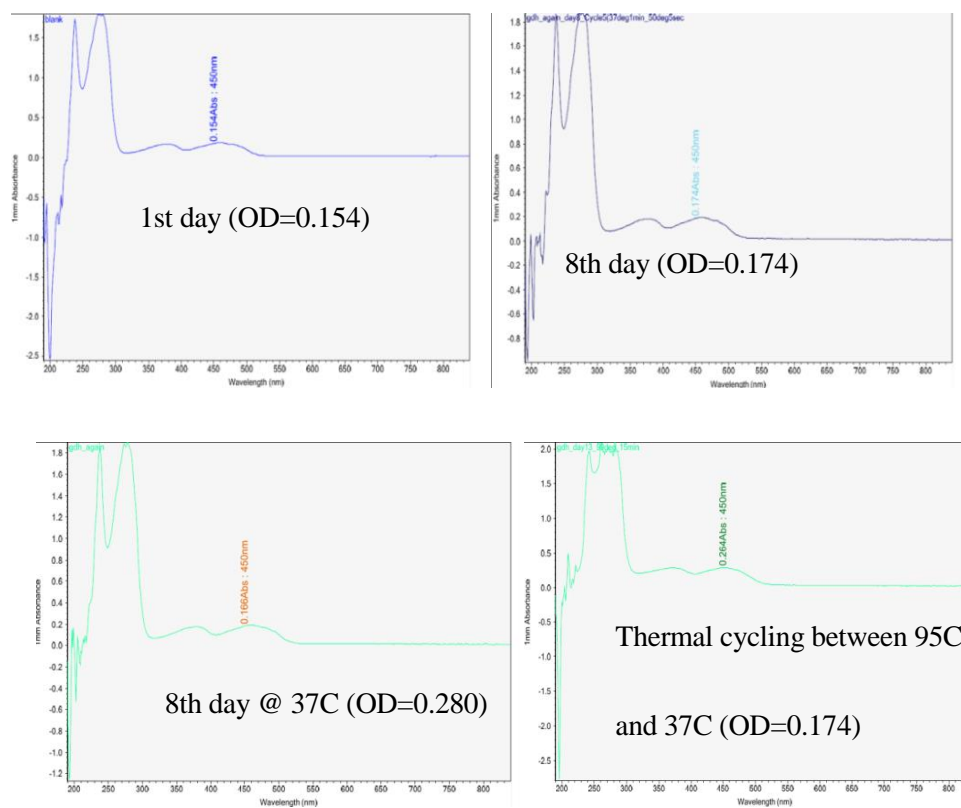


Figure 152 : GDH Thermal Cycling Test

Glucose activity was measured by a change in the absorption near 420nm after glucose addition.

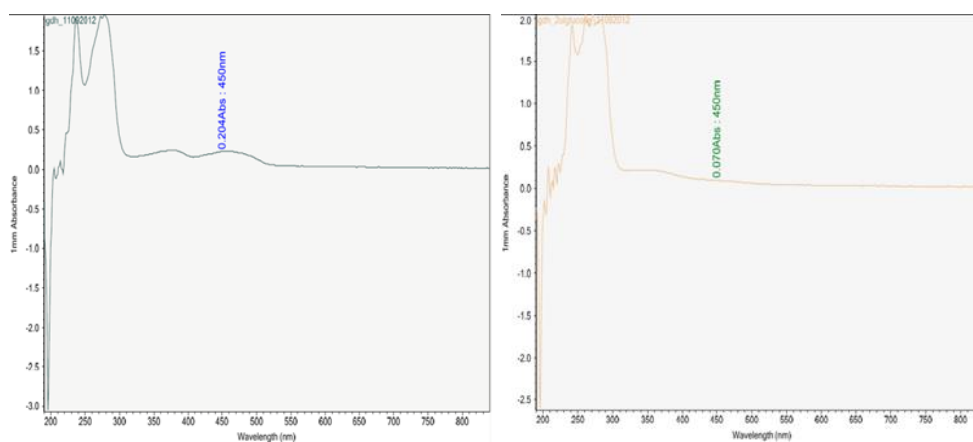


Figure 153 : Glucose sensing activity of GDH after 1 month

APPENDIX III Photovoltaic Efficiency and FF Calculations

Optical Powering:

Standard CMOS

Efficiency calculations: spot size (1mmx6mm), PV area=100umx100um

Power on the PV area (fraction of laser illuminating the diode)= $0.8 \times 8.5 \times 10^{-4}$

For device d1, Effective Efficiency= $(0.7 \times 0.7 \times 1.5 \times 25 \times 10^{-6}) / (0.8 \times 8.5 \times 10^{-4}) = 13.5$ percent

With tissue, Efficiency= $(0.7 \times 0.7 \times 1.2 \times 7 \times 10^{-6}) / (0.8 \times 8.5 \times 10^{-4}) = 3$ percent

Apparent Efficiency (without considering spot size) = $(P_m / 0.8 \text{ Watts}) \times 100$

The apparent efficiency is around 0.0001% (0.95Vx18uA is the maximum power point)

SOI devices

With Shutter

215 microampere * 2.95 volts is 634 microwatts over a 250 micron * 250 micron array of 4 diodes.

Resulting energy density is 10.144 kW/m². The most focused laser is (.8 watts)/(2mm * 4mm) = 100 kW/m². Hence, 10.14/100 gives a 10.14% conversion efficiency.

without the shutter

The PV current is 51 microamps and voltage is 2.91 volts. 51 microampere * 2.91 volts is 150 microwatts over a 250 micron * 250 micron array of 4 panels results in power density of 2.4 kW/m². The unfocused laser has power density of (.8 watts)/(3mm * 1cm) = 25000 W/m². Ratios of both power densities provide the efficiency of the cell 2.5kW/25kW results in 9.6% efficiency.

Thermal Capacity of Silicon Membranes in SOI

Rough calculation for membrane absorption (1mmx1mm membrane for 0.5mmx0.5mm Si PV cell)

$$(0.2 \text{ microns} * 1 \text{ mm} * 1 \text{ mm}) * (2.3 \text{ g/cm}^3 \text{ silicon density}) = 4.6 \times 10^{-7} \text{ grams}$$

and amount of energy transferred in a 50ms focused pulse to membrane

$$100 \text{kw/m}^2 * 1 \text{ mm} * 1 \text{ mm} * 50 \text{ ms} = 5 \text{ mJ}, \text{ Maximum PV energy} = 215 \text{ uA} * 2.9 \text{ V} * 50 \text{ ms} = 31 \text{ uJ (ideal)}$$

Heating of Si membrane (heat capacity):

$$(1 / (0.46 \text{ micrograms} * (0.7 \text{ J/g}^{\circ}\text{C}))) * 5 \text{ mJ} = 15.5 \times 10^6 \text{ C (Too high)}$$

Electrical Powering Calculations

In Air,

$$\text{Output Power} = V * I = 1.2 \text{ V} * 8 \text{ uA} = 10 \text{ uWatt}, \text{ Input Power} = 16 \text{ dbm}$$

$$\text{Efficiency} = (10 \text{ uWatt} / 40 \text{ mWatt}) * 100 = 0.25\%$$

Through Tissue

$$\text{Output Power} = V * I = 1.2 \text{ V} * 8 \text{ uA} = 10 \text{ uWatt}, \text{ Input Power} = 19 \text{ dbm}$$

$$\text{Efficiency} = (10 \text{ uWatt} / 100 \text{ mWatt}) * 100 = 0.01\%$$

For thicker tissues, 22dBm was required to power the circuit.

$$\text{Efficiency} = (10 \text{ uWatt} / 158.5 \text{ mWatt}) * 100 = 0.006\%$$

These calculations were done under simplistic assumptions to understand the basic parameters and are not meant for very accurate numerical results.

APPENDIX IV OPTICAL TISSUE PARAMETERS IN NIR REGION

From equation (4.4);

$$\ln(I/I_0) = -\{\alpha + \mu_s'\} \cdot d, \log_{10}(I/I_0) = \ln(I/I_0)/2.3, \text{Loss (dB)} = 10 \times \log_{10}(I/I_0)$$

Using typical parameters, 3mm thick skin (ignoring tissue for subcutaneous implantation), 850nm light, 100% transmission (ideal), $\alpha = 0.1 \text{mm}^{-1}$, $\mu_s' = 1.6 \text{mm}^{-1}$

$$10 \times \log_{10}(I/I_0) = -(0.1 + 1.6) \cdot 30 / 2.3 = -22.17 \text{dB}$$

Including effect of less than 100% transmission (due to reflections)

$$\ln(I/I_0) = \ln(\Gamma) - \{\alpha + \mu_s'\} \cdot d, \text{For 70\% transmission, } \Gamma = 0.7$$

This gives, $10 \times \log_{10}(I/I_0) = 10(-0.35) - 22.17 = -25.67 \text{ dB}$, Loss/mm = 8.5dB/mm

$$\text{Transmission Efficiency} = (I/I_0) \cdot 100 = 0.27\%$$

APPENDIX V CMOS PV PARAMETER CALCULATIONS

The process parameters for a typical CMOS process were used to simulate these devices. The parameters were used from literature[136] and are given in Table 17 and Table 18.

Table 17 Doping Concentrations for Different CMOS regions

Region	Doping
Psub	10^{15}
Pwell	5×10^{17}
Nwell	10^{18}
P+	10^{20}
N+	10^{20}

Minority carrier lifetimes and resulting diffusion lengths are found from graphs in [136] and are listed in Table 18 .

Table 18 Minority carrier lifetimes and Diffusion Lengths for CMOS

Parameter	Value
$\tau_{np\text{subs}}$	110us
$\tau_{np\text{well}}$	10us
τ_{np+}	1.1ns
$\tau_{pn\text{well}}$	1us
τ_{pn+}	1ns
$L_{np\text{subs}}$	130um
$L_{np\text{well}}$	30um
L_{np+}	0.3um
$L_{pn\text{well}}$	10um
L_{pn+}	0.1um

Resulting junction Widths are calculated in Matlab and are given in table 19.

Table 19 Junction Widths in CMOS Process (calculated using doping densities)

Junction	Depletion Width (Junction Width)
P+/Nwell	30nm
N+/Psub	1um
Nwell/Psub	1um

Bibliography

- [1] World Health Organization, "World Health Statistics," 2013.
- [2] Eric Topol, *The Creative Destruction of Medicine: How the Digital Revolution Will Create Better Health Care*. New York, NY: Basic Books, 2012.
- [3] Joseph Wang, "Electrochemical Glucose Biosensors," *Chem. Rev.*, vol. 108, pp. 814-825, 2008.
- [4] World Health Organization. *Factsheets*. Available: <http://www.who.int/mediacentre/factsheets/fs312/en/>
- [5] Chang Ming Li et al., *Implantable Electrochemical Sensors for Biomedical and Clinical Applications: Progress, Problems, and Future Possibilities*, vol. 14: Bentham Science Publishers, 2007.
- [6] A. Milenkovic et al., "Wireless sensor networks for personal health monitoring: Issues and an implementation," *Computer Communications*, vol. 29, pp. 2521-2533, 2006.
- [7] Richard C. Eastman, Timothy C. Dunn, and Janet A. Tamada, "Rates of Glucose Change Measured by Blood Glucose Meter and the GlucoWatch Biographer During Day, Night, and Around Mealtimes," *Diabetes Care*, vol. 27, 2004.
- [8] K. Kreutz-Delgado D. A. Gough, and T. M. Bremer, "Frequency characterization of blood glucose dynamics," *Ann. Biomed. Eng.*, vol. 31, pp. 91-97, 2003.
- [9] *Symptoms of Diabetic*. Available: www.symptomsofdiabetic.com
- [10] R. Hovorka, "Continuous glucose monitoring and closed-loop systems," *Diabetic Medicine*, vol. 23, pp. 1-12, June 2005.
- [11] David A. Gough and Jon C. Armour, "Development of the Implantable Glucose Sensor What Are the Prospects and Why Is It Taking So Long?," *Diabetes*, vol. 44, September 1995.
- [12] A. Caduff et al., "First human experiments with a novel non-invasive, non-optical continuous glucose monitoring system" *Biosensors and Bioelectronics*, vol. 19, pp. 209-217, 2003.
- [13] Janet A. Tamada, Russell O. Potts, and Michael J. Tierney, "Glucose monitoring by reverse iontophoresis," *Diabetes Metab. Res.*, vol. 18, pp. S49-S53, 2002.

- [14] Ishan Barman et al., "Accurate Spectroscopic Calibration for Noninvasive Glucose Monitoring by Modeling the Physiological Glucose Dynamics," *Anal. Chem.*, vol. 82, pp. 6104–6114, 2010.
- [15] U.A. Müller et. al., "Non-invasive blood glucose monitoring by means of near infrared spectroscopy: methods for improving the reliability of the calibration models.," *The International Journal of Artificial Organs*, vol. 20, pp. 285-290, 1997.
- [16] *Shining Light on diabetes*. Available: <http://web.mit.edu/newsoffice/2010/glucose-monitor-0809.html>
- [17] John C. Pickup et al., "In vivo glucose sensing for diabetes management: progress towards non-invasive monitoring," *British Medical Journal*, vol. 319, pp. 1289-U31, Nov. 1999.
- [18] John C. Pickup et al., "In vivo glucose monitoring: the clinical reality and the promise," *Biosensors and Bioelectronics*, vol. 20, pp. 1897-1902, 2005.
- [19] E. Wilkins and P. Atanosov, "Glucose Monitoring: state of the art and future possibilities," *Med. Eng. Phys.*, vol. 18, pp. 273-288, 1996.
- [20] Dae-Hyeong Kim et al., "Epidermal Electornics," *Science*, vol. 333, pp. 4887–4892, 2011.
- [21] Yu-Te Liao et al., "A 3uW CMOS Glucose Sensor for Wireless Contact-Lens Tear Glucose Monitoring," *IEEE Journal of Solid-State Circuits*, vol. 47, January 2012.
- [22] *Tattoo Sensor*. Available: <http://www.iflscience.com/health-and-medicine/tattoo-sensor-actively-monitors-patient>
- [23] *Echo Therapeutics*. Available: <http://www.echotx.com/>
- [24] W. Greatbatch and C.F. Holmes, "History of Implanted Devices," *IEEE Engineering in Medicine and Biology*, pp. 38-49, Sep. 1991.
- [25] P. Zoll et al., "Long-term electric stimulation of the heart for Stokes-Adams disease," *Annals of Surgery*, vol. 154, 1961.
- [26] C.W. Parkins, "Cochlear Implant: A sensory Prosthesis Frontier," *Engineering in Medicine and Biology Magazine*, vol. 2, pp. 18-27, 1983.
- [27] P. Troup, "Early development of defibrillation devices," *Engineering in Medicine and Biology Magazine*, vol. 9, pp. 19-24, 1990.
- [28] K.D. Wise et al., "Wireless Implantable Microsystems: High-Density Electronic Interfaces to the Nervous System," *Proceedings of The IEEE*, vol. 92, pp. 76-97.
- [29] M. Nardin and K. Najafi, "A multichannel neuromuscular microstimulator with bi-directional telemetry," presented at the Transducers, 1995.

- [30] C.C. Collins, "Miniature Passive Pressure Transensor for Implanting in the Eye," *IEEE Transactions on Biomedical Engineering*, vol. BME(14), pp. 74-83, Apr. 1967.
- [31] J. Mouine and K. Ali Ammar, "A miniaturized implantable spinal cord microstimulator for treating intractable chronic pain," presented at the 1st Annual International Conference on Microtechnologies in Medicine and Biology, 2000.
- [32] M. Koudelka-Hep and N. F. de Rooij, "In vivo evaluation of an amperometric glucose sensor implanted subcutaneously in rats," in *Engineering in Medicine and Biology Society*, Oct. 1992, pp. 155-156.
- [33] C. Hierold et al., "Low power integrated pressure sensor system for medical applications," *Sensors and Actuators A-Physical*, vol. 73, pp. 58-67, Mar 1999.
- [34] J. G. Webster, *Medical Instrumentation, Application and Design*. New York, NY: John Wiley & Sons, Inc., 1998.
- [35] D. A. Gough et al., "Function of an Implanted Tissue Glucose Sensor for More than 1 Year in Animals," *Sci. Transl. Med.*, pp. 1-8, 2010.
- [36] Yun Jung Heo and Shoji Takeuchi, "Towards Smart Tattoos: Implantable Biosensors for Continuous Glucose Monitoring," *Adv. Healthcare Mater.*, vol. 2, pp. 43-56, 2013.
- [37] A. Heller, "Implanted electrochemical glucose sensors for the management of diabetes," *Annu. Rev. Biomed. Eng.*, vol. 1, pp. 153-175, 1999.
- [38] George D. Winter, "Transcutaneous implants: Reactions of the skin-implant interface," *Journal of Biomedical Materials Research*, vol. 8, pp. 99-113, 1974.
- [39] *Diatrobe*. Available: www.diatrobe.us
- [40] W. Ryu et al., "Biodegradable micro-osmotic pump for long-term and controlled release of basic fibroblast growth factor," *Journal of Controlled Release*, vol. 124, pp. 98-105, 2007.
- [41] Mohammad Mahdi Ahmadi and Graham A. Jullien, "A Wireless-Implantable Microsystem for Continuous Blood Glucose Monitoring," *IEEE Transactions on Biomedical Circuits And Systems*, vol. 3, June 2009.
- [42] Santhisagar Vaddiraju et al., "Design and Fabrication of a High-Performance Electrochemical Glucose Sensor," *Journal of Diabetes Science and Technology*, vol. 5, September 2011.
- [43] David C. Cunningham and Julie A. Stenken, *In-Vivo Glucose Sensing*: John Wiley & Sons, Inc., 2010.

- [44] W. K. Ward et al., "The effect of microgeometry, implant thickness and polyurethane chemistry on the foreign body response to subcutaneous implants," *Biomaterials* pp. 4185–4192, 2002.
- [45] Behzad Razavi, *CMOS Analog Integrated circuits*: Mcgraw-Hill, 2001.
- [46] J.Ji and K.D.Wise, "An implantable CMOS circuit interface for multiplexed multielectrode recording arrays," *IEEE J. Solid-State Circuits*, vol. 27, pp. 433-443, 1992.
- [47] G.Santhanam et al., "HermesB: A Continuous Neural Recording System for Freely Behaving Primates," *IEEE Trans. BIOCAS*, vol. 54, pp. 2037-2050, 2007.
- [48] K. Najafi, T. Akin, and R. M. Bradley, "A wireless implantable multichannel digital neural recording system for a micromachined sieve electrode," *IEEE J. Solid-State Circuits*, vol. 33, pp. 109-118, 1998.
- [49] Stephen R. Platt. et al., "The Use of Piezoelectric Ceramics for Electric Power Generation Within Orthopedic Implants," *IEEE/ASME Transactions on Mechatronics*, vol. 10, August 2005.
- [50] E.O. Torres and G.A. Rincon-Mora, "A 0.7- μm BiCMOS Electrostatic Energy-Harvesting System IC," *IEEE Journal of Solid-State Circuits*, vol. 45, Feb. 2010.
- [51] R. Venkat Subramanian et al., "Energy Harvesting for Electronics with Thermoelectric Devices using Nanoscale Materials," *Electron. Devices Meeting*, pp. 367-370, Dec. 2007.
- [52] F. Yildiz, "Potential Ambient Energy-Harvesting Sources and Techniques," *Journal of Technology Studies*, vol. 35, pp. 40-48, 2009.
- [53] B. Smith et al., "An externally powered, multichannel, implantable stimulator for versatile control of paralyzed muscle," *IEEE Trans. Biomed. Eng.*, vol. BME-34, pp. 499-508, July 1987.
- [54] N. Tesla, "Apparatus for Transmitting Electrical Energy," U.S. Patent, 1902.
- [55] L. Yang et al., "RF powering for embedded glaucoma sensors in miniature packages," in *Proc. Union Radio Scientifique Internationale General Assembly*, Chicago, IL, Aug. 2008.
- [56] D. Kurup et al., "Path-loss model for in-body communication in homogeneous human muscle tissue," *Electron. Lett.*, vol. 45, pp. 453-454, Apr. 2009.
- [57] N. Guilar et al., "Integrated solar energy harvesting and storage," *IEEE Trans. Very Large Scale Integr. (VLSI) Syst.*, vol. 17, pp. 627-637, May 2009.

- [58] U. Jow and M. Ghovanloo, "Optimization of data coils in a multiband wireless link for a neuroprosthetic implantable devices," *IEEE Trans. Biomed. Circuits Syst.*, vol. 4, pp. 301-310, Jun. 2010.
- [59] W.J. Heetderks, "RF Powering of Millimeter- and Submillimeter-Sized Neural Prosthetic Implants," *IEEE Transactions On Biomedical Engineering*, vol. 35, 1988.
- [60] Dr. Michael Ackermann Jr., "Designing the Optical Interface of a Transcutaneous Optical Telemetry Link," *IEEE Trans Biomed Eng.*, vol. 55, pp. 1365–1373, April 2008
- [61] W. K. Ward, "A review of the foreign-body response to subcutaneously-implanted devices: the role of macrophages and cytokines in biofouling and fibrosis," *J. Diabetes. Sci. Technol.*, vol. 2, pp. 768-777, 2008.
- [62] M. Frost and M.E. Meyerhoff, "In vivo chemical sensors: tackling biocompatibility," *Anal. Chem.*, vol. 78, pp. 7370-7, Nov. 2006.
- [63] Peter Ulrich Abel et al., "Stability of immobilized enzymes as biosensors for continuous application in vitro and in vivo," *Journal of Molecular Catalysis B: Enzymatic*, vol. 7, pp. 93–100, 1999.
- [64] Yoshinori Onuki et al., "A Review of the Biocompatibility of Implantable Devices: Current Challenges to Overcome Foreign Body Response," *Journal of Diabetes Science and Technology*, vol. 2, 2008.
- [65] Mark H. Schoenfisch et al., "Improving the Thromboresistivity of Chemical Sensors via Nitric Oxide Release: Fabrication and in Vivo Evaluation of NO-Releasing Oxygen-Sensing Catheters," *Anal. Chem.*, vol. 72, pp. 1119-1126, 2000.
- [66] B. J. Gilligan et al., "Feasibility of continuous long-term glucose monitoring from a subcutaneous glucose sensor in humans " *Diabetes Technol. Ther.*, vol. 6, 2004.
- [67] Min Chen et al., "Body Area Networks: A Survey," *Mobile Netw. Appl.*, vol. 16, pp. 171–193, 2011.
- [68] Muhammad Mujeeb-U-Rahman and Axel Scherer, "Miniaturized Implantable Electrochemical Sensor Devices," U.S. Patent, 2013.
- [69] Pankaj Vadgama and Paul W. Crump, "Biosensors: Recent Trends, A Review," *Analyst*, vol. 117, November 1992.
- [70] X. Huang et al., "A MEMS Dielectric Affinity Glucose Biosensor," *Journal of Microelectromechanical Systems*, vol. 23, Feb. 2014.
- [71] Leland C.Clark Jr. and Eleanor W.Clark, "A Personalized History of the Clark Oxygen Electrode," *International Anesthesiology Clinics*, vol. 25, pp. 1-29, Fall 1987.

- [72] S. J. Updike and G. P. Hicks, "The Enzyme Electrode," *Nature Biotechnology*, vol. 214, pp. 986-988, June 1967.
- [73] P. H. Kvist et al., "Biocompatibility of an enzyme-based, electrochemical glucose sensor for short-term implantation in the subcutis," *Diabetes Technol. Therapeut.*, vol. 8, pp. 546-559, 2006.
- [74] Santhisagar Vaddiraju et al., "Technologies for Continuous Glucose Monitoring: Current Problems and Future Promises," *J Diabetes Sci. Technol.*, vol. 4, 2010.
- [75] Megan C. Frost and Mark E. Meyerhoff, "Implantable chemical sensors for real-time clinical monitoring: progress and challenges," *Current Opinion in Chemical Biology*, vol. 6, pp. 633-641, 2002.
- [76] Allen J. Bard and Larry R. Faulkner, *Electrochemical Methods: Fundamentals and Applications*, 2nd ed.: John Wiley&Sons, Inc., 2001.
- [77] M. Lambrechts and W. Sansen, *Biosensors: Microelectrochemical Devices*: IOP Publishing, 1992.
- [78] Muhammad Mujeeb-U-Rahman et al., "Micro/Nano Patterned Integrated Electrochemical Sensors for Implantable Applications," in *Nanotech*, 2013.
- [79] Jiri Janata and Mira Josowicz, "Chemical Sensors " *Anal. Chem.*, vol. 70, pp. 179R-208R, 1998.
- [80] Ronald L. Fournier, *Basic Transport Phenomenon in Biomedical Engineering*: Taylor & Francis Group, 2007.
- [81] Dorothee Grieshaber et al., "Electrochemical Biosensors - Sensor Principles and Architectures," *Sensors*, vol. 8, pp. 1400-1458, 2008.
- [82] Makoto Motoyoshi, "Through Silicon Via (TSV)," in *Proceedings of the IEEE*, 2009.
- [83] Hankil Boo, Sejin Park, and Taek Dong Chung, "Electrochemical non-enzymatic glucose sensors," *Analytica Chimica Acta*, vol. 556, pp. 46-57, 2006.
- [84] Peter B. Lillehoj, Fang Wei, and Chih-Ming Ho, "DNA Diagnostics: Nanotechnology-enhanced Electrochemical Detection of Nucleic Acids," *Pediatr Res.* , vol. 67, pp. 458-468, 2010.
- [85] M. Waleed Shinwari et al., "Microfabricated Reference Electrodes and their Biosensing Applications," *Sensors*, vol. 10, pp. 1679-1715, 2010.
- [86] Guigen Zhang, "Design and Fabrication of 3D Skyscraper Nanostructures and Their Application as Electrodes " in *Biosensors, New Perspectives in Biosensors Technology and Applications*, Prof. Pier Andrea Serra, InTech Publishers, 2011.

- [87] Jay W. Grate, Jungbae Kim, and Ping Wang, "Nanostructures for enzyme stabilization," *Chemical Engineering Science*, vol. 61, pp. 1017-1026, 2006.
- [88] Muhammad Mujeeb-U-Rahman and Axel Scherer, "Fabrication of Three-Dimensional High Surface Area Electrodes " U.S. Patent, 2013.
- [89] M. R. Howlader, S. Mohtashami, and T. E. Doyle, "Comparative Electrochemical Investigation of Pt, Au and Ti Electrodes on Liquid Crystal Polymer for the Application of Neuromuscular Prostheses," *ECS Transactions*, vol. 35, pp. 23-33, 2011.
- [90] Geng-huang Wu et al., "Non-enzymatic electrochemical glucose sensor based on platinum nanoflowers supported on graphene oxide," *Talanta*, vol. 105, pp. 379-385, 2013.
- [91] Syed M. Usman Ali et al., "Wireless Remote Monitoring of Glucose Using a Functionalized ZnO Nanowire Arrays Based Sensor," *Sensors* vol. 11, pp. 8485-8496, 2011.
- [92] K.E. Petersen, "Silicon as a mechanical material," in *Proc. of the IEEE.*, 1982.
- [93] S.M. Park and J.S. Yoo, "Electrochemical impedance spectroscopy for better electrochemical measurements," *Analytical Chemistry*, vol. 75, pp. 455A-461A, 2003.
- [94] Gamry Instrument, "Electrochemical Impedance Spectroscopy Theory: A Primer," 2005
- [95] Roger A. Sheldon, "Enzyme Immobilization: The Quest for Optimum Performance," *Adv. Synth. Catal.*, vol. 349, pp. 1289-1307, 2007.
- [96] Stefan Zimmermann et al., "In-device enzyme immobilization: wafer-level fabrication of an integrated glucose sensor," *Sensors and Actuators A-Physical*, 2003.
- [97] Jean Marie Glandie, Ahmed Haouz, and Bernard Alpert "Involvement of protein dynamics in enzyme stability: The case of glucose oxidase," *FEBS Letters*, vol. 506, pp. 216-220, 2001.
- [98] P.N. Bartlett and J.M. Cooper, "A review of the immobilization of enzymes in electropolymerized films," *Journal of Electroanalytical Chemistry*, vol. 362, pp. 1-12, 1993.
- [99] Nico F. de Rooji, Milena Koudelka-Hep, and David J. Strike, "Immobilization of Enzymes and Cells." vol. 1, Gordon F. Bickerstaff, New Jersey: Humana Press, 1997, pp. 77-82.
- [100] P.N. Bartlett and K.F.E. Pratt, "Theoretical treatment of diffusion and kinetics in amperometric immobilized enzyme electrodes. Part I: Redox mediator entrapped within the film," *Journal of Electroanalytical Chemistry*, vol. 397, pp. 61-78, 1995.

- [101] Philip N. Bartlett and Daren J. Caruana, "Electrochemical Immobilization of Enzymes Part V. Microelectrodes for the Detection of Glucose Based on Glucose Oxidase Immobilized in a Poly(phenol) Film " *ANALYST*, vol. 117, August 1992.
- [102] Seiya Tsujimura et al., "Novel FAD-dependent Glucose Dehydrogenase for a dioxygen insensitive glucose biosensor," *Biosc. Biotech. Biochem.*, vol. 70, pp. 654-659, 2006.
- [103] L. Gorton et al., "Direct electron transfer between heme-containing enzymes and electrodes as basis for third generation biosensors " *Analytica. Chimica. Acta.* , vol. 400, pp. 91-108, 1999.
- [104] Adrian C. Michael Michael V. Pishko, and Adam Heller "Amperometric Glucose Microelectrodes Prepared through Immobilization of Glucose Oxidase in Redox Hydrogels," *Anal. Chem.* , vol. 1001, pp. 2268-2272.
- [105] Anthony E. G. Cass et al., "Ferrocene-mediated enzyme electrode for amperometric determination of glucose," *Anal. Chem.*, vol. 56, pp. 667-671, 1984.
- [106] I. Willner et al., "Integrated Enzyme-Based Biofuel Cells—A Review," *Fuel Cells*, vol. 9, pp. 7-24, 2009.
- [107] Arjang Hassibi et al., "Comprehensive study of noise processes in electrode electrolyte interfaces," *J. Appl. Phys.*, vol. 96, July 2004.
- [108] Izabela Galeska et al., "Calcification-Resistant Nafion/Fe³⁺ Assemblies for Implantable Biosensors," *Biomacromolecules*, vol. 1, pp. 202-207, 2000.
- [109] Katsuhiko Kojima Stefano Ferri, and Koji Sode, "Review of Glucose Oxidases and Glucose Dehydrogenases: A Bird's Eye View of Glucose Sensing Enzymes," *Journal of Diabetes Science and Technology*, vol. 5, 2011.
- [110] Kenneth Lan et al., "A Disposable Tear Glucose Biosensor—Part 3: Assessment of Enzymatic Specificity," *Journal of Diabetes Science and Technology*, vol. 5, September 2011.
- [111] Michael G. Hill, T. Gregory Drummond, and Jacqueline K. Barter, "Electrochemical DNA Sensors," *Nature Biotechnology*, vol. 21., pp. 1192-1199, 2003.
- [112] A.A. Rowe et al., "Fabrication of Electrochemical-DNA Biosensors for the Reagentless Detection of Nucleic Acids, Proteins and Small Molecules," *Jove*, vol. 52, 2011
- [113] Kagan Kerman and Eiichi Tamiya Mun'delanji Vestergaard, "An Overview of Label-free Electrochemical Protein Sensors," *Sensors*, vol. 7, pp. 3442-3458, 2007.
- [114] Jennifer Y. Gerasimov et al., "Development of an electrochemical insulin sensor based on the insulin-linked polymorphic region," *Biosensors and Bioelectronics*, vol. 42, pp. 62–68, 2013.

- [115] Chiharu Kiyohara Kazunori Ikebukuro, and Koji Sode, "Novel electrochemical sensor system for protein using the aptamers in sandwich manner," *Biosensors and Bioelectronics* vol. 20, pp. 2168–2172, 2005.
- [116] R. D. O'Neill, "Microvoltammetric techniques and sensors for monitoring neurochemical dynamics in vivo. A review," *Analyst*, vol. 119, pp. 767-779, 1994.
- [117] T.R. Melen et al., "A CMOS Implantable Multielectrode Auditory Stimulator for the Deaf," *IEEE Journal of Solid-State Circuits*, vol. 10, pp. 472-479, 1975.
- [118] Dongjin Seo et al., "Neural Dust: An Ultrasonic, Low Power Solution for Chronic BrainMachine Interfaces", Available: <http://arxiv.org/abs/1307.2196>
- [119] Muhammad Mujeeb-U-Rahman , Chieh-Feng Chang and Axel Scherer , "Optical Methods for Wireless Implantable Sensing Platforms," in *SPIE San Diego, USA*, 2013.
- [120] Sahar Ayazian and Arjang Hassibi , "Delivering Optical Power to Subcutaneous Implanted Devices," in *33rd Annual International Conference of the IEEE EMBS*, August 2011.
- [121] David K. Cheng, *Field and Wave Electromagnetics*: Prentice Hall, 1989.
- [122] A.N. Bashkatov et al., "Optical properties of human skin, subcutaneous and mucous tissues in the wavelength range from 400 to 2000nm," *J. Phys. Dermatology:Appl. Phys.*, vol. 38, pp. 2543-2555, 2005.
- [123] R.R. Anderson and J.A. Parrish, "The Optics of Human Skin," *Journal of Investigative Dermatology*, vol. 77, pp. 13-19, 1981.
- [124] Joseph Jasper. *Layers of human skin*. Available: <http://sketchup.google.com/3dwarehouse/details?mid=fb67c58b41a468dc2347fdb8269abb0&prevstart=0>
- [125] Aravind Krishnaswamy and G. Baranoski, "A study on skin optics," University of Waterloo, Canada, 2004.
- [126] C.R. Simpson et al., "Near-infrared optical properties of ex vivo human skin and subcutaneous tissues measured using the Monte Carlo inversion technique," *Phys. Med. Biol.*, vol. 43, pp. 2465-2478, 1998.
- [127] Van Gemert et al., "Skin Optics," *IEEE transactions on Biomedical Engineering*, vol. 36, pp. 1146-1154, 1989.
- [128] I.V. Meglinski and S. J. Matcher, "Quantitative assessment of skin layers absorption and skin reflectance spectra simulation in the visible and near-infrared spectral regions," *Physiol Meas.*, vol. 23, pp. 741-753, Nov. 2002.

- [129] Julie Bykowski, George Zonios, and Nikiforos Kollias, "Skin Melanin, Hemoglobin, and Light Scattering Properties can be Quantitatively Assessed In Vivo Using Diffuse Reflectance Spectroscopy," *Journal of Investigative Dermatology* vol. 117, pp. 1452-1457, 2001.
- [130] S.A. Prahl, W. Cheong, and A.J. Welch, "A review of the optical properties of Biological Tissues," *IEEE J. of Quantum Electronics*, vol. 26, pp. 563-568, 1990.
- [131] S.A. Prahl, "Light Transport in Tissues," PhD, U.T. Austin, 1988.
- [132] I. M. Vellekoop and C. M. Aegerter, "Focusing light through living tissue," Physics Institute, University of Zurich, Feb. 2010.
- [133] Jan M. Rabaey, *Digital Integrated Circuits : A Design Perspective*: Prentice Hall, 1995.
- [134] Edward D. Palik, *Handbook of Optical Constants of Solids*. New York & Boston: Goodwin House Publishers, 1997.
- [135] *PV Education*, Available: <http://www.pveducation.org/pvcdrom/solar-cell-operation/quantum-efficiency>
- [136] S.M. Sze and Kwok K. NG, *Physics of Semiconductor Devices*, John Wiley & Sons, 2007.
- [137] R.J. Perry, "Analysis and Characterization of the Spectral Response of CMOS based Integrated Circuit (IC) Photodetectors," presented at the Proceedings of the Thirteenth Biennial Microelectronics Symposium, 1999.
- [138] Richard I. Hornsey, Ji Soo Lee, and David Renshaw, "Analysis of CMOS Photodiodes—Part I: Quantum Efficiency," *IEEE Transactions on Electron Devices*, vol. 50, May 2003.
- [139] Kartikeya Murari et al., "Which Photodiode to Use: A Comparison of CMOS-Compatible Structures," *IEEE Sensors Journal*, vol. 9, July 2009.
- [140] M. K. Law et al., "High-Voltage Generation with Stacked Photodiodes in Standard CMOS Process," *Electron. Devic. Lett.*, vol. 31, pp. 1425-1427, 2010.
- [141] O. Aktan et al., "Optoelectronic CMOS Power Supply Unit for Electrically Isolated Microscale Applications," *IEEE J. Sel. Top. Quant.*, vol. 17, pp. 747-756, 2011.
- [142] Dr. Michael Ackermann Jr. et al., "Design of a High Speed Transcutaneous Optical Telemetry Link", EMBS Annual International Conference, New York City, USA, 2006.
- [143] *U-L-M Photonics*. Available: <http://www.photonics.philips.com/>
- [144] Y. Ito. et al., "Assessment of heating effects in skin during continuous near infrared spectroscopy," *Journal of Biomedical Optics*, vol. 5, pp. 383-390, Oct. 2000.

- [145] B. Onaral and A. Bozkurt, "Safety assessment of near infrared light emitting diodes for diffuse optical measurements," *Biomedical Engineering Online*, vol. 3, 2004.
- [146] Office for Research Safety, *Laser Safety Handbook*, Northwestern University, 2011.
- [147] Sanghoek Kim, John S. Ho, and Ada S. Y. Poon, "Midfield Wireless Powering for Implantable Systems," in *Proceedings of the IEEE*, pp. 1369 - 1378, , June 2003
- [148] M. Soma et al., "Radio-Frequency Coils in Implantable Devices: Misalignment Analysis and Design Procedure," *IEEE Transactions on Biomedical Engineering*, vol. BME-34, pp. 276-282, 1987.
- [149] Z. Tang et al., "Data Transmission from an Implantable Biotelemetry by Load-Shift Keying Using Circuit Configuration Modulator," *IEEE Transactions on Biomedical Engineering*, vol. 42, May 1995.
- [150] Nathan M. Neihart and Reid R. Harrison, "A Low-Power FM Transmitter for Use in Neural Recording Applications," in *Proceedings of the 26th Annual International Conference of the IEEE EMBS*, September 1-5, 2004.
- [151] Christian Sauer et al., "Power Harvesting and Telemetry in CMOS for Implanted Devices," *IEEE Transactions On Circuits And Systems—I: Regular Papers*, vol. 52, December 2005.
- [152] M. Ghovanloo et al., "A Wide-Band Power-Efficient Inductive Wireless Link for Implantable Microelectronic Devices Using Multiple Carriers," *IEEE Trans. CAS I*, vol. 54, pp. 2211 - 2221, Oct. 2007.
- [153] M. Kesler, "Highly Resonant Wireless Power Transfer: Safe, Efficient, and over Distance," WiTriCity, 2013.
- [154] N. Chaimanonart and D. J. Young, "Remote RF Powering System for Wireless MEMS Strain Sensors," *IEEE Sensors Journal*, vol. 6, April 2006.
- [155] R. W. Lau, S. Gabriel, and C. Gabriel, "The dielectric properties of biological tissues: III. parametric models for the dielectric spectrum of tissues," *Phys. Med. Biol.*, vol. 41, pp. 2271–2293, Nov. 1996.
- [156] Sanghoek Kim, Anatoly Yakovlev, and Ada Poon. (April 2012) Implantable Biomedical Devices: Wireless Powering and Communication. *IEEE Communications Magazine*
- [157] Mohamad Sawan and Benoit Gosselin, "CMOS Circuits for Biomedical Implantable Devices," in *VLSI Circuits for Biomedical Applications*, Krzysztof Iniewski, Artech house.
- [158] Zhen Ning Low et al., "Design and Test of a High-Power High-Efficiency Loosely Coupled Planar Wireless Power Transfer System," *IEEE Transactions On Industrial Electronics*, vol. 56, May 2009.

- [159] W.J. Heetderks, "RF Powering of Millimeter- and Submillimeter-Sized Neural Prosthetic Implants," *IEEE Transactions On Biomedical Engineering*, vol. 35, May 1988.
- [160] S.P. Liang W.H. Ko, and C.D. Fung, "Design of radio-frequency powered coils for implant instruments " *Comput. Med. Biol. Eng.* , vol. 15, pp. 634–640, 1977.
- [161] D. C. Galbraith et al., "A wide-band efficient inductive transdermal power and data link with coupling insensitive gain," *IEEE Transactions on Biomedical Engineering*, vol. 34, pp. 265-275, Apr 1987.
- [162] T. H. Lee, *The Design of CMOS Radio-Frequency Integrated Circuits*, 2nd ed.: Cambridge University Press, 2003.
- [163] Ada S. Y. Poon, Stephen O'Driscoll, and Teresa H. Meng, "A mm-Sized Implantable Power Receiver with Adaptive Link Compensation," in *ISSCC*, Feb. 2009.
- [164] *Saturn PCB Design*. Available: www.saturnpcb.com
- [165] A. Scuderi et al., "A lumped scalable model for silicon integrated spiral inductors," *IEEE Transactions on Circuits and Systems I: Regular Papers*, vol. 51, pp. 1203-1209,, 2004.
- [166] J. Del Pino et al., "Models and Tools for CMOS Integrated Inductors," *Analog Integrated Circuits and Signal Processing*, vol. 33, pp. 171-178, 2002.
- [167] C. P. Yue et al., "A physical model for planar spiral inductors on silicon ," presented at the International Electron Devices Meeting, 1996.
- [168] *An Internet Resource for the Calculation of the Dielectric Properties of Body Tissues*. Available: <http://niremf.ifac.cnr.it/tissprop/>
- [169] J. M. Lopez-Villegas et al., "Improvement of the quality factor of RF integrated inductors by layout optimization," presented at the IEEE Radio Frequency Integrated Circuits (RFIC) Symposium, 1998.
- [170] M. Danesh and J. R. Long, "Differentially driven symmetric microstrip inductors," *IEEE Transactions on Microwave Theory and Techniques*, vol. 50, pp. 332-341, 2002.
- [171] J. Y. C. Chang et al., "Large suspended inductors on silicon and their use in a 2- μ m CMOS RF amplifier," *IEEE Electron Device Letters*, vol. 14, pp. 246-248, May 1993.
- [172] J. N. Burghartz et al., "Multilevel-spiral inductors using VLSI interconnect technology," *IEEE Electron Device Letters*, pp. 428-430, Sep 1996.

- [173] Muhammad Mujeeb-U-Rahman Meisam Honarvar Nazari, and Axel Scherer, "Implantable Wireless Miniature Fully Integrated Sensing Platform for Healthcare Monitoring," U.S.A Patent, 2014.
- [174] Kyriaki Fotopoulou and Brian W. Flynn, "Wireless Power Transfer in Loosely Coupled Links:Coil Misalignment Model," *IEEE Transactions on Magnetics*, vol. 47, February 2011.
- [175] J. J. Casanova et al., "Transmitting coil achieving uniform magnetic field distribution for planar wireless power transfer system," in *IEEE Radio Wireless Symp*, Jan. 18–22, 2009, pp. 530–533.
- [176] M. Sawan et al., "Multicoils-based inductive links dedicated to power up implantable medical devices: modeling, design and experimental results," *Biomedical Microdevices*, vol. 11, pp. 1059-1070, Oct 2009.
- [177] S. O'Driscoll, "A mm-Sized Implantable Power Receiver with Adaptive Matching," presented at the 9th Annual IEEE Conference on Sensors, Big Island, Hawaii, USA, 2010.
- [178] J. Uei-Ming and M. Ghovanloo, "Design and Optimization of Printed Spiral Coils for Efficient Inductive Power Transmission " presented at the IEEE Electronics, Circuits and Systems, 2007.
- [179] R. R. Harrison et al., "A low-power integrated circuit for a wireless 100-electrode neural recording system," *IEEE Journal of Solid-State Circuits*, vol. 42, pp. 123-133, 2007.
- [180] Ashraf Bin Islam, "Design of Wireless Power Transfer and DataTelemetry System for Biomedical Applications," PhD Dissertation, University of Tennessee.
- [181] Federal Communications Commission (FCC), "Code of Federal Regulations," in Article 47
- [182] G. Lazzi. (2005) Thermal effects of bioimplants. *Engineering in Medicine and Biology*,pp. 75-81.
- [183] IEEE, "IEEE Standard for Safety Levels with Respect to Human Exposure to Radio Frequency Electromagnetic Fields, 3 kHz to 300 GHz," , ed: 2001.
- [184] *FCC SAR*. Available: <http://www.fcc.gov/encyclopedia/specific-absorption-rate-sar-cellular-telephones>.
- [185] B. Odom, "Ultrasound Analog Electronics Primer," , 1999.
- [186] C. Polk and E. Postow, *CRC Handbook of Biological Effects of Electromagnetic Fields*. Boca Raton, FL: CRC Press, 1986.

- [187] Jarir Fadlullah and Mohsen Kavehrad, "Indoor High-Bandwidth Optical Wireless Links for Sensor Networks," *Journal of Lightwave Technology*, vol. 28, November 2010.
- [188] J. B. Carruthers and S. Padma, "Estimation of the capacity of multipath infrared channels," in *Intl. Conf. on Wireless and Optical Communication*, June 2001, pp.148-153.
- [189] B.P. Lathi, *Modern Digital and Analog Communication Systems*: Oxford University Press, 1998.
- [190] B.C. Larson, "An optical telemetry system for wireless transmission of biomedical signals across the skin," Ph.D. dissertation, Dept. Elect. Eng., Massachusetts Institute of Technology, Cambridge, MA, 1999.
- [191] K.I. Inoue et al., "Transcutaneous optical telemetry system using laser diode," *Japanese Journal of Artificial Organs*, vol. 27, pp. 363-367, 1998.
- [192] S.B. Alexander, *Optical Communication Receiver Design*. Bellingham,WA: SPIE Optical Engineering Press, 1997.
- [193] J. Kahn and J. Barry, "Wireless Infrared Communication," in *Proceedings of the IEEE*, pp. 265-298, 1997.
- [194] *FPD510 Sereis Data Sheet*. Available: <http://www.thorlabs.us/catalogpages/V21/1541.PDF>
- [195] J. M. Herrmann G. Hausler Eigensee, and M. W. Lindner, "A new method of short-coherence-interferometry in human skin (in vivo) and in solid volume scatterers," in *Proc. European Biomedical Optics Week, SPIE 2925*, pp. 169-178 , Sept 1996.
- [196] M. R. Haider et al., "Low-Power Low-Voltage Current Readout Circuit for Inductively Powered Implant System," *IEEE Transactions on Biomedical Circuits and Systems*, vol. 4, pp. 205-213, Aug 2010.
- [197] Atif Shamim et al., "Wireless Dosimeter: System-on-Chip Versus System-in-Package for Biomedical and Space Applications," *IEEE Transactions On Circuits And Systems—I: Express Briefs*, vol. 55, July 2008.
- [198] K. V. Seshagiri Rao et al., "Antenna Design for UHF RFID Tags:A Review and a Practical Application," *IEEE Transactions On Antennas And Propagation*, vol. 53, December 2005.
- [199] ECMA International, "Near Field Communication - Interface and Protocol," ed: 2013.
- [200] W. Lih sien et al., "An efficient wireless power link for high voltage retinal implant," presented at the Biomedical Circuits and Systems Conference, 2008.
- [201] B. Smith et al., "An externally powered, multichannel, implantable stimulator telemeter for control of paralyzed muscle," *IEEE Transactions on Biomedical Engineering*, vol. 45, pp. 463-475, Apr 1998.

- [202] Johnson I. Agbinya, "Investigation of Near Field Inductive Communication System Models, Channels And Experiments," *Progress In Electromagnetics Research B*, vol. 49, pp. 129-153, 2013.
- [203] M. Carla L. Busoni, and L. Lanzi, "A comparison between potentiostatic circuits with grounded work or auxiliary electrode," *Rev. Sci. Instrum.*, vol. 73, pp. 1921-1923, Apr. 2002.
- [204] Wei-Song Wang et al., "Wide Dynamic Range CMOS Potentiostat for Amperometric Chemical Sensor," *Sensors*, vol. 10, pp. 1782-1797, 2010.
- [205] Sunitha Ayers et al., "Design of a CMOS Potentiostat Circuit for Electrochemical Detector Arrays," *IEEE Transactions on Circuits And Systems—I: Regular Papers*, vol. 54, April 2007.
- [206] D.J. Harrison, R.B.F. Turner, and H.P. Baltes, "A CMOS potentiostat for amperometric chemical sensors," *IEEE J. Solid-State Circuits*, vol. 22, pp. 473-478, 1987.
- [207] M.M. Ahmadi and G. Jullien, "A low power CMOS potentiostat for bioimplantable applications," in *5th International Workshop on System-on-Chip*, pp. 184–189, 2005.
- [208] Mohammad Mahdi Ahmadi and Graham A. Jullien, "Current-Mirror-Based Potentiostats for Three-Electrode Amperometric Electrochemical Sensors," *IEEE Transactions on Circuits And Systems—I: Regular Papers*, vol. 56, July 2009.
- [209] R. Doelling, "Potentiostats," Bank Elektronik application note, March 2000.
- [210] R. Kakerow et al., "Low-power single-chip CMOS potentiostat," in *8th International Conference on Solid-state sensors and actuators*, pp. 142–145, 1995.
- [211] S. Kounaves, R. Reay, and G. Kovacs, "An integrated CMOS potentiostat for miniaturized electroanalytical instrumentation," in *IEEE International Solid-State Circuits Conference*, 1994, pp. 162–163.
- [212] A. Gore et al., "A multichannel femtoampere sensitivity potentiostat array for biosensing applications," *IEEE Trans. on Circuits and Systems I: Regular Papers*, vol. 53, pp. 2357–2363, 2006.
- [213] H.S. Narula and J.G. Harris, "A time-based VLSI potentiostat for ion current measurements," *IEEE Sensors Journal*, vol. 6, pp. 239–247, 2006.
- [214] Yanan Zhang, Dilbir S. Bindra, and George S. Wilson, "Design and in Vitro Studies of a Needle-Type Glucose Sensor for Subcutaneous Monitoring," *Anal. Chem.*, vol. 53, pp. 1692-1696, 1991.

- [215] Adam Heller and Ben Feldman, "Electrochemistry in Diabetes Management," *Accounts of Chemical Research* vol. 43, pp. 963-973, July 2010.
- [216] Paolo Rossetti et al., "Estimating Plasma Glucose from Interstitial Glucose: The Issue of Calibration Algorithms in Commercial Continuous Glucose Monitoring Devices," *Sensors*, vol. 10, pp. 10936-10952, 2010.
- [217] Oktay Akkus et al., "Evaluation of Skin and Subcutaneous Adipose Tissue Thickness for Optimal Insulin Injection," *J. Diabetes Metabolism*, pp. 3-8, 2012.
- [218] *Myclickfine*. Available: www.myclickfine.com
- [219] *Acino Pharma*. Available: www.acino-pharma.com
- [220] Itamar Willner, "Biomaterials for Sensors, Fuel Cells, and Circuitry," *Science*, vol. 298, pp. 2407-2408, 2002.
- [221] I. Willner et al., "Integrated Enzyme-Based Biofuel Cells—A Review," *Fuel Cells*, vol. 9, pp. 7-24, 2009.
- [222] Fan Yuan Matthew T. Novak, and William M. Reichert, "Modeling the relative impact of capsular tissue effects on implanted glucose sensor time lag and signal attenuation," *Anal Bioanal Chem.*, vol. 398, pp. 1695-1705, 2010.
- [223] George S. Wilson and Raeann Gifford, "Biosensors for real-time in vivo measurements," *Biosensors and Bioelectronics*, vol. 20, pp. 2388-2403, 2005.
- [224] Fotios Papadimitrakopoulo, Siddhesh D. Patil, and Diane J. Burgess, "Concurrent delivery of dexamethasone and VEGF for localized inflammation control and angiogenesis," *Journal of Controlled Release* vol. 117, pp. 68-79, 2007.
- [225] A.S. Sadek, M. Mujeeb-U-Rahman, and A. Scherer, "Implantable vascular system biosensor with grown capillary beds and uses thereof," U.S. Patent, 2012.
- [226] T.M. Seese et al., "Characterization of tissue morphology, angiogenesis, and temperature in the adaptive response of muscle tissue to chronic heating," *Lab Invest.*, vol. 78, pp. 1553-62, 1998.
- [227] Th. von Woedtke et al., "Sterilization of enzyme glucose sensors: problems and concepts," *Biosensors & Bioelectronics*, vol. 17, pp. 373-382, 2002.
- [228] B. J. Gilligan et al., "Evaluation of a subcutaneous glucose sensor out to 3 months in a dog model," *Diabetes Care*, vol. 17, pp. 882-887, 1994.
- [229] Bansi D. Malhotra and Asha Chaubey, "Biosensors for clinical diagnostics industry," *Sensors and Actuators B*, vol. 91, pp. 117-127, 2003.

- [230] D. Henry et al., "Alumina Etch Masks for Fabrication of High-Aspect-Ratio Silicon Micropillars and Nanopillars," *Nanotechnology*, vol. 20, 2009.